

Cardiff University
School of Engineering

Development of techniques for verification of advanced radiotherapy by portal dosimetry

Yasmin Md Radzi

A thesis presented to the School of Engineering,
Cardiff University in partial fulfilment of the requirements
for the degree of Doctor of Philosophy

2018

ACKNOWLEDGEMENTS

Firstly, I wish to thank God for giving me the opportunity to embark on my PhD and for completing this long and challenging journey successfully. My gratitude and thanks go to all my supervisors: Dr. Emiliano Spezi as the academic supervisor and Prof. D. Geraint Lewis and Dr. Rebecca Windle as the clinical/research supervisors. Thank you for the endless support, patience and ideas in assisting me with this project. I also would like to express my gratitude to the staff of the Velindre Cancer Centre (VCC), and Universiti Sains Malaysia (USM), especially School of Physics, for providing the facilities, knowledge and assistance during this endurance.

My greatest appreciation goes to the financier of this PhD study, Ministry of Education Malaysia, for the funds provided for me to go abroad and fulfil my dreams of further study. To the country, I serve.

Finally, this thesis is dedicated to my husband for the trust and support that he has given me, especially when balancing work and family life seemed impossible. Thank you to the friends who were always with me through thick and thin. Finally, yet importantly, this achievement is dedicated to my loving parents for the vision and determination to educate me. Alhamdulillah.

TABLE OF CONTENTS

	Page
DECLARATION / STATEMENTS	II
ACKNOWLEDGEMENTS	II
TABLE OF CONTENTS	III
LIST OF TABLES	VII
LIST OF FIGURES	IX
GLOSSARY OF ABBREVIATIONS	XVII
SUMMARY	1
CHAPTER 1 INTRODUCTION	2
1.1 External Beam Radiotherapy	2
1.2 Radiotherapy accidents and errors	4
1.3 The types of radiotherapy verification	7
1.4 Portal imaging in geometric and dosimetric verification	8
1.4.1 Development of portal imaging	8
1.4.2 Role of EPIDs in advanced radiotherapy verification	9
1.5 Motivation of the research	11
1.6 Thesis outline	14
CHAPTER 2 RADIOTHERPY VERIFICATION	17
2.1 Evolution of IMRT/VMAT verification using portal dosimetry	17
2.1.1 Film-based dosimetry	17
2.1.2 Thermo-luminescent and diode dosimeters	21
2.1.3 EPID dosimetry	22
2.2 Digital network systems and environment	29

2.2.1 PACS system	29
2.2.2 DICOM-RT	34
2.2.3 IMRT/VMAT treatment workflow	40
2.2.4 Record and Verify systems	45
2.2.5 Treatment Planning System	48
CHAPTER 3 DOSE CALCULATION ALGORITHMS IN ADVANCED RADIOTHERAPY	52
3.1 Convolution-based Methods	52
3.1.1 Energy fluence of a photon beam	52
3.1.2 Dose calculation using kernel models in OMP	57
3.2 Monte Carlo dose calculation algorithm	67
3.2.1 Photon transport modelling using EGSnrc package	67
3.2.2 Distributed computing system in VCC	71
3.3 A Deconvolution-based Method	73
3.3.1 Dose calculation algorithm in “Dosimetry Check”	73
CHAPTER 4 MONTE CARLO VERIFICATION OF LINEAR ACCELERATOR AND TREATMENT PLANNING SYSTEM	77
4.1 Monte Carlo modelling of linear accelerator	77
4.1.1 Determination of source size and energy photon	78
4.1.2 Results	87
4.1.3 Discussion	96
4.2 MLC and EPID modelling	96
4.3 Monte Carlo simulation accuracy and efficiency	99
4.3.1 Uncertainty and Variance Reduction Techniques	99
4.4 Verification of OMP using Monte Carlo simulation	105
4.4.1 Methods	106
4.4.2 Results	107

4.4.3 Discussion	115
CHAPTER 5 COMMISSIONING OF DOSIMETRY CHECK FOR VERIFICATION OF ADVANCED RADIOTHERAPY	116
5.1 Dosimetry Check performance	116
5.1.1 Dosimetry Check as an IMRT/VMAT verification tool	116
5.2 Commissioning and validation of Dosimetry Check in VCC	120
5.2.1 Results	121
5.2.2 Clinical implementation	123
5.3 Dosimetry Check and non-uniform backscatter	126
5.3.1 Scatter effect from Varian EPID robotic arm	126
5.3.2 Methods employed to overcome the scatter effect	127
5.3.3 Results	134
5.3.4 Discussion	155
CHAPTER 6 APPLICATION OF DOSIMETRY CHECK TO THE VERIFICATION OF VOLUMETRIC MODULATED ARC THERAPY	157
6.1 New Verification Tool for VMAT Treatment Verification	157
6.1.1 EPID challenges with VMAT delivery technique	157
6.1.2 Rationale of Dosimetry Check use in VMAT verification	161
6.1.3 Methods	162
6.1.4 Introduction of backscatter correction into the VMAT technique	174
6.2 CASE STUDY: VMAT Head-and-Neck pre-treatment verification	178
6.2.1 Methods	178
6.2.2 Results and discussion	181
6.3 Adaptive Arm Backscatter Solution (AdABS) for treatment verification using Dosimetry Check	185
6.3.1 Results and discussion	190
CHAPTER 7 CONCLUSION	195

7.1 Conclusion	195
7.2 Future Work	197
REFERENCES	199
PUBLICATIONS/PRESENTATIONS	213

LIST OF TABLES

	Page
Table 4.1 - Example of parameters used in Monte Carlo EGSnrc package ((I) BEAMnrc / (II) DOSXYZnrc) for the simulation of photon transport through water phantom.	84
Table 4.2 – Gamma passing rates for example of IMRT Head-and-Neck MC simulation for OMP TPS verification result.	113
Table 5.1- Results for several square field sizes tested with the M4 correction matrix. Dose at the POI after correction shows better than 2% agreement with TPS, the profiles are more symmetrical and gamma is improved for coronal and sagittal planes.	135
Table 5.2 - Examples of improvement in asymmetry before (β) and after (α) correction for equidistant points on several strips including some off-axis strips (a) 3x20cm ² field size (b) 5x20cm ² field size	139
Table 5.3 - Percentage point dose measurement difference between Oncentra MasterPlan TPS and Dosimetry Check showing agreement within 3% after application of correction and indicating that this method can be applied to off-axis fields.	142
Table 5.4 - Percentage reduction in point dose for Dosimetry Check relative to the TPS after the application of the correction for (a) transit in-vivo dosimetry (b) pre-treatment dosimetry	145
Table 5.5 - Percentage of points passing gamma criterion of 5%/3mm above a threshold of 20% for transit dosimetry at (a) POI and (b) d _{max} POI.	150
Table 5.6 – Percentage of points passing gamma criterion of 3%/3mm above a threshold of 20% for pre-treatment dosimetry at (a) POI and (b) d _{max} POI	151
Table 5.7 - Gamma index pass rates results for volume V1 delineated within a water phantom.	153
Table 5.8 - Gamma index results for volume V2 delineated within a water phantom.	154
Table 6.1 - Number of acquired images in continuous mode irradiation for a clinical setting compared to number of images acquired in service mode (true value).	166

Table 6.2 - (a) Comparison between dose generated by Dosimetry Check for 600MU 10x10cm ² square field in continuous mode. (b) Comparison between dose generated by Dosimetry Check for 300MU 10x10cm ² square fiend in continuous mode.	168
Table 6.3 - Tabulated result of points passing the gamma criterion and GVH for a pre-treatment VMAT Head-and-Neck pre-treatment plan.	183

LIST OF FIGURES

	Page
Figure 1.1 - Reporting section taken from quarterly data summary issue 8 which focuses on radiotherapy related incidents (National Health Service, UK, 2017).	5
Figure 1.2 - An analysis of the reported accuracy in radiotherapy treatment delivery errors (Taken from Patient Safety Data Summary Issue 8 report (National Health Service, UK, 2017)).	5
Figure 1.3 - An illustration set-up of a typical modern linac with EPID mounted to the linac by a support arm system, i.e. “Exact” arm type for Varian Trilogy system. <i>Red dotted arrow</i> -the linac primary beam, <i>Green dotted arrow</i> -direction of scattered radiation from the arm to the EPID.	12
Figure 1.4 - The coordinate system defined for a linear accelerator with cross-line direction of the beam (X-axis), in-line direction of the beam (Y-axis) and direction perpendicular to the beam (Z-axis)	12
Figure 1.5 - An example of 10x10cm ² field size EPID image acquired with linac (LA5) shows the effect of non-uniform backscatter (<i>red dotted line</i>) shown by in-line beam profile in (b) as the beam cuts through the Y axis of the EPID image (<i>black dotted line</i>) in (a).	13
Figure 1.6 - Illustration of thesis architecture.	16
Figure 2.1 - Structural diagram of (a) radiographic film, and (b) i), ii) and iii); 3 generations of EBT radiochromic film (Image taken from Devic et al. (2005)).	20
Figure 2.2 - Examples of the earliest versions of EPIDs which have been on the market.	24
Figure 2.3 - The structural principle of an indirect flat panel detector, comprising a scintillator, an array (comprising photodiodes D, switch elements S and an active readout matrix made of amorphous silicon) of activation and readout electronics, (with line driver Z and a multiplexer amplifier M) (Soukal and Spahn, 2012).	26
Figure 2.4 - i) A cut out layer of the new Varian PortalVision aS1200 consisting of the detector elements and also a built-in lead plate as shielding from the linac arm backscatter.	26

Figure 2.5 – Radiotherapy network within Velindre Cancer Centre.	31
Figure 2.6 – Examples of PACS mapping employed in Velindre Cancer Centre consisting of preferred and fall-back features of DICOM data transfer.	33
Figure 2.7 – Chart illustrating 5 DICOM-RT objects extending from the DICOM standard. The other 2 objects are extended from the RT Treatment Record (Brachy and EBRT Treatment Record).	35
Figure 2.8 – General procedures involved in RT treatment planning and delivery. STEP 1-5: Treatment Planning, STEP 6-8: Treatment Delivery.	38
Figure 2.9 - Illustration of typical data exchanges between the R&V system and other pieces of equipment in the Velindre Cancer Centre radiotherapy department. DRR - Digitally Reconstructed Radiograph.	47
Figure 2.10 – A screenshot of a DVH analysis of several PTVs, CTVs and OARs (example on a patient’s DVH evaluation done by using Velindre Cancer Centre Oncentra MasterPlan TPS).	51
Figure 3.1 - Interaction history of all dose categories commonly associated with TPS and referred to in dose calculation: primary dose, phantom scatter dose, contaminant charged particle dose, and head scatter dose (Image extracted and reproduced from Ahnesjo and Aspradakis, 1999).	56
Figure 3.2 - Collimating and modulating devices in the beam path (Image taken from Nucletron (2008b)). <i>Red dotted arrow</i> shows the direction of the primary beam	57
Figure 3.3 - (a) A single pencil beam kernel , (b) An example of a 2D fluence dose distribution using the pencil beam model , (c) An actual situation showing the limitation of the pencil beam kernel in underestimating dose at the calculation point because of the lack of backscatter and side-scatter (Radiology Imaging, 2017).	61
Figure 3.4 - (a) Collapsed angular cones within the central axis with energy rectilinearly transported and deposited on the axis. (b) Consequences of the CC approximation to transport energy along a discrete axis. The energy that should be deposited in voxel B’ from interactions at the vertex of the lower cone is deposited in voxel B and vice versa (Image taken from (Ahnesjo, 1989)).	64
Figure 3.5 - Set of directions of the point kernel with angular binnings. There are 106 different directions used in the Oncentra standard configuration. (Image taken from Oncentra –Physics and Algorithms manual version 4.3).	64

Figure 3.6 - A screenshot image of the RTGrid Portal showing the status of a particular simulation job. All 20 distributed machines are in 100% 'Running' mode but not yet completed.	73
Figure 4.1 - A preview of the linac head modelled using BEAMnrc, consisting of the main component modules such as X-ray target, primary collimator, flattening filter, ion chamber, the collimator jaws and also the MLC. (A) XZ view, (B) YZ view	80
Figure 4.2 - A phantom consisting of water equivalent slabs was used in DOSXYZnrc dose calculation for the validation exercise.	80
Figure 4.3 - A flowchart of the general steps involved in the initial validation process.	82
Figure 4.4 - Source type of Elliptical beam with Gaussian distribution in X and Y direction, ISOURCE=19 in BEAMnrc code. A source size with FWHM of 0.1cm (1mm) was used in the simulation (From BEAMnrc User Manual).	83
Figure 4.5 - (a) MC simulation of PDD for a 6MV photon beam energy with field size 10x10cm ² compared to measurement data, normalized at 5cm depth. (b) Relative percentage difference between the MC simulation and the measurement data. The simulation uncertainty is within 2%.	88
Figure 4.6 - (a) Depth dose curve comparison between measured data and MC data for 3 primary electron beam energies (5.9MeV, 6.0MeV and 6.1MeV). (b) Fluctuation of percentage difference for the 3 beam energies.	89
Figure 4.7 - Beam profiles for a 40x40cm ² field in the 'X' direction at two shallow depths in a water phantom (d _{max} and 5cm). Good agreement achieved between simulation and measured data with a percentage difference of less than 2% in the high dose region.	91
Figure 4.8 - Clear graphic of profile shape (zoomed plot from Figure 4.7) for viewing the matching between simulation and measurement. The 'horns' and 'dip' on the simulation profiles were found to be fairly consistent with measurement profiles (uncertainty within 2%).	91
Figure 4.9 - Dose profile comparisons for varying field size at 1.5cm (d _{max}), 5cm, 10cm, 20cm and 30cm depth for 6MV photon beam energy, at 100cm SSD. All the profiles were normalised to 5cm deep (2x2cm ² and 5x5cm ²) and to 10cm (10x10cm ²).	93
Figure 4.10 - MC simulation of PDD for various field sizes showing agreement with the measurement data and giving percentage difference of less than	

2%. Percentage depth dose applied in order to retain the dose relative to d_{max} .	94
Figure 4.11 - Field size output correction factors generated by MC simulation against the measurement output factors (OF) before and after correction for backscatter from the collimators. Note: blue labels – OF before correction, yellow labels - OF after correction. Good agreement of OF after correction with OF from measurement (<i>solid black line</i>) were achieved.	95
Figure 4.12 - (a) VARIAN Millennium 120-leaf MLC, Source: Varian Medical System. (b)Detailed cross-section of the three leaves construction of the VARIAN Millennium 120-leaf MLC; DYNVMLC component module, Source: (Rogers et al., 2011).	97
Figure 4.13-The relationship between MC calculation time, T (hour) and Uncertainty, σ (%) with increasing number of histories, N.	100
Figure 4.14 - N_SPLIT relationship with the efficiency of simulation.	102
Figure 4.15 - 'X' and 'Y' profile comparison between MC and Ionisation Chamber measurement (IC) for 5x30cm ² . All profiles were normalised to central axis depth doses in order to retain the value of 100% at d_{max} . Good agreement was achieved within $\pm 2\%$ in the high dose region.	104
Figure 4.16 – Comparison of percentage Depth Dose curves for 10x10cm ² field between OMP, MC simulation and Ionisation Chamber measurement. Excellent agreement was found (less than $\pm 1\%$). Plotted curves were normalised to 5cm depth and PDD was used to retain the dose distribution of maximum dose along the central axis.	107
Figure 4.17 - 'X' and 'Y' profile comparison between MC and OMP TPS for 10x10cm ² , 5x5cm ² and 3x3cm ² fields. All profiles were normalised to 5cm depth.	109
Figure 4.18 - 'X' and 'Y' profile comparison between IC and OMP TPS for 10x10cm ² , 5x5cm ² and 3x3cm ² fields. All profiles were normalised to 5cm depth.	110
Figure 4.19 – Example of MC simulation of IMRT beam (B01) of Head-and-Neck case compared to the dose calculated by on-site treatment planning. (a) B01 IMRT beam showing the cut along profile; cross-line profile (white dotted line) and in-line profile (green dotted line). (b) cross-line and (c) inline profiles comparison between dose simulated by MC and dose calculated by OMP TPS. The two profiles are in a good agreement; dose differences are within 3% in high dose regions.	111
Figure 4.20 - Example of MC simulation of IMRT beam (B05) of Head-and-Neck case compared to the dose calculated by on-site treatment planning. (a) B05 IMRT beam showing the cut along profile; cross-line profile	

	(<i>white dotted line</i>) and in-line profile (<i>green dotted line</i>). (b) cross-line and (c) inline profiles comparison between dose simulated by MC and dose calculated by OMP TPS. The two profiles are in a good agreement; dose differences are within 3% in high dose regions.	112
Figure 4.21	– Examples of 2D gamma maps for IMRT Head-and-Neck beams showing percentage of points passing two different gamma criteria, 3%, 3mm and 4%, 4mm. (a) B01 and (b) B05	114
Figure 5.1	- (a) Results of the repeated sub-set of commissioning test with the improved kernels from Math Resolutions giving excellent agreement between DC and Oncentra MasterPlan TPS.	122
Figure 5.2	- Non-uniform backscatter from VARIAN imager arm for different field sizes. Effect clearly significant in 3x20cm ² (narrow field size) relative to a standard flood-field calibration. Images of beam profiles were part of the report of the internal commissioning for Dosimetry Check on LA5 at Velindre Cancer Centre.	123
Figure 5.3	- A flow diagram representing the process involved in conformal/IMRT treatment verification using Dosimetry Check software.	125
Figure 5.4	- (a) An example of 2D colourmaps of a 5x20cm ² field case with multiple abutting strips (labelled with A-E) covering the active area of aS1000 EPID as shown in (b).	129
Figure 5.5	- (a) An example of multiple strips from a 5x20cm ² field (labelled with A-E) case where strips were mirrored by the central pixel row (black dotted line) of the EPID image to produce a symmetric profile on the Gantry side along Y axis. Vertical yellow dotted lines represent the points of interpolation taken to get a complete set of correction factors for the EPID.	130
Figure 5.6	– Example of coding in Matlab script for the implementation of the M4 correction matrix and generation of updated EPID images after correction.	132
Figure 5.7	- A process map describing the correction stages from the application of the correction matrix to the analysis of the results.	133
Figure 5.8	- (a) Profile for a 20x20cm ² field in the Y direction generated by Dosimetry Check illustrates that (i) The ‘humps’ before correction are overcorrected by the application of M4 (b) Profile for a 2x2cm ² field (i)before correction, (ii) after the application of the correction	136
Figure 5.9	– (a) Examples of 2D colourmaps of 3x20cm ² strips with equidistant points taken along the superior-inferior direction from the central row of the EPID respectively to certain off-axis distance from the central pixel after correction. <i>Yellow-3cm, red-6cm, green-9cm.</i> (b)	

Corresponding points illustrated on symmetric profiles with the same colour coded marks.	138
Figure 5.10 – Testing of correction matrix with series of off-axis square field patches (labelled with A, C, E and G) in the inferior area (positive values of Y axis of the EPID image) with 2x2cm ² , 3x3cm ² and 5x5cm ² field sizes). Cut through profiles show improvement after correction (<i>blue solid lines</i>) compared with before correction (<i>red dotted lines</i>).	141
Figure 5.11 - Representation of a beam profile B03 cut along Y axis of the EPID image before and after the application of the correction for an IMRT Head-and-Neck case.	147
Figure 5.12 - (a) Change in image intensity at the EPID level before and after correction. (b) Profile comparison between TPS dose and EPID reconstructed dose (in vivo) given by the Dosimetry Check software. Black solid line is TPS dose, <i>red dotted line</i> is DC dose before correction and <i>blue dotted line</i> is Dosimetry Check dose after correction. Agreement between <i>black solid line</i> and <i>blue dotted line</i> is within 1% after correction from more than 3% before correction.	148
Figure 5.13 - Examples of beams involving small segmented fields in the inferior region (the cut through black dashed line varies for each beam). The cut-through profiles show improvement after application of the correction.	149
Figure 5.14 - Outlines of arbitrary volumes V1 (red) and V2 (blue) within a water phantom to demonstrate the difference in Gamma Volume results calculated by Dosimetry Check.	152
Figure 6.1 - Points of interest (POI) set up in TPS on a 10x10cm ² square field size to calculate the difference in dose measured by Dosimetry Check for software reproducibility	163
Figure 6.2 – Dosimetry Check dose response per MU delivered as a function of total MU and dose rate for the integrated acquisition mode showing nearly 0% difference between the two dose rates. Dose responses were normalised at 100MU.	165
Figure 6.3 - Dosimetry Check dose response per MU delivered as a function of total MU and dose rate for the continuous acquisition mode. Dose responses were normalised at 100MU.	165
Figure 6.4 - Dose profiles in the cross-line and in-line directions for a 10x10cm ² arc irradiated at 600MU and calibrated at 300MUmin ⁻¹ with their respective percentage difference (within ±1% in high dose region).	171
Figure 6.5 - Dose profiles in the cross-line and in-line directions for a 10x10cm ² arc irradiated at 600MU and calibrated at 600MUmin ⁻¹ with their	

respective percentage difference (mostly greater than 1.5% in high dose region).	172
Figure 6.6 - Dose profiles in the cross-line and in-line directions for a 10x10cm ² arc irradiated at 600MU and calibrated with a single image produced by the integration of an arc with their respective percentage difference (within 2% in most high dose region).	173
Figure 6.7 - Example of coding in Matlab script used to obtain a set of corrected cine images.	175
Figure 6.8 - Y-axis profiles of TPS (<i>black bold line</i>) and Dosimetry Check dose before and after correction for a 10x10cm ² arc. The Dosimetry Check dose profile before correction (<i>red dotted line</i>) shows the effect of backscatter from the linac arm on the left. The backscatter is improved after correction (<i>yellow bold line</i>). The profiles are normalised to the TPS central axis dose. A zoomed plot is also shown for clarity.	176
Figure 6.9 - Y-axis profiles of TPS (<i>black bold line</i>) and Dosimetry Check dose before and after correction for a 5x18cm ² arc. The Dosimetry Check dose profile before correction (<i>red dotted line</i>) shows the effect of backscatter from the linac arm on the left. The backscatter is improved after correction (<i>yellow bold line</i>). The profiles are normalised to the TPS central axis dose. A zoomed plot is also shown for clarity.	177
Figure 6.10 – (a) Head and Neck phantom used as the RT structure image in the optimisation process through OMP TPS.	179
Figure 6.11 - (a) Profiles cut through the Y axis of a coronal plane of the VMAT plan (<i>yellow dotted line</i>) before (<i>red dotted line</i>) and after correction (<i>blue bold line</i>) for backscatter compared with TPS calculated dose (<i>black bold line</i>). (b) Correction produced an average reduction of 3% in dose difference (taken from the central axis 0cm to-10cm) relative to TPS dose.	181
Figure 6.12 - Graphic presentation of 2D gamma evaluation of the pre-treatment Head-and-Neck VMAT plan for a 3%/5mm criterion. Red area shows regions with failing gamma reconstructed and reported in Dosimetry Check.	184
Figure 6.13 – Step 1: Plan and beam selection.	187
Figure 6.14 - Step 2: Application of correction.	188
Figure 6.15 - Step 3: Calibration of the image.	189

Figure 6.16 - Comparison of in-line profiles for simple fields ($10 \times 10 \text{cm}^2$ and $5 \times 20 \text{cm}^2$) before correction (*red dashed line*), after correction with Matlab script (*green bold line*) and AdABS (*yellow bold line*). Black dashed line is the TPS dose. Good agreement is achieved with dose difference of less than 1.5% for both methods (*purple dotted line*). 192

Figure 6.17 – In-line profiles for a $20 \times 20 \text{cm}^2$ field size before correction (*red dashed line*) and after backscatter correction. The plots show the adjustment to the part of the field (left side of the plots) using the correction matrix for the Matlab script and AdABS methods. However, both methods were in agreement with nearly 1% in percentage dose difference (*purple dotted line*). 193

GLOSSARY OF ABBREVIATIONS

This glossary gives a list of abbreviations used in this thesis with a reference to the page where the term was used for the first time.

a-Si	Amorphous Silicon (page 25)
CaF	Calcium Fluoride (page 21)
CaNISC	Welsh Cancer Network Information System Cymru (page 30)
CPU	Central Processing Unit (page 99)
CT	Computed Tomography (page 7)
DBS	Directional Bremsstrahlung Splitting (page 69)
DICOM	Digital Image and Communication in Medicine (page 14)
IAEA	International Atomic Energy Agency (page 45)
ICRU	International Commission of Radiation Units (page 3)
IR(ME)R	Ionising Radiation (Medical Exposure) Regulations (page 4)
LiF	Lithium Fluoride (page 21)
Linac	Linear Accelerator (page 2)
MRI	Magnetic Resonance Imaging (page 22)
NHS	National Health Service (page 4)
NRLS	National Reporting and Learning System (page 4)
OD	Optical Density (page 18)
PACS	Picture Archiving and Communication System (page 29)
PDD	Percentage Depth Dose (page 55)
QA	Quality Assurance (page 8)
SBS	Selective Bremsstrahlung Splitting (page 85)
TAR	Tissue Air Ratio (page 55)
TERMA	Total Energy Released per unit MAss (page 65)
TFT	Thin-Film-Transistor (page 25)
TMR	Tissue Maximum Ratio (page 55)
TPR	Tissue phantom Ratio (page 55)
UBS	Universal Bremsstrahlung Splitting (page 85)

SUMMARY

This research work is related to the development of an enhanced method for the treatment verification of Intensity Modulated Radiotherapy (IMRT) and Volumetric Modulated Arc Therapy (VMAT). Such advanced treatment techniques require accurate verification procedures to ensure treatments are delivered as correctly as possible.

This work focused on the use of the Varian aS1000 Electronic Portal Imaging Device (EPID) with Dosimetry Check software-based verification system. This EPID-based patient dose verification had been widely discussed and proposed as a way to achieve treatment delivery accuracy and patient safety, and as an 'in vivo' verification technique that helps to avoid or minimise dosimetric errors.

In this work, a novel matrix-based software method to correct for backscatter effects from the Varian aS1000 EPID support arm has been developed. The methodology allows a reliable quantification of the backscatter effect to be applied directly to the Dosimetry Check calibration and verification system. This process includes the use of a clinical treatment planning system (Oncentra MasterPlan, Nucletron) to calculate predicted dose distribution within a phantom or patient, which may be compared to the dose reconstructed by Dosimetry Check.

It has been demonstrated that the developed method can be applied to both 'pre-treatment' and 'on treatment' portal dosimetry for IMRT Head-and-Neck. The Gamma Index Method confirmed excellent validation rates of 97% (3%/3mm) and 95% (5%/3mm) for the 'pre-treatment' and 'on treatment' approach respectively. Pre-treatment verification of VMAT Head-and Neck treatment also reported excellent validation rates of 96% (3%/5mm). In addition, a convenient way to use the developed methodology within Dosimetry Check software was also piloted and tested. This presents an opportunity of future clinical implementation of the techniques developed in this investigation.

Chapter 1

INTRODUCTION

1.1 EXTERNAL BEAM RADIOTHERAPY

External Beam Radiotherapy (EBRT) is one of the radiation delivery methods available to treat cancer using high-energy X-ray beams. The beams are generated by a linear accelerator (linac) to transmit the X-rays through the patient's body to kill cancer cells while sparing the surrounding unaffected normal tissues where possible. Ideally, minimal radiation should pass through normal healthy tissue for a treatment to be successful. Apart from utilising this physical treatment technique, radiotherapy's aim also relies on the biological effects achieved through dose fractionation (The Royal College of Radiologists, 2008(a)).

The rationale of dose fractionation is based on the fact that the cancerous cells and normal tissues possess different radiobiological properties. After irradiation, injured normal tissues can be repaired in around 3-24 hours and this will give a potential therapeutic advantage over the tumour cells to heal from the radiation. Over a period of treatment time, fractionation increases the damage to cancer cells through reoxygenation and redistribution of cells into radiosensitive phases of the cell cycle between fractions. At the same time, normal tissue is able to repopulate and regenerate with reduction of any acute side effects. In

summary, dose fractionation maximises the killing of cancer cells while limiting the damage to surrounding healthy tissues.

The introduction of conformal treatment techniques (Aird, 1989a, Aird, 1989b) has allowed geometrical sparing of organs at risk (OAR) (Chavaudra and Bridier, 2001) and healthy tissues, originally using basic rectangular collimators and blocks and latterly multi-leaf collimators (MLCs) now present in modern radiotherapy linacs. MLC automation takes control of the beam modulation to create a field of any shape required. As a result, complex radiotherapy treatment techniques such as Intensity Modulated Radiation therapy (IMRT) (Galvin et al., 2004) and Volumetric Modulated Arc Therapy (VMAT) (Bertelsen et al., 2010, Alvarez-Moret et al., 2010) can be practically delivered. These treatment techniques offer the capability to deliver highly conformal dose distributions to tumours with steep dose gradients that allow better sparing of adjacent normal tissues.

Treatment outcome is dependent on the accuracy and reproducibility of treatment delivery although both dose fractionation and conformity of treatment improve tumour control and reduce side effects (Thames et al., 1982, Thames, 1992). With steep dose gradients applied to complex radiotherapy treatments, tighter target margins have to be carefully quality assured. Delivery uncertainties as stated in International Commission on Radiation Units (ICRU) reports 50 and 62 may lead to under-dosing of target and/or over-dosing of the OARs (ICRU 1994, 1999). Despite limiting systematic and random uncertainties, occasional treatment errors can sometimes occur with modern radiotherapy as it is a complex multi-step process which requires many inputs from different modalities and sources.

1.2 RADIOTHERAPY ACCIDENTS AND ERRORS

Radiotherapy errors occasionally occur, and their consequences can be significant for patients undergoing treatment. According to “Towards Safer Radiotherapy”, it has been reported that there were 181 incidents affecting 338 patients in the UK under the Ionising Radiation (Medical Exposure) Regulations¹ 2000 (IR(ME)R 2000) from all the radiotherapy departments in the England, Wales and Scotland over the period of May 2000 to August 2006 (The Royal College of Radiologists, 2008(a)). In about 80% of the 181 cases, the patient was not expected to suffer any adverse clinical effects from the error. From the incidents, 90% were caused by a variety of error sources which included practical aspects of the treatment design, preparation or delivery.

A quarterly data summary report issued by the UK National Health Service (NHS), through their National Reporting and Learning System (NRLS), has identified seven main themes, from which radiotherapy errors are most likely to occur (National Health Service, UK, 2017) (Figure 1.1 and Figure 1.2).

¹ Requirements of Ionising Radiations from Department of Health, England with regard to exposures much greater than intended and diagnostic reference levels. Available on : <https://www.gov.uk/government/publications/the-ionising-radiation-medical-exposure-regulations-2000>

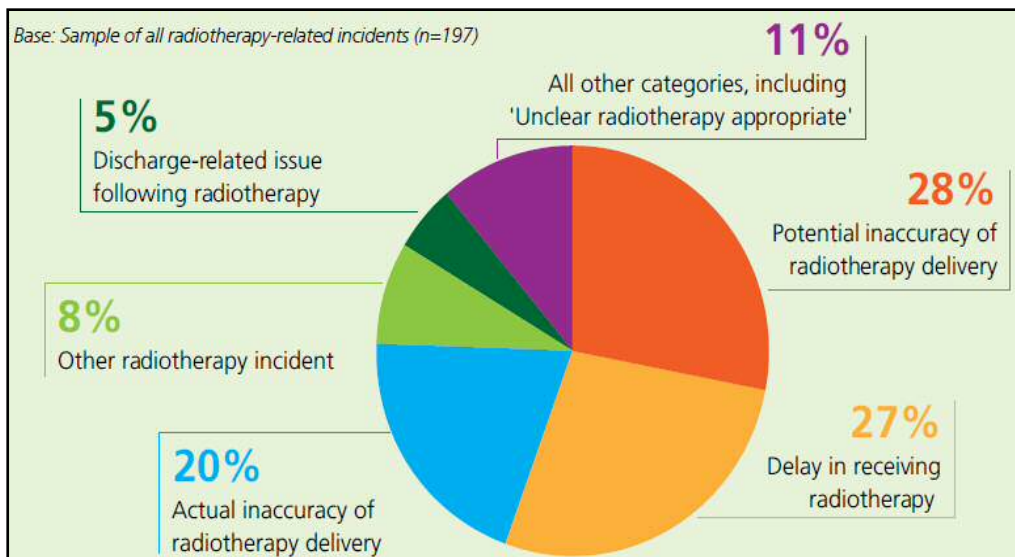


Figure 1.1 - Reporting section taken from quarterly data summary issue 8 which focuses on radiotherapy related incidents (National Health Service, UK, 2017).

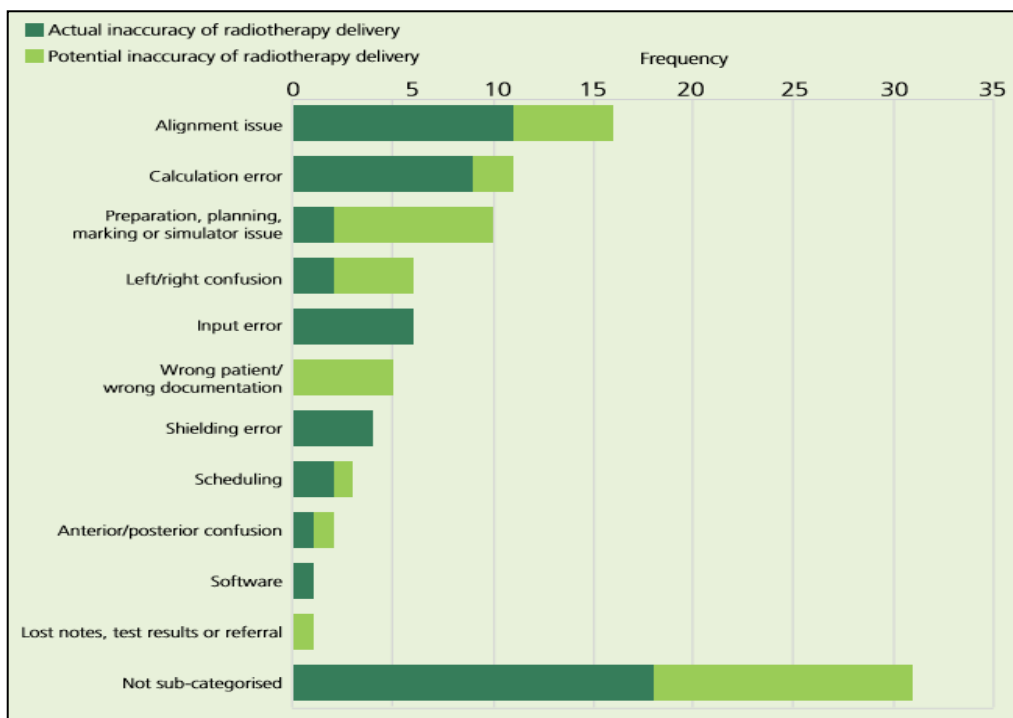


Figure 1.2 - An analysis of the reported accuracy in radiotherapy treatment delivery errors (Taken from Patient Safety Data Summary Issue 8 report (National Health Service, UK, 2017)).

Generally, out of the 197 reviewed radiotherapy-related incidents, the vast majority of incidents were either coded as 'no harm' (77%) or 'low harm' (19%). The remaining four per cent were coded as 'moderate harm' (National Health Service, UK, 2017). One of the recent quarterly radiotherapy Newsletters of Public Health England on radiotherapy incidents and errors, reported that 98.1% of events during April to July 2017 were classified as minor radiation incidents, near misses, or other non-conformances (Public Health England, 2017b). In addition, the previous newsletter published in January 2017 noted some of the points that the Towards Safer Radiotherapy report stated should be considered to prevent future occurrence of similar errors.

“Calculations should be independently checked by a different entitled operator using a different method, for example a reverse calculation (Toward Safer Radiotherapy recommendation 7 and 11)” (Public Health England, 2017a).

Therefore, it is an important requirement to have an accurate system for radiotherapy verification to complement the existing planning and delivery systems. Improving safety in radiotherapy departments has induced a broad set of key recommendations (The Royal College of Radiologists, 2008(a)) from many important areas, one of which is for every radiotherapy centre to have protocols for in vivo dosimetry (IVD) monitoring to be used at the beginning of the treatment course for most patients. IVD is a direct method of measuring radiation doses to cancer patients receiving radiation treatment while helping in identifying possible errors in treatment delivery. This intervention was also recommended by the Chief Medical Officer of NHS England in his Annual Report in 2006 (Donaldson, 2007).

1.3 THE TYPES OF RADIOTHERAPY VERIFICATION

In order to establish whether or not the right radiation dose has been delivered to the right target, two measurement parameters are needed: a) geometric verification, and b) dosimetric verification.

The aim of geometric verification (The Royal College of Radiologists, 2008(b)) is to ensure positional accuracy i.e. that the radiotherapy delivered is within the target limits set by the uncertainty margin defined in the treatment plan. This is achieved by comparing spatial information from the delivery against what is planned. In dosimetric verification, dose information from the treatment delivery, which has been recorded by a detector, is compared to what has been generated by the dose calculation algorithm in the treatment planning system. This is done to ensure that a correct dose is delivered to the patient within the accepted dose tolerance. Moreover, a treatment plan for a patient undergoing radiotherapy should be independently checked prior to the first treatment to ensure the accuracy and validity of the plan throughout the treatment period. There are several steps involved in the process of treatment delivery from the Computed Tomography (CT) imaging and simulation procedures to the volume of interest (VOI) delineation procedures, through to the verification procedures related to the delivery of the treatment. Details on how the radiotherapy physics planning and verification process are implemented in Velindre Cancer Centre, where this work was carried out, will be elaborated in Chapter 2.

1.4 PORTAL IMAGING IN GEOMETRIC AND DOSIMETRIC VERIFICATION

1.4.1 Development of portal imaging

Originally and now, geometric verification of radiotherapy was done using 'portal' radiographic films on kV imaging. While not providing information on patient dosimetry, the use of film made it possible to analyse positional information from the image prior to the delivery of the full treatment. In addition, improved port-film systems for verification purposes were able to produce relatively high-quality images (Langmack and Goss, 1999, Langmack, 2001). Hence, portal radiographic film-based verification has been used routinely over several decades as an essential part of Quality Assurance (QA) in radiotherapy.

Meanwhile, dosimetric verification in radiotherapy can be undertaken by comparing a point dose measurement (either inside or outside the patient) with the dose predicted at the equivalent point by the Treatment Planning System (TPS) (Boyer et al., 1992). Formerly, this was usually done using Thermoluminescent (TLD) or conventional diode dosimeters. However, technology developments in portal imaging over 20 years have given rise to the use of more electronically based planar devices to provide real-time 2D treatment verification (Munro, 1995, Antonuk et al., 1998, Antonuk, 2002). Since then, such devices have had widespread use in radiotherapy as part of the modern linac's design and function. The development of EPIDs for dosimetry has been reviewed by many authors (van Elmpt et al., 2008, McCurdy et al., 2001, McCurdy and Greer, 2009, Mans et al., 2010, Mijnheer et al., 2013a). These authors also reviewed the strategies and approaches for the use of EPIDs in clinical dose

verification and current clinical experience. Some details on the use of TLDs, diodes and EPID dosimeters for radiotherapy verification will be given in Chapter 2.

1.4.2 Role of EPIDs in advanced radiotherapy verification

The role of verification becomes particularly important with the introduction of complex treatment techniques such as IMRT and VMAT that use inverse planning. This is because an accurate radiotherapeutic dose is required to eradicate a tumour while at the same time minimising the radiation exposure to healthy tissue.

Advanced methods for treatment delivery such as IMRT and VMAT require accurate specification of the tumour target volume, sensitive structures (or organs at risk) and associated dose constraints. There is a higher probability of errors occurring in introducing a new and complex technique. This prompted several international bodies to publish QA guidelines to perform patient-specific treatment verification when IMRT was initially introduced into clinical use (Ezzell et al., 2003). There are several EPID dosimetry verification approaches with various methods of dose distribution evaluation either pre-treatment or in-vivo (transit dosimetry). Pre-treatment evaluation essentially refers to the verification of an individual treatment plan before the start of the delivery. It allows detection, and ideally rectification, of an error before the radiation is delivered to the patient. For example, in Stereotactic Radiosurgery, in which high dose is given to the patient in a single fraction, a treatment error could be impossible to correct.

Routinely devised methods to improve verification of IMRT and VMAT have been widely discussed for pre-treatment and transit dosimetry either at the detector plane (Ma et al.,

2000, Leal et al., 2003, Cufflin et al., 2010) or within the patient (*in-vivo*) (Vinall et al., 2010, Sabet et al., 2012, Greer, 2013). However, the latter does not mean that the measurement is taken literally inside the patient, but that the dosimetric information is retrieved via a back-projection method to calculate the dose to the patient. As well as having the advantages of providing actual treatment validity, *in-vivo* dosimetry QA can also detect errors in patient positioning, change in patient anatomy, or obstruction due to the linac table arm or immobilizer devices. An analysis done by Mans et al. (2010) has reported that out of 17 serious errors, nine of them would not have been detected by pre-treatment verification. This has made evident the importance of *in vivo* EPID dosimetry for all treatment plans as well as the ability of the method to assess the dosimetric impact of deviations that were found.

The latest and more sophisticated method to deal with *in-vivo* transit dosimetry is the use of software and EPID-based verification instead of more conventional approaches like port films and diodes. Usually, by using EPID-based verification, an independent dose calculation is performed and verified against the TPS; therefore, no further physical measurement is required on each treatment plan. Moreover, EPID-based software verification offers significant time saving compared to other hardware-based verification (Siochi et al., 2013).

Dosimetry Check™ is an EPID-based verification software system that has been utilised and evaluated in several centres (Fafi et al., 2013, Reilly et al., 2013, Narayanasamy et al., 2015). It has provided a potentially useful and effective treatment verification tool. Furthermore, its features include point dose and profile verification with gamma analysis (see detail in Chapter 3) as well as dose volume histogram (DVH) presentation in full report form (Math Resolutions,

2017). More detailed explanation on the Dosimetry Check algorithm and its features are included in Chapter 3.

1.5 MOTIVATION OF THE RESEARCH

Methods and challenges with EPID verification have been well documented over the past few years, especially for amorphous silicon EPIDs (Boyer et al., 1992, Cremers et al., 2004, Winkler et al., 2005, Parent et al., 2007, Mans et al., 2010, Pejman et al., 2010, Rowshanfarzad et al., 2010b, Greer, 2013). Still, one of the main technical challenges with certain EPID imagers (especially the Varian aS500 and aS1000 panels currently in widespread use) is that they produce a non-uniform dose distribution resulting from backscatter from the linac support arm (Monville et al., 2014), leading potentially to systematic errors in verification measurements.

Figure 1.3 shows the linac set-up with the EPID mounted on the linac by a support system beneath the imager. The cartesian coordinates for the linac are shown in Figure 1.4. The backscattered radiation from the support arm contributes to a significant (>5%) non-uniformity and asymmetry in the beam profiles along 'in-line' (Y) direction on the EPID image (Figure 1.5). It has also been reported that the magnitude of the 'cross-line' (X) directional asymmetry was around 1%, due to some additional wiring and casing to one side of the imager (Cufflin, 2012). However, for the aim of this study, attention was driven to the asymmetry formed in the in-line direction. Detailed studies should be done beyond the scope of this research, to investigate the dependency of certain parameters contributing to the cross-line asymmetry.

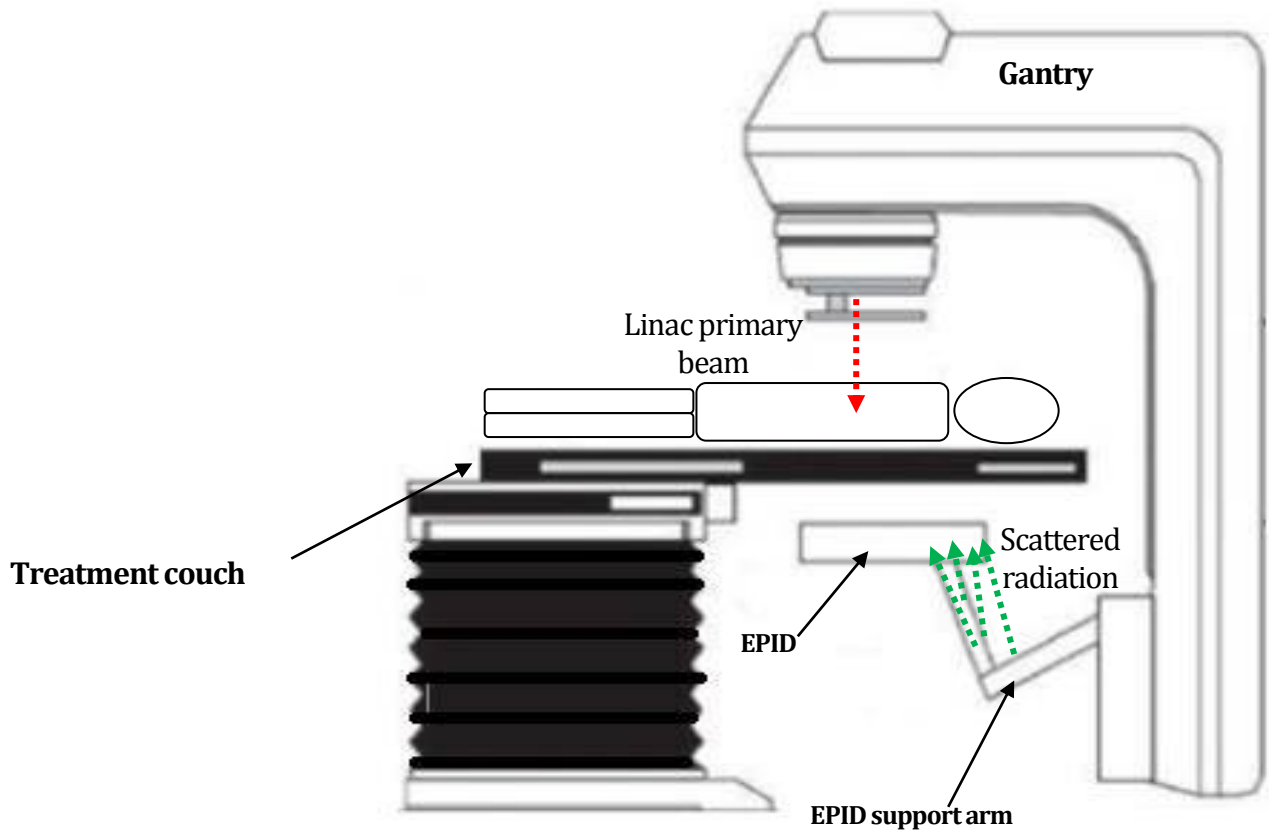


Figure 1.3 - An illustration set-up of a typical modern linac with EPID mounted to the linac by a support arm system, i.e. "Exact" arm type for Varian Trilogy system. *Red dotted arrow*-the linac primary beam, *Green dotted arrow*-direction of scattered radiation from the arm to the EPID.

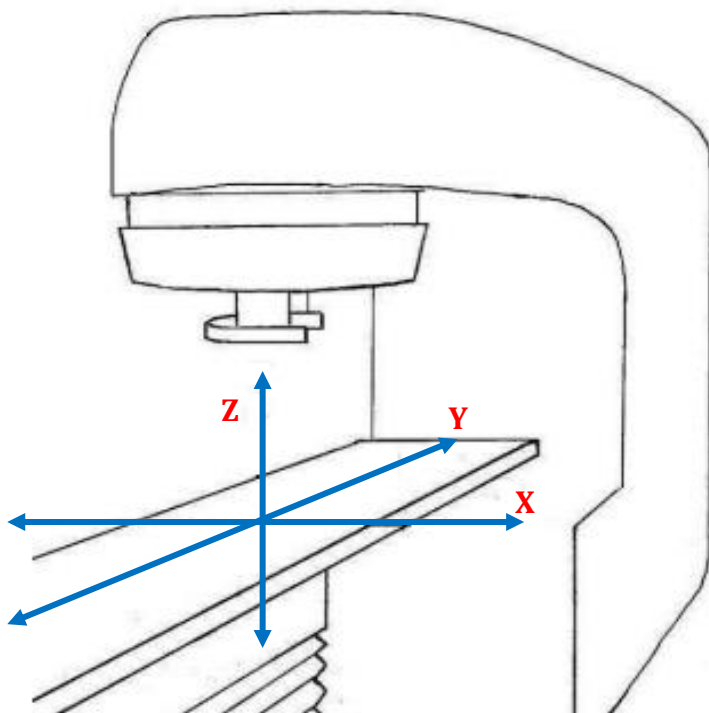


Figure 1.4 - The coordinate system defined for a linear accelerator with cross-line direction of the beam (X-axis), in-line direction of the beam (Y-axis) and direction perpendicular to the beam (Z-axis)

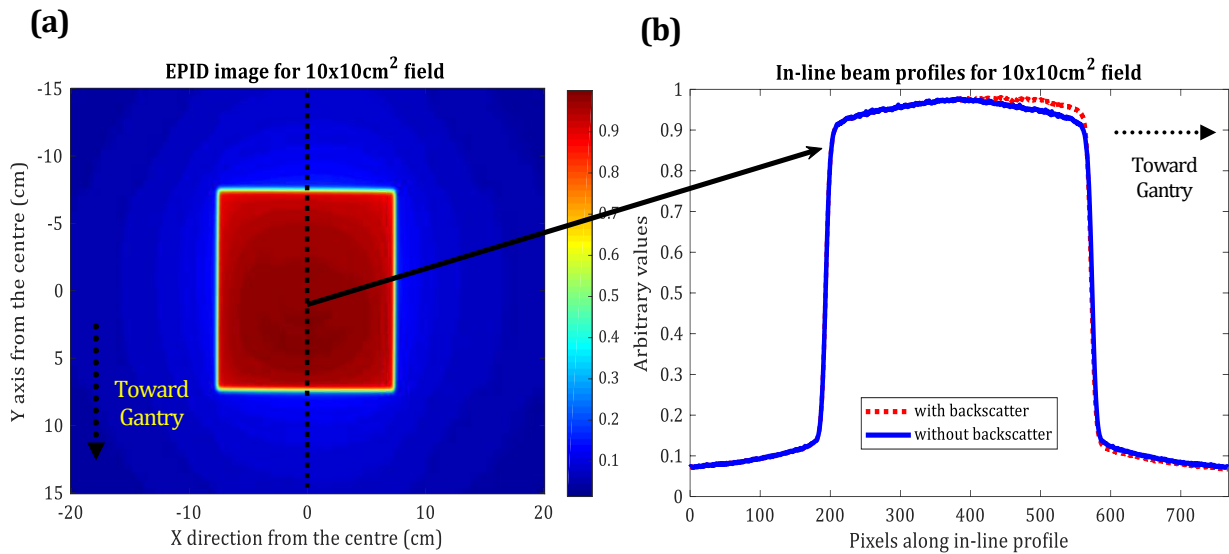


Figure 1.5 - An example of 10x10cm² field size EPID image acquired with linac (LA5) shows the effect of non-uniform backscatter (*red dotted line*) shown by in-line beam profile in (b) as the beam cuts through the Y axis of the EPID image (*black dotted line*) in (a).

From the literature, as the ionising radiation passes through the patient, it undergoes interaction with tissues in the body as described in Chapter 3, Figure 3.1. Dose which has been absorbed in the patient's body is a result of the contribution of the various components of the radiation interaction processes such as primary dose, phantom scatter dose, contaminant charged particle dose, and head scatter dose. Radiation passing through the patient's body without interaction, along with an amount of scattered radiation reaches the EPID positioned 'downstream' from the patient. Section 3.2.1 discusses in detail the relevant interaction processes and their dependencies on energy and atomic number.

The radiation incident on the EPID is converted to measurable signal as detailed in Chapter 2, section 2.1.3. Radiation backscattered from the EPID support arm and auxiliary components introduce an artificial asymmetry in the EPID image as illustrated in Figure 1.3. The effect is known as "non-uniform backscatter" and is visible in the in-plane direction in the

upper half of the imager panel where the arm is mounted, which provides the largest source of backscatter (Figure 1.5). This effect has to be accounted for when performing dose verification.

Hence, for this research, emphasis will be given in addressing this issue by introducing a novel method of reducing this backscatter effect from the EPID (Varian aS1000) arm in use locally. This research aims to develop a key correction to improve the accuracy of radiotherapy verification (IMRT/VMAT) by evaluation of the long-standing challenge of EPID non-uniform backscatter, to make Dosimetry Check a reliable independent radiotherapy verification tool.

1.6 THESIS OUTLINE

This thesis is organised in the following way and summarised pictorially in Figure 1.6.

Chapter 2 introduces the evolution of verification techniques used in radiotherapy and how their application to modern methods enhances treatment verification. This chapter also includes a description of the Velindre Cancer Centre networking system, including the Picture Archiving and Communication System (PACS), and how medical image and radiotherapy data are transmitted, stored and used in the Digital Image and Communication in Medicine (DICOM²) format.

Chapter 3 discusses the methods involved in radiotherapy dose calculation and includes a description of algorithms used in the Oncentra MasterPlan TPS used clinically in Velindre

² <http://dicom.nema.org/standard.html>

Cancer Centre and the photon transport modelling algorithm in the Electron Gamma Shower (EGSnrc) Monte Carlo (MC) code. This chapter also includes the deconvolution-based method used in the Dosimetry Check software package for dosimetric back projection, which is the core methodology of this research.

Chapter 4 reports on the modelling work of the Varian 2100CD TRILOGY linac system (in use clinically at Velindre Cancer Centre) carried out using the BEAMnrc and DOSXYZnrc Monte Carlo codes which are based on the EGSnrc code system. In addition, Oncentra dose calculations were verified by Monte Carlo simulation and 3-way comparison was done with measurements by diode and ionisation chamber.

Chapter 5 gives details on the commissioning of the Dosimetry Check system performed as part of this work, including the application of a novel backscatter correction from the EPID arm to improve the verification accuracy for IMRT delivery techniques for pre-treatment and exit dosimetry.

Chapter 6 investigates the application of the novel backscatter correction method to the VMAT technique for pre-treatment verification purposes. In addition, the utilisation of the correction method is explored in terms of benefit to clinical use by enhancing the accuracy of Dosimetry Check.

Chapter 7 summarises the whole thesis and discusses the outcomes of the research. This chapter also identifies areas for future development.

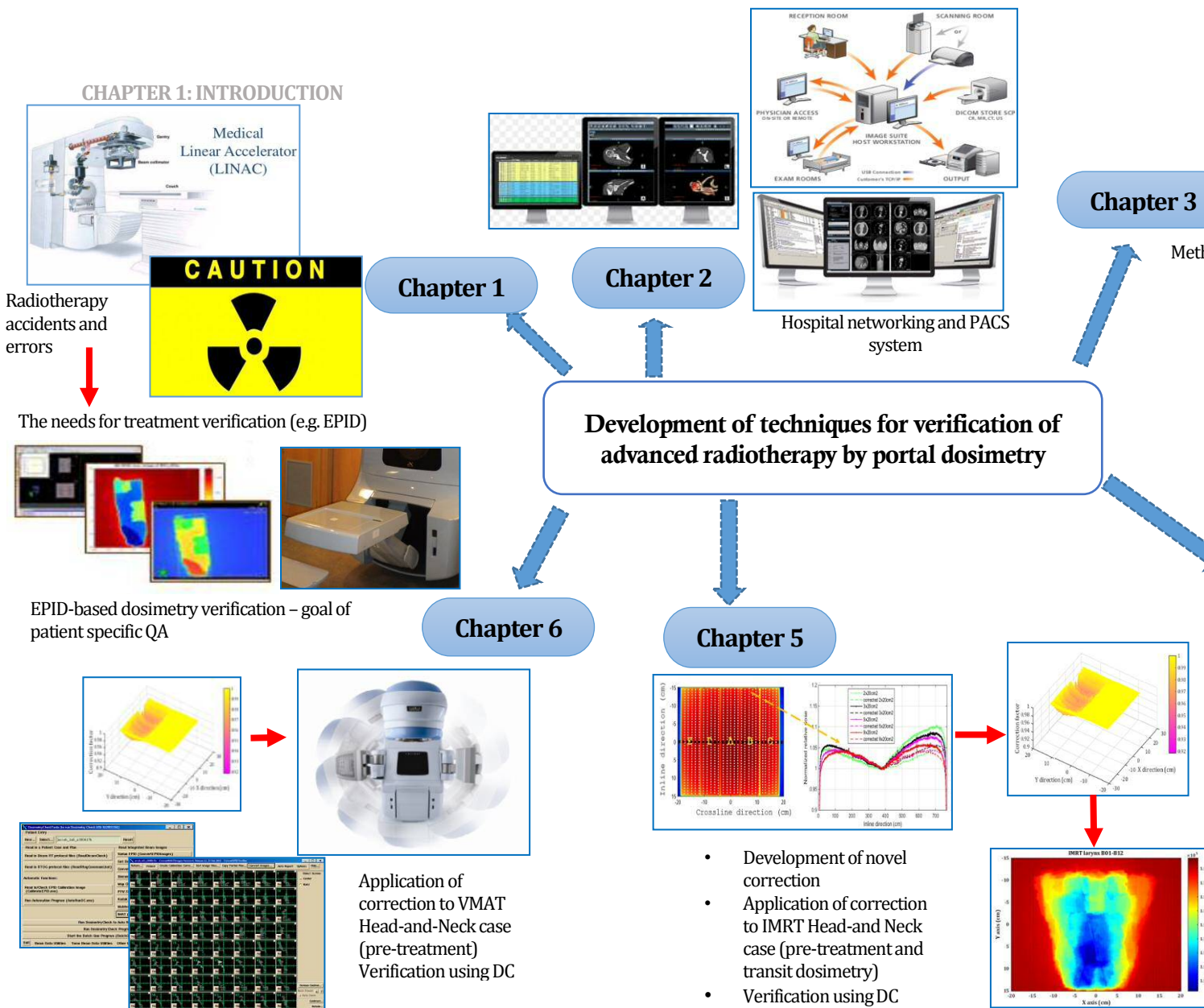


Figure 1.6 - Illustration of thesis architecture.

Chapter 2

RADIOTHERAPY VERIFICATION

This chapter describes how radiotherapy treatment verification is achieved using various portal dosimetry techniques. It also considers advantages and limitations of such methods in providing the accuracy required for radiotherapy verification purposes. In addition, the connectivity of hospital networks, especially in radiotherapy and physics departments such as those in the Velindre Cancer Centre, are discussed to provide a clear picture of how communication between different modalities and systems is achieved.

2.1 EVOLUTION OF IMRT/VMAT VERIFICATION USING PORTAL DOSIMETRY

2.1.1 Film-based dosimetry

In this section, discussion is centred particularly on the role of film-based dosimetry in the verification of radiotherapy. Film-based dosimetry can be divided into two categories: one is dosimetry based on radiographic film that is traditionally used for diagnostic purposes and the other is radiochromic film dosimetry that is now widely used in radiotherapy verification. As well as being different in their principles of operation, they are also different as regards certain other physics characteristics.

Radiographic film (Figure 2.1(a)) consists of a radiation sensitive emulsion, which is silver bromide, AgBr, or silver chloride, AgCl. It is flexible and transparent. When exposed to radiation, a chemical reaction takes place and some of the Br⁻ or Cl⁻ ions liberate electrons that are captured by Ag⁺ ions to form neutral silver atoms. This change is so small in nature that it cannot be detected using any devices and forms what is called a “latent” (hidden) image. However, silver halide crystals with a latent image are more sensitive to a developing process when exposed to a chemical solution (developer), and the reaction results in the formation of black, metallic silver. Hence, an image is formed when this silver (Ag) is embedded in the emulsion on both sides of the film. The degree of film darkening or Optical Density (OD) depends on the amount of silver deposited and is a function of absorbed dose as described by the Hurter-Driffield curve, a plot of OD (log of opacity) versus the log of exposure in the radiographic field (Hurter, 1890).

Radiochromic film (Figure 2.1(b)) consists of a single or double layer of radiation sensitive organic microcrystal monomers, on a thin polyester base. The crystals in the radiosensitive layer undergo polymerisation when exposed to radiation and cause the film colour to change progressively into different shades of blue (Sankar et al., 2006). The darkness of the film increases with increasing absorbed dose and can be measured as OD by using a flatbed document scanner in transmission mode (Devic et al., 2005, Paelinck et al., 2007, Devic, 2011).

Although both types of film have been used for 2D patient-specific pre-treatment QA, radiochromic film has many advantages over radiographic film. One of them is that radiochromic films are insensitive to visible light and do not require chemical processing in a 'dark room' environment. Radiochromic film also responds to a larger dynamic range of megavoltage treatments (up to 40Gy for Gafchromic EBT2 film) and is suitable for pre-treatment verification of planar dose and individual field dose maps (Tangboonduangjit et al, 2003).

Another major advantage of radiochromic over radiographic film is that it has a low energy dependency (Arjomandy et al, 2010) due to its nearly tissue equivalent radiosensitive layer. A study by Moylan et al. (2013) proved the capability of Gafchromic EBT3 film to provide an accurate dose measurement for in vivo dosimetry for QA verification. Mancosu et al. (2015) also studied Gafchromic EBT3 film for VMAT verification and demonstrated that the delivered dose agreed with the planned dose when a gamma agreement index of 5%/5mm was computed.

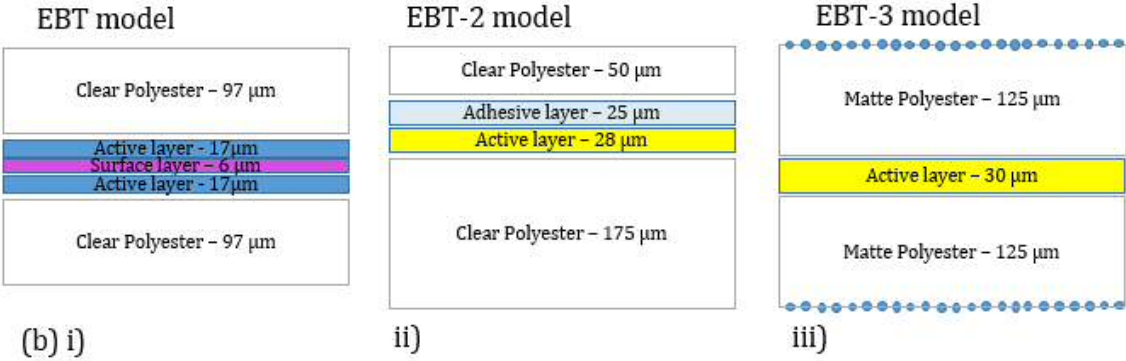
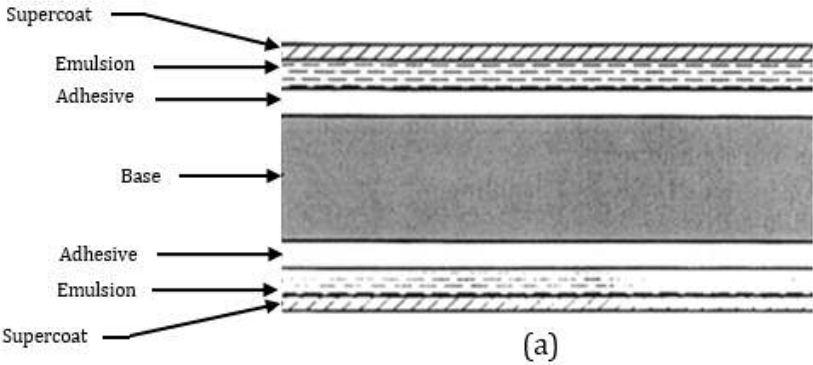


Figure 2.1 - Structural diagram of (a) radiographic film, and (b) i), ii) and iii); 3 generations of EBT radiochromic film (Image taken from Devic et al. (2005)).

2.1.2 Thermo-luminescent and diode dosimeters

For in vivo verification, especially when it involves only point dose measurements, the use of TLD is a standard technique. Basically, TLD determines a dose by measuring the intensity of visible light emitted from a crystal in the detector when the crystal is heated post-irradiation. The importance of this thermo-luminescence phenomenon in radiation dosimetry is the fact that the amount of light emitted is proportional to the dose. Calibration at the relevant dose range enables the dose received to be determined. The two most common types of TLD materials are Calcium Fluoride (CaF) and Lithium Fluoride (LiF).

In TLD, the crystals to be used for patient dosimetry are annealed or heated in an oven for 24 hours prior to use. They are placed on the patient during treatment and subsequently read post-irradiation by a specialised TLD reader. The reader consists of a heating element and photomultiplier tube. However, while being appropriate for point dose measurement, the major disadvantage of TLD is that it is very time consuming because of the necessary processes of dosimeter preparation before and readout after the delivery of treatment. Moreover, TLDs are relatively sensitive to light causing them to “fade” and decrease the signal sensitivity to radiation.

An alternative technique is diode dosimetry. Semiconductor diodes are primarily useful in radiation dosimetry because they are relatively small resulting in high radiation sensitivity per unit volume and good spatial resolution, especially for small field radiation. Most diode dosimeters operate in a similar way to photodiodes (where light is absorbed by a diode and generates an induced current). Some of the drawbacks of the diode are due to the fact that it is

an energy dependent device. For example, in clinical treatment for a deep-seated tumour, such as prostate cancer, a diode is not the preferred dosimeter because the treatment requires higher energy (usually 10MV) compared to Head-and-Neck or breast treatment (Essers and Mijnheer, 1999, Mijnheer et al., 2013a).

2.1.3 EPID dosimetry

The EPID was first developed with the intention to replace film for positional verification in radiotherapy as the complexity of radiotherapy techniques increased. This incentive was due to the fact that incorrect delivery of megavoltage energy beams could lead to serious harm to the patient's healthy tissues and ineffective treatment to the target tumour. In addition, it became increasingly important to ensure that the validity of delivery of the prescribed dose to the patient was within the dose constraints set by publications ICRU 62 (ICRU, 1999) and ICRU 83 (ICRU, 2010). Regarding positioning of patients who undergo treatments of several weeks' duration, some of them lose weight during this time. Therefore, their anatomy will be changed compared to that in the CT or magnetic resonance image taken before the treatment. EPIDs have practically replaced portal positioning films and are used to obtain real-time digital images with techniques such as Image Guided Radiation Therapy (IGRT) (The Royal College of Radiologists, 2008(b)). These devices have become a standard incorporated part of medical linear accelerators offered by major manufacturers (Parsaei et al., 1998).

Among the earliest generation of EPIDs was the Scanning-Liquid Ionisation Chamber type. It was designed in the Netherlands Cancer Institute by van Herk and Meertens (1988)

and consisted of liquid-filled ionisation chambers in a 256x256 compact matrix with ~1mm thickness of sensitive organic liquid (iso-octane) as the medium. The long-term stability of a SLIC-EPID compared to a diode is one of its advantages. However, the relatively long read-out time for this device (~20ms for each row, image scan time of 5.6s) (Essers et al., 1996) made it incapable of instantaneous dose measurement but suitable for integrated dose-rate measurement. The measured dose-rate can be converted into absolute dose by recording a continuous readout of the linac monitor chamber signal during image acquisition and the number of MUs delivered for the measured dose image. The dose rate dependency of the SLIC EPID has been discussed by several authors (Essers et al., 1996, Tateoka et al., 2006).

Another early type of EPID was the camera-based photon detector which consisted of a fluorescent phosphor-screen with a metal plate on top (x-ray converter). The device converted x-rays to visible photons via the production of high-energy electrons. These electrons escaped the plate into the phosphor and energy was transformed into that of visible light. The visible photons were then imaged with a video camera by mirrors and a lens. Most of the cameras used were based on charged couple devices. Essentially, the photons which fell within the area defined by one of the pixels were converted to one or more electrons. The amount of electronic charge collected was proportional to the irradiation intensity of the respective pixel. Thus, a reconstructed dose was measured by the number of electrons in each pixel. The characteristic and dosimetric properties of camera-based EPIDs such as dose response, stability and warm-up behaviour have been studied by several groups (Heijmen et al., 1995, Althof et al., 1996, Franken et al., 2004, 2006, Anvari et al., 2015). One of the limitations that were identified was

the scatter effect for large field sizes occurring in the optical system of the EPID (Heijmen et al, 1995, Pasma et al, 1998).

The most common type of EPID available today is the amorphous-silicon EPID (aSi EPID) or 'flat-panel' imager. As with all types of EPIDs, the main advantage is in providing 2D high-resolution (up to 0.33mm for the new Varian aS1200 EPID) digital images without the need for manual processing. The EPID is particularly attractive for dose measurement due to the convenience of the panel being readily available as a fixed attachment to most linacs and requiring minimal set-up. Most importantly, it can be used for pre-treatment as well as transit dosimetry verification purposes. Figure 2.2 (a) and (b) shows an example of a SLIC and camera-based type of EPID mounted on linacs respectively manufactured by different vendors. In the remainder of this section, the discussion considers the modern amorphous-silicon (aSi) type EPID rather than the previous generations of this device.



Figure 2.2 - Examples of the earliest versions of EPIDs which have been on the market.

(a) LC250 PortalVision 'SLIC' EPID (Varian, Palo Alto, CA, USA),

(b) TheraView NT (Cablon, Leusden, The Netherlands)

An aSi flat panel imager consists of a copper plate, a fluorescent layer and a photodiode system (Figure 2.3). The copper plate functions as a 'converter' to produce electrons when photons strike it. At the same time, it absorbs low energy scattered radiation that reduces image contrast. A layer of Gadolinium Oxysulphide ($Gd_2O_2S:Tb$) phosphor is used to convert incident radiation into visible light. An array of photodiodes underneath the fluorescent layer absorbs this visible light and integrates the resulting charge through Thin-Film-Transistors (TFTs) embedded on the aSi panel. Each TFT acts as a switch for the row-by-row read-out process.

Read-out, amplification, and digitisation of the signals are controlled by the acquisition electronics of the panel imager (either IAS2 or IAS3 systems for Varian a-Si EPID). Review articles on the aSi imager discuss its characteristics and its advantages over other detectors (Boyer et al., 1992, Antonuk et al., 1996, Berger et al., 2006, Parent et al., 2007, van Elmpt et al., 2008, Greer et al., 2009). Figure 2.4 shows the newest EPID panel, aS1200 provided by Varian (Varian, Palo Alto, CA, USA).

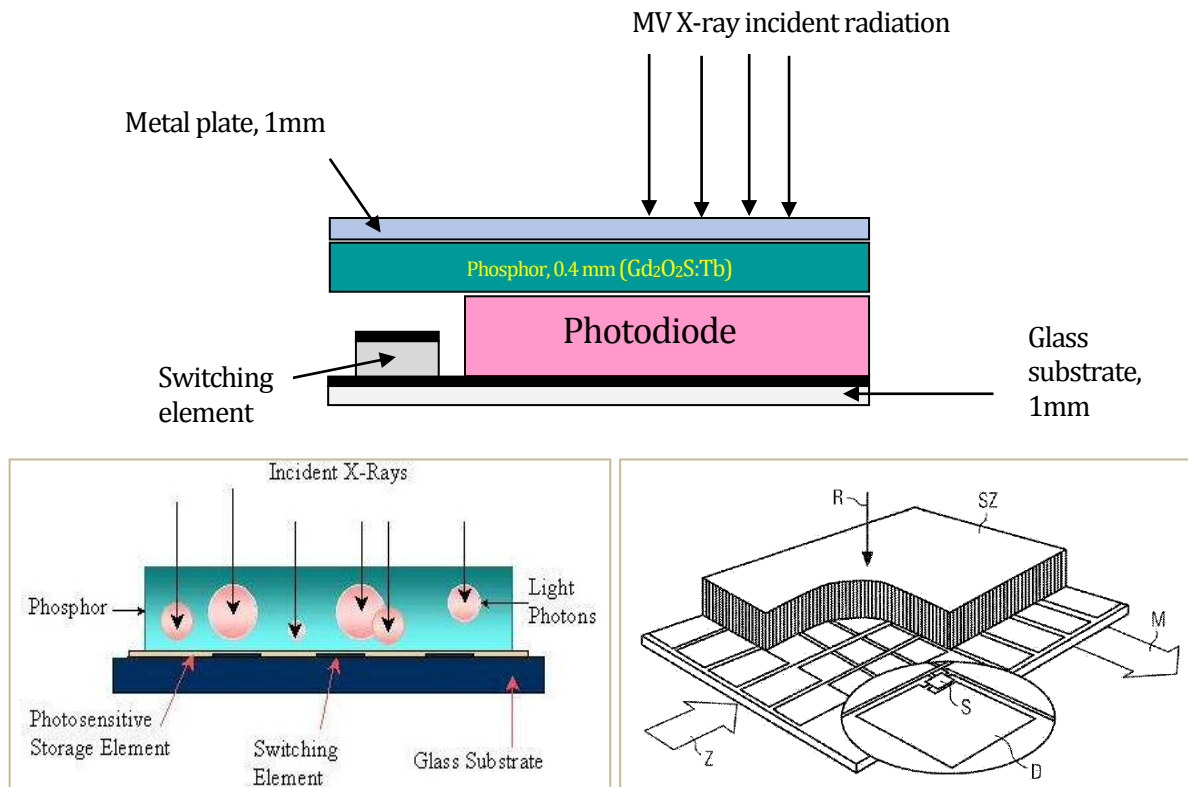


Figure 2.3 - The structural principle of an indirect flat panel detector, comprising a scintillator, an array (comprising photodiodes D, switch elements S and an active readout matrix made of amorphous silicon) of activation and readout electronics, (with line driver Z and a multiplexer amplifier M) (Soukal and Spahn, 2012).



Figure 2.4 - i) A cut out layer of the new Varian PortalVision aS1200 consisting of the detector elements and also a built-in lead plate as shielding from the linac arm backscatter.

ii) aS1200 detector panel (Taken from MyVarian Webinar (Reilly, 2016(b))).

There are many aspects of the aSi EPID that can illustrate its advantages over other types of detectors. For instance, the aSi EPID is a 2D detector with much finer resolution (0.08cm for Varian aS500 and 0.04cm for Varian aS1000) compared to other 2D array devices (0.13cm pixel pitch for LC250 SLIC EPID). In addition, the cost for treatment verification is relatively low since there is no need to purchase additional hardware or consumable items for this purpose. Most importantly, aSi-EPIDs can be used for both pre-treatment (Vinall et al., 2010, Greer, 2013) and transit dosimetry (Boissard et al., 2009, Mans et al., 2010, Mijnheer et al., 2013b, Blake et al., 2014, Mijnheer et al., 2015) (at imager level or in vivo) as the panel imager can be positioned at any level automatically and it is very convenient to set-up for most Varian linacs.

In addition, passive measurement of radiation without interfering with the treatment delivery is intrinsic since the panel is perpendicular to the central axis of the radiation beam and downstream from the patient. More recently, following the development of EPID-based treatment verification techniques, centres are now becoming more inclined towards EPID-based dosimetry using various software analysis systems (Reilly et al., 2013, Fafi et al., 2013, Narayanasamy et al., 2015) as part of their patient-specific QA and verification for most IMRT and VMAT cases.

Although arguably becoming the detector of choice for IMRT/VMAT verification nowadays, EPIDs also suffer from some drawbacks such as image ghosting and lag effects. Image ghosting is due to trapped charge in the photodiode, which later modifies the electric field strength in the photodiode. The result is an undesirable latent EPID signal when

subsequent frames are read out. EPIDs have also been reported to be over-responsive to low energy photons (particularly below 0.5MeV) as compared to water equivalent detectors (Jaffray et al., 1994, McCurdy and Pistorius). This is because of the increase in cross-section for low energy photoelectric interactions in the copper layer of the non-water equivalent EPID. Next, optical photons generated in the EPID potentially experience “self-scattering” within the EPID that will contribute to the image signal (McCurdy et al., 2001). In addition, x-ray photon scatter generated by the treatment beam interacting with the patient can create undesirable effects when these relatively low energy photons are incident on the EPID. As for the aSi-EPID, the system is mounted on the linac robotic arm and this has been shown to contribute significantly to an additional image signal due to backscattered photons. The backscatter signal in the EPID (as discussed elsewhere in this thesis) is known to be asymmetrical, field size dependent, and field location dependent (Rowshanfarzad et al., 2010a, Berry et al., 2010, Cufflin et al., 2010).

Differences in acquisition mode for aSi EPIDs in linac operating systems have been investigated by Greer and Popescu (2003) and McCurdy and Greer (2009) for Varian linacs and by McDermott et al. (2004) and Winkler et al. (2005) for Elekta linacs. For example, in ‘cine mode’ (a continuous rather than integrated image acquisition mode) in Varian aSi-EPIDs, it has been shown that a certain amount of image dose is missing from the total acquisition. This results from some ‘missing images’ when acquiring the frames in cine mode. Hence, the expected accuracy of the aSi-EPID’s performance for VMAT application needs investigation regarding the optimal methods and solutions for EPID verification. Further explanation and work on the dosimetric application of cine mode acquisition will be discussed in Chapter 6.

2.2 DIGITAL NETWORK SYSTEMS AND ENVIRONMENT

In many hospital installations, including Velindre Cancer Centre, the development of Picture Archiving and Communication System (PACS) technology involves four major components: (i) imaging systems such as Magnetic Resonance Imaging (MRI), X-ray imaging equipment and Computed Tomography (CT), (ii) a secure network for the distribution and exchange of patient information, (iii) workstations for viewing, processing and interpreting images and data, and (iv) archives for the storage and retrieval of images and related documents and reports. Along with the maturing PACS technology, it has become increasingly recognised that standardised data exchange is required. Hence, the whole system should use the DICOM standard. In this sub-section, the importance of PACS and a brief introduction to DICOM are discussed to set the scene for the later chapters.

2.2.1 PACS system

PACS is commonly used in healthcare technology to store data and to allow communication between devices, especially when dealing with equipment from different vendors. To overcome the storage and communication issues, a single well-managed storage solution is often preferred by most centres, including Velindre Cancer Centre.

In Velindre Cancer Centre, the DICOM Explorer³ package from PUKKA_J⁴ is employed within Medical Physics for the storage of radiotherapy-related DICOM data for which purpose it is capable of centralising storage and sharing oncology data across a heterogeneous mix of radiotherapy modalities. There are 8 linear accelerators currently available in Velindre Cancer Centre: 4 of them are Elekta Synergy linacs, 2 Varian TRUEBEAM linacs and 2 others Varian linacs (Clinac and Trilogy). Within the radiotherapy network, DICOM data (Metadata⁵ information) are transferred electronically via PACS between CT-simulators, treatment planning systems, Oncology Management Systems (Mosaiq for Elekta and Aria for Varian), as well as RT portal verification software - Dosimetry Check (Figure 2.5). Other hospital information, such as the patient's health data, is managed by the Welsh Cancer Network Information System Cymru (CaNISC).

³ A software for Web-based image viewing, and reporting developed by PUKKA-J

⁴ A UK specialist medical technology firm which provides smart software solutions for enterprise imaging and reporting in healthcare, with particular experience in all medical imaging related fields

⁵ DICOM metadata provide information about the image data, such as the size, dimensions, bit depth, modality used to create the data, and equipment settings used to capture the image

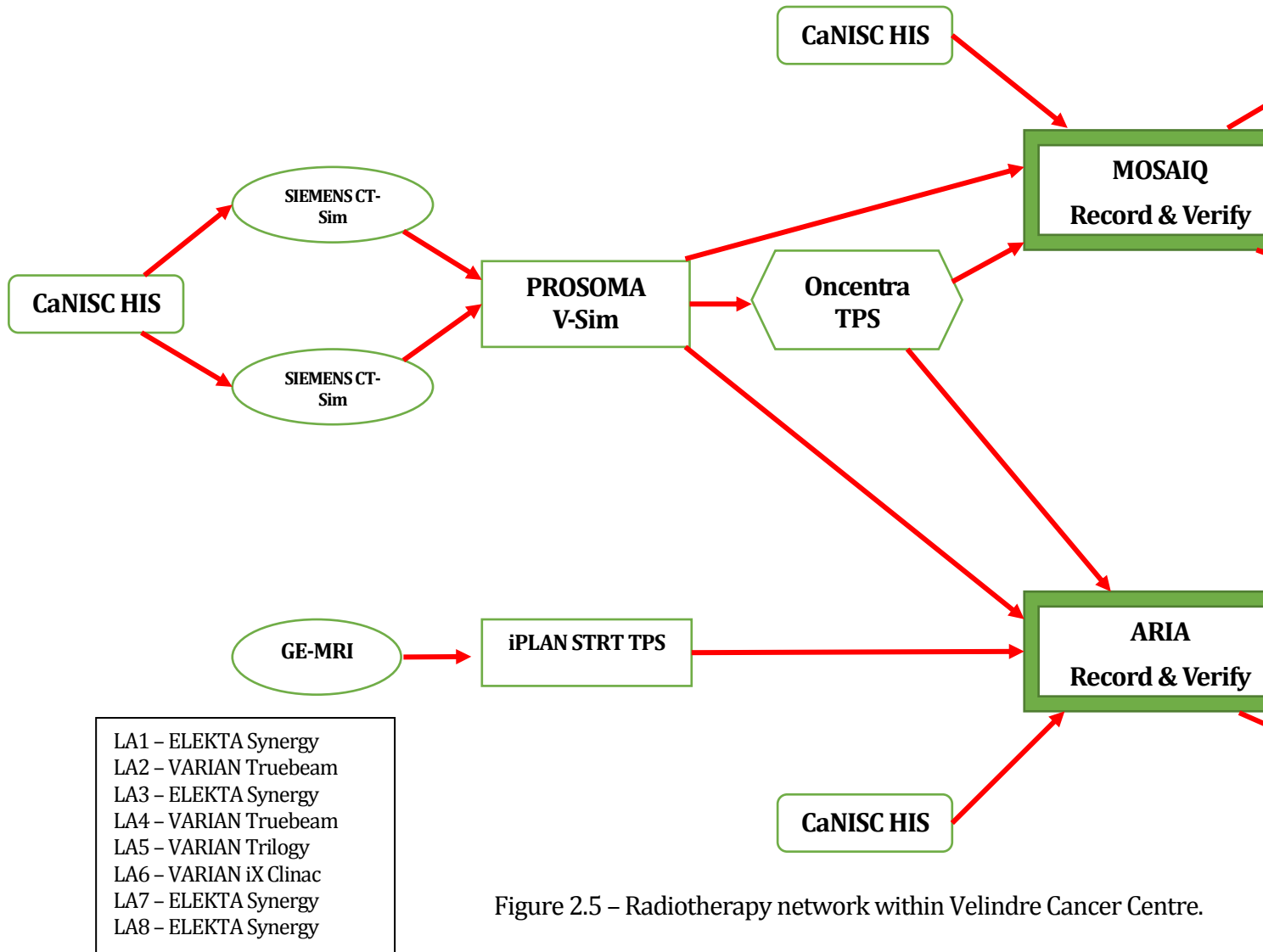


Figure 2.5 – Radiotherapy network within Velindre Cancer Centre.

initial planning decisions by enhancing visualisation of the patient data set and treatment parameters. Oncentra MasterPlan (Nucletron) is 3D TPS software for outlining targets and OARs, beam modelling, dose calculation and plan reviewing. Oncentra MasterPlan is used for EBRT and brachytherapy planning while BRAINLAB iPlan is used for stereotactic radiosurgery and stereotactic radiotherapy. The record and verify systems are Mosaiq and Aria from Elekta and Varian respectively. These interface and record information exchange between treatment planning and treatment delivery system.

Meanwhile, PACS servers and storage systems act as temporary and permanent repositories and enable transmission of DICOM data backwards and forwards between mixed manufacturer radiotherapy planning modalities. Images are automatically routed between the processes and computers that perform RT services such as treatment planning and treatment delivery. Details of the PACS mapping in Velindre Cancer Centre are shown in Figure 2.6.

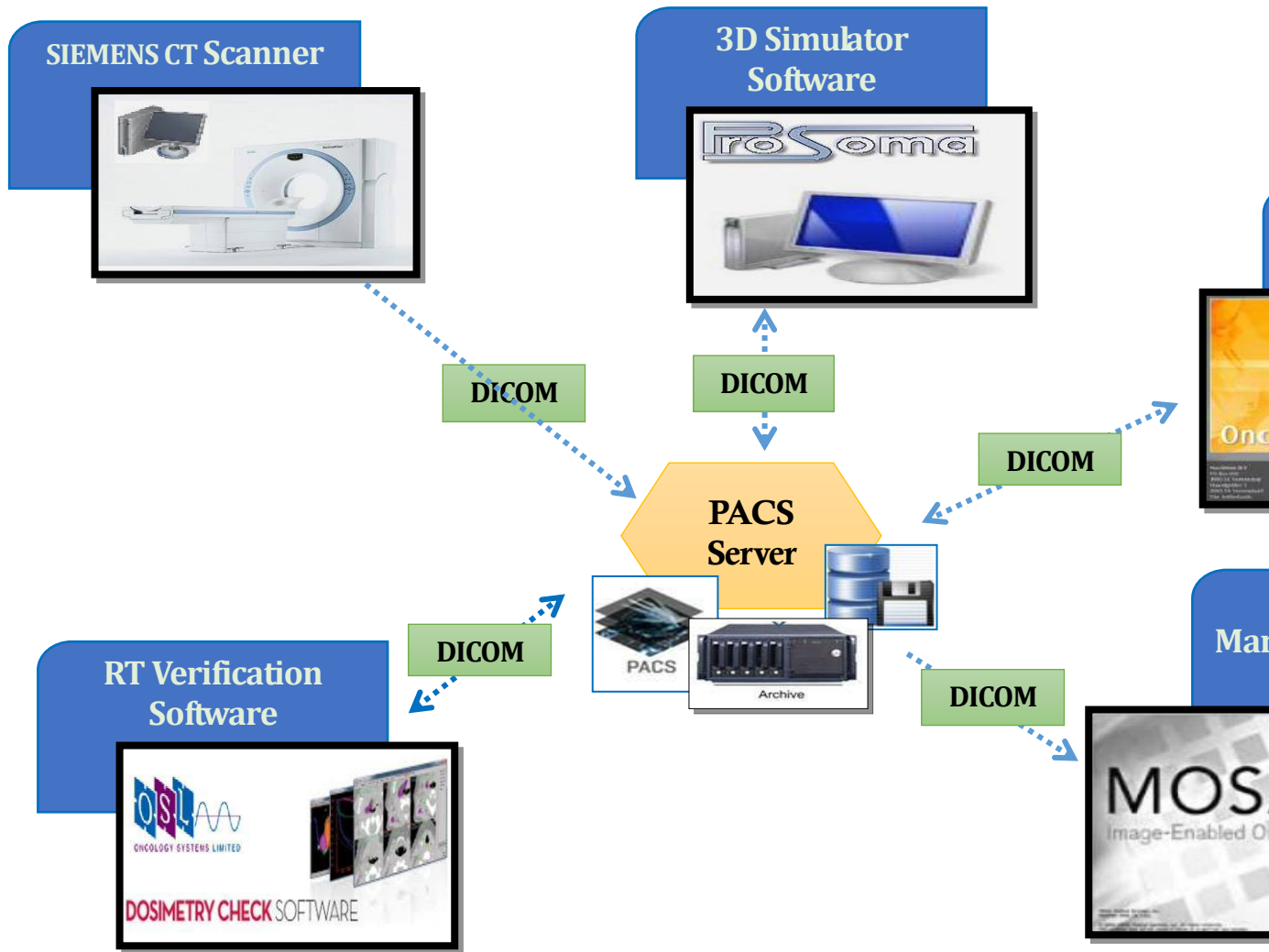


Figure 2.6 – Examples of PACS mapping employed in Velindre Cancer Centre consisting of preferred and fall-back

2.2.2 DICOM-RT

As the DICOM standard is now widely implemented in radiology, it has been extended for use in various sub-specialties such as radiation therapy. In fact, one of the first extensions was applied to radiation therapy and this is known as DICOM-RT. In addition to the protocol used in the DICOM standard, seven DICOM-RT objects have been created, each with a well-defined data model (Law et al., 2009): (i) RT Image, (ii) RT Dose, (iii) RT Structure Set, (iv) RT Plan, (v) RT Beams Treatment Record (Figure 2.7). The other two objects are extended from the RT Treatment Record, being (vi) RT Brachy Treatment Record and (vii) EBRT Treatment Summary Record.

2.2.2.1 Radiotherapy DICOM objects

Being specific to radiotherapy, information retrieval from the set of DICOM-RT objects is different from the radiology DICOM information model but it is an extension of the DICOM standard as shown in Figure 2.7.

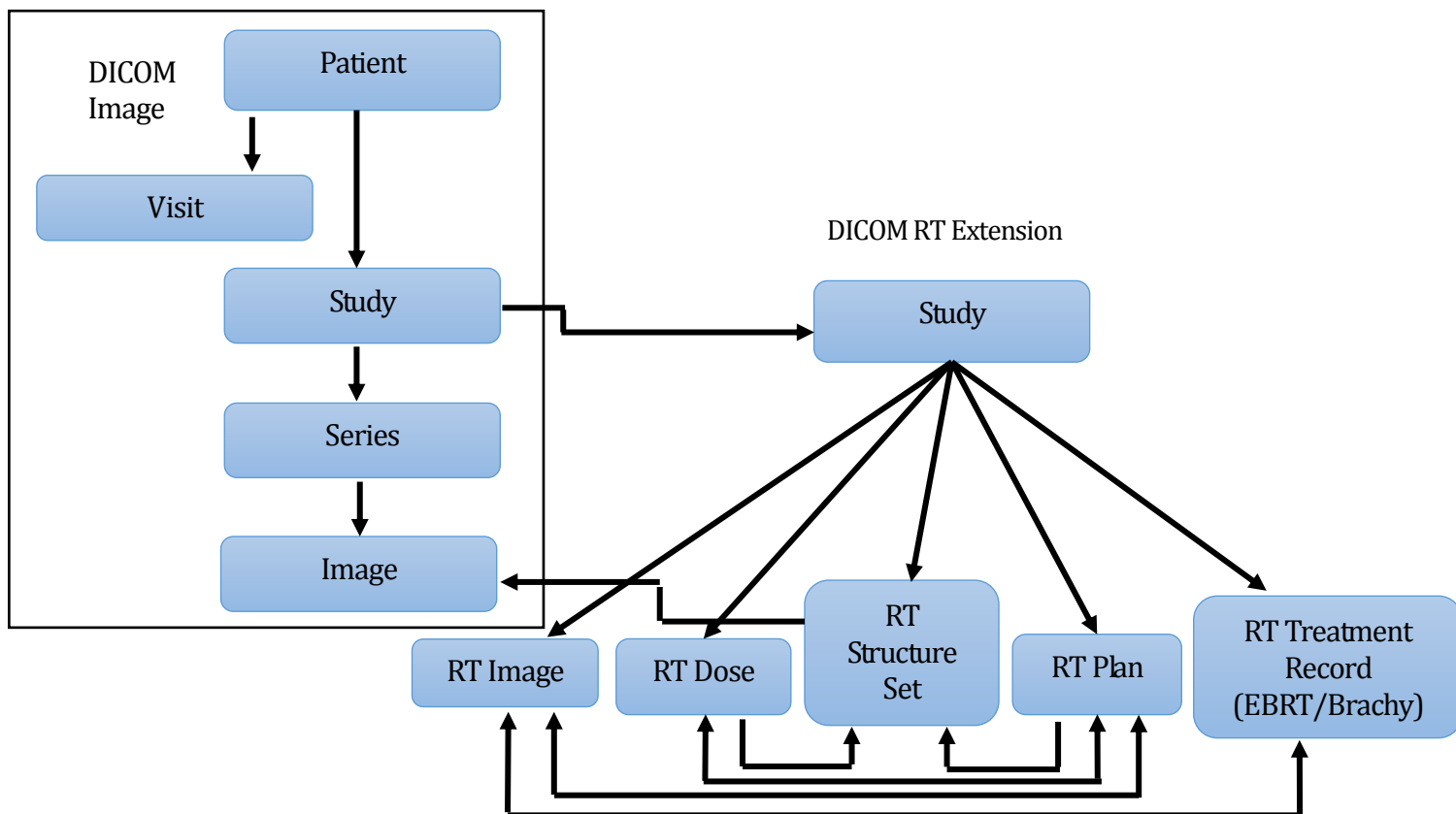


Figure 2.7 – Chart illustrating 5 DICOM-RT objects extending from the DICOM standard. The other 2 objects are extended from the RT Treatment Record (Brachy and EBRT Treatment Record).

- (i) **RT Structure** – This is a set of parameters which clinically describe items of significance in radiation therapy such as body contours, tumour volumes (e.g. gross tumour volume (GTV), clinical target volume (CTV), planning target volume (PTV), organs at risk (OARs) and other regions of interest (ROIs)) as defined by the International Commission on Radiation Units and Measurements (ICRU) in the ICRU 50 and ICRU 62 guidelines (ICRU 1994, 1999). As a simplified example, in a case of prostate

cancer, the target volume is the prostate gland and any periglandular cancerous area. The OARs are the urinary bladder, the rectum and the femoral heads.

- (ii) **RT Plan** – Treatment planning is an important process for the determination of appropriate radiation beams to give an optimal dose distribution (section 2.2.5). A clinical treatment plan may include all the structures marked on the CT scan, beam positions and sizes, and the dose distribution displayed on an image. In other words, the RT Plan object refers to the documented information in the treatment plan which is generated by the TPS. The modules described by the RT Plan are prescription, tolerance table, patient set-up, fraction scheme, brachytherapy or RT beams used in EBRT.
- (iii) **RT Dose** – The dose distribution for a typical treatment plan in the TPS is usually represented by isodose lines given as a percentage or in dose units (Gray). Hence, RT Dose contains such radiation dose data from the TPS in the form of a ‘dose matrix’.
- (iv) **RT Image** – Attributes in RT image include data from Digitally Reconstructed Radiographs (DRRs) generated using CT scans by a TPS, and those from images acquired at linear accelerators. In contrast to ordinary CT scan images, RT Image data include supplemental information about the presentation of the images e.g. position, plane and orientation of the image and distance from radiation source to imaging plane. In addition, table position, isocentre location and the MLCs or jaws used can be added into RT Image if necessary.

- (v) **RT Treatment Record** – This can be divided into **RT Beams Treatment Record** and **RT Brachy Treatment Record**. **RT Beams Treatment Record** includes mainly information from the treatment verification system gathered during the course of EBRT or during treatment delivery. Examples include machine used, radiation type and energy, date and time of treatment, beam details and accessories, treatment fractions, Monitor Units (MU), calculated dose, cumulative dose, verification image obtained and treatment summary. These information elements are mostly in the term of textual data. For **RT Brachy Treatment Record**, the content is mainly information acquired during the course of brachytherapy along with an optional treatment summary.
- (vi) **RT Treatment Summary Record** – This is a cumulative summarisation of the radiation treatment, including both EBRT and Brachytherapy.

In summary, using the DICOM-RT standard and following the PACS model makes it possible to integrate radiation therapy information to provide a complete radiation therapy patient record. These DICOM-based RT databases can be used as a platform for sharing data and future research e.g. in medical informatics, outcome analysis of standardised data and what has become known as “Radiomics” (Gillies et al., 2015). This type of research shall not be discussed any detail as it is not related to work presented in this thesis. The relationship between DICOM-RT objects from treatment planning to treatment delivery is summarised and illustrated in Figure 2.8.

CHAPTER 2: RADIOTHERAPY VERIFICATION

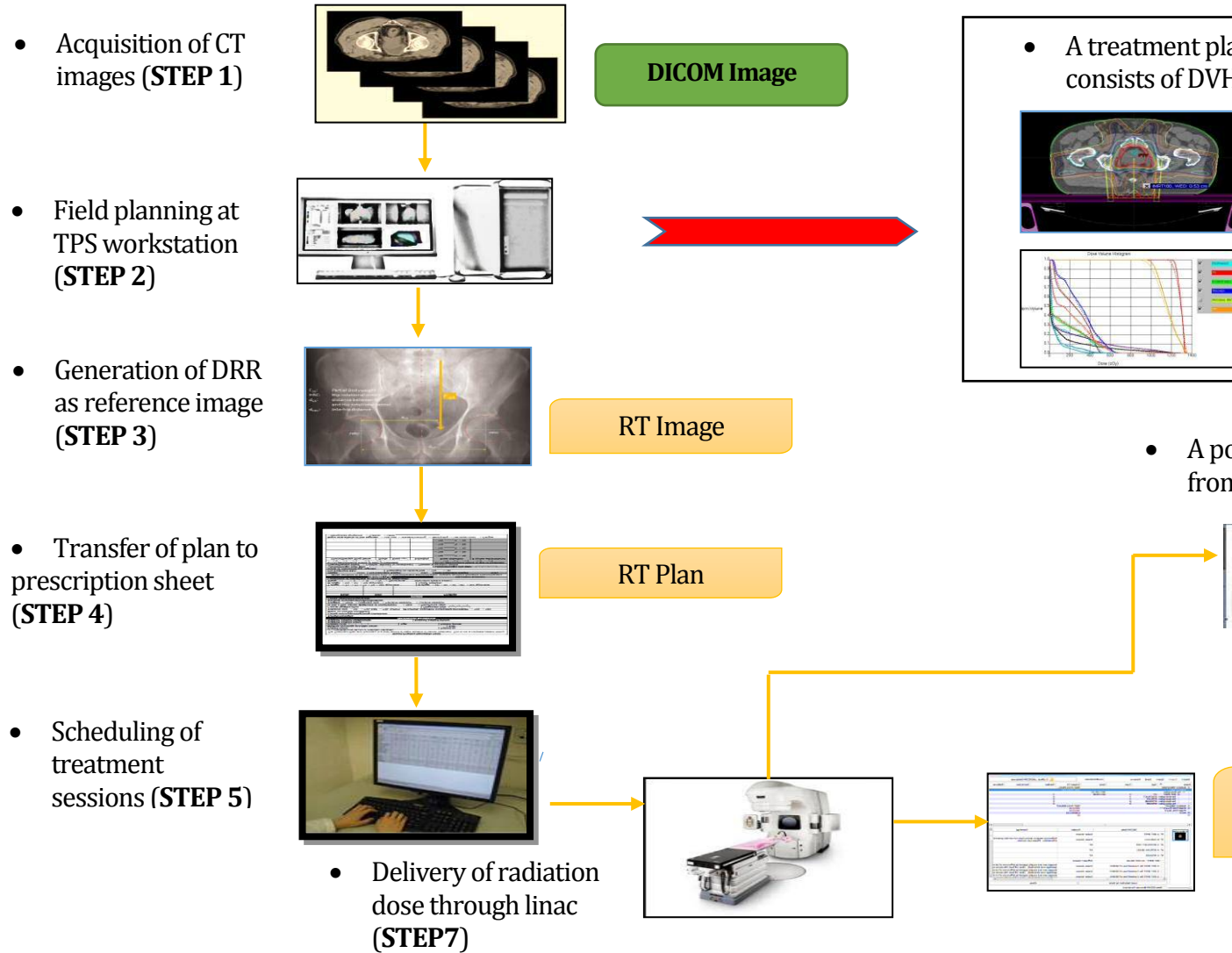


Figure 2.8 – General procedures involved in RT treatment planning and delivery. STEP 1-5: Treatment Planning

2.2.2.2 Modality LUT of DICOM standard

All DICOM files are typically generated from medical imaging devices such as CT and MRI scanners. The values of each pixel on DICOM files are the raw values coming out from the scanners. Therefore, to use or visualise these pixel values, transformations are often necessary. The mechanism used in these transformations is called a LUT, look up table (Pianykh, 2008).

While the DICOM standard is full of LUTs of various kinds, among them is the most basic one, modality LUT. Modality LUT is used to map stored pixel values to a meaningful physical unit. For example, in a CT scan image, modality LUT is used to transform the output from the device to a Hounsfield Unit. A typical modality LUT is stored in the DICOM file as a slope (0028, 1053) and an intercept (0028, 1052) of a linear transformation or simply called the rescale operation (Equation 2.1).

$$y = (m * x) + b \quad \text{(Equation 2.1)}$$

where x = the stored pixel values,

m = the value of Rescale slope (0028, 1053),

b = the value of Rescale intercept (0028, 1052),

y = the rescaled values, the meaningful unit.

2.2.3 IMRT/VMAT treatment workflow

In most radiotherapy physics departments, EBRT accounts for approximately 90% of the workload compared to Brachytherapy (internal radiation therapy) and therapeutic Nuclear Medicine. Brachytherapy often plays a supplementary or complementary role to EBRT and can be used in the treatment of gynaecological and prostate cancers while therapeutic Nuclear Medicine has become largely independent of other forms of radiation therapy in most hospitals. Note that for this research, only EBRT workflow in the Velindre Cancer Centre Medical Physics department will be discussed.

There are several steps involved from treatment planning to treatment delivery in radiation therapy workflow. As an example, IMRT treatment planning and delivery could be different from the more conventional 3D Conformal Radiotherapy (3DCFR) in aspects like beam intensity modulation tools and QA processes (Nishimura and Komaki, 2015). Hence, in this section, for simplification, an example of an IMRT prostate case workflow from treatment planning to treatment delivery is described.

(1) Imaging and delineation

The process starts with the localisation of the prostate tumour volume by the oncologist using pelvic images from a CT scanner (mostly) and/or other complementary modalities such as Positron Emission Tomography and Magnetic Resonance Imaging. Images are generated in DICOM format. Volumes of interest like gross tumour volume (GTV), clinical target volume (CTV) and planning target volumes (PTV), are delineated as

prescribed by the International Commission on Radiation Units and Measurements (ICRU) (Chavaudra and Bridier, 2001, Stroom and Heijmen, 2002).

Other important features like organs at risk (OARs) are also described. These volumes are not only applicable to IMRT but also to other treatments like 3DCRT. The accuracy and quality of the volume definitions is essential in IMRT since this information is the basis for the creation of treatment plans by inverse planning algorithms (Ezzell et al., 2003). The inverse-planning algorithm will be discussed later in this thesis.

(2) Configuration of the radiation beams

The number of beams is configured and the treatment isocentre determined. Standard practice for isocentre placement varies among clinics. In Velindre Cancer Centre, for most of the prostate cases, the isocentre is defined at the centre of the primary target (i.e. the centre of the prostate). However, when a relatively wide target is to be treated, the isocentre is placed so as to minimise the number of adjacent fields needed to cover the entire target. In IMRT, the width of the fields is limited by the travel of the MLCs. The images are then transferred to the TPS workstation for the radiation field planning.

Plan optimisation is done in the TPS based on the defined beams. The use of several beams provides a higher degree of freedom in shaping the dose distribution, but an excessive number of beams could add extra treatment time.

(3) Treatment plan objectives

Once the configuration has been determined, the next step is to determine doses to the intended treatment target and normal tissue. Some objectives must be achieved (such as dose constraints in an IMRT plan) and dose analysis functions like dose volume histograms (DVHs) can be utilised. Normally, the specified objectives in combination with suitable “consequences” lead to an acceptable approximation of what is desired, but the criteria vary among clinics. Dose constraints and DVHs for IMRT will be described under section 2.2.3.

(4) Optimisation

In this phase, an optimum intensity distribution for each beam is determined and a weighting method used to create a dose distribution. For example, dose at each voxel in the patient is calculated from a radiation ray that is passing through. For advanced treatment techniques like IMRT or VMAT, there are some additional optimisation procedures that must be taken into account, such as determining the MLC sequence. Hence, MLC constraints should also be included in the optimisation process. However, this process will not be discussed in detail.

(5) Dose calculation

For a clinical situation, a Collapsed Cone (CC) algorithm for dose calculation is used most of the time nowadays, compared to the previous widespread Pencil Beam (PB). The PB algorithm has several disadvantages when dealing with heterogeneity in tissue density

(such as lung) although it provides faster dose calculation (Ahnesjo et al, 1992, Knoos et al, 1995, Buzdar et al, 2010). These calculation algorithms will be elaborated further in Chapter 3.

In some cases, critical normal tissues often overlap with the PTV creating a potential conflict between target objectives and normal tissue constraints as occurs particularly in Head-and-Neck treatments. The solution is to use pseudo (dummy) structures⁶ to help force the optimisation to minimize the dose to surrounding structures close to the PTV.

(6) Treatment plan evaluation

To evaluate a plan, DVHs are useful tools for summarising and comparing the treatment plans either in conformal RT or in IMRT.

(7) Treatment delivery hardware

The majority of modern IMRT delivery systems use MLCs. They are small, individually motorised leaves that can be used to shape or modulate the intensity of the treatment field. The ability of MLCs to shape fields (produce segments of IMRT fields) depends on several factors related to their physical design and control mechanism. A common design has up to 60 opposed leaf pairs, with a width at the isocentre plane in the beam's eye view (BEV) between 2mm and 10mm, depending on the manufacturer model.

⁶ Pseudo structures – A 'dummy' structure is often used to help in the optimisation of treatment planning. The structures are not necessarily related to specific anatomic structures in the patient.

In 'segmented IMRT', "step-and-shoot" and "stop-and-shoot" methods are used, and the gantry does not move during irradiation.

Another design consideration which must be taken into account is radiation leakage through the MLC leaves, as the cross-sectional shape of the MLCs is very complex. The leaves must incorporate beam divergence in the direction perpendicular to their travel and adjacent MLCs must overlap to minimise radiation transmission between them. This effect is called tongue-and-groove and has been discussed in detail elsewhere (Wang et al., 1996, Jonathan and Peter, 1998, Salari et al., 2011). As in VMAT treatment delivery, leaf sequencing is crucial because as the MLCs move, the gantry is also rotating. Since VMAT is delivered in one or more dynamically modulated arcs, the rate of rotation of the gantry and the linac dose rate can be modulated during treatment to give the required delivered dose for each gantry angle (Otto, 2008, Bedford, 2009, Bzdusek et al., 2009). The leaf sequencing algorithm involved in VMAT delivery first converts the optimised intensity distribution into separate values of gantry spacing (usually termed control points). By shifting MLC leaves, all control points are processed to comply with machine motion constraints of the treatment units (such as maximum leaf speed, valid dose rates and treatment delivery time) (Nucletron, 2008a).

In summary, the more complex the treatment, the greater is the number of optimization considerations that have to be taken into account in parallel with the design limitations of the MLCs. However, a productive and co-operative multidisciplinary team in the radiotherapy department including treatment planner, medical physicist, dosimetrist and radiographers, should ensure the quality and success of treatment delivery to the patient with the correct

prescribed dose. In order to achieve this, a specific quality assurance process must be applied to accommodate the needs of treatment accuracy and precision (van Elmpt et al., 2009, Klein et al., 2009, Bakhtiari et al., 2011, El-Maraghy et al., 2014).

2.2.4 Record and Verify systems

Record and Verify (R&V) systems were originally developed to reduce the risk of treatment errors. Parameters required during the treatment course such as skin markings and image verification were obtained through the treatment planning process either from the simulator or TPS. Some early R&V systems were attached to individual treatment machines and designed to capture treatment parameters (such as collimator opening, gantry and collimator angle or presence of wedge filters) and compare them against the intended parameters either derived from the TPS or manually entered (International Atomic Energy Agency, IAEA, 2017). However, over time, the R&V system was no longer exclusively used as the consistency check between prescription and actual set-up, but rather to provide effective control for the treatment machine while giving access to complicated treatment techniques that would not be feasible without such a system (Fraass, 2008).

In fact, the R&V system has evolved into a component of a wider and more complete radiotherapy and oncology information management system that interconnects with the imaging systems, treatment planning computers and treatment delivery systems. Today's R&V systems serve not simply to record and verify the treatment set-up, but to function as an integral link in planning, delivery and record-keeping processes such as scheduling capabilities,

clinical assessment tools, image storage capabilities, dose alert functionality and other functions (Baiotto et al., 2009).

As mentioned previously, Velindre Cancer Centre is a dual vendor centre and so two types of R&V system are used in parallel as platforms in the Oncology Management System (OMS) (Figure 2.9).

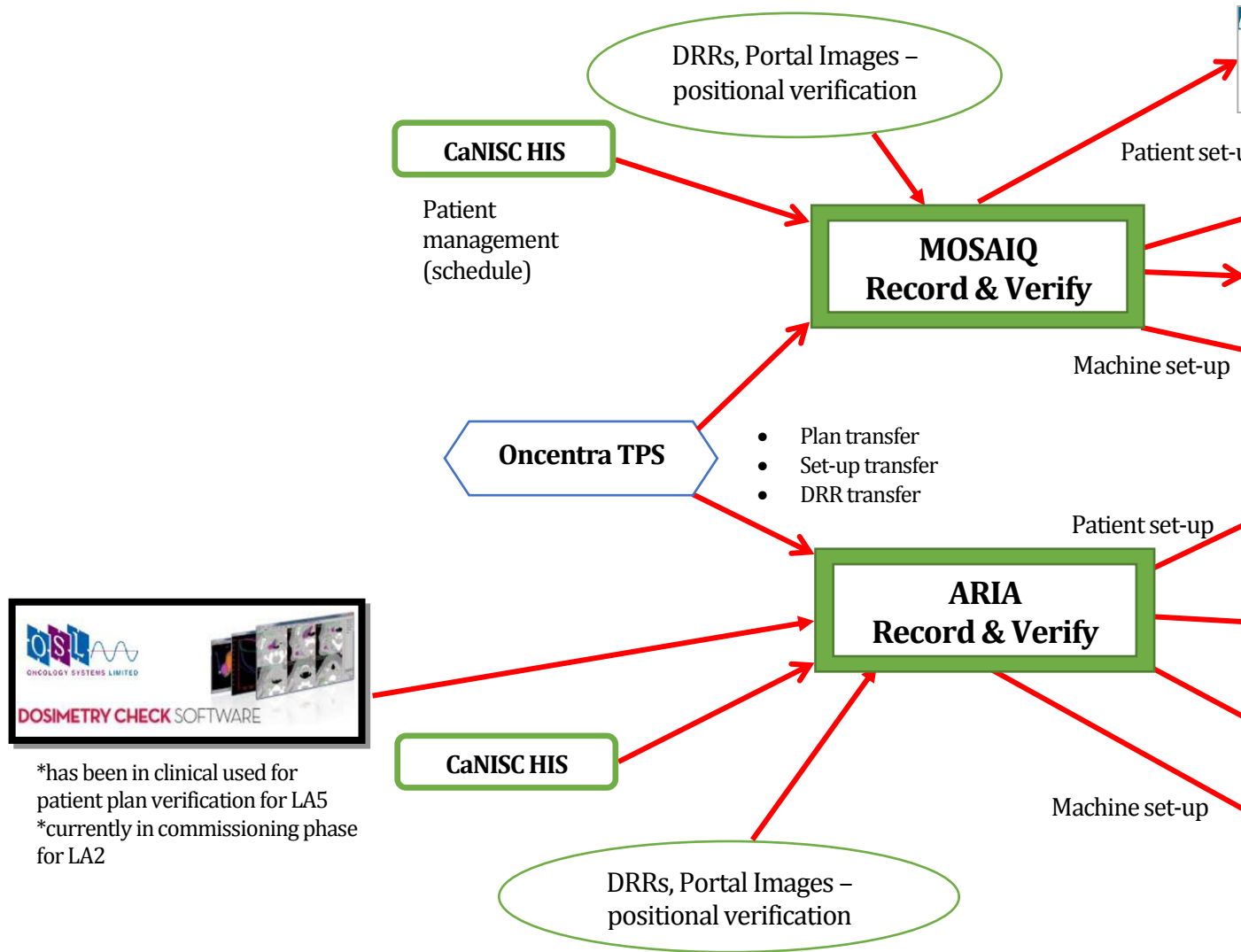


Figure 2.9 - Illustration of typical data exchanges between the R&V system and other pieces of equipment in a radiotherapy department. DRR - Digitally Reconstructed Radiograph.

2.2.5 Treatment Planning System

The International Commission on Radiation Units and Measurements (ICRU) produced guidelines on the use of computers in treatment planning and subsequently produced a report on prescribing, recording and reporting procedures in EBRT (ICRU 1994, 1999, 2010). Nowadays, radiotherapy planning is almost exclusively performed using computer-based treatment planning systems. Advances in patient imaging and radiotherapy delivery techniques have driven the development of more sophisticated dose calculation algorithms which will be discussed in Chapter 3.

Inverse treatment planning involving IMRT has been discussed in section 2.2.3 along with treatment delivery. In this section, the discussion relates to the tools and features available in a Velindre Cancer Centre planning system such as Oncentra MasterPlan.

TPSs have evolved greatly in the use of graphic capabilities for the development of more powerful 3D visualisation and treatment planning techniques in clinically useful timescales. Moreover, these have additional tools and features to accommodate planning and dose optimisation for every case. The features include:

- (i) **Contouring tools** - for accurate VOI delineation such as those for OARs.
- (ii) **Beam modelling** – to enable BEV display of the field where the observer's viewing point is at the radiation source and the image shows the plane of the internal patient contours (perpendicular to the beam central axis). Plan field sizes and locations can be

adjusted manually by a user-specified margin or graphically on screen with the help of MLCs to shape the beam according to the shape of the tumour.

- (iii) **Dose calculation** – usually dose is computed within a 2-5mm range in grid spacing. If the matrix size is reduced, it will take a longer time for the system to compute the dose. Based on ICRU report 50, the position of the maximum dose within the plan and the reference point are specified (ICRU, 1994). Normalisation should be done either such that the ICRU reference point lies on the 100% isodose, or such that the mean (or median) target dose is equal to the 100% isodose value.
- (iv) **Evaluation tools** – to allow fast assessment of dose distributions in order to determine whether the tolerances for the target and critical structures have been achieved. A key method of analysing the 3D dose distribution in all modern treatment planning systems is the DVH, with cumulative DVH mostly commonly used. DVHs are used to determine the percentage of that volume receiving a dose above and below the required tolerances. Higher values of the target dose below the prescription dose and a sharper fall-off of the DVH indicate an improved dose distribution. In contrast, desirable dose distributions for critical OARs are represented by lower values of dose. An example of a particular DVH assessment consisting of several PTVs, CTVs and OARs is shown in Figure 2.10.

Other essential tools that are available include (v) the **Export** feature and (vi) the **Specific type of treatment planning modality**, such as forward and inverse IMRT planning, electron beam planning, stereotactic radiosurgery planning, and brachytherapy planning.

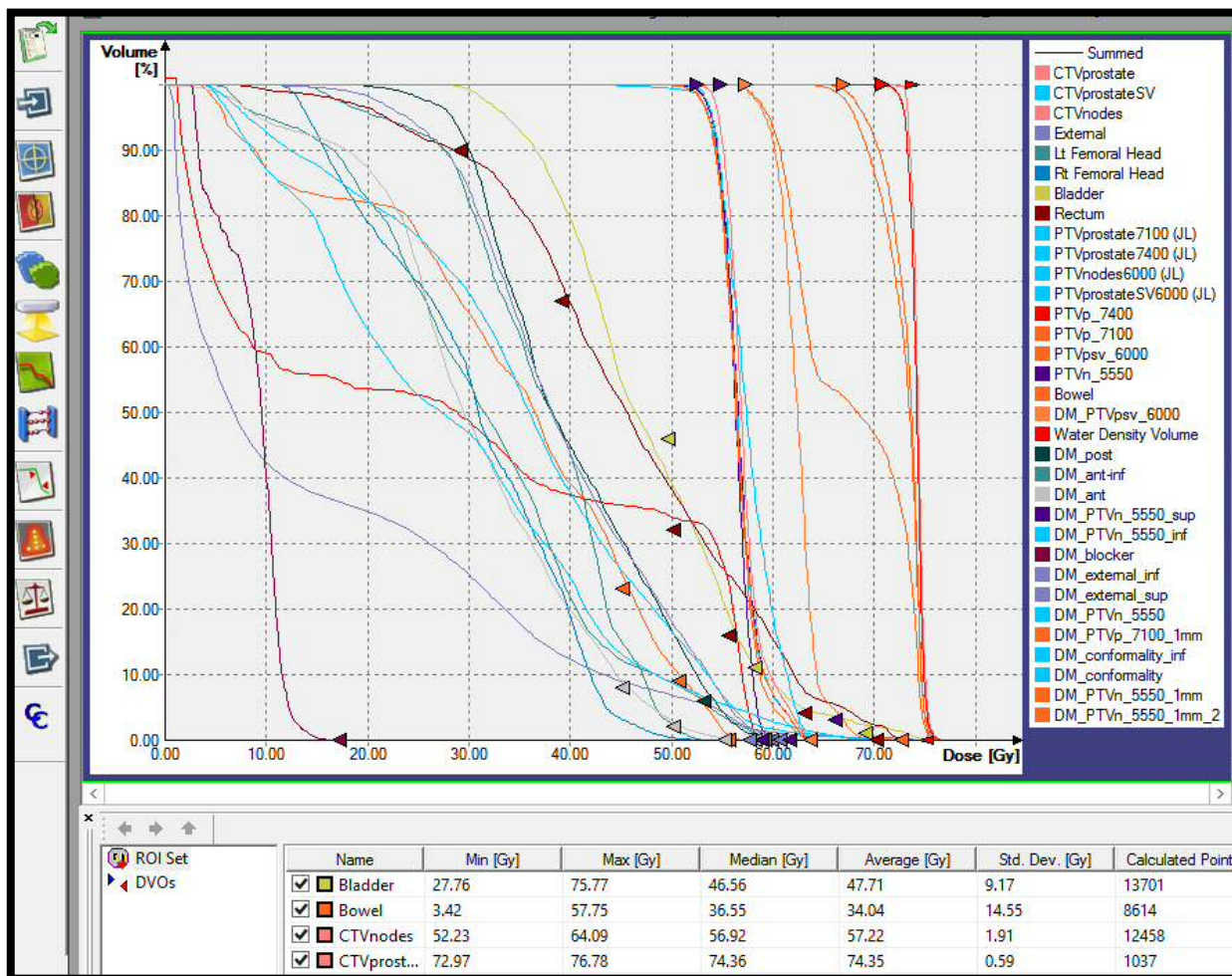


Figure 2.10 – A screenshot of a DVH analysis of several PTVs, CTVs and OARs (example DVH evaluation done by using Velindre Cancer Centre Oncentra MasterPlan TPS).

Chapter 3

DOSE CALCULATION ALGORITHMS IN ADVANCED RADIOOTHERAPY

This chapter considers the various dose calculation algorithms that were involved during this research. These include the 'gold standard' Monte Carlo method for tracking particle histories, algorithms used in the TPS and the dose reconstruction algorithm employed in the Dosimetry Check software. The 'RTGrid' high throughput computing system available to the Velindre Cancer Centre is also highlighted as a facility for timely Monte Carlo simulations.

3.1 CONVOLUTION-BASED METHODS

3.1.1 Energy fluence of a photon beam

The object of radiotherapy has never deviated far from its primary goal to deliver accurately a dose considered sufficient to achieve local control of malignant disease whilst minimising the occurrence and severity of normal healthy tissue complications. Since the publication and widespread adoption of the ICRU 50 and 62 reports on volume definitions (ICRU 1994, 1999), and the development of prescribing, recording and reporting for photon beam therapy, considerable efforts have been made to improve treatment accuracy, with uncertainties in the final delivered dose to the patient of $\leq 5\%$. A major contribution in achieving this goal has come about as the result of improvements in the treatment planning

aspect of external beam therapy (Knoos et al., 2006). At present, for most non-stereotactic cases at Velindre Cancer Centre, dose distributions are principally determined by Nucletron's Oncentra™ MasterPlan (OMP) TPS, with calculation available in two 'kernel-based' algorithms. One algorithm is known as Pencil Beam (PB) and the other is called Collapsed-Cone (CC).

OMP simulates the geometry and physics of the beam set-up and patient anatomy for 3D radiotherapy treatment planning in order to represent the actual situation. Before the energy is absorbed as dose, there is a cascade of interactions which occurs in the treatment machine itself, prior to interactions within the patient or phantom (Figure 3.1). Within OMP a calculation dose grid is used to represent the embedded radiation ray path, and this directly mimics the transport of primary photon beams. Secondary photon components are also generated following irradiation of the treatment head element. The transport and dose deposition of secondary particles is implicitly considered through the use of *energy deposition kernels* i.e. 'pencil' kernel for the PB algorithm (Ahnesjo et al., 1992, Zhang et al., 2014), and 'point' kernel for the CC algorithm (Ahnesjo, 1989). The term *energy deposition kernel* is used generically to describe the dose response to an incident elementary radiation beam in water while the elementary radiation geometry can be of various different types.

Absolute dose per treatment machine MU⁷ is calculated relative to the dose at reference or calibration conditions. The recommended standard set-up for treatment linacs with a source-axis distance (SAD) of 100cm is to have the isocentre at 10cm depth and a source-

⁷ Monitor Unit, MU - a measure of machine output from a clinical accelerator for radiation therapy such as a linear accelerator or an orthovoltage unit.

surface distance (SSD) of 90cm along the central axis of an open 10x10cm² field. However, it is possible to use other appropriate depth and SSD values, provided that the depth is well beyond the position of maximum dose, d_{\max} ⁸ in the water phantom.

In general, the dose (D) calculated by a TPS at any point in a water phantom or a patient is based on an 'energy fluence'⁹ formalism, which is associated with machine-related beam quantities. This formalism (Equation 3.1) generally includes the treatment head scatter fluence, which is a consequence of radiation interactions and transport through various linac component modules such as flattening filter, collimators (X and Y jaws, MLCs), modulating filters (wedges, compensators), and monitor ion chamber (Figure 3.2) (Khan and Gibbons, 2014). However, this formalism is dependent on whether a SSD or SAD set-up is applied, and its discussion is limited given the scope of this thesis.

⁸ d_{\max} – depth in water where the deposited dose is at its maximum

⁹ Energy fluence - describes the energy flow in a photon beam and is defined as the amount of energy dE crossing a unit area dA . Its usual unit is MeV/cm².

$$D = MU \times O \times OF \times ISq \times DDF \times OAF \times TF \quad (\text{Equation 3.1})$$

where:

MU = monitor unit setting for given conditions

O = calibrated output (cGy/MU) for standard conditions

OF = output (scatter, phantom/patient, total) factor(s): S_C , S_P , S_T according to which approach is applicable)

ISq = inverse-square correction (if needed) depending on calibration conditions and treatment conditions.

DDF = depth-dose factors (Percentage Depth Dose (PDD), Tissue Maximum Ratio (TMR), Tissue Phantom Ratio (TPR), Tissue Air Ratio (TAR) according to which approach is applicable)

OAF = off-axis factors, open and wedge

TF = transmission factors-attenuation

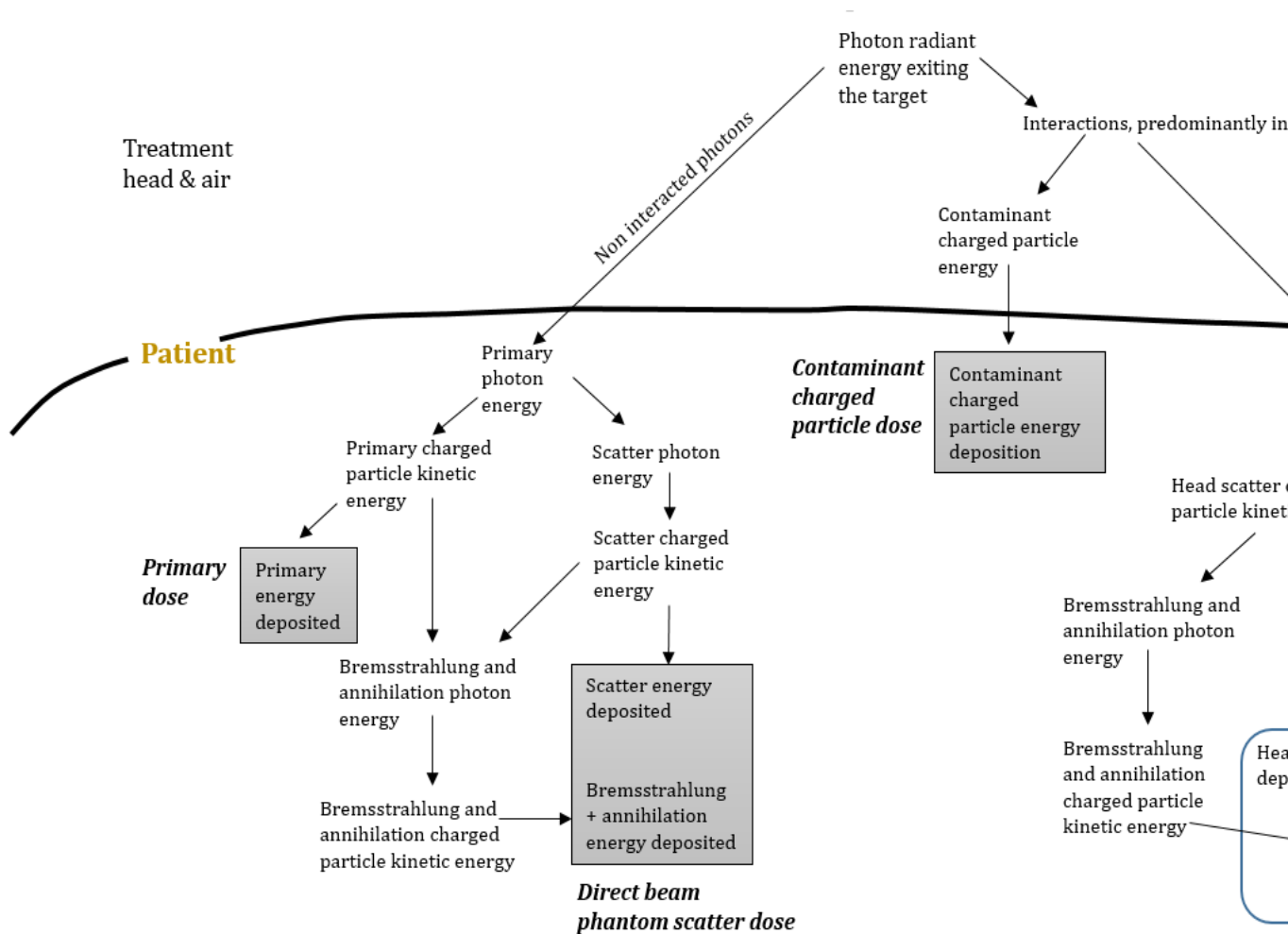


Figure 3.1 - Interaction history of all dose categories commonly associated with TPS and referred to as primary dose, phantom scatter dose, contaminant charged particle dose, and head scatter dose (reproduced from Ahnesjo and Aspradakis, 1999).

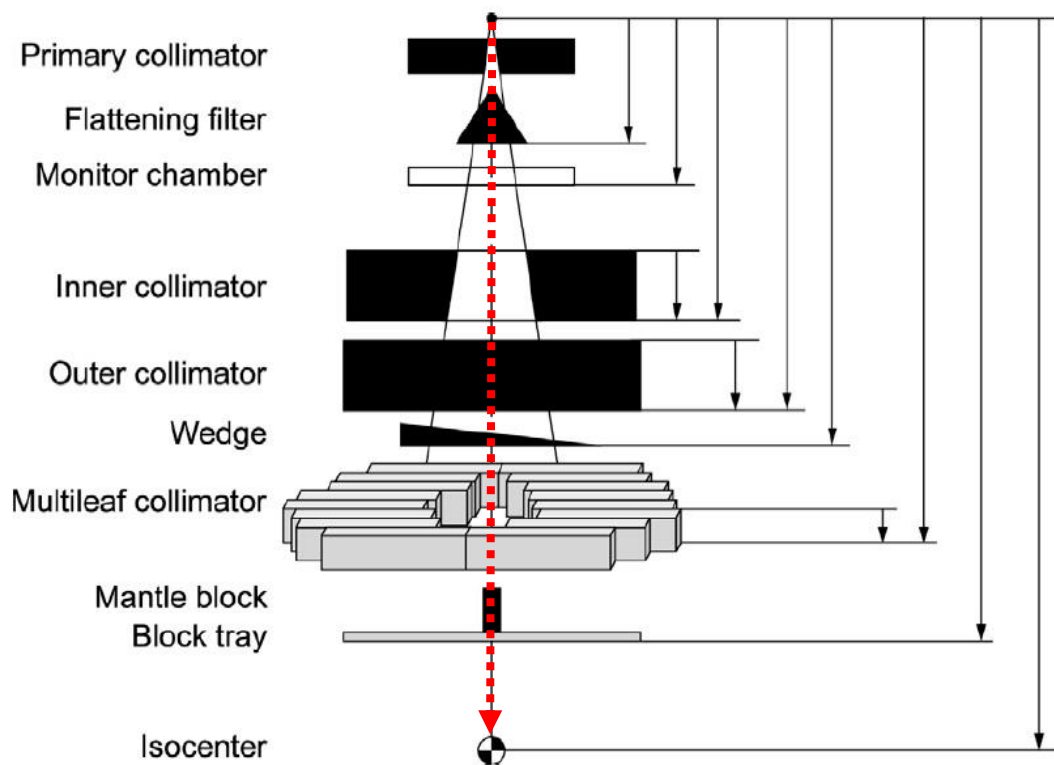


Figure 3.2 - Collimating and modulating devices in the beam path (Image taken from Nucletron (2008b)). *Red dotted arrow* shows the direction of the primary beam

3.1.2 Dose calculation using kernel models in OMP

Within OMP the patient tissue distribution is represented by a 3D density matrix, and the properties of each voxel are either derived from pixel values in a CT image or from user-specified values of mass or electron density. Dose per unit incident energy fluence is calculated by the algorithm (PB or CC) for a given beam and patient set-up, characteristic of the beam and the patient anatomy. In some publications, PB kernels are regarded as a “pre-convolution” of point kernels, thus their employment results in significant gains in computation time compared with point kernel-based approaches (Ahnesjö et al., 1992, Hong et al., 1996, Zhang et al., 2014). The PB algorithm is also known as a ‘type a’ algorithm (Knoos et al., 2006). In contrast CC,

which is a full 3D superposition or convolution method based on point kernels (Ahnesjo, 1989, Buzdar et al., 2010) is known as a ‘type b’ algorithm (Knoos et al., 2006). These descriptions are elaborated further below.

3.1.2.1 Pencil Beam algorithm

PB models were introduced to provide a more accurate and suitable method to use in the dosimetry of conformal radiotherapy in situations that did not involve much tissue heterogeneity. The model assumes that when any collimated photon beam is incident on a target, the beam is actually an accumulation of lots of smaller and narrower “pencil beams”. Each of these pencil beams has its own central axis along which it deposits some dose.

The dose deposition patterns, however, will vary with the intensity and energy spectrum of the beam that is hitting the target. For instance, taking an IMRT case as an example where the linac beam profile is non-uniform and modulated, the weighting and arrangement of the pencil beams is adjusted appropriately. In practice, the primary photon intensity at the entry point on the patient and electron contamination are included. The total incident energy of a pencil beam is referred to as the primary dose and the head scatter dose.

When a single pencil beam is incident on the surface of the patient, typically a teardrop-shaped dose distribution (Figure 3.3) results from the process of scattering and absorption of the primary and secondary electrons. In principle, one might produce and use an extremely small collimator and detector to determine the kernel dose distribution in water experimentally, but practically, the more common approach is to use Monte Carlo simulations

to calculate the dose distribution from a pencil beam in water (Ahnesjo and Aspradakis, 1999). These simulations also allow us to generate dose kernels for different photon energy spectra very easily. In summary, the energy deposited in a medium for PB algorithm is obtained in the following manner:

- (i) the irradiation geometry is firstly represented as a 3-D matrix of voxels (based on the CT density matrix)
- (ii) the centre of each pixel on the irradiated surface is assigned as the origin of a pencil kernel and all photons incident on a pixel are assumed to be concentrated at this point
- (iii) the primary fluence at each point on the surface is convolved for the entire field
- (iv) all dose contributions at each location in the 3-D matrix are integrated to calculate the total dose

However, there are some limitations to the accuracy of the pencil beam kernel model. In the literature (Hong et al., 1996, Buzdar et al., 2010, Zhang et al., 2014), it has been pointed out that PB convolution is prone to inaccuracy in certain inhomogeneous tissue situations, especially in lung. Its inability to model electron transport in close proximity to tissue boundaries is the main limitation of PB kernel methods (Knoos et al., 2006, Aspradakis et al., 2003). In other words, the PB algorithm is unable to model accurately the transport of electron across tissues of different density (relative to water) in the patient, as in the case of lung.

Furthermore, PB kernels are most likely to be lacking accuracy in calculating backscatter and lateral scatter (as is the case in most clinical situations) where there are invariably inhomogeneities and/or missing tissues, thus resulting in inaccuracies in the clinical result. Figure 3.3 describes the pencil beam kernel algorithm in detail.

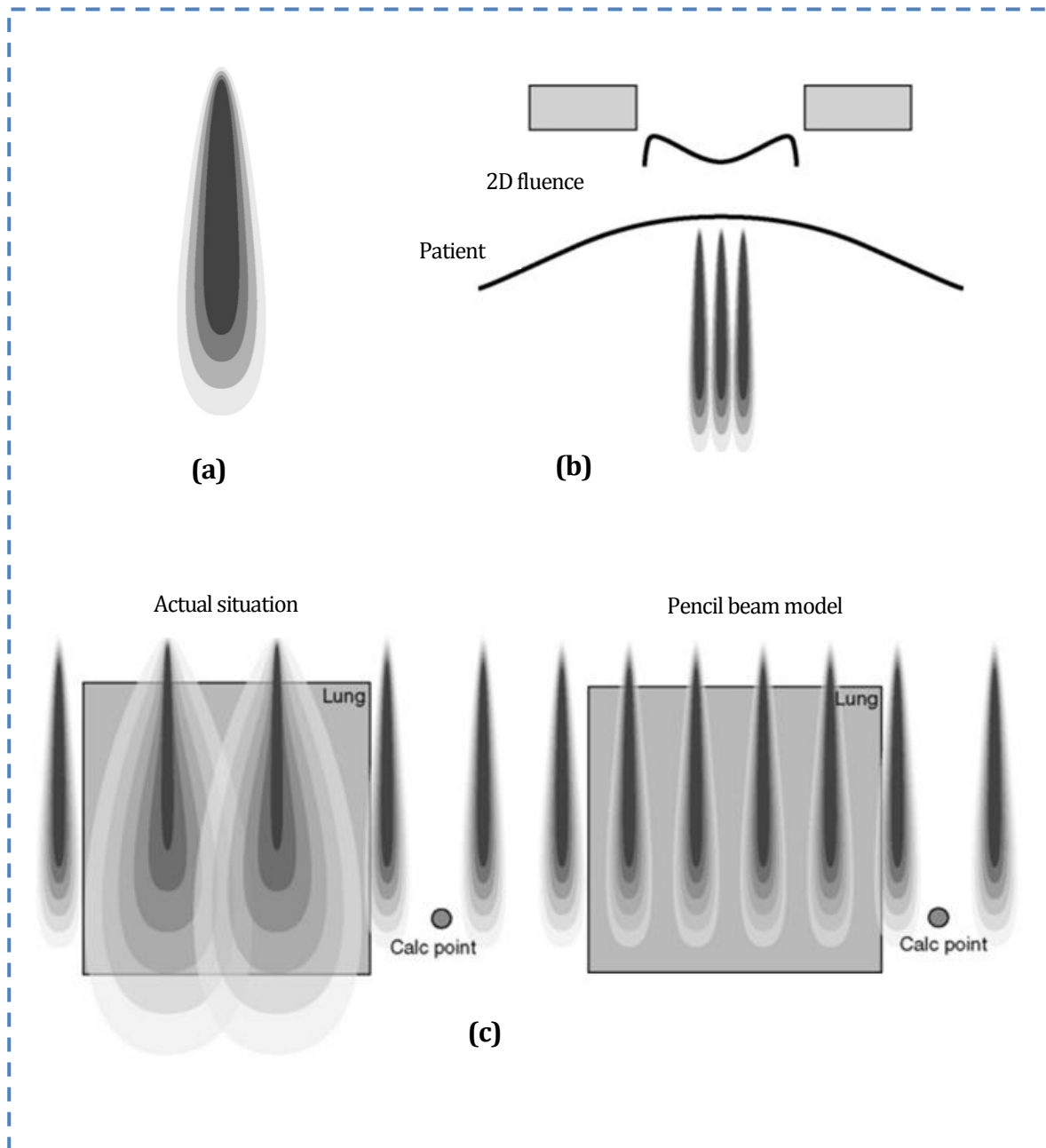


Figure 3.3 - (a) A single pencil beam kernel , (b) An example of a 2D fluence dose distribution using the pencil beam model , (c) An actual situation showing the limitation of the pencil beam kernel in underestimating dose at the calculation point because of the lack of backscatter and side-scatter (Radiology Imaging, 2017).

The pencil kernel method within OMP calculates dose within the patient using 1D convolution. A measured depth dose is used to derive an effective spectrum during a beam characterisation process. A poly-energetic pencil kernel is then derived by superposing mono-energetic pencil kernels. Mathematically, at each depth z , the poly-energetic pencil kernel (which is defined as dose deposited at point p where ρ is the electron density at p) is parameterised as a sum of two exponentials over the radius r in Equation 3.2 below (Ahnesjo et al., 1992, Ahnesjo and Aspradakis, 1999).

$$\frac{p}{\rho}(r, z) = \frac{A_z e^{-a_z r} + B_z e^{-b_z r}}{r} \quad (\text{Equation 3.2})$$

where A_z , a_z , B_z and b_z are depth-dependent parameters determined by least square fitting. In normal conditions, the primary dose is limited to a range within the small region surrounding the pencil beam axis, while the scatter dose is spread over larger region as secondary photons may travel longer distances before the next interaction. So, $a_z > b_z$ interprets the two terms as primary dose and phantom scatter dose respectively. By making this separation, the calculation improves the heterogeneity correction (Nucletron, 2008a).

3.1.2.2 Collapsed Cone algorithm

The Collapsed Cone (CC) algorithm is an approximation to a point kernel model that describes the deposition of the energy from a photon interaction site as a function of direction and distance (Ahnesjo, 1989). Each of the point kernels is divided in 3D into a number of variable solid angular bins or cones. Figure 3.4 (a) shows the approximation that all energy released from primary photons travelling in any direction within the cone is rectilinearly transported and deposited onto the axis. Hence, in energy deposition terms the cone is '*collapsed*' onto the axis.

Figure 3.4 (b) shows the consequences of the collapsed cone approximation in transporting the energy along a discrete axis. The energy that should be deposited in voxel B' from interactions at the vertex of the lower cone is deposited in voxel B and vice versa (Ahnesjo, 1989). The displacement between voxel B' and B is increased with distance, but the first scatter fraction decreases with increasing distance. This allows the total energy deposited to be conserved. Most energy is deposited close to where it is released, making displacement errors less important.

In the standard implementation of the CC algorithm in OMP, 106 different cones are used: 60 lie in the forward direction, 40 in the lateral direction and 6 in the backward direction from the kernel origin (Figure 3.5).

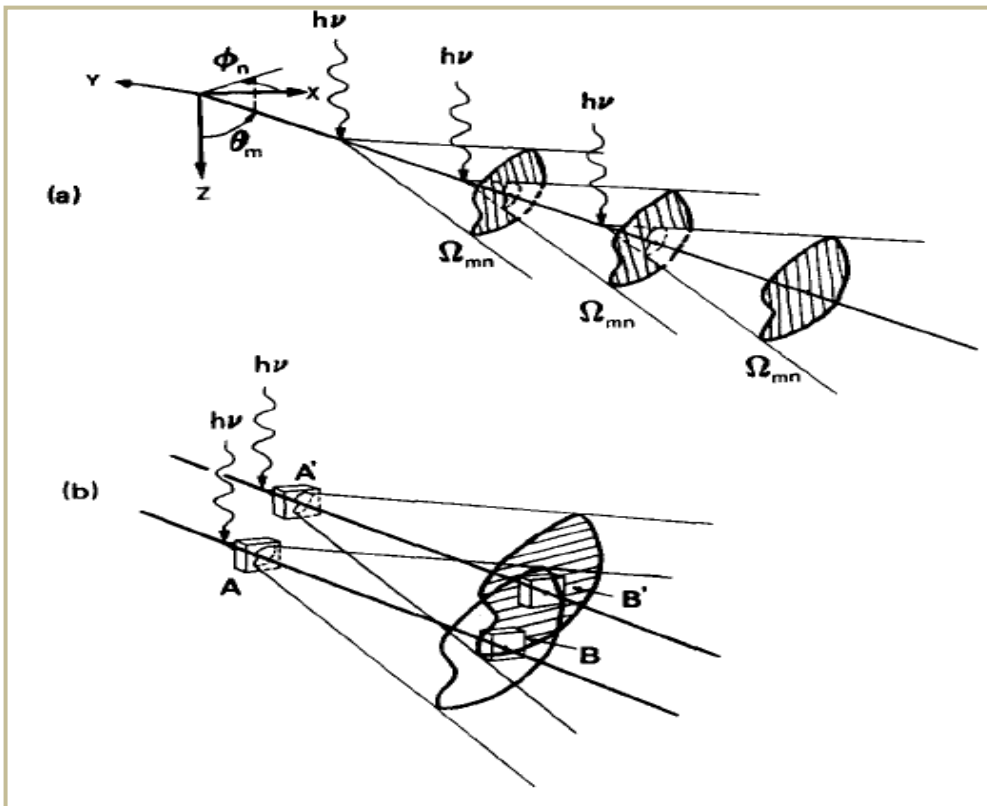
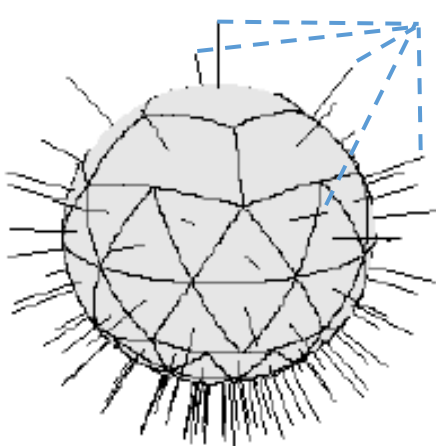


Figure 3.4 - (a) Collapsed angular cones within the central axis with energy rectilinearly transported and deposited on the axis. (b) Consequences of the CC approximation to transport energy along a discrete axis. The energy that should be deposited in voxel B' from interactions at the vertex of the lower cone is deposited in voxel B and vice versa (Image taken from (Ahnesjo, 1989)).



Direction of point kernels

Figure 3.5 - Set of directions of the point kernel with angular binnings. There are 106 different directions used in the Oncentra standard configuration. (Image taken from Oncentra -Physics and Algorithms manual version 4.3).

Convolution based point kernel models use the fact that in homogeneous media the point is independent of location. Total energy released in the medium (TERMA) is calculated by this point kernel which enables dose for a clinical beam to be computed. For each direction the kernel is parameterised as:

$$h(r) = \frac{Ae^{-ar}}{r^2} \quad (\text{Equation 3.3})$$

where r indicates the distance to the interaction point, a is the range of energy transport from the interaction point and A/a equals the fraction of energy transported in the given direction per unit solid angle. Two sets of point kernels are used in OMP, one to obtain primary dose by energy released from the primary photons and the other to obtain phantom scattered dose by energy released from scattered photons. These two main parameters are deposited as the total absorbed dose. Hence, Equation 3.3 is modified to give Equation 3.4 for the CC algorithm in order to speed up computational time.

$$h(r) = \frac{Ae^{-a\theta} + Be^{-a\theta}}{r^2} \quad (\text{Equation 3.4})$$

For the calculation of dose in heterogeneous media, any modulation in the 'primary' part of the kernel (for example changes in relative mass stopping power of secondary

electrons¹⁰) and in the 'scatter' part (for example changes in relative mass attenuation coefficient¹¹ of scattered photons) are both approximated with variations in electron density between media. So, this model is more capable of dealing with electron transport at tissue boundaries (Aspradakis et al., 2003) in heterogeneous media compared to the PB algorithm.

Despite the advantage of CC relative to PB, CC has its own limitations. One known limitation is the extension of the penumbral region (Knoos et al., 1995, Aspradakis et al., 2003, Knoos et al., 2006) in the fluence matrix. However, this can be improved by ensuring that the dose matrix and patient density matrix are of close or equal dimensions prior to calculation.

For the optimisation work using the TPS discussed hereafter in this research, calculations involved the PB algorithm unless stated otherwise. This is because most of the verification and proof of concept work in this research was done using a homogeneous water phantom, rather than the 'real' patient, and PB is the algorithm currently deployed in VCC as described in Section 3.3 below.

¹⁰ Mass stopping power of secondary electron - the energy released by the charged particles (secondary electrons and possibly positrons) per unit areal density.

¹¹ Mass attenuation coefficient - fractional number of photons lost (or fractional decrease in intensity) per unit areal density (which units in gcm^{-2}) in the direction of the radiation travelled.

3.2 MONTE CARLO DOSE CALCULATION ALGORITHM

3.2.1 Photon transport modelling using EGSnrc package

To understand the fundamentals of radiotherapy, photon and electron radiation interaction with matter is an essential aspect which needs to be covered. For example, in the kilovoltage energy range, 5–140keV (Ali and Rogers, 2008), the photoelectric effect predominates since the probability of interaction decreases strongly as photon energy increases ($\sim E^{-3} \sim h\nu^{-3}$). This is independent of the fact that photoelectric absorption cross-section, σ_{ph} also increases as the atomic number, Z of the material subject to radiation ($\sim Z^4$).

$$\sigma_{ph} \approx \frac{kZ^4}{h\nu^3} \quad \text{(Equation 3.5)}$$

In intermediate energies (ranging from 100keV to 10MeV), incoherent Compton scattering events take place, which depend on electron density, which is proportional to Z/A (where A is the mass number). For most elements, Z/A is about 0.5; the main exception is for hydrogen, for which Z/A is 1. At some high energies (above 5MeV), pair production dominates. Electrons lose their energy via collision and radiation as they traverse across matter. Therefore, tracking the passage of radiation is crucial and requires a transport analysis which accounts for electron trajectory through any geometry.

MC codes provide numerical and statistical methods to model radiation transport (involving entities such as photons, electrons, neutrons, protons, charged nuclei, atoms, and molecules) in the field of Medical Physics (Seco and Verhaegen, 2013) as well as other

disciplines. MC offers a reliable radiation transport algorithm, which was widely discussed in the literature by medical physics practitioners and researchers in the later decades of the 20th century. Since then, it has been intensively used for research and development in medical applications (Rogers, 2006). Chetty et al. (2007) have also described MC as follows.

“As a technique for calculating dose in a patient, the underlying physical basis is much simpler in concept than analytic algorithms because the MC method consists of a straightforward simulation of reality and does not involve complex approximations nor models of dose deposition, but only a knowledge of the physics of the various interactions which have been well understood for over 50 years in most cases”.

One of the most widely used MC codes at present, the EGSnrc package, was developed from the EGS4 (Electron Gamma Shower version 4) code (Nelson et al., 1985) by several authors at the Stanford Linear Accelerator Centre and National Research Council of Canada in the 1980s and 1990s. Subsequently, work by researchers such as Kawrakow (2000) and Kawrakow and Rogers (2013) demonstrated several improvements in the EGSnrc package compared to the earlier EGS4 version. This project uses the BEAMnrc package (Rogers et al., 2011), upgraded from the original BEAM user code (Rogers et al., 1995) for linac simulation and associated with the DOSXYZnrc code for dose distribution calculation within a rectilinear matrix. BEAMnrc and DOSXYZnrc are part of EGSnrc. A powerful facility in BEAMnrc allows for user input and easy modelling of a linear accelerator to incorporate the basic elements and component modules found in a real linac head (like jaws, flattening filter, secondary collimators, MLCs). Therefore it is considered to be the ‘gold standard’ for photon-electron MC simulation in radiotherapy applications (Hasenbalg et al., 2008).

Usually a “phase-space” file (which fully characterises the incident beam) is used to represent the input to DOSXYZnrc simulations in a phantom or patient, or subsequently to be fed into further BEAMnrc simulations. This file records information regarding all the particle types, energies and directions when crossing the relevant scoring planes. However, there are practical limits to the number of particles that can be stored in a phase-space file. For instance, a file storing ZLAST (the last simulated component module) would require about 69 Gigabytes for 2^{31} particles (Rogers et al., 2011).

Due to potential storage issues, an option to use a full BEAMnrc simulation of a treatment head as a particle source for DOSXYZnrc simulations has been made available, with the advantage of by-passing the intermediate phase-space data. However, to generate a full linac simulation to represent each source particle requires extra computational time and this results in reduced temporal efficiency. A direct comparison of efficiency between phase space sources and full BEAMnrc simulation sources has been made by Kawrakow and Walters (2006). They reported that full BEAMnrc simulation improves efficiency (through reducing time) by up to a factor of about 5 for fields defined using photon jaws, and up to a factor of 6.5 for secondary collimation with a MLC, compared with phase-space file sources. This was achieved primarily by the efficient use of Variance Reduction Techniques (VRTs) such as photon splitting in DOSXYZnrc and directional bremsstrahlung splitting, DBS within BEAMnrc, rather than just particle recycling in the phase-space file. These techniques will be explained in more detail in Chapter 4.

Monte Carlo photon transport relies on accurate interaction cross-section datasets for the simulation. Material compositions and densities are based on the data that has been set out

in ICRU report 37 (ICRU 1984). In the EGSnrc package, there are 2 data sets available: ICRU 521 and ICRU 700, which correspond to a threshold kinetic energy for secondary electron production of 10keV and 189keV respectively (relative to the 511keV electron rest energy).

Electron cut off (ECUT) is used in conjunction with photon cut off (PCUT) to increase the calculation speed in MC simulations. This means that if the particle energy falls below the relevant cut off, the particle trajectory is terminated, and its energy is deposited in the current region. This reflects the main reason for using different cross-sectional data, as different secondary electron cut-off energy may be used to increase the accuracy or the speed of calculation. In addition, electron range rejection involves terminating electron tracks with the residual range and this keeps them from getting to the scoring plane.

As an example of ICRU cross-section dataset selection, if ICRU 521 is used as ECUT (which will be explained in later sections), the kinetic energy cut off is $521\text{keV} - 511\text{keV} = 10\text{keV}$. Similarly, when ICRU 700 is selected as ECUT, the kinetic energy cut off is $700\text{keV} - 511\text{keV} = 189\text{keV}$. Hence, as soon as the total energy is below ECUT, the particle history is terminated, and energy is deposited locally. However, the cut-off energy of photons (PCUT) is the same (10keV) for both data sets.

For the transport of secondary electrons, the situation is far more complicated than for the transport of photons, since electrons undergo large numbers of collisions during the slowing down process. To accommodate these, MC codes use 'condensed history' techniques (Kawrakow and Bielajew, 1998) to incorporate a large number of these electron interactions into a single step. If the step is short, it increases the accuracy of the simulation. ESTEPE and

SMAX are parameters introduced into EGSnrc, which represent the maximum fractional electron energy loss per electron step and the maximum electron step allowed respectively.

3.2.2 Distributed computing system in Velindre Cancer Centre

Most of the validation work for the linac modelled in this thesis was undertaken using the Cardiff University and Velindre Cancer Centre 'RTGrid' web-based service (version 2.0) (Downes et al., 2009) powered by GridSphere¹², although some of the basic simulations were done by using a single processor for the purpose of basic understanding of the EGSnrc MC system. The RTGrid system is used as a platform to provide high throughput simulations, together with appropriate variance reduction techniques, to reduce the calculation time for treatment plan verification to clinically useful levels.

RTGrid is based on a graphical user interface using a service-oriented architecture similar to that discussed by Yaikhom et al. (2008). Any MC simulation jobs sent to the RTGrid use a simulation template known as the 'Profile'. This 'Profile' contains simulation data including executable scripts to be run at a specific phase when the simulation takes place. The running of the simulation is then controlled by the 'experiment manager' that interacts with the RTGrid database and changes the simulation status depending on whether the simulation is 'Pending', 'Running' or 'Completed' (Figure 3.6).

¹² GridSphere – US based software development company responsible for designing and developing of high range of software solutions.

The user can leave the job running overnight and upon completion of the job, the simulation output files are generated from the collated distributed machines. Currently, the deployment of distributed computing resources in Velindre Cancer Centre is based on a batch queuing system which utilises a Condor architecture¹³ based on local machines which mainly operate with INTEL X86_64 AMD processors.

¹³ Condor architecture – a batch scheduling system which provides a job queueing mechanism, scheduling policy, priority scheme, and resource monitoring. Users submit their serial or parallel jobs to Condor, Condor places them into a queue, chooses when and where to run the jobs based upon a policy, carefully monitors their progress, and ultimately informs the user upon completion.

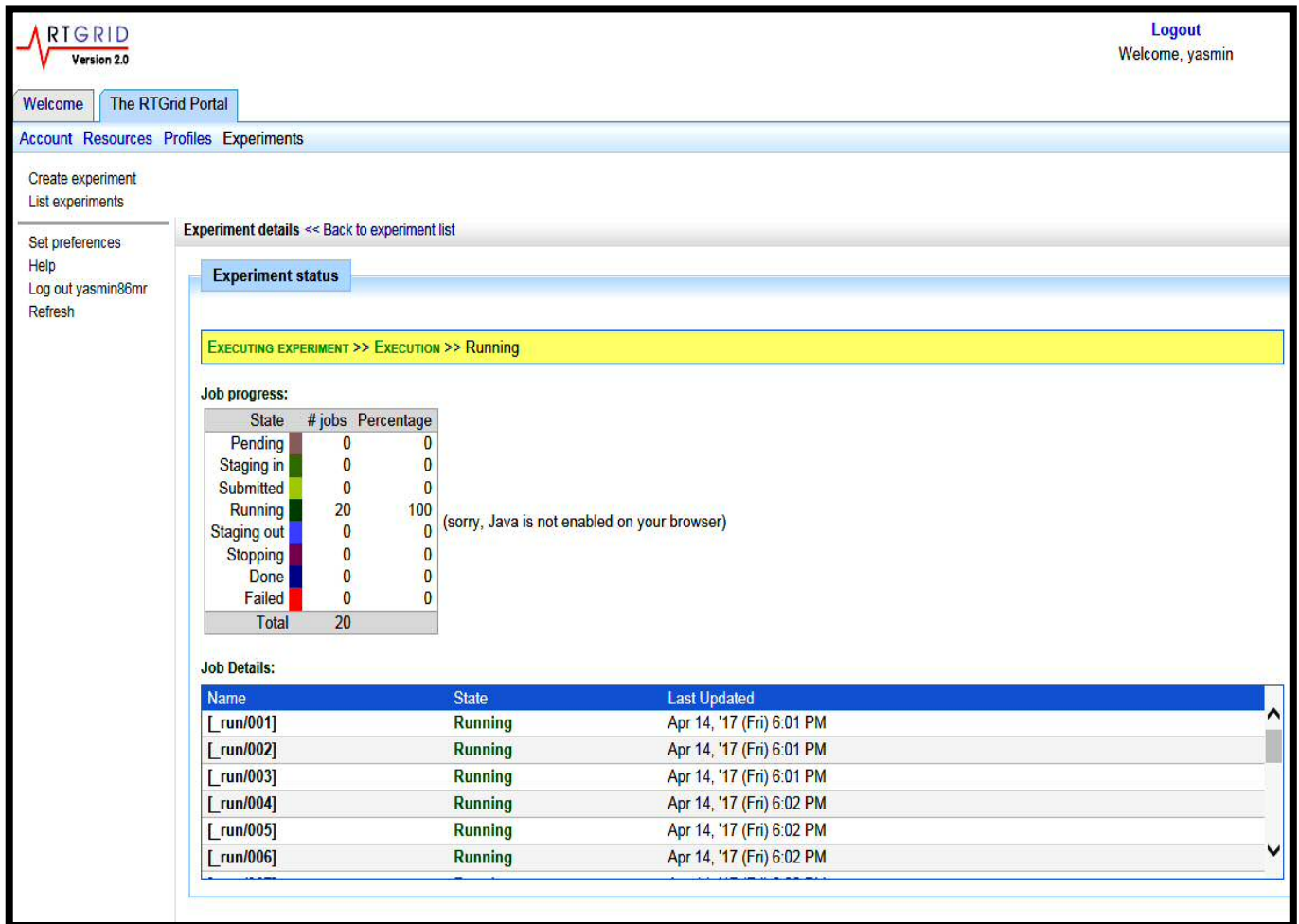


Figure 3.6 - A screenshot image of the RTGrid Portal showing the status of a particular simulation job. All 20 distributed machines are in 100% 'Running' mode but not yet completed.

3.3 A DECONVOLUTION-BASED METHOD

3.3.1 Dose calculation algorithm in “Dosimetry Check”

The Dosimetry Check system developed by Math Resolutions™ is an alternative to direct 3D IMRT and VMAT dose verification. It is a software-based verification tool that may be used in conjunction with an EPID or other image acquisition array to verify dose, Map Check

diode array, Ion Chamber array and other devices. It is quite widely used as a system of dosimetric verification, which compares the planar dose reconstructed from the relevant detector arrays with the dose originally calculated by the TPS. For example, by using an EPID panel as detector array, Dosimetry Check reconstructs and recalculates the fluence distribution algorithmically. It uses EPID images acquired during treatment or before treatment for transit dosimetry or pre-treatment dosimetry respectively. There are two dose calculation algorithms that can be used in Dosimetry Check, these being the PB and CC algorithms. The CC version did not obtain a CE mark until December 2017 and hence was unavailable for clinical use at the time of writing. The system uses an in-air fluence map calculated from data recorded by the portal imager to reconstruct a 3D dose distribution on the planning CT dataset. The delivered dose calculated by Dosimetry Check is then compared against the original patient treatment plan. A detailed description of the dose reconstruction method employed in the Dosimetry Check software is given in Chapter 5.

For the work described within this thesis, a Varian ‘Trilogy’ linac was used with an ‘aS1000’ EPID mounted on an ‘Exact’ arm (Varian Medical System, Palo Alto, CA, USA). This machine has been clinically commissioned for Dosimetry Check in Velindre Cancer Centre although, to date, it has been verified with the PB kernel only. Thus, only the Dosimetry Check PB algorithm will be discussed hereafter in this section. More details of the CC kernel algorithm are available in the Dosimetry Check manual¹⁴.

¹⁴ www.mathresolutions.com/dcman.d/dcalgor.htm#_Toc451433041

Generation of the kernel is done by the Dosimetry Check UK distributor, OSL¹⁵, with input (in the form of relevant acquired data) from clinics. Briefly, the PB algorithm dose kernel is directly computed from measured percentage depth dose data obtained from the clinics (Velindre Cancer Centre for example) and Monte Carlo generated pencil kernels.

There is a specific program within the Dosimetry Check system which computes the pencil kernel from measured data. The program first calculates mono-energetic point spread functions using MC and then uses these functions to compute mono-energetic pencil beam kernels. Next, central axis data at different field sizes is used to generate a spectrum of measured depth dose. These spectra and kernels are then used to compute the dose. The process of kernel generation is done by the manufacturer and a detailed description is given in the manual. Following that, the commissioning process is completed by the clinic.

In the analysis of IMRT and VMAT images, Dosimetry Check also uses the so-called 'gamma method'. This is a vector calculation method developed by Low et al. (1998). The gamma method is a way to compare two dose distributions by taking dose difference and spatial displacement between two analysis points to provide an index of comparison. For example, an analysis point may be separated by a large spatial displacement from the reference point, but by a small dose difference such as occurs in a low gradient area. Conversely, in a steep gradient area, a point maybe be separated by a large dose difference with a reference point, but, the spatial displacement between them might be small. Hence, the gamma method

¹⁵ <http://www.osl.uk.com/>

can be used in assessing dose difference and distance to agreement between points and is used to investigate the validity of a certain treatment plan.

In Dosimetry Check, the gamma distribution is evaluated by taking the TPS as the reference distribution, and the dose computed by Dosimetry Check as the evaluated distribution. Equation 3.5 describes the gamma method in mathematical detail,

$$\Gamma(r_e, r_r) = \sqrt{\frac{|r_e - r_r|^2}{d_m^2} + \left(\frac{D_e(r_e) - D_r(r_r)}{D_m}\right)^2} \quad \text{(Equation 3.5)}$$

where, r_r and r_e are the reference point and evaluated point respectively. Given the reference point, r_r , the volume around that point is searched for the minimum gamma value Γ . $D_r(r_r)$ is the dose at the reference point while $D_e(r_e)$ is the dose at evaluation point, d_m is the distance criterion (for example 0.3cm), D_M is the dose criterion (for example 3% x 200 cGy/100 = 6 cGy). D_M would normally be the target dose at the isocentre (Math Resolutions, 2017). However, there are some practical considerations to be taken into account for the evaluation of gamma. Matrix spacing for dose calculation in Dosimetry Check has to be the same as the distance to agreement that the user has defined, since Dosimetry Check interpolates the values for gamma distribution on planar images. For example, if the user defined the distance to agreement to be 0.3cm, but the matrix spacing for interpolation in Dosimetry Check is 0.5cm, the resulting dose is compromised for the gamma calculation.

The dose algorithms utilised in this research have been discussed in this chapter. The application of these algorithms to obtain the necessary data to fulfil the aims of this research will be explained further in subsequent chapters.

Chapter 4

MONTE CARLO VERIFICATION OF LINEAR ACCELERATOR AND TREATMENT PLANNING SYSTEM

In this chapter, the simulation of radiation transport through a model of a local linear accelerator using Monte Carlo simulation techniques is described. Parameters used for the simulation are discussed, as well as workflow through the validation steps. Simulation of radiation output from some standard field configurations are presented and compared with measured data and equivalent fields generated by the local TPS, mainly to demonstrate that the simulation gives reliable baseline data in comparison with other techniques discussed in subsequent chapters.

4.1 MONTE CARLO MODELLING OF LINEAR ACCELERATOR

There is now a standard expectation that radiation treatment beams should be highly geometrically conformal and produce the most accurate dose distributions possible in relation to the tumour. Modern radiation therapy equipment is increasingly capable of delivering small fields of arbitrary shape, as a consequence of increased availability of high-definition MLCs on conventional accelerators and specialised machines capable of providing IGRT, IMRT and VMAT treatment techniques.

Hence such regimes necessitate tighter target margins for clinical accuracy and require strict dosimetry demands. The aim of this work was to model the linac as accurately as possible to provide reliable verification of the research.

4.1.1 Determination of source size and energy photon

In this work, the linear accelerator, which is the subject of the modelling exercise, is a 6MV Varian 2100CD 'TRILOGY' system available in the Velindre Cancer Centre. This has been previously modelled and validated using BEAMnrc (Rogers et al., 1995) and DOSXYZnrc (Kawrakow and Walters, 2006) Monte Carlo codes as part of an earlier project (Spezi and Lewis, 2002, Chin et al., 2003). The model was reviewed and checked for continued accuracy for the purposes of the current project. Validation of the LINAC model started with performing a full Monte Carlo modelling exercise, although this was intrinsically time consuming. The validation process began with the determination of source size and energy of the incident electron beam. A nominal energy of 6MeV and a source size of 1.0mm were chosen as starting points in defining the incident electron beam based on values provided by the manufacturer.

A number of component modules such as SLABS, CONS3R, FLATFILT, CHAMBER, JAWS and DYNMLC were used to model features of the LINAC including target, primary collimator, flattening filter, ion chamber, mirror, secondary and tertiary collimators (jaws and MLC) (Figure 4.1). A topical review of the Monte Carlo modelling of external photon beams (Verhaegen and Seuntjens, 2003), suggested that tuning of the primary electron energy by comparing the depth dose results for a 10x10cm² field with measured data is a necessary first step. For this purpose, local commissioning data of percentage depth dose for a 10x10cm² field taken with a

Scanditronix Wellhoffer CC13-S Ionisation Chamber¹⁶ (with typical active volume of 0.13cm³) was compared with simulated data using MC.

A water equivalent phantom of geometry and dimensions as shown in Figure 4.2 was used to represent a 50x50x50cm³ water tank for dose calculation using DOSXYZnrc. SSD was set to 100cm and each field size was defined at the surface of the phantom. Analysis of the comparison work was carried out using the Matlab software image processing toolbox previously developed locally (Spezi et al., 2002).

¹⁶ Scanditronix Wellhoffer CC13-S Ionisation Chamber used for the relative dosimetry of photon and electron beams in radiotherapy and as a standard chamber for use in a water phantom.

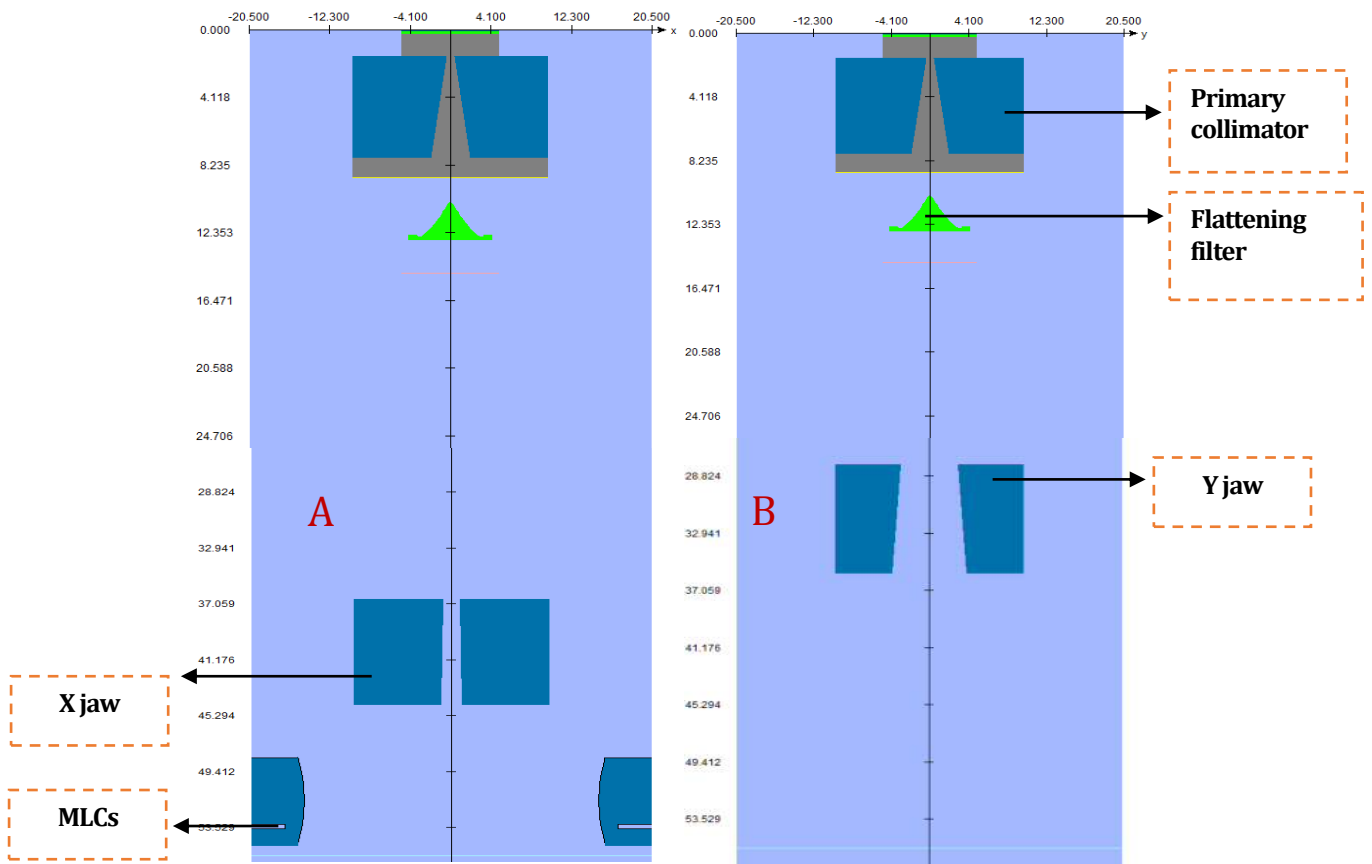


Figure 4.1 - A preview of the linac head modelled using BEAMnrc, consisting of the main component modules such as X-ray target, primary collimator, flattening filter, ion chamber, the collimator jaws and also the MLC. (A) XZ view, (B) YZ view

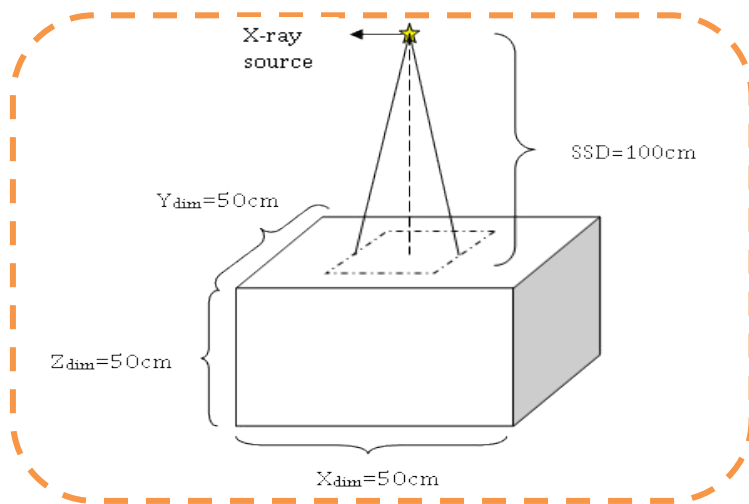


Figure 4.2 - A phantom consisting of water equivalent slabs was used in DOSXYZnrc dose calculation for the validation exercise.

In order to investigate the effect of different electron energies, depth dose curves were also obtained at 5.9MeV and 6.1MeV and their differences investigated. Once the depth-dose energy match had been found, large field size (40x40cm² beam) profiles were obtained to investigate any inconsistencies in the profile shape caused by incorrect source size. The importance of finely tuning the electron focal spot size in the investigation of MC calculation accuracy has been described previously (Scott et al., 2008, Scott et al., 2009). The profile (at shallow depth) obtained by simulation was matched against the commissioning data acquired using a Scanditronix Wellhoffer Photon Field Diode (PFD)¹⁷.

Both depth doses and profiles were simulated and plotted in relation to a homogenous water phantom created using DOSXYZnrc. The computation was fed into the distributed computing RTGrid portal (described in Chapter 3) for faster calculation. In order to fully verify the linac for this work, beam profiles were also plotted for smaller field sizes such as 5x5cm², 3x3cm² and 2x2cm². All the fields were then normalised to a depth of 5cm. The early steps in the process of energy and field size tuning are illustrated in the flowchart in Figure 4.3.

⁴ Scanditronix Wellhoffer photon field diode, used for beam profile measurement in a water tank

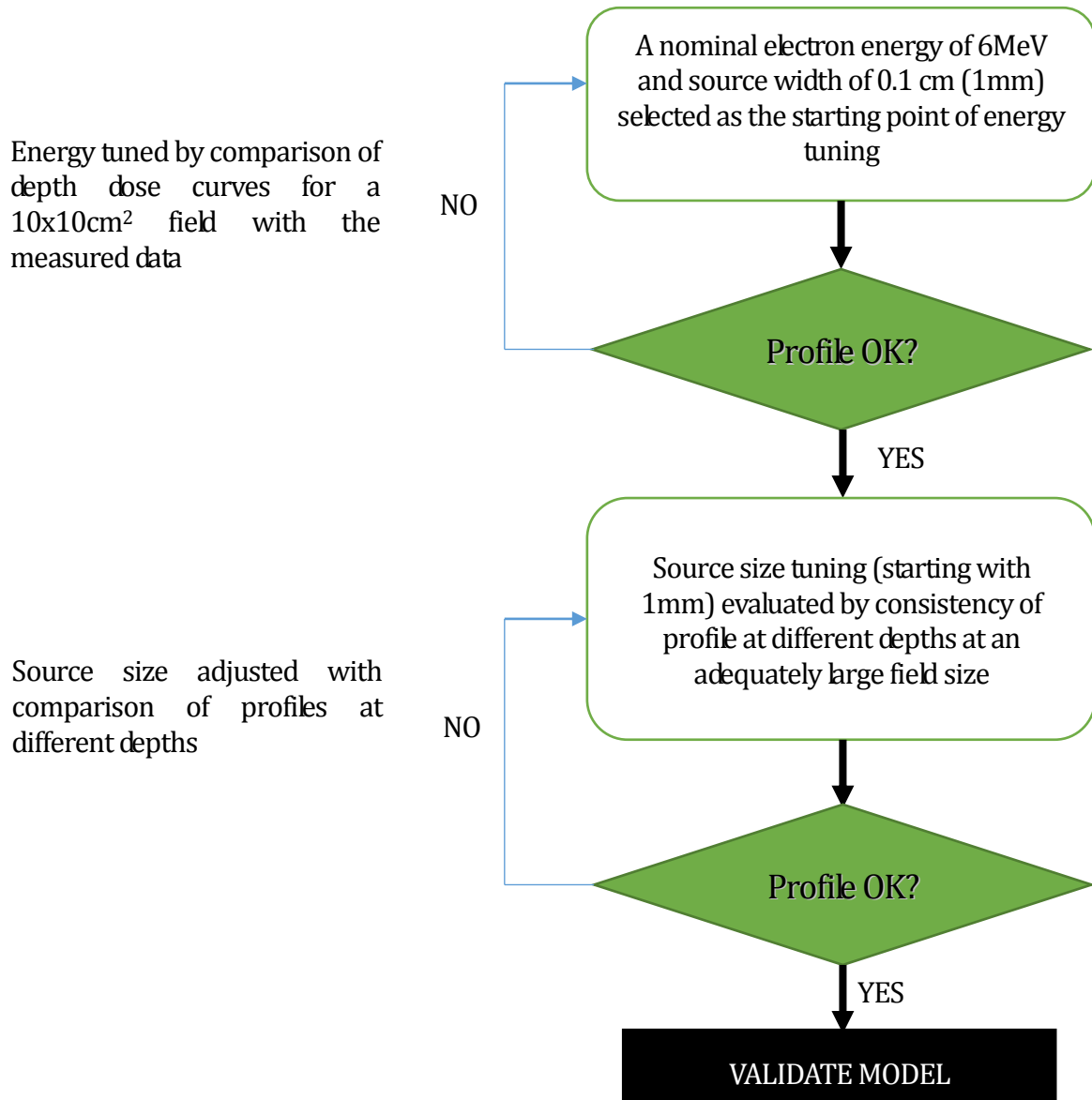


Figure 4.3 - A flowchart of the general steps involved in the initial validation process.

The key parameters used in running the BEAMnrc and DOSXYZnrc simulations are shown in Table 4.1 (I) and (II). It is essential that correct parameters are used to make sure that the simulations are of the appropriate level of accuracy. For that purpose, the BEAMnrc parameter ISOURCE=19 (Figure 4.4) was selected as the source type to match the Gaussian distribution of the electron beam entering the centre of the X-ray target. This is due to the fact that the direction and spatial distribution of the accelerated electron beam has a significant effect on the angular distribution of the generated X-ray beam. It is assumed that the trajectory of the electron beam within the linac is perpendicular to the surface of the X-ray target with an unknown spatial distribution. From measured data elsewhere, it has been suggested that the spatial spread of the electron beam resembles a Gaussian distribution (Sheikh-Bagheri et al, 2000).

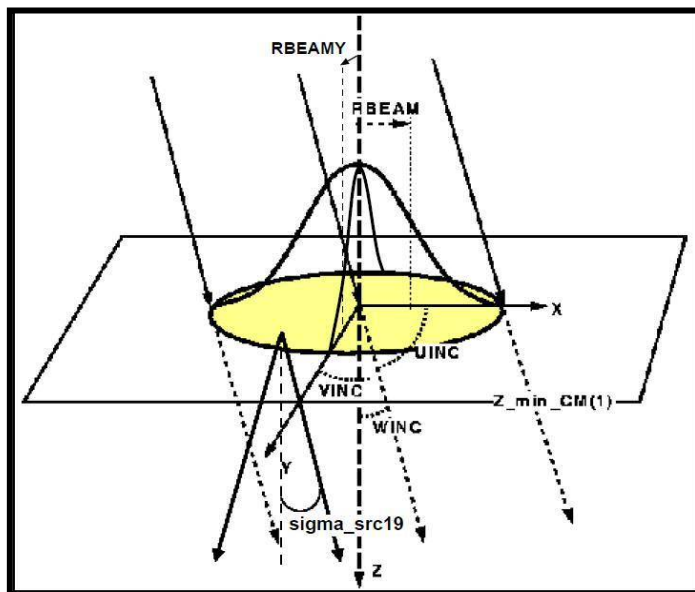


Figure 4.4 - Source type of Elliptical beam with Gaussian distribution in X and Y direction, ISOURCE=19 in BEAMnrc code. A source size with FWHM of 0.1cm (1mm) was used in the simulation (From BEAMnrc User Manual).

Table 4.1 - Example of parameters used in Monte Carlo EGSnrc package ((I) BEAMnrc / (II) DOSXYZnrc) for the simulation of photon transport through water phantom.

(I) BEAMnrc	
ITEM	VALUE
SOURCE BEAM ENERGY	6.00 MV
BEAM ENERGY TYPE	Monoenergetic
ECUT	0.700 MeV
PCUT	0.010 MeV
BREMSTRAHLUNG SPLITTING	Directional
DBS SPLITTING RADIUS	30cm (changeable with field size selected)
SOURCE TO SURFACE DISTANCE (SSD)	100cm
BREMSTRAHLUNG SPLITTING NUMBER, NBRSP	1000
USE REJECTION PLANE	None
CM FOR E-/E+ SPLITTING	4 (FILTER)
E-/E+ SPLITTING PLANE NO.	19 (Z=12.6153)
Z OF RUSSIAN ROULETTE PLANE	12.6cm
REDISTRIBUTE OF SPLIT E-/E+	ON
AUGMENTED RANGE REJECTION	None
BREMS CROSS-SECTION ENHANCEMENT	OFF
SPLIT ELECTRONS OR PHOTONS AT CM	None
SOURCE TYPE (ISOURCE)	ISOURCE=19; source size with FWHM=1mm
(II) DOSXYZnrc	
ITEM	VALUE
PHOTON BEAM ENERGY	6.00 MV
ECUT	0.700 MeV
PCUT	0.010 MeV
MEDIUM OF PHANTOM	H20521ICRU
RANGE REJECTION	ON
HOWFARLESS	ON
SOURCE TO SURFACE DISTANCE (SSD)	100cm
SOURCE TYPE (ISOURCE)	9 = Treatment Head Simulation
INCIDENT BEAM SIZE	10cm
DBS SPLITTING FIELD RADIUS	30cm (changeable with field size selected)
SSD OF SPLITTING RADIUS	100cm
Z WHERE SOURCE SCORED	70cm
DISTANCE FROM SOURCE TO ISOCENTRE (SID)	30cm
PHOTON SPLITTING NUMBER, N_SPLIT	100
GLOBAL SMAX	5cm
XIMAX	0.5cm
X DIMENSION OF WATER PHANTOM	0.1mm x 500 voxels
Y DIMENSION OF WATER PHANTOM	0.1mm x 500 voxels
Z DIMENSION OF WATER PHANTOM	0.1mm x 30 voxels 0.2mm x 235 voxels

While the main aim of this chapter is to verify the accuracy of the linac model in delivering fields of interest in this work, the accelerating potential used throughout the work was 6MV to provide some simplicity. ICRU 521 was selected as the cross-section dataset for the materials used in the simulation, with a secondary electron production cut-off of 10keV (see details in Chapter 3). It contains physical properties such as mass density, electron density and atomic number of the materials that make up the component modules as set out in ICRU report 37 (ICRU 1984). ECUT (electron cut-off) and PCUT (photon transport cut-off) were set to 0.7MeV and 0.01MeV respectively to increase the accuracy and efficiency of the simulation as much as possible (Seco and Verhaegen, 2013). This meant that those electrons and photons whose energy fell below these values were discarded from the simulation and any remaining energy was deposited to the current region in the simulation.

Another important factor that can significantly increase the efficiency of the simulation is the application of the directional bremsstrahlung splitting (DBS) (Kawrakow et al., 2004) parameter compared to uniform or selective splitting (UBS or SBS). With DBS, bremsstrahlung photons which fall into a field of interest are split as they are created, while those out of the field are not. The magnitude of the DBS parameter is variable and dependent on the energy and other details of the beam. For this work, DBS was set to 1000 (Kawrakow et al., 2004) while its splitting radius was set to 10cm in both BEAMnrc and DOSXYZnrc for a 10x10cm² field. It was varied for other field sizes to avoid 'fat' photons being included in the region of interest.

As a further step in the validation of the linac model, correction for backscatter radiation from the Varian linac collimator jaws into the monitor chambers has been shown previously to

be an essential part of the process. From the literature, the effect of the backscatter radiation has been shown to be small compared to that due to head scatter and phantom scatter. However, in order to achieve accurate dose calculation, it is important to include this correction when using the convolution algorithm or any other model-based methods including MC (Liu et al., 1997a, Liu et al., 1997b). Moreover, the use of advanced treatment techniques such IMRT using dynamic jaw movement requires the photon output to be predicted with a high degree of accuracy for individual component fields. Hence, it is important to investigate the cause of variation in photon output in relation to the field collimation.

The method devised by Liu et al. (2000) was used for the correction of backscatter from the jaws for this work. In this method, MC simulations were used to estimate the ratio of backscatter radiation to the forward radiation $R(x, y)$ scored at the monitor chamber by investigating the amount of backscatter radiation as a function of X and Y jaws individually as a compound contribution to the photon output. $R(x_0, y_0)$ is the ratio of backscatter radiation from a reference field (10x10cm²). The dose ratios $R(x, y)$ were then used to calculate the change in photon output caused by the backscatter, $S_{cb}(x, y)$. Data from this study showed that the backscattered radiation contributes approximately 3% to the monitor-chamber-scored dose. Mathematically, the calculation for the correction follows Equation 4.1:

$$S_{cb}(x, y) = \left[\frac{1 + R(x_0, y_0)}{1 + R(x, y)} \right] \quad \text{(Equation 4.1)}$$

4.1.2 Results

From Figure 4.5, it is apparent that excellent agreement between the simulation and measured data of percentage depth dose (PDD) for a standard field size ($10 \times 10 \text{cm}^2$) was achieved, giving percentage differences within 1% beyond the build-up region (after d_{max}). This statement is supported by the results of PDD calculations for two slightly different energies (5.9MeV and 6.1MeV) as illustrated in Figure 4.6. PDD simulation using a 6.0 MeV electron beam gave better (i.e. smaller) overall percentage difference than the other electron beam energies. For the 6.0 MeV electron beam, the percentage difference clearly fluctuates around 0% and is not more than 1%, while values for the other beams are more offset from the horizontal (0% difference) axis. The normalisation of depth dose curves was done to a point at a depth (5cm in water in this work) that was appropriate to avoid effects due to an unstable state at d_{max} caused by variable electron contamination. Point d_{max} is always subsequently rescaled to the value of 100% unless stated otherwise in the thesis.

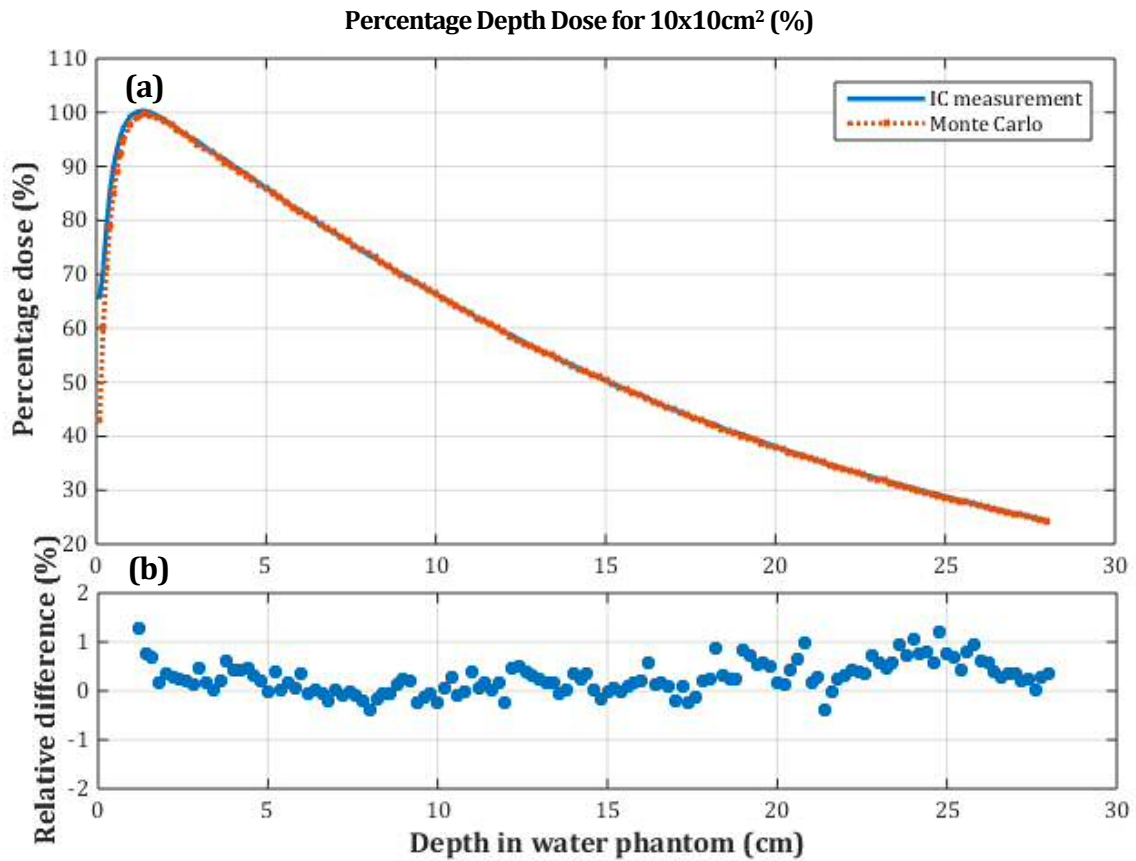


Figure 4.5 – (a) MC simulation of PDD for a 6MV photon beam energy with field size 10x10cm² compared to measurement data, normalized at 5cm depth. (b) Relative percentage difference between the MC simulation and the measurement data. The simulation uncertainty is within 2%.

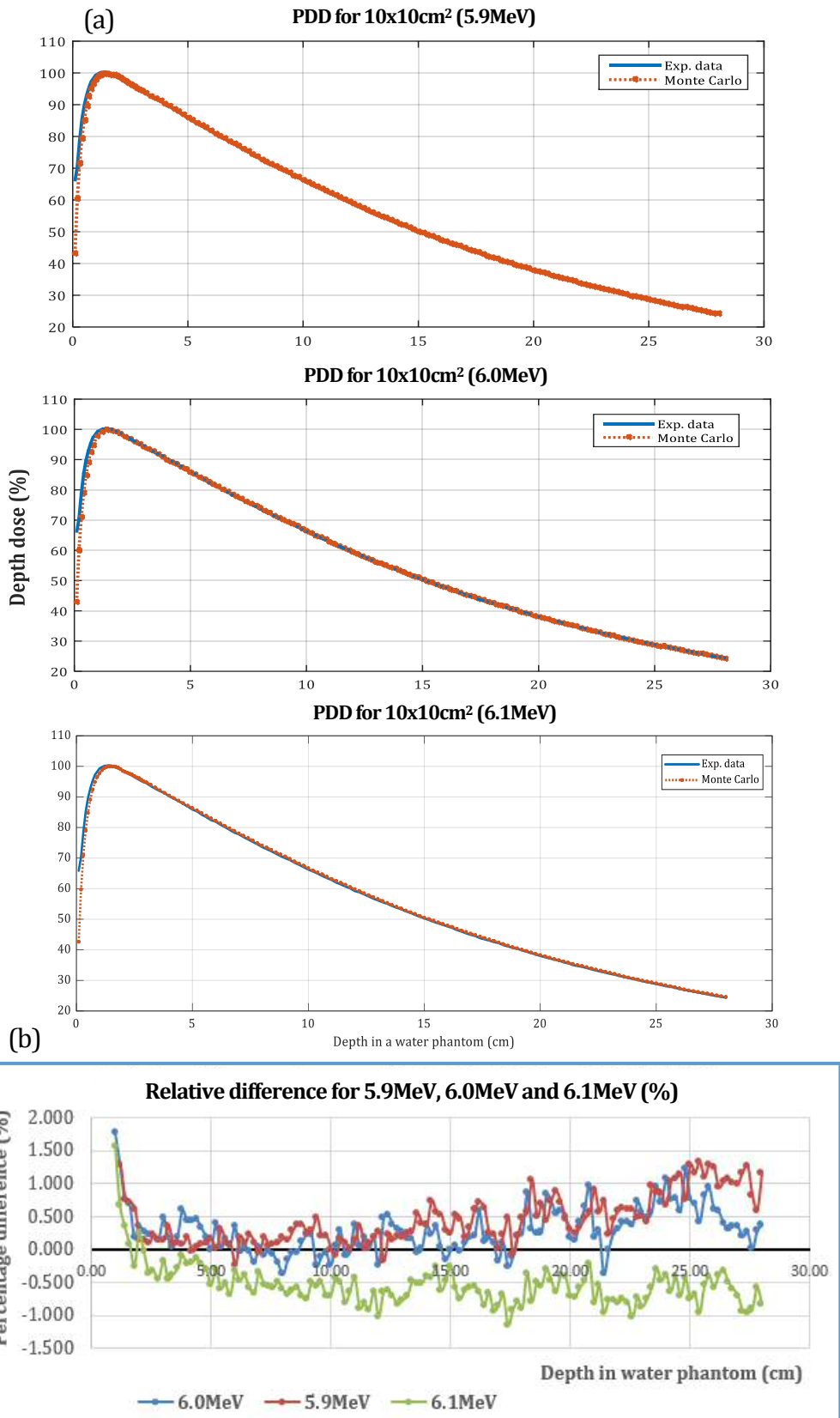


Figure 4.6 – (a) Depth dose curve comparison between measured data and MC data for 3 primary electron beam energies (5.9MeV, 6.0MeV and 6.1MeV). (b) Fluctuation of percentage difference for the 3 beam energies.

To check the accuracy of source size modelling, the behaviour of a large field size at a shallow depth is presented in Figure 4.7. A field size of 40x40cm² (linac maximum) is large enough to reveal any significant discrepancies in simulation for a 6MV photon beam. From the figure, the agreement for cross-plane profiles was deemed excellent (i.e. within 2%) when comparing measured and calculated relative dose at d_{max} and 5cm depth. A 'zoomed' plot (Figure 4.8) shows some degree of variation of agreement in the dose distribution along the beam profiles. This is not unusual for large fields since they are sensitive to scattered radiation and variation in primary photon energy across the field due to 'beam hardening' from the flattening filter.

Since the MC simulation and measured data were in good agreement, it was felt there was no need to undertake further investigation on source-related parameters for the purposes of this study.

40x40cm² cross-plane profiles at different depths in water phantom

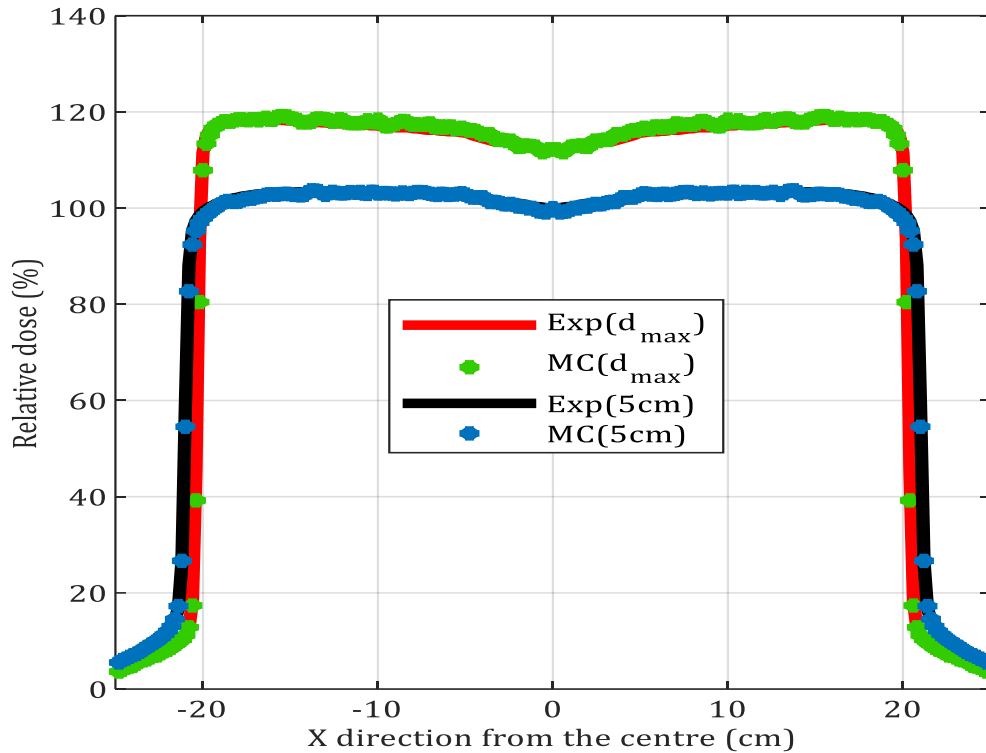


Figure 4.7 - Beam profiles for a 40x40cm² field in the 'X' direction at two shallow depths in a water phantom (d_{max} and 5cm). Good agreement achieved between simulation and measured data with a percentage difference of less than 2% in the high dose region.

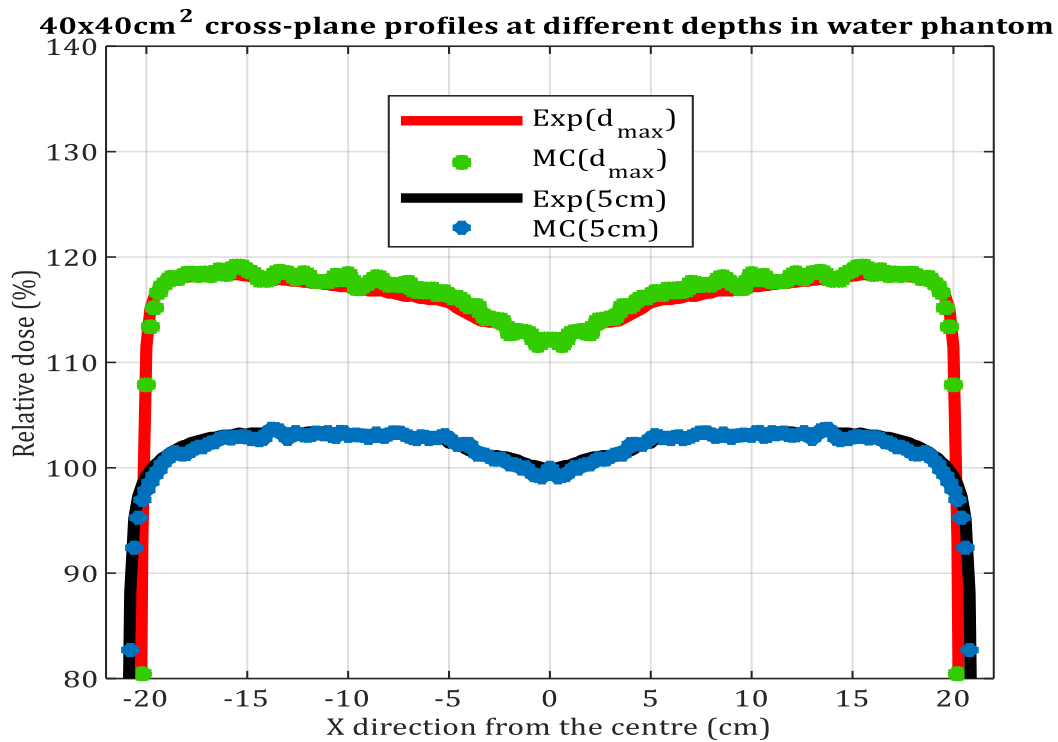


Figure 4.8 - Clear graphic of profile shape (zoomed plot from Figure 4.7) for viewing the matching between simulation and measurement. The 'horns' and 'dip' on the simulation profiles were found to be fairly consistent with measurement profiles (uncertainty within 2%).

Subsequently, an analysis of a range of beam profiles was performed by comparing measured and simulated data for several example field sizes. This showed excellent agreement in both X and Y directions for varying depths (Figure 4.9). Furthermore, the PDD analysis for all the field sizes revealed percentage differences of less than 2%, also demonstrating a good match between simulation and measurement as shown in Figure 4.10.

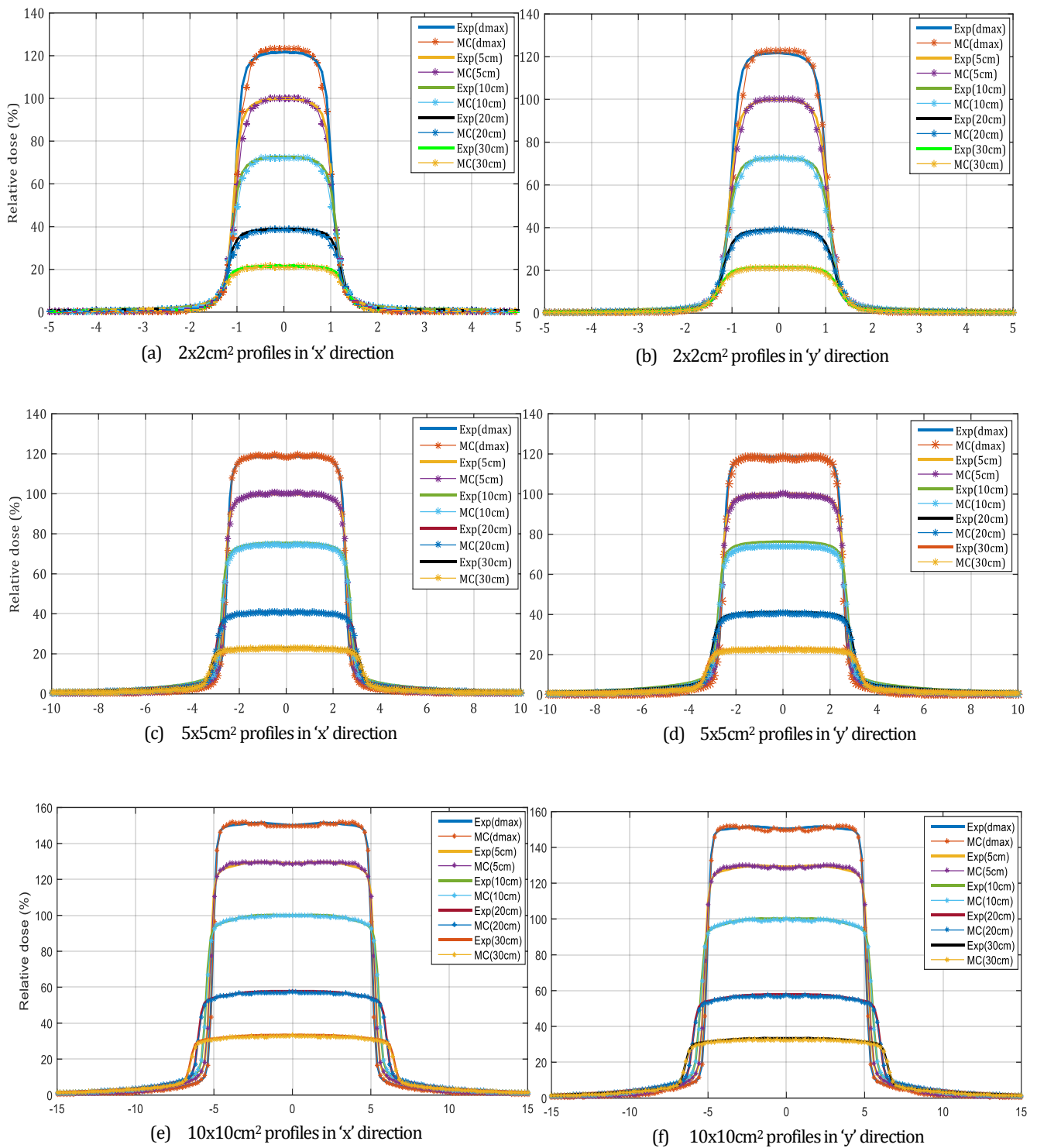


Figure 4.9 – Dose profile comparisons for varying field size at 1.5cm (d_{max}), 5cm, 10cm, 20cm and 30cm depth for 6MV photon beam energy, at 100cm SSD. All the profiles were normalised to 5cm deep ($2 \times 2 \text{cm}^2$ and $5 \times 5 \text{cm}^2$) and to 10cm ($10 \times 10 \text{cm}^2$).

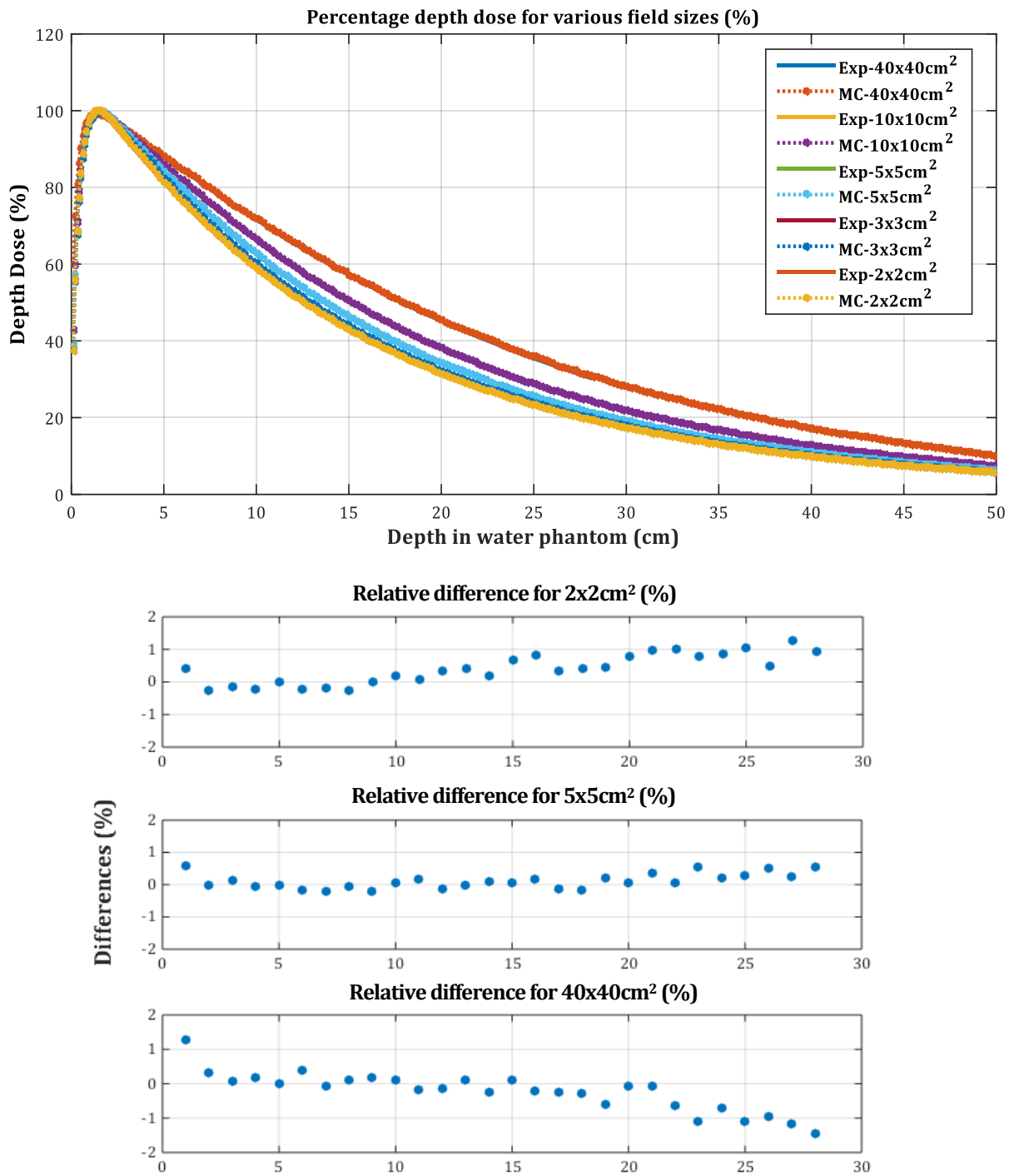


Figure 4.10 - MC simulation of PDD for various field sizes showing agreement with the measurement data and giving percentage difference of less than 2%. Percentage depth dose applied in order to retain the dose relative to d_{max} .

The results of the analysis of backscatter from the collimator jaws into the monitor chamber, before and after correction using the method devised by Liu *et al.*, is shown in Figure 4.11. With this correction included, the output factor significantly improved in terms of the agreement between MC simulation and measured field size output factors for the 6MV photon beam energy. The correction factors varied from 1.13 for the smallest field size (2x2cm²) to 0.91 for the largest field size (40x40cm²). Data were normalised to a reference field size (10x10cm²).

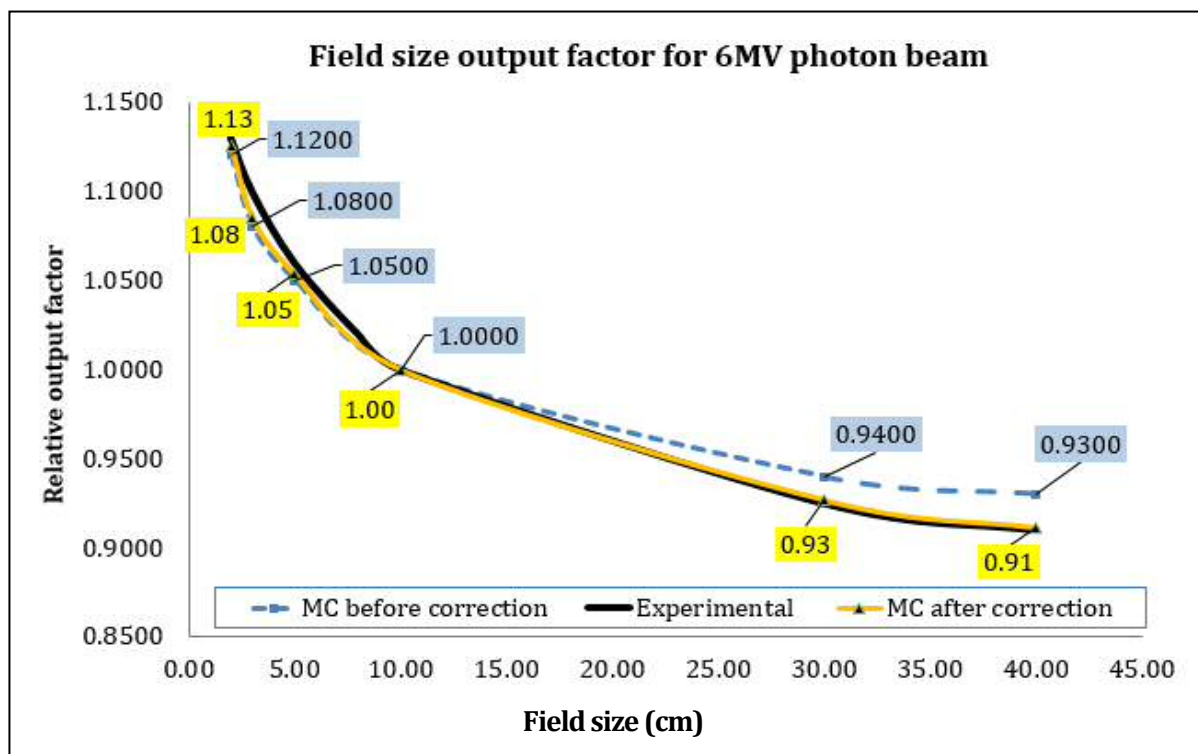


Figure 4.11 - Field size output correction factors generated by MC simulation against the measurement output factors (OF) before and after correction for backscatter from the collimators. Note: blue labels – OF before correction, yellow labels - OF after correction. Good agreement of OF after correction with OF from measurement (*solid black line*) were achieved.

4.1.3 Discussion

From the data presented in this validation work, simulated depth dose and dose profile plots were shown to be in a very good agreement with the measurement data (Figure 4.5 to Figure 4.10). All experimental data for depth doses were measured using a Scanditronix Wellhoffer CC13-S Ionisation Chamber. A Scanditronix Wellhoffer photon field diode was used for beam profiles across a 50x50x50cm³ water tank.

During the matching procedure, normalisation of depth doses and dose profiles between measurement and Monte Carlo simulation were done using a scaling factor which referred to a percentage depth dose in the central axis, in order to retain the dose relative to its maximum value. Hence, the maximum dose will always be 100% (unless stated otherwise). Finally, the optimum photon energy that best represents the linac model in this work (nominal 6MV) corresponds to a 6.0 MeV primary electron energy and 0.1cm electron beam width.

4.2 MLC AND EPID MODELLING

There are variety of MLCs available across a range of linacs, which provide the necessary performance and accuracy for improving treatment verification and delivery. For this accelerator modelling, a Millennium 120 MLC (Figure 4.12), which has 'tongue-and-groove' construction to minimise radiation transmission between adjacent leaves (Mayles et al., 2007), was used (as it forms part of the Velindre Cancer Centre Varian 2100CD Trilogy unit). The MLC is one of the component modules (DYNVMLC) from the original modelling work of Heath and

Seuntjens (2003). It consists of 40 inner leaves and 20 outer leaves for each bank and the width projects to 0.5 cm and 1.0 cm, respectively, at the isocentre distance. The MLC leaves move perpendicular to the radiation beam. Tungsten based alloy is the most suitable material of leaf construction as it has the highest density of most metals. The maximum field size that can be modulated using the Millennium 120 MLCs is 20x20cm², which allows an IMRT segmented beam of less than this size.

During its initial release within BEAMnrc (Heath and Seuntjens, 2003), the model only allowed for ‘static’ mode MC calculation. Later, the introduction of a ‘step-and-shoot’ simulation mode enabled multiple segmented IMRT beams to be simulated in a single calculation run. Within the Velindre Cancer Centre, the modelling of this DYNVMLC CM has been validated by previous work (Cufflin et al., 2010).

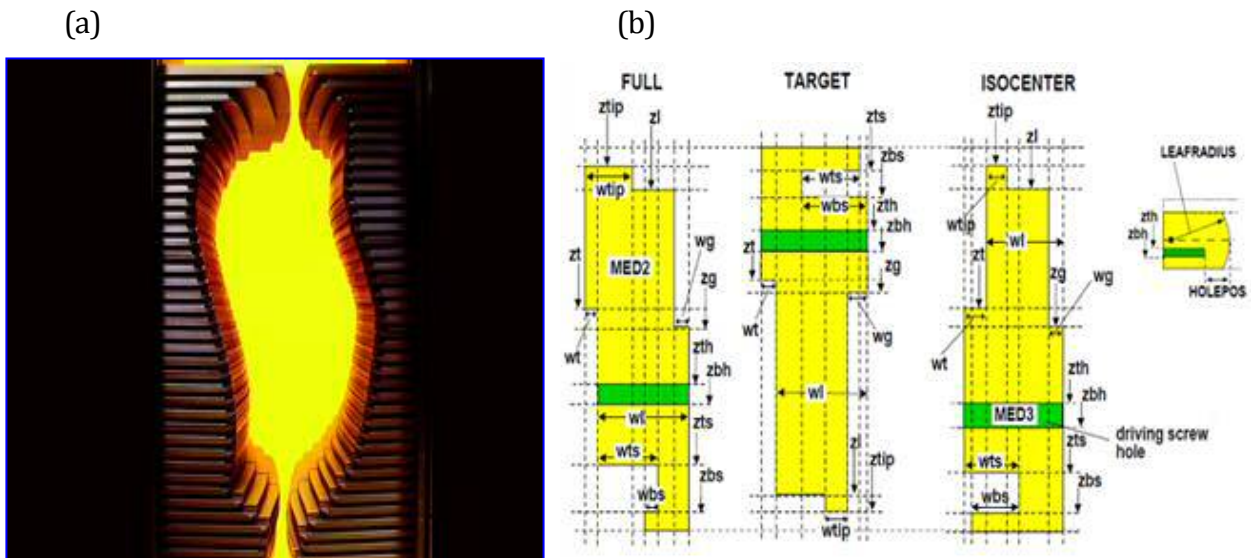


Figure 4.12 - (a) VARIAN Millennium 120-leaf MLC, Source: Varian Medical System. (b) Detailed cross-section of the three leaves construction of the VARIAN Millennium 120-leaf MLC; DYNVMLC component module, Source: (Rogers et al., 2011).

Previous work has highlighted the suitability and efficiency of Monte Carlo as a 'gold standard' method in modelling the radiotherapy beam and its good correlation with phantom measurement in verifying the transmission dose through to the EPID. In some studies, the results of the experimental and measured data matched the gamma criterion within 3%/3mm for beam profiles in most IMRT clinical treatments (Blake et al., 2013, Blake et al., 2014).

With regard to IMRT, which intrinsically involves irregular segmented fields with very steep dose gradients, an effective method of verifying IMRT plans during treatment delivery using EPIDs has been discussed by Cufflin et al. (2011). Their results showed that MC calculations of exit dose in water-equivalent material at the EPID level verified the ability of the TPS to calculate the dose correctly for this situation. Nowadays, there is wide recognition of the ability of the EPID to perform 3D in vivo dosimetry and to give more useful clinical results than a pre-treatment verification of the patient plan (Mijnheer et al., 2013a, Mijnheer et al., 2013b, Mijnheer et al., 2017). This EPID-based approach is believed to be able to identify most of the patient-specific errors due to anatomical changes or deviations from routine clinical procedure, i.e. the ones that intrinsically cannot be detected by pre-treatment verification.

Throughout this research, the Varian imager is the PortalVision aS1000 EPID mounted on a support arm of the Varian 2100CD Trilogy linac. In this section, no further work is carried out to validate EPID portal dosimetry, since this has already been done in a previous project (Cufflin et al., 2009, 2010) and the main aim of this chapter is to produce an accurate model of the linac output that can be used for comparative purposes for the rest of the work described herein.

4.3 MONTE CARLO SIMULATION ACCURACY AND EFFICIENCY

4.3.1 Uncertainty and Variance Reduction Techniques

Within BEAMnrc and DOSXYZnrc, the statistical method for fluence calculation and estimating uncertainty is based on the history-by-history approach described by Sempau et al. (2001). The estimation of the uncertainty of a scored quantity X is given by:

$$s = \sqrt{\frac{1}{N-1} \left(\frac{\sum_{i=1}^N X_i^2}{N} - \left(\frac{\sum_{i=1}^N X_i}{N} \right)^2 \right)} \quad \text{(Equation 4.2)}$$

where X_i is the quantity scored in a statistically independent event i (i.e. history i) and N is the number of independent events, i.e. histories.

As a result of using Equation 4.2, the problem of small sample size is eliminated. N is now the number of histories which is large enough to be statistically analysed, rather than the number of batches (usually 10) as before in the old BEAM code method of uncertainty estimation.

Figure 4.13 demonstrates the relationship between the number of histories and MC simulation time (Central Processing Unit, CPU time) for 100cm SSD, 30x30x30cm³ homogeneous voxel water phantom and 2MeV mean electron energy, using 1 Million particle histories (1x10⁶) as a starting point. The CPU time taken to finish the simulation obviously increases with increasing number of histories as more time is taken to track the particle

trajectories. For simplicity, these particular MC simulations were performed using a personal computer with Intel (R) Core i5-3317U, 1.70GHz processor.

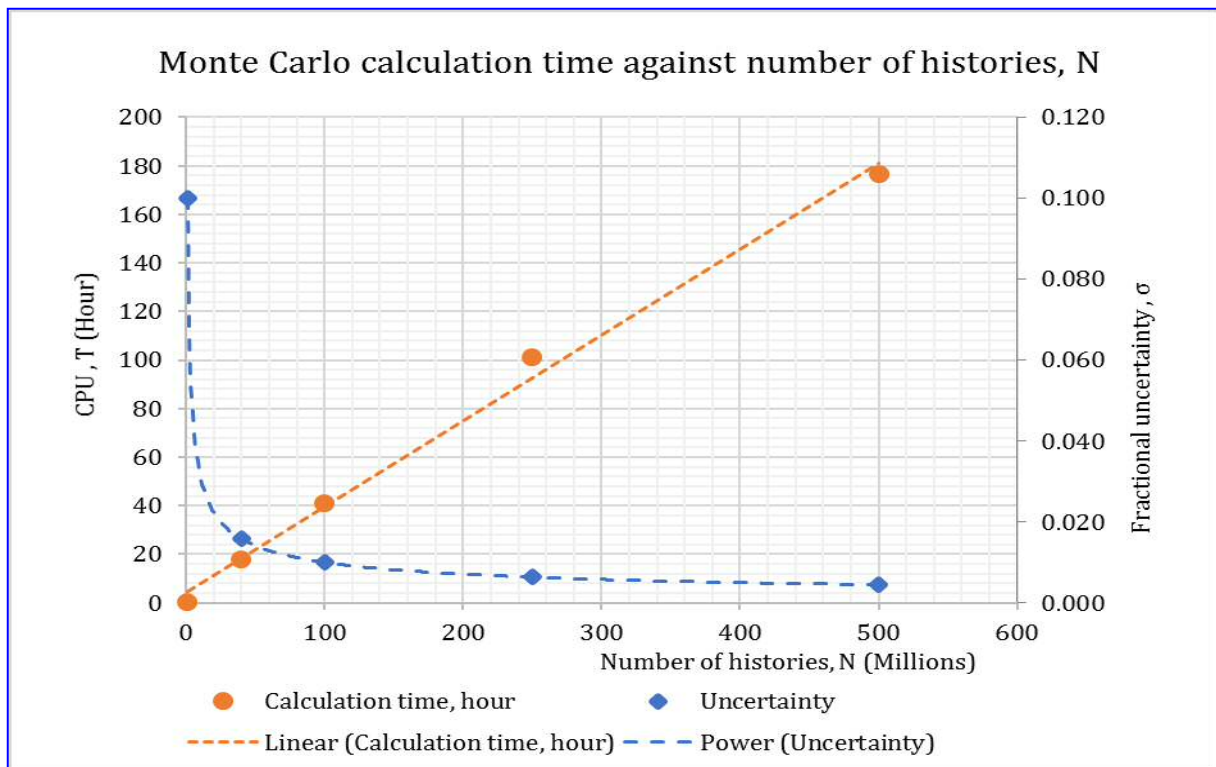


Figure 4.13-The relationship between MC calculation time, T (hour) and Uncertainty, σ (%) with increasing number of histories, N.

As the accuracy of Monte Carlo calculation is limited by its statistical uncertainty, Variance Reduction Techniques (VRTs) are often used to decrease the calculation time by modifying the algorithm while ensuring that the results of MC do not deviate systematically from the corresponding results without VRT (Verhaegen and Seuntjens, 2003). Hence, the

efficiency of MC simulation with VRTs is often optimised to minimize the calculation time without modifying the results of the simulation. The simulation Efficiency ε , is defined by Equation 4.3.

$$\varepsilon = \frac{1}{[S(N)]^2 T^2(N)} \quad \text{(Equation 4.3)}$$

where $S(N)^2$ is the average variance from the simulation of a region of interest (central axis depth dose distribution in a water phantom) and $T(N)$ is the average CPU time for a particular job to finish (Ma et al., 2005, Mohammed et al., 2016). During this validation work, some basic VRTs were used to speed up the calculation time and increase the efficiency of the simulation. These were determined beforehand and used as simulation set-up parameters using the Velindre Cancer Centre RTGrid portal (detailed in Chapter 3).

The bremsstrahlung splitting number, NBRSP, and the particle splitting number, N_SPLIT, in BEAMnrc and DOSXYZnrc respectively, were used to create a large number of photons to minimise the statistical uncertainty while reducing the time required for the creation of the split photons. For this work, a NBRSP of 1000 was used in all simulations as it has been reported to give the highest efficiency (Kawrakow et al., 2004, Rogers et al., 2011). The N_SPLIT value was set to 100 since it was shown from the initial experiment to lie between 75 and 125 for the modelled accelerator (Figure 4.15). Simulation efficiency was calculated using Equation 4.3. The optimum N_SPLIT value (of 100) improved efficiency by a factor of 29 when compared to simulations with no splitting (Figure 4.14). Hence, this value is used

throughout the MC simulations. The number of events was set to be 4×10^8 histories for $0.2 \times 0.2 \times 0.2 \text{ cm}^3$ voxel dimensions in a homogeneous water phantom.

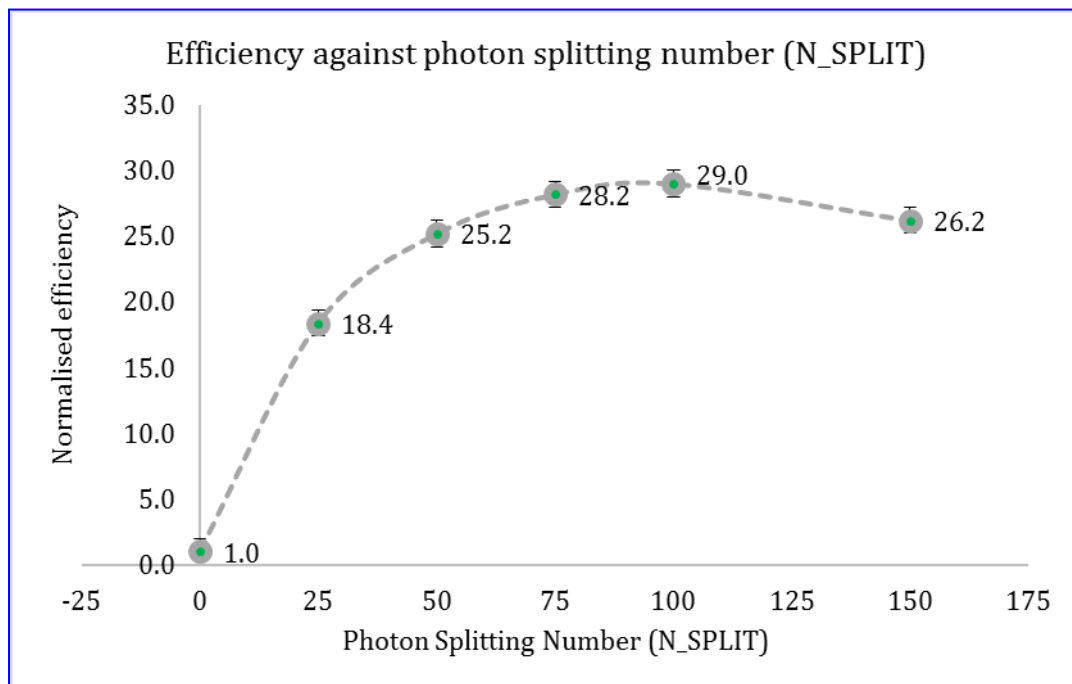


Figure 4.14 - N_SPLIT relationship with the efficiency of simulation.

As a specific exercise linked to the main aim of this research (discussed in subsequent chapters) some validations were required for elongated rectangular field sizes, e.g. $5 \times 30 \text{ cm}^2$, using MC simulation. These data were then compared to experimental data obtained from the LA5 commissioning using a Scanditronix Wellhoffer CC13-S Ionisation Chamber in a $50 \times 50 \times 50 \text{ cm}^3$ water tank. The simulation used 4×10^8 histories in a $40 \times 40 \times 30 \text{ cm}^3$ water phantom with 6MV photon energy. Dose distributions at different depths were normalised to the central axis depth doses for an equivalent square field corresponding to $5 \times 30 \text{ cm}^2$

(approximately 8.5cm) and to retain the maximum dose at d_{\max} (100%). The results of the experiment are presented in Figure 4.15.

CHAPTER 4: MONTE CARLO VERIFICATION OF LINEAR ACCELERATOR AND TREATMENT PLANNING SYSTEM

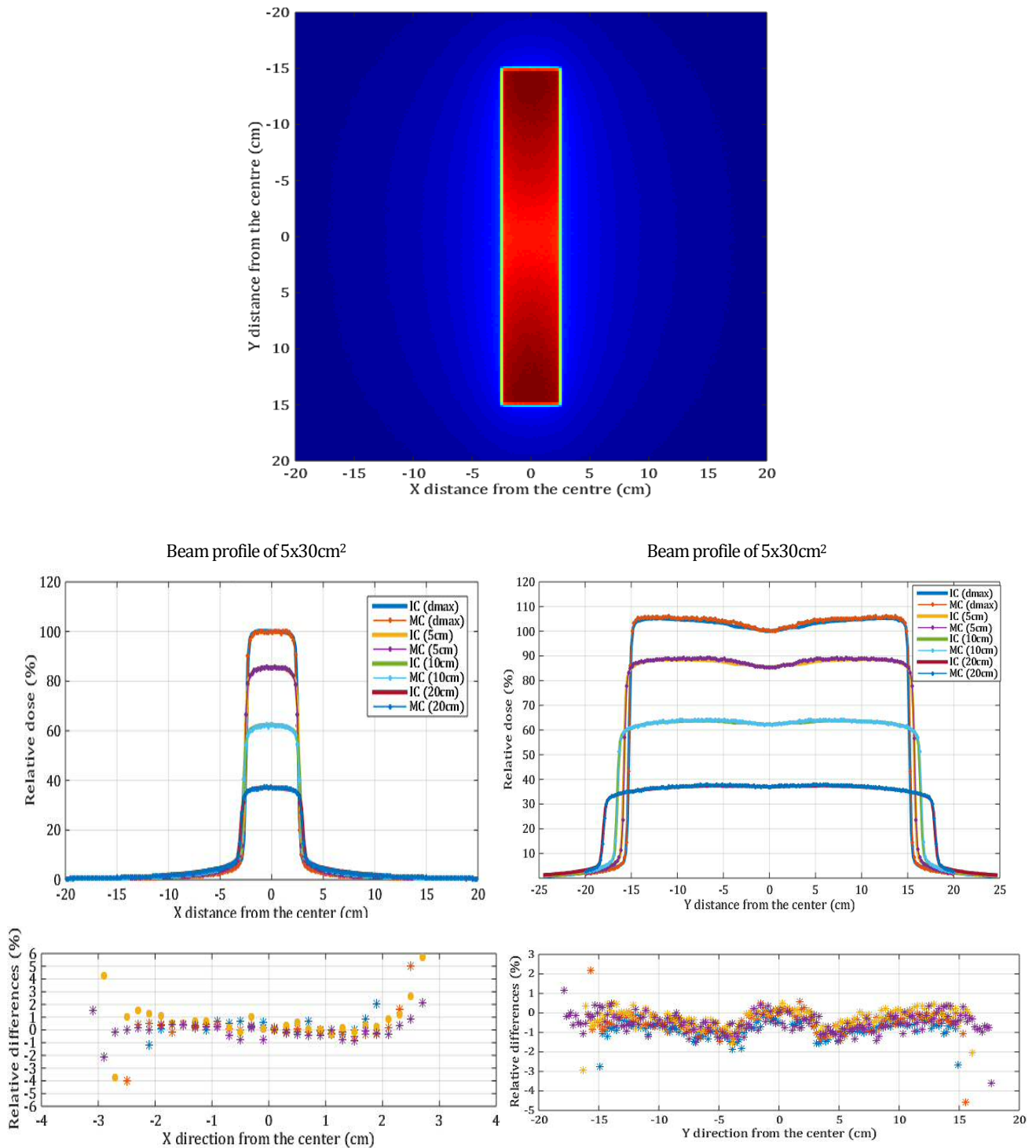


Figure 4.15 - 'X' and 'Y' profile comparison between MC and Ionisation Chamber measurement (IC) for 5x30cm². All profiles were normalised to central axis depth doses in order to retain the value of 100% at d_{max}. Good agreement was achieved within ±2% in the high dose region.

4.4 VERIFICATION OF OMP USING MONTE CARLO SIMULATION

The accuracy of dose calculation algorithms implemented in a TPS can be verified by a variety of phantom measurements and techniques. The QA measurements for a typical patient's treatment plan are normally performed at a reference point using an Ionisation Chamber or 2D detector array in a phantom. Although some 3D detector solutions (e.g. gel dosimetry) have been developed in the research domain, they ultimately require a realistic (i.e. heterogeneous) phantom geometry to record the dose accurately. As a complementary approach, MC methods can also be used to represent the patient's CT scan or heterogeneous patient geometry with a high degree of accuracy. There are many published results on dose comparison between Monte Carlo and various TPSs highlighting MC as an effective IMRT QA verification tool (Ma et al., 2000, Li et al., 2001, Francescon et al., 2003).

While Monte Carlo is proven as a 'gold standard' dose calculation algorithm, in practice, it requires extra computational time, although in some centres it has been configured to be an automated QA system (Leal et al., 2003). In Velindre Cancer Centre, both PB and CC approximation algorithms are employed in the Oncentra MasterPlan (Nucletron) TPS for most of the treatment plans, though CC now predominates for clinical use. Details on the dose calculation algorithms have been discussed in Chapter 3.

4.4.1 Methods

In this section, the BEAMnrc and DOSXYZnrc Monte Carlo packages are considered as benchmark tools in assessing the validity of on-site OMP dose calculations. First, a simple set of square field sizes ($3 \times 3 \text{cm}^2$, $5 \times 5 \text{cm}^2$ and $10 \times 10 \text{cm}^2$) was used to provide comparison between MC and OMP while applying the same voxel dimension on a water slab phantom with 100cm SSD.

The validation of the on-site treatment planning system was also performed with Monte Carlo simulation of a sequence of 6MV Head-and-Neck IMRT beams in a water slab phantom and profile comparison was done against the OMP dose calculation. A calibration factor was required to convert MC simulation to dose. To do this, simulation of $10 \times 10 \text{cm}^2$ field size in a water phantom at SSD 100cm was performed to find the energy deposited per unit mass, per incident particle (the unit from the result of MC simulation), at a reference point (in this case 10cm deep in a water phantom) at which the dose from 100MU is known. Note that, extended voxels of $\sim 2 \text{cm}$ around the central axis of the $10 \times 10 \text{cm}^2$ field were averaged to avoid the calibration value being affected by the statistical uncertainty of the value in a single voxel. The calibration factor was then applied to following IMRT simulations to get dose per MU delivered to the water slab phantom. The experiment was further evaluated with 2D gamma for a 20% dose threshold so that the results were representative of the area of the treatment field. Percentage of points within the field passing a range of gamma criteria were calculated with the aid of Matlab programming. This Head-and-Neck clinical case will be later used in the Dosimetry Check comparison as detailed in Chapter 5 and Chapter 6.

As calculated previously using Equation 4.5, a backscatter factor from the jaws into the monitor chamber was also included as part of the calculation to get the dose. Mathematically, the MC dose was calculated as: Monte Carlo dose (Gy) = (MC raw value/Calibration factor) x (BSF) x (Field Monitor Unit) where BSF is the backscatter factor from the jaws.

4.4.2 Results

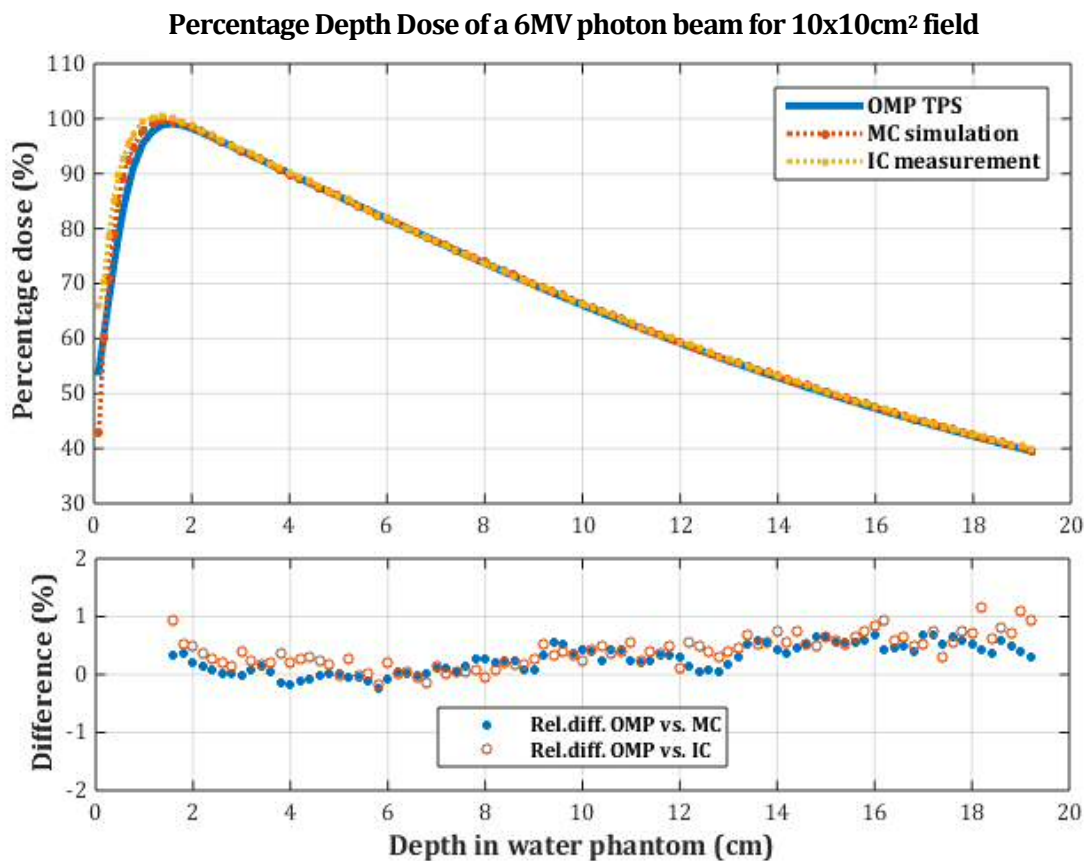


Figure 4.16 – Comparison of percentage Depth Dose curves for 10x10cm² field between OMP, MC simulation and Ionisation Chamber measurement. Excellent agreement was found (less than ±1%). Plotted curves were normalised to 5cm depth and PDD was used to retain the dose distribution of maximum dose along the central axis.

Figure 4.16 shows excellent agreement between OMP and MC simulation with $\pm 1\%$ depth dose difference beyond the build-up region, in a three-way comparison (involving OMP, MC and ionisation chamber measurements). Similarly, the evaluation of the OMP dose profiles relative to MC profiles for the simple field sizes further validated the Treatment Planning System (OMP) convolution algorithm in these cases. The results of the profile comparison are shown in Figure 4.17 (MC vs. OMP) and Figure 4.18 (OMP vs. I.C) for $10 \times 10 \text{cm}^2$, $5 \times 5 \text{cm}^2$ and $3 \times 3 \text{cm}^2$ fields. Dose differences are within $\pm 2\%$ in the high dose region.

For two beams (B01 and B05) in the example IMRT Head-and-Neck case, good agreement was seen between the MC simulation beam profiles and the OMP dose profiles in high dose regions, where dose differences were within 3% as shown in Figure 4.19 and Figure 4.20. However, there was some dose disagreement in the penumbra regions.

The gamma index pass rates for B01 and B05 are shown in Table 4.2. Figure 4.21 shows representative 2D gamma maps with excellent agreement of 90.8% and 96.9% for points passing the 4% 4mm gamma criterion for B01 and B05 respectively. For the 3% 3mm criterion, the corresponding values are 84.1% and 88.4% respectively. These results are reasonably consistent with the 85% recommendation for acceptance given in ICRU 83 (ICRU,2010) for the percent of pixels within a 3% and 3mm threshold in gamma analysis for a complex plan such as Head-and-Neck IMRT.

CHAPTER 4: MONTE CARLO VERIFICATION OF LINEAR ACCELERATOR AND TREATMENT PLANNING SYSTEM

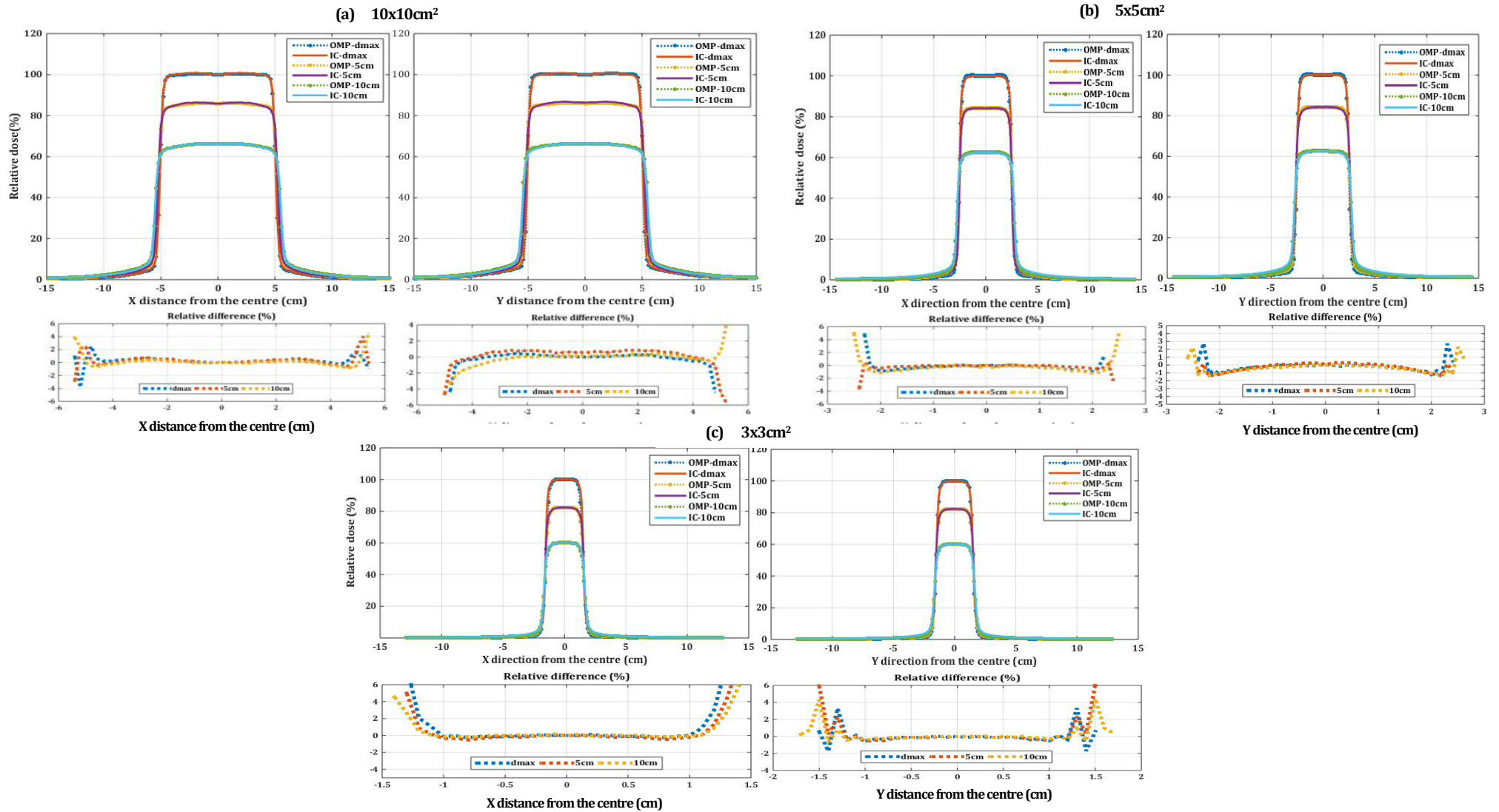


Figure 4.17 - 'X' and 'Y' profile comparison between MC and OMP TPS for $10 \times 10 \text{cm}^2$, $5 \times 5 \text{cm}^2$ and $3 \times 3 \text{cm}^2$ fields. All profiles were normalised to 5cm depth.

CHAPTER 4: MONTE CARLO VERIFICATION OF LINEAR ACCELERATOR AND TREATMENT PLANNING SYSTEM

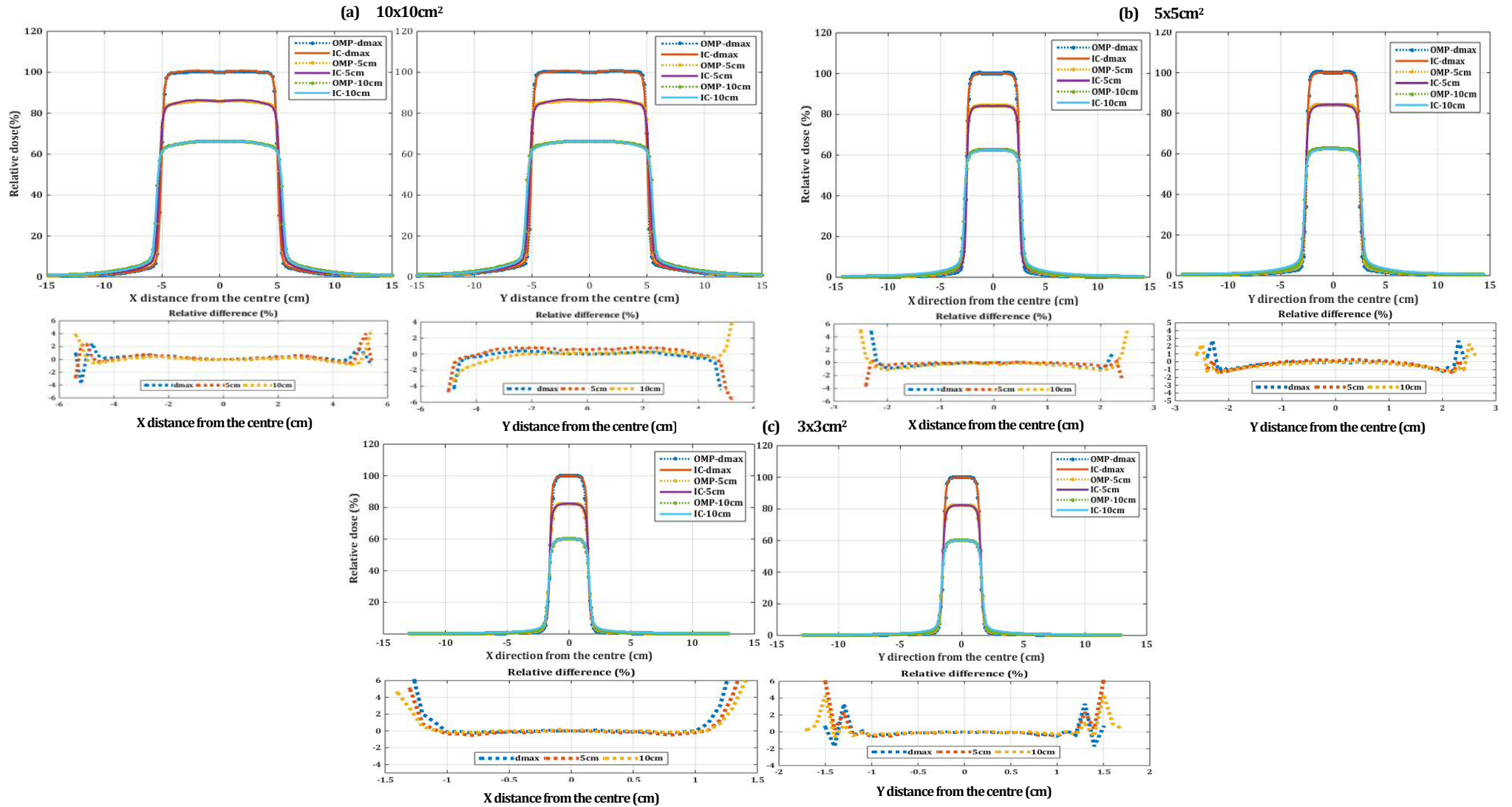


Figure 4.18 - 'X' and 'Y' profile comparison between IC and OMP TPS for 10x10cm², 5x5cm² and 3x3cm² fields. All profiles were normalised to 5cm depth.

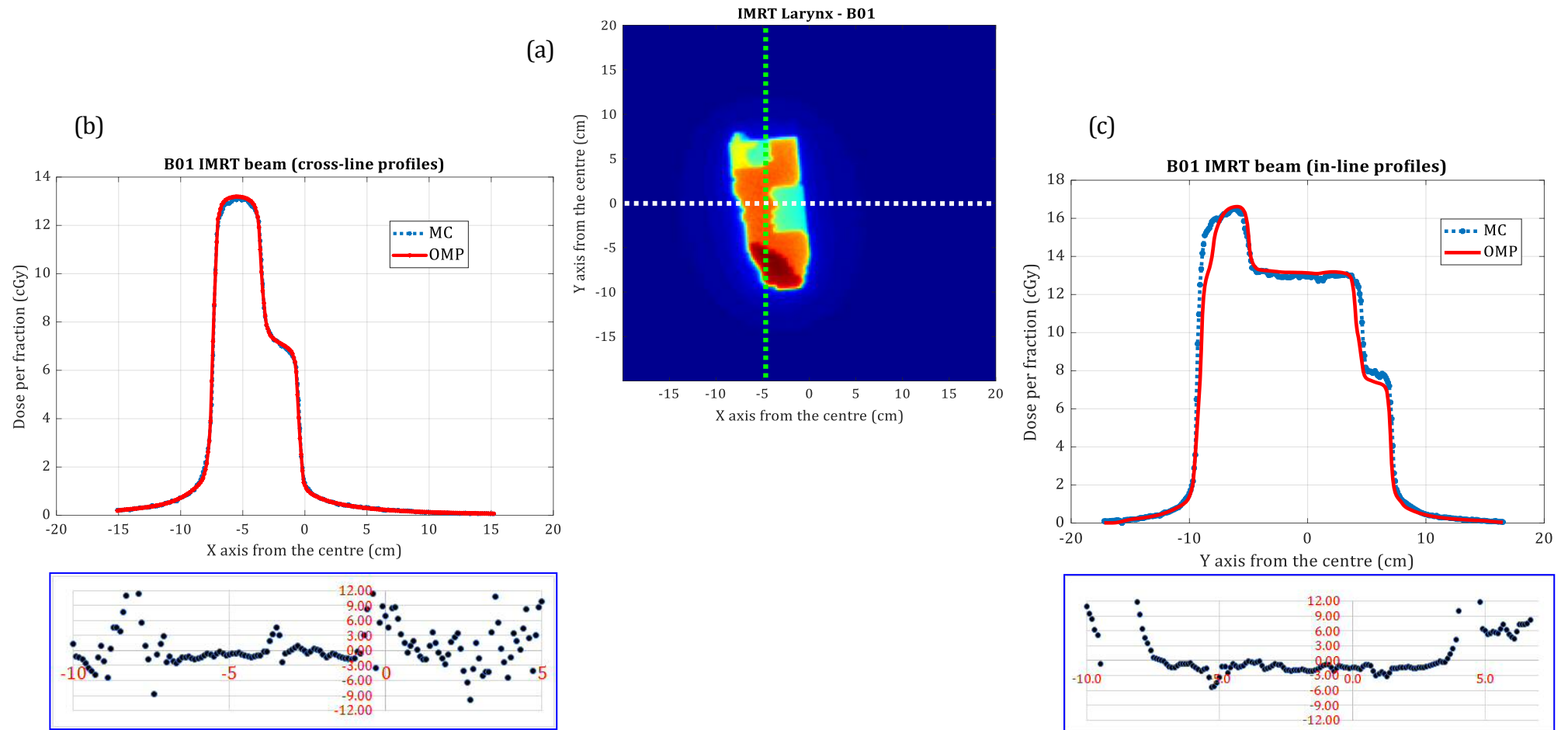


Figure 4.19 – Example of MC simulation of IMRT beam (B01) of Head-and-Neck case compared to the dose calculated by on-site treatment planning. (a) B01 IMRT beam showing the cut along profile; cross-line profile (white dotted line) and in-line profile (green dotted line). (b) cross-line and (c) inline profiles comparison between dose simulated by MC and dose calculated by OMP TPS. The two profiles are in a good agreement; dose differences are within 3% in high dose regions.

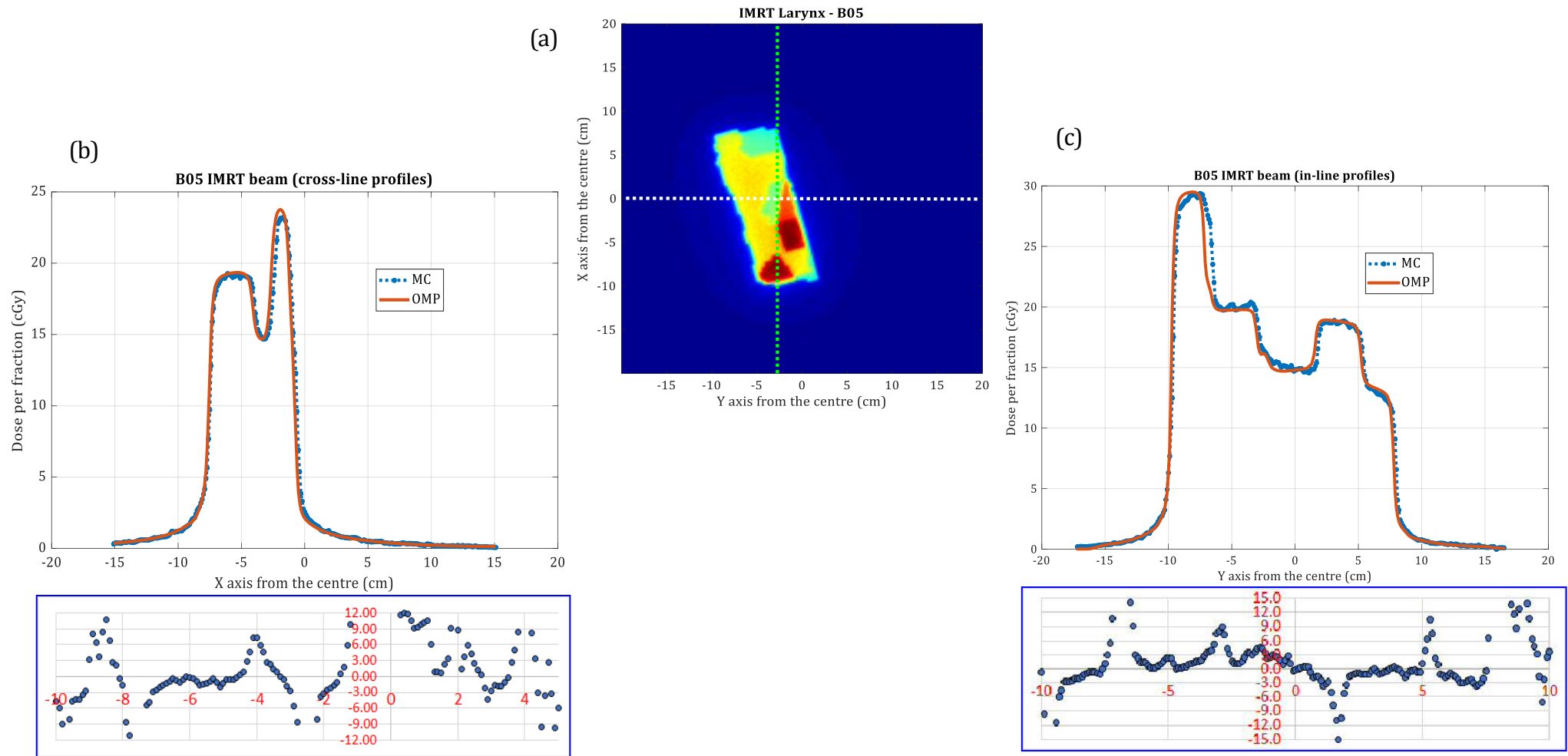


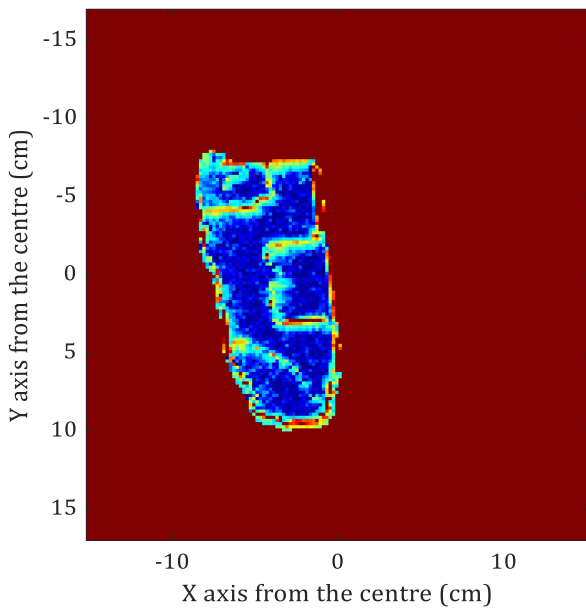
Figure 4.20 - Example of MC simulation of IMRT beam (B05) of Head-and-Neck case compared to the dose calculated by on-site treatment planning. (a) B05 IMRT beam showing the cut along profile; cross-line profile (*white dotted line*) and in-line profile (*green dotted line*). (b) cross-line and (c) inline profiles comparison between dose simulated by MC and dose calculated by OMP TPS. The two profiles are in a good agreement; dose differences are within 3% in high dose regions.

Table 4.2 – Gamma passing rates for example of IMRT Head-and-Neck MC simulation for OMP TPS verification result.

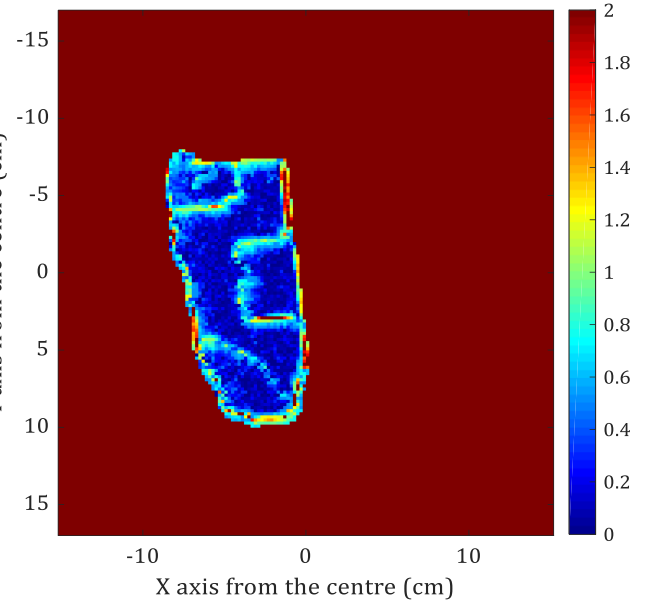
Gamma Criteria	Gamma passing rates for IMRT beam (%)	
	B01	B05
3%, 3mm	84.1	88.4
3%, 4mm	88.0	92.8
3%, 5mm	91.3	97.5
4%, 3mm	88.0	92.9
4%, 4mm	90.8	96.9
4%, 5mm	93.6	99.0
5%, 3mm	90.8	95.7

(a) B01

Gamma Plot for 3%, 3 mm. Pass =85%

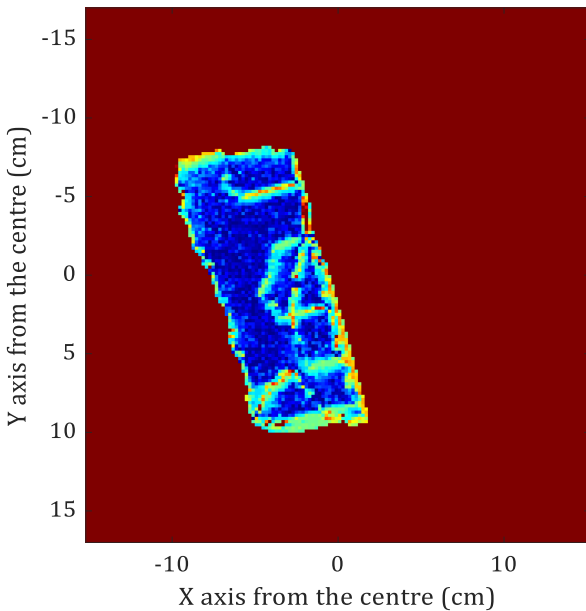


Gamma Plot for 4%, 4 mm. Pass =90.8%



(b) B05

Gamma Plot for 3%, 3 mm. Pass =88.4%



Gamma Plot for 4%, 4 mm. Pass =96.9%

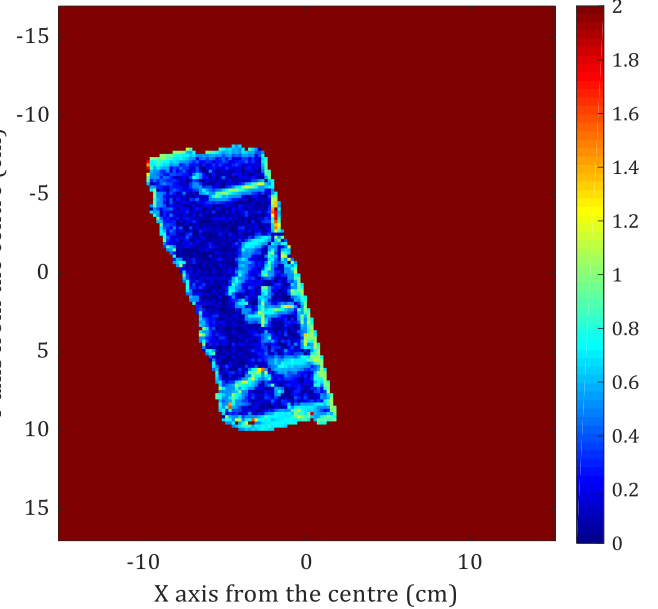


Figure 4.21 – Examples of 2D gamma maps for IMRT Head-and-Neck beams showing percentage of points passing two different gamma criteria, 3%, 3mm and 4%, 4mm. (a) B01 and (b) B05

4.4.3 Discussion

All plans in this work have been optimised using the OMP TPS. The results for the simple fields that were used to compare the OMP TPS against Monte Carlo calculation (section 4.4.1) and ionisation chamber (IC) measurement revealed good agreement to within $\pm 2\%$ in high dose regions. In addition, the validity of OMP was further investigated by Monte Carlo simulation of segmented IMRT fields used in the Head-and-Neck test case discussed in subsequent chapters. The dose differences found were relatively small (typically 3%) and consistent with the tolerances applied for clinical IMRT at the Velindre Cancer Centre.

While it cannot be denied that MC is a state-of-art method for the verification of treatment planning, there are many and various complexities in accurately modelling clinical cases using MC on patient CT datasets as discussed by several authors (Keall et al., 2001, Chetty et al., 2007, Chetty, 2008, Ma and Li, 2009, Jabbari, 2011).

Furthermore, detailed MC-based validation of the local OMP system for IMRT has been undertaken in a previous study (Cufflin et al., 2010, Cufflin, 2012). The present validation work gives contemporary confirmation and provides a good degree of confidence that the OMP system remains a sufficiently accurate platform for comparison with Dosimetry Check as discussed in subsequent chapters.

Chapter 5

COMMISSIONING OF DOSIMETRY CHECK FOR VERIFICATION OF ADVANCED RADIOTHERAPY

5.1 DOSIMETRY CHECK PERFORMANCE

The aim of this chapter is to introduce the current application of the software-based EPID verification system, Dosimetry Check. It also explicitly addresses the main motivation of the research, which is to improve verification accuracy by introducing into the existing Dosimetry Check system a novel correction method for backscatter from the EPID arm. Some of the concepts which apply to Head-and-Neck IMRT are also be discussed in this chapter.

5.1.1 Dosimetry Check as an IMRT/VMAT verification tool

Dosimetry Check is a one of a number of software systems currently being used in various radiotherapy centres in conjunction with EPIDs to verify the accuracy of treatment delivery. It is a stand-alone piece of application software intended to work with modern linacs equipped with EPIDs. Dosimetry Check was developed by Math Resolutions¹⁸, and is currently (2017) distributed by OSL Ltd. in the UK. The software is advertised as being capable of

¹⁸ <http://www.mathresolutions.com/rtqasys.htm>

providing pre-treatment and in-vivo transit dosimetric QA information for IMRT/VMAT and conformal radiotherapy treatments. The system works using an in-air fluence map, calculated from data recorded by the portal imager, to reconstruct a 3D dose distribution using the planning CT dataset. The dose reconstructed in Dosimetry Check can then be compared against the dose in the original patient treatment plan. The system is based on the original work of Renner et al. (2003, 2005). IMRT/VMAT treatment verification has become a major topic of interest among radiotherapy researchers and practitioners (Renner et al., 2003, Mijnheer et al., 2013a, 2013b), especially as regards 3D EPID-based patient-specific dose verification.

Dosimetry Check uses a pencil beam dose calculation algorithm (Chapter 3) with fluence distribution, derived from the EPID image, as its input. It is intended to be a part of the patient-specific QA system to compute and verify dose delivered to the patient. This measured source model (Renner et al., 2005, Math Resolutions, 2017) used in Dosimetry Check inherently accounts for leaf leakage, position and movement. An EPID image of a standard ($10 \times 10 \text{cm}^2$) field size is used for calibration. Each pixel on the patient's EPID image is then mapped relative to this calibration intensity, forming a 'Relative Monitor Unit' map. Each of the pixels on the Relative Monitor Unit image is back-projected on to a plane in front of the patient and the PB algorithm is then forward calculated and used as an individual 'weight' to derive the fluence map.

The PB is divided into small 'subrays' to calculate the radiation energy that each ray deposits throughout the 3D representation of the patient. This process directly determines the dose to the patient in cGy. Dosimetry Check provides a variety of dose analysis facilities such as

2D and 3D multiple point doses, comparison between 2D and 3D isodose distributions and Gamma evaluation with Dose Volume Histogram (DVH) comparison.

EPID-based verification with the aid of Dosimetry Check software is also expected to improve on-set verification time compared to the use of diodes, along with the advantages of having multi-dimensional information, high resolution and high levels of reproducibility (Greer, 2013). As previously discussed in Chapter 2, the ‘Towards Safer Radiotherapy’ report (The Royal College of Radiologists, 2008(a)) recommended the need for in-vivo dosimetry as a routine protocol in every UK centre, in order to make sure each patient correctly receives the planned dose. This work aims to investigate, and where possible improve, the verification accuracy of Dosimetry Check for better performance in pre-treatment and in transit dosimetry. Further details of the work are given in section 5.3.

As an implementation of in-vivo verification, Dosimetry Check has been utilised by a number of centres and is claimed to be a reliable verification tool. Pinkerton et al. (2010) described their clinical experience of the practicality of Dosimetry Check in verifying IMRT and RapidArc in pre-treatment QA. Excellent agreement was found (within $\pm 1\%$) for reference point doses in a multiple field pre-treatment prostate case and within $\pm 2\%$ for an exit dosimetry Head-and-Neck case.

Similarly, as identified by Gimeno et al. (2014), typical discrepancies between Dosimetry Check dose and TPS dose in early commissioning are less than 2% in homogeneous phantoms, but greater in the presence of heterogeneities (reaching up to 15%). Discrepancies are also found in transit dosimetry due to the inability of Dosimetry Check to properly include the couch attenuation and air gap between the patient and couch into the kernel (Gimeno et al.,

2014). In clinical experience, Dosimetry Check performance has been evaluated and compared with TPS using conventional detectors (MOSFET), and the results showed that deviation between MOSFET and Dosimetry Check relative to TPS was about 3% (Fafi et al., 2013).

Commissioning and validation work published by the Clatterbridge Cancer Centre, UK demonstrated Dosimetry Check to be an efficient platform for in-vivo dosimetry based on its advantages in providing volumetric dose delivery information. Tests were done on almost all their linacs (Varian and Elekta). There was excellent agreement, in general within 1% standard deviation, with TPS calculations (Reilly et al., 2013).

In spite of the evidence of good performance mentioned above, confidence in Dosimetry Check for clinical use must be gained locally by clinical staff, especially radiographers and physicists, in the hospital. Therefore, Dosimetry Check commissioning and necessary to ensure accuracy of the reconstructed dose for each patient who receives radiotherapy.

5.2 COMMISSIONING AND VALIDATION OF DOSIMETRY CHECK IN VCC

The set-up of Dosimetry Check for use with a local linac (Varian Trilogy 'LA5') at Velindre Cancer Centre was initially undertaken during 2014 by the physics team. This involved infrastructure configuration to enable Dosimetry Check to run on the hospital system, including the introduction of a Citrix¹⁹ application server setting, which allowed the use of Dosimetry Check through the hospital network. By September 2015, the commissioning work had finished, and a pilot study started, prior to introducing Dosimetry Check for clinical use in January 2016.

Initially, measurement data were taken with LA5 at gantry 0° using a water tank (supplied by OSL, UK) at depths ranging from 0-50cm in order to generate the dosimetric information required to configure the required deconvolution kernels. The data were then sent to OSL UK and full commissioning began upon receiving the kernels from OSL. The commissioning started with the acquisition of data for a series of basic square fields ranging from 5x5cm² to 20x20cm² and verification at different gantry angles and different energy settings (6MV and 10MV). The commissioning involved data from anthropomorphic pelvic and lung phantoms, as well as 27 patient cases to validate the results obtained.

¹⁹ Citrix Systems - software designed to provide server, application and desktop visualisation, networking, and cloud computing technologies to remote to hospital network. http://en.wikipedia.org/wiki/Citrix_Systems

5.2.1 Results

Results of the initial commissioning process varied according to the type of case used. For transit dosimetry using simple geometries and a water medium, Dosimetry Check gave 1.5% difference to TPS dose at the isocentre for a 10x10cm² field at gantry angle 0°. However, the dose difference increased to 2.5% compared to TPS for 6MV photon energy at gantry angle 270°. The greater discrepancy was later identified as being due to an incorrect kernel, which had not taken into account couch attenuation in the initial water tank measurement. Couch factors have been reported to influence treatment delivery dose because of attenuation of the photon beam, especially at increasing obliquity (Munjal et al., 2006, van Prooijen et al., 2010, Olch et al., 2014).

Later in August 2015, new (corrected) deconvolution kernels were obtained from OSL/Math Resolutions, which accounted for the couch. It was confirmed that couch attenuation had been excluded in their previous kernels and hence this explained the dose deviation cited above. The new deconvolution kernels incorporated 0.4cm water equivalent material representing the couch. With the correct kernels, a sub-set of commissioning tests were repeated, and the results improved as summarised in Figure 5.1 (a, b).

(a)

Gantry angle	Energy	
	6MV	10MV
0°	-0.3%	+1.0%
90°	+1.6%	+1.0%
270°	+1.7%	+1.0%
360°	+0.4%	+0.5%

(b)

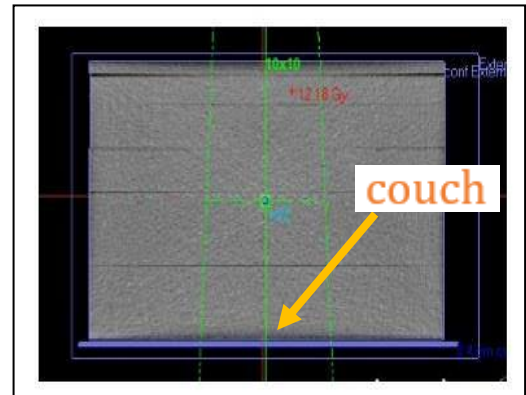


Figure 5.1 - (a) Results of the repeated sub-set of commissioning test with the improved kernels from Math Resolutions giving excellent agreement between DC and Oncentra MasterPlan TPS.

(b) Water slab phantom modelled in OMP with added 0.4cm water equivalent material representing the couch.

Some systematic errors were evident in Dosimetry Check commissioning, arising from the effect of non-uniform backscatter from the Varian imager support arm located at the Gantry side of the G-T²⁰ direction. Hence, when an image is acquired with a large flood-field (covering the whole imager area), the backscatter effect is not readily apparent. This is because the same backscatter is present in both the acquired and the flood-field images, thus cancelling each other out. However, since scatter conditions vary with field size (Cufflin et al., 2010), when the field size changes there will be a mismatch in the scatter for both images, hence backscatter becomes apparent. This condition is likely to be insufficient to ensure accurate verification of small off-axis fields and narrow rectangular fields for example (Figure 5.2).

²⁰ G-T direction – is defined as Gun-Target or ‘in-line’ direction of electron travel in a linac set-up

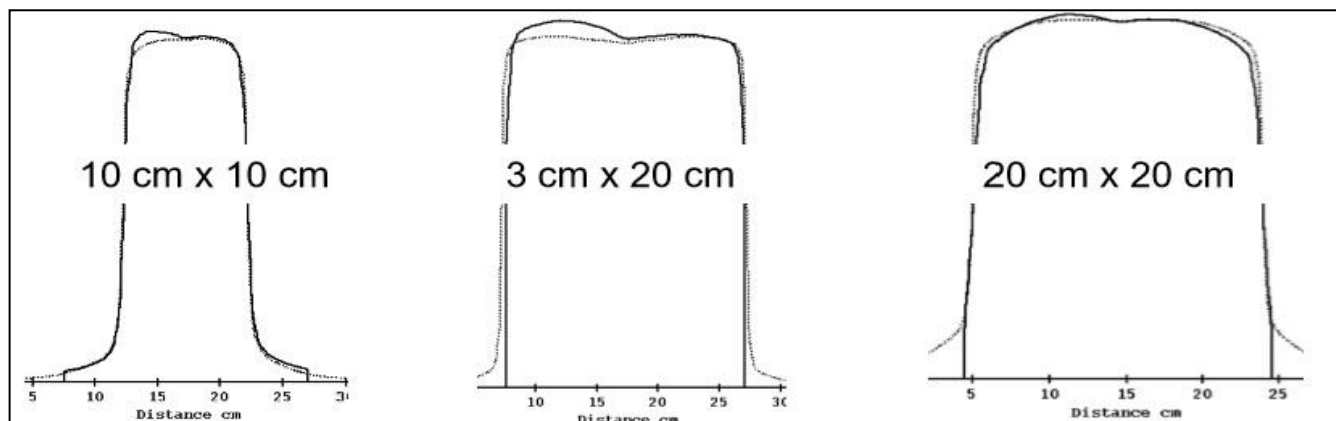


Figure 5.2 - Non-uniform backscatter from VARIAN imager arm for different field sizes. Effect clearly significant in $3 \times 20 \text{ cm}^2$ (narrow field size) relative to a standard flood-field calibration. Images of beam profiles were part of the report of the internal commissioning for Dosimetry Check on LA5 at Velindre Cancer Centre.

Following the local commissioning phase for LA5, Dosimetry Check was approved for use to verify conformal plans except for Head-and-Neck IMRT (due to the relatively poor results found in the initial commissioning). Further investigation was required in the anticipation that correcting for non-uniform backscatter would improve these results, enabling them in due course to be verified clinically. Investigation work in Velindre Cancer Centre continues with the eventual aim of utilising Dosimetry Check for all plans, including verification of Head-and-Neck IMRT and arc treatments (Chapter 6).

5.2.2 Clinical implementation

Since January 2016, Dosimetry Check has been in clinical use on a single linac (LA5) in Velindre Cancer Centre for all conformal treatments (mostly breast patients) but excluding Head and Neck IMRT. The steps in the process include importing and exporting the necessary patient file information using a network between Dosimetry Check and TPS as illustrated in the

flow diagram in Figure 5.3. Physicists have responsibility for confirming that a request for images has been made and responding to any 'out of tolerance' results on the dose comparison between Dosimetry Check and TPS reported by radiographers. The tolerance levels being used currently are $\pm 5\%$ for all conformal plans and -5% to $+10\%$ for breast (as the Dosimetry Check PB algorithm over-responds when calculating oblique breast fields on the patient CT scan).

The Dosimetry Check report includes analysis of dose comparison with TPS using a variety of approaches including 2D dose profiles with isodose distribution map, DVH and Gamma Volume Histogram (GVH)²¹, which can be selected within Dosimetry Check. For initial routine use, Velindre Cancer Centre has clinically implemented point dose comparisons and occasionally 1D dose profiles and isodose distributions. Full gamma analysis is not yet realistic due to asymmetry caused by non-uniform backscatter.

²¹ Gamma Volume Histogram – represents the cumulative passing rate for a volume defined in TPS, which consists of multiple 2D planes within the volume.

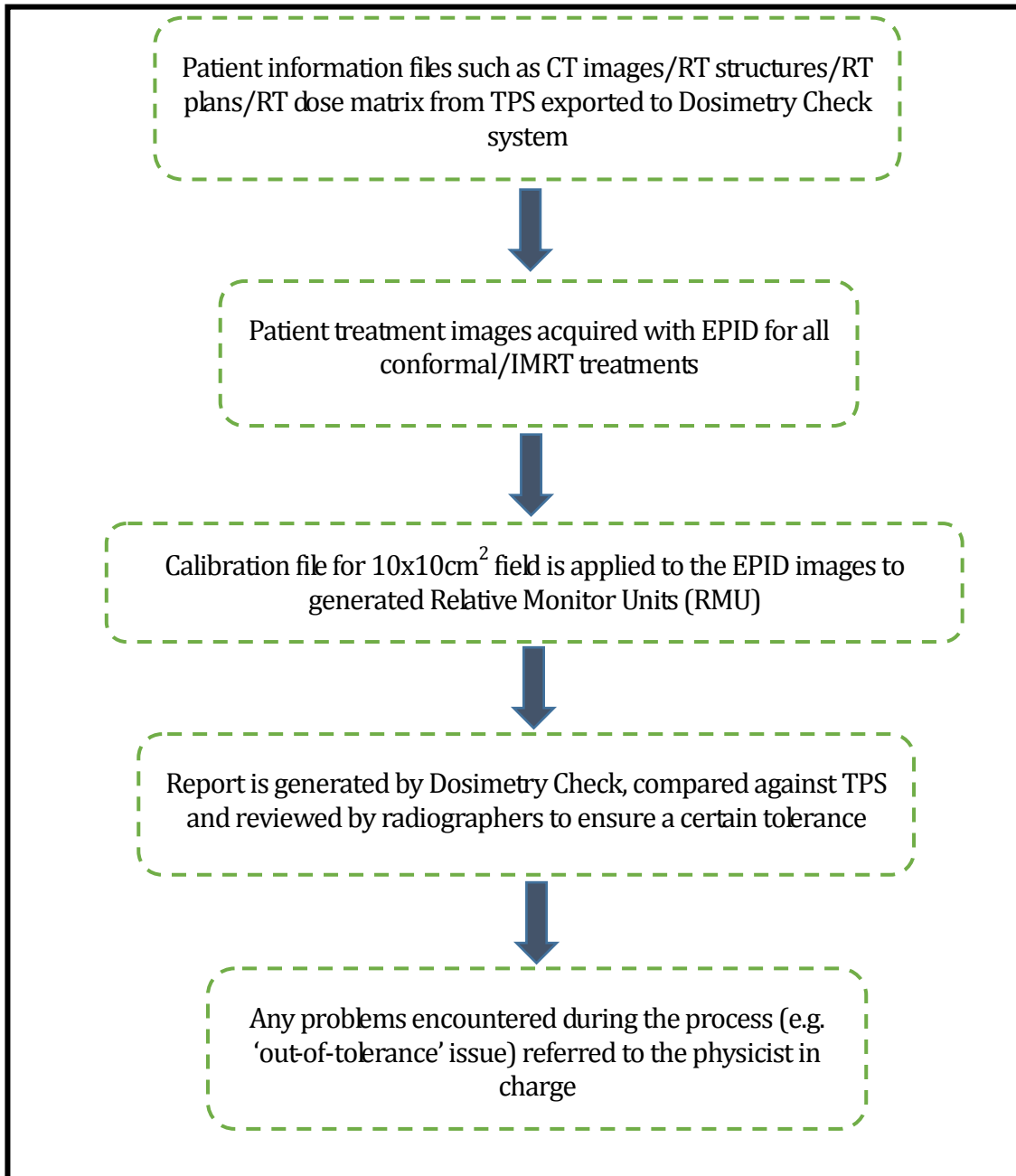


Figure 5.3 - A flow diagram representing the process involved in conformal/IMRT treatment verification using Dosimetry Check software.

5.3 DOSIMETRY CHECK AND NON-UNIFORM BACKSCATTER

5.3.1 Scatter effect from Varian EPID robotic arm

Dosimetry Check provides a non-invasive technique suitable for in-vivo dosimetry verification and it also provides a reconstructed treatment-time patient dose distribution. However, the system inevitably comes with limitations, which means that there is not necessarily full agreement with calculations from the local TPS. Some papers have indicated that a discrepancy in dose between TPS and Dosimetry Check, as a result of a difference in calculation algorithm, might raise concerns about the utility of the software as a highly accurate tool for treatment verification (Reilly et al., 2013, Fafi et al., 2013, Narayanasamy et al., 2015). It is well known that the PB algorithm does not accurately correct for tissue heterogeneity in dose calculation with Dosimetry Check (Fafi et al., 2013, Reilly et al., 2013). Furthermore, Dosimetry Check also has an issue with scattered dose from the Varian EPID support arm and to the best of current knowledge, work has not previously been done to correct the latter issue within the Dosimetry Check system.

As discussed by Bawazeer et al. (2015), none of the available solutions for radiotherapy dose verification (Portal Dosimetry²², EPIDose²³, Epiqa²⁴, Dosimetry Check²⁵, and EPIgray software²⁶), corrects for backscatter from the Varian EPID support arm. This correction is the

²² Portal Dosimetry (Varian, Palo Alto, CA, USA)

²³ EPIDose (Sun Nuclear Corporation, Melbourne, Florida)

²⁴ Epiqa (EPI dos, Ivanka pri Dunaji, Bratislava, Slovakia)

²⁵ Dosimetry Check (Math Resolutions, LLC, Columbia)

²⁶ EPIgray (DOSIsoft S.A. (Cachan, France))

main focus of the work detailed in this chapter. The aim is to apply a key correction for non-uniform backscatter from the EPID arm to improve the accuracy of patient specific dose verification using Dosimetry Check.

5.3.2 Methods employed to overcome the scatter effect

The impact of the backscatter from the EPID arm has been reported elsewhere (see Chapter 1, section 1.5). It is known to cause up to 5% discrepancy between the delivered dose and calculated dose. Some groups have investigated the addition of customised lead shielding beneath the imager panel to make the scattered radiation more uniformly distributed across the Varian aS500 EPID (Lung et al., 2004, Joseph and Jeffrey, 2005, Rowshanfarzad et al., 2010b). The newest Varian EPID panel (aS1200) incorporates this extra shielding in the design to help overcome the non-uniform scatter issue (Reilly, 2016a, Reilly, 2016b). However, there are still many systems in use worldwide with earlier versions of the EPID panel and replacement with the newest version is not necessarily feasible due to the high cost of such equipment (~ £100K per unit).

An alternative approach involving a convolution kernel model was developed by Greer et al. (2009) following research by Rowshanfarzad et al. (2010a). This evaluated a 'stand-alone' EPID measurement involving the direct subtraction of a $1 \times 1 \text{cm}^2$ pencil beam kernel at a sample position on the EPID active area when the EPID arm was 'on' from the same measured kernel when the EPID arm was 'off'. It was claimed that this provided a more accurate incorporation of backscatter (using a backscatter pencil beam kernel) into their existing Pinnacle TPS EPID dose prediction model.

In this work, a series of rectangular field ($2 \times 20 \text{cm}^2$, $3 \times 20 \text{cm}^2$, $5 \times 20 \text{cm}^2$ and $9 \times 20 \text{cm}^2$) images were acquired. Multiple abutting strips (alphabetically labelled) for each field size were used; for example (i) $2 \times 20 \text{cm}^2$ has 11 strips (A-K), (ii) $3 \times 20 \text{cm}^2$ has 7 strips (A-G), (iii) $5 \times 20 \text{cm}^2$ has 5 strips (A-E) and (iv) $9 \times 20 \text{cm}^2$ has 3 strips (A-C). These were sufficient to cover the EPID active area as illustrated in Figure 5.4. Correction factors were derived for each case by mirroring half of the Y-axis beam profiles (on the EPID Couch side) about the central row to obtain symmetrical profiles (along the Y-axis of EPID imager) as shown in Figure 5.5 (a) and (b). The images were taken with variable rectangular field sizes in order to highlight the effect of backscatter from the EPID arm in the inferior region of the EPID and to record the variation of backscatter with the field sizes and location utilised.

As the aim the work is to provide a correction method to remove the effect of backscatter, the corrected matrix should necessarily display profiles that are symmetric or close to symmetric in the absence of backscatter in all clinical situations.

These symmetric profiles were then interpolated across the whole aS1000 EPID area (comprising 768×1024 pixels) to obtain a correction matrix corresponding to each case. An average correction matrix (denoted as the 'M4' matrix) was also constructed by taking the average of the 4 matrices obtained from all the field sizes (as detailed above). In order to check the symmetry of the profiles after the application of M4, several equidistant point doses in the superior-inferior region of the EPID image were also set up in TPS on central strips through a water phantom for every field size (Figure 5.9 (a)).

EPID image of multiple abutting strips for 5x20cm² field

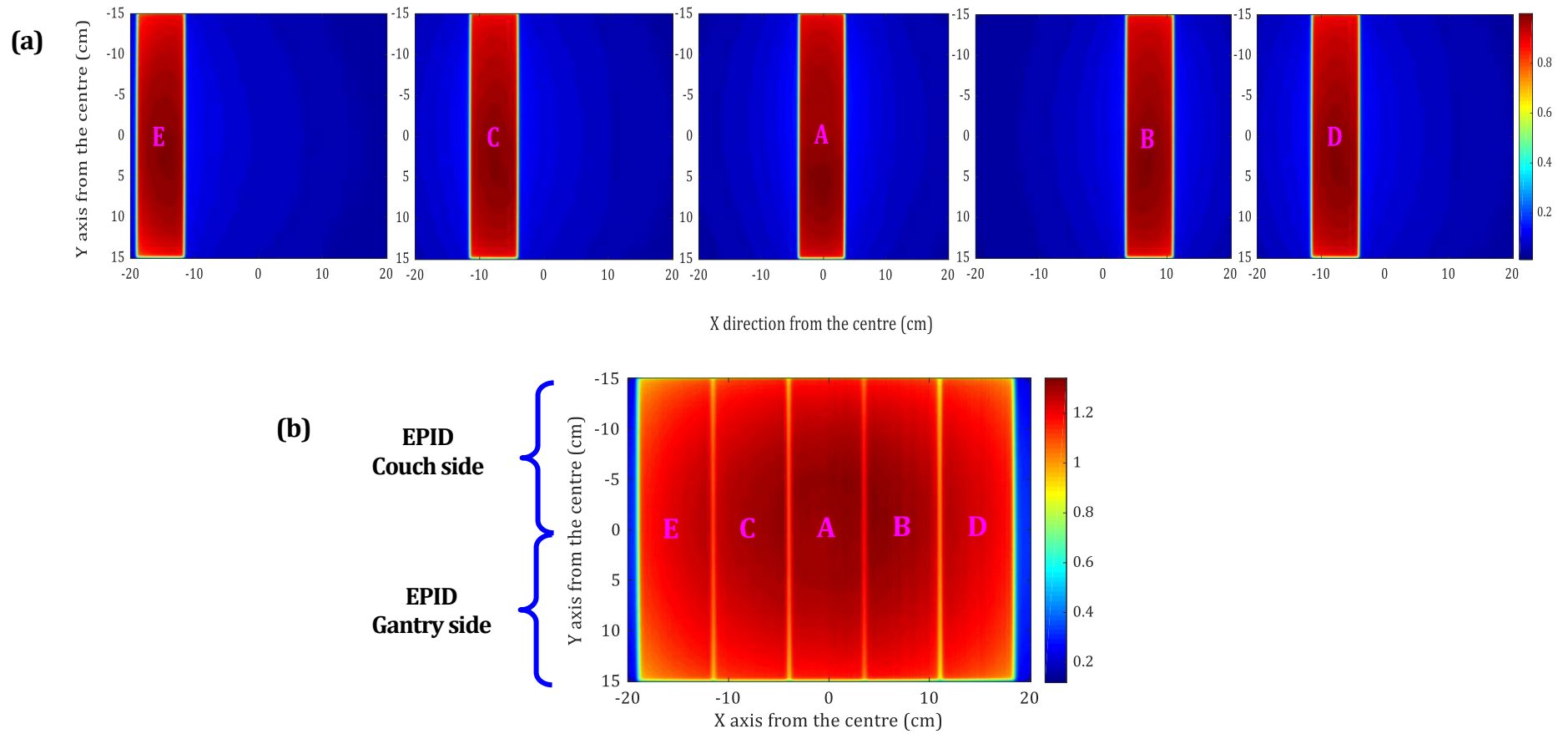


Figure 5.4 - (a) An example of 2D colourmaps of a 5x20cm² field case with multiple abutting strips (labelled with A-E) covering the active area of aS1000 EPID as shown in (b).

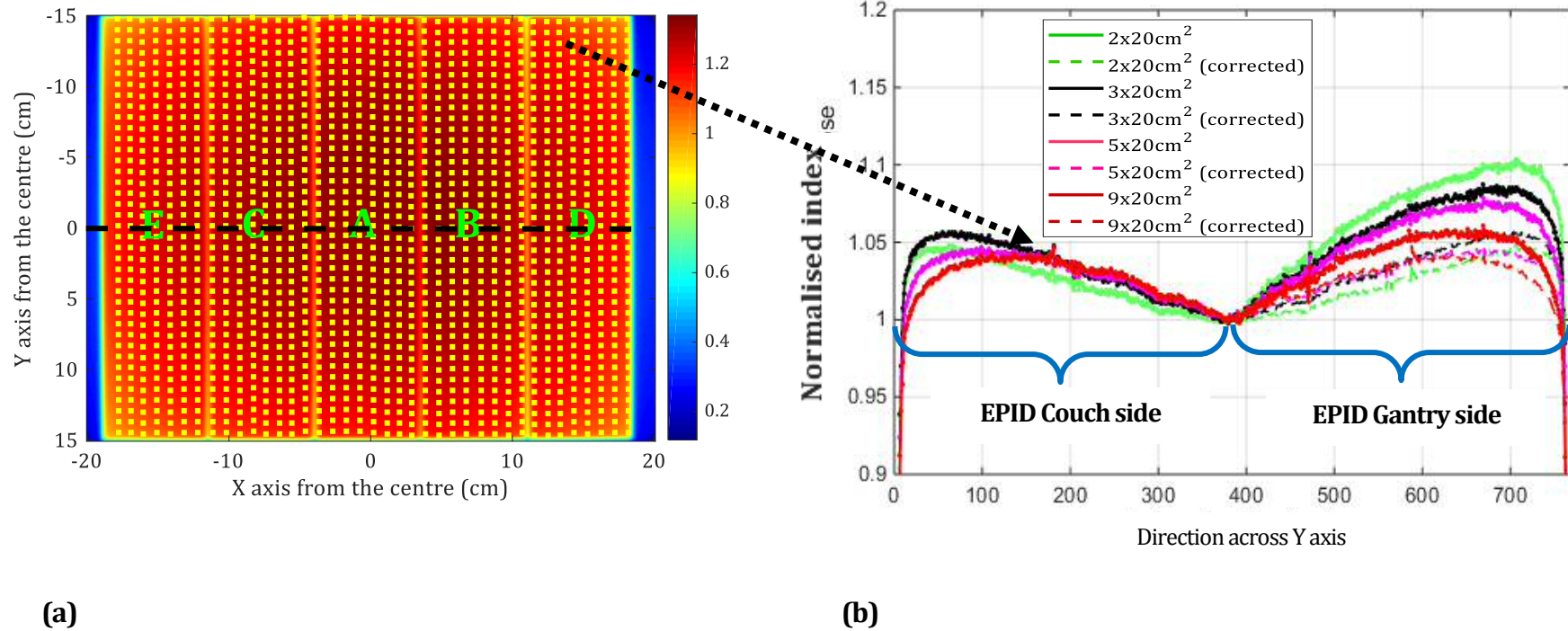


Figure 5.5 - (a) An example of multiple strips from a 5x20cm² field (labelled with A-E) case where strips were mirrored by the central pixel row (black dotted line) of the EPID image to produce a symmetric profile on the Gantry side along Y axis. Vertical yellow dotted lines represent the points of interpolation taken to get a complete set of correction factors for the EPID.

(b) Examples of profiles for different field sizes cut through the in-line direction (yellow dotted lines from (a)) of EPID image; dashed lines-corrected profiles on the gantry side (positive values of Y axis).

Next, the utility of this M4 correction matrix was tested with a series of central square field sizes ($2 \times 2 \text{ cm}^2$, $3 \times 3 \text{ cm}^2$, $5 \times 5 \text{ cm}^2$, $10 \times 10 \text{ cm}^2$ and $20 \times 20 \text{ cm}^2$). Firstly, to investigate the dose before applying the correction, the field images were fed into Dosimetry Check and analysed for the percentage difference between measured dose in Dosimetry Check and calculated TPS dose. Next, images in DICOM format were read as double precision array following a linear transformation (detailed in section 2.2.2.2) and then used to convert the corresponding image pixel to a useful measurement. These steps were done with the aid of a Matlab script as illustrated in Figure 5.6.

Next, rescaled values were obtained by multiplying these useful values with the M4 matrix. Subsequently, to be able to represent the newly generated rescaled values as image pixels in DICOM format, the linear transformation was again used to reproduce new pixel values that belong to the new image. Finally, this corrected image was then written as a DICOM file with all metadata information retained from the original DICOM image structure.

For a comparison to dose before correction, these corrected images for all fields were fed back into Dosimetry Check to investigate dose after correction being applied. The analysis was done at point of interest (POI) in the inferior region of the EPID for each field size, for the corresponding Y axis profiles and for a gamma of 3%/3mm (Chapter 3) above a 20% threshold.

```

%%This script follows the generation of a new image after correction being
%%applied

figure;
%Read and rescale the original image to obtain the meaningful data
B03_RPO=(double(dicomread('RTIMAGE_6000X_B03_RPO-3_1_30_174527.dcm')));
inf_B03=dicominfo('RTIMAGE_6000X_B03_RPO-3_1_30_174527.dcm','dictionary','dicom-
dict-mod2.txt');
B03dat=inf_B03.RescaleIntercept+inf_B03.RescaleSlope.*B03_RPO;

    %%Apply M4 correction matrix to the rescaled values to obtain the
    %%corresponding pixel values
    WTI_B03_rponewdat=B03dat.*(M4);
    WTI_B03_rponewdat=uint16((WTI_B03_rponewdat-inf_B03.RescaleIntercept).
/(inf_B03.RescaleSlope));
    %%write new corrected image as DICOM file and display new corrected image
    dicomwrite(WTI_B03_rponewdat,'RI_B03_RPO_corrected.dcm',inf_B03,'CreateMode','copy');

```

Figure 5.6 – Example of coding in Matlab script for the implementation of the M4 correction matrix and generation of updated EPID images after correction.

In addition to the utility of the M4 correction matrix with the central square fields, the matrix was also validated and verified with an example of an IMRT Head-and-Neck case comprising a series of segmented fields. All calibrations and irradiations were carried out at a dose-rate of 300 MUmin⁻¹. IMRT images (without any correction applied) were first evaluated and read in Dosimetry Check. Subsequently, IMRT images corrected for backscatter (by means of multiplying images with M4 matrix using Matlab script) were obtained and read into Dosimetry Check. The dose calculation grid in OMP TPS and Dosimetry Check was set to 0.3cm.

In summary, the compatibility of the M4 matrix was tested with central square fields, off-axis square fields, rectangular fields and a clinical IMRT case. The following comparisons between pre-correction and post-correction data were undertaken:

- i) point dose calculated by Dosimetry Check and TPS at the point of interest (POI) in the inferior region,
- ii) beam profiles along the in-line direction (refers to Y axis of an EPID image),
- iii) pass rate of gamma criterion (3%/3mm) on an IMRT Head-and-Neck case at both POI and d_{max} for the respective beams.

An overview of the whole process is described in Figure 5.7.

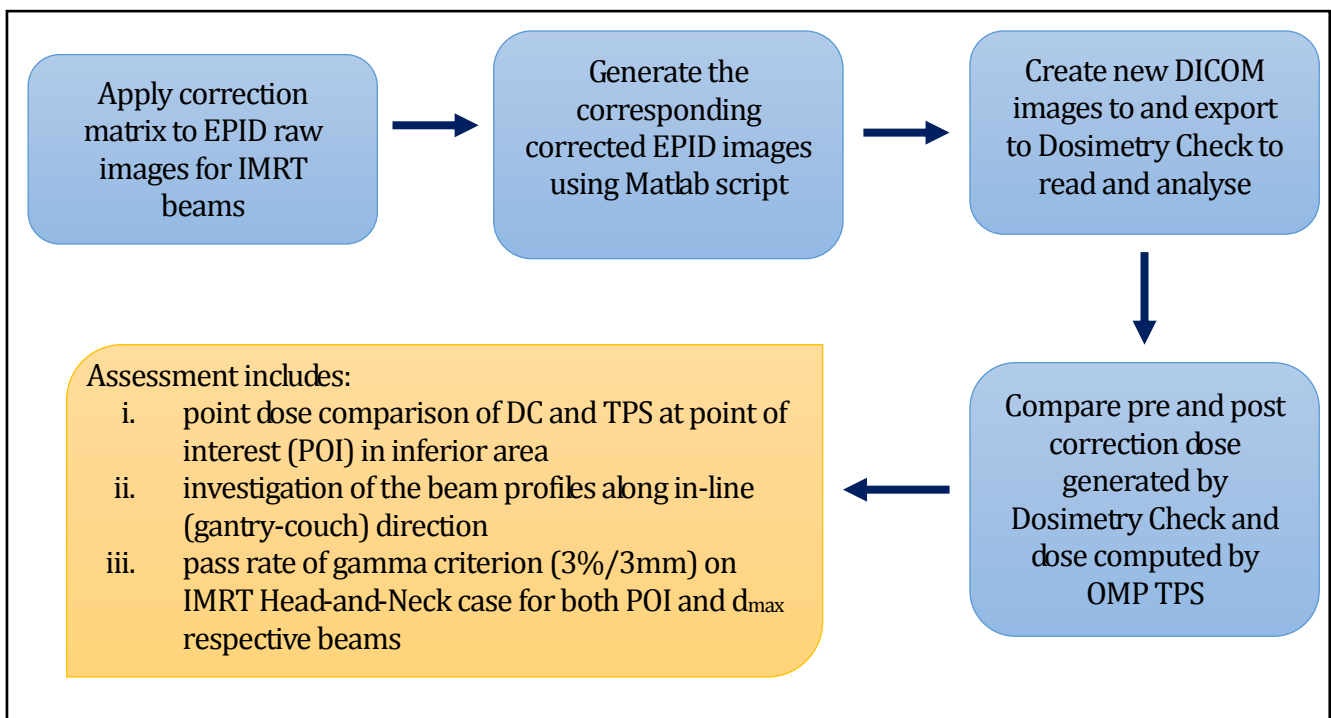


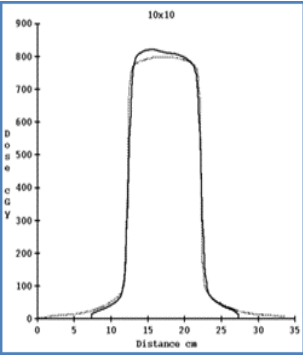
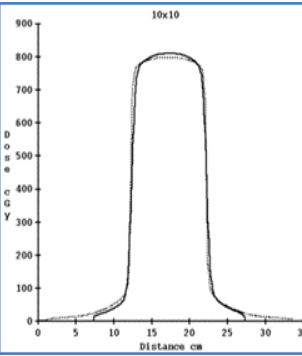
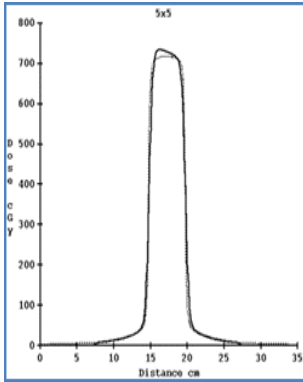
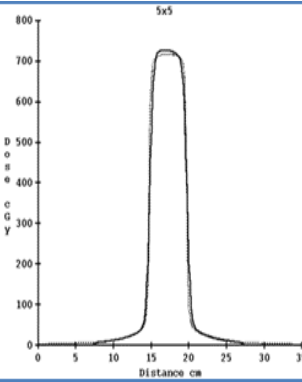
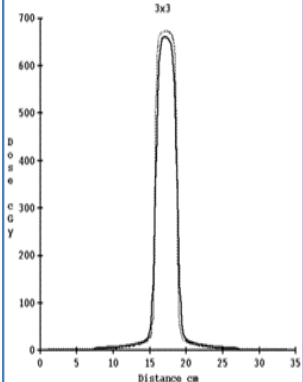
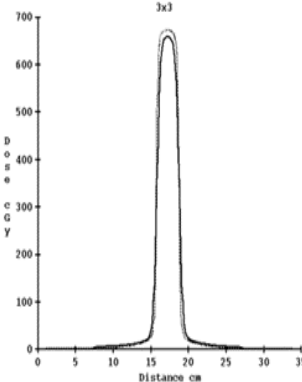
Figure 5.7 - A process map describing the correction stages from the application of the correction matrix to the analysis of the results.

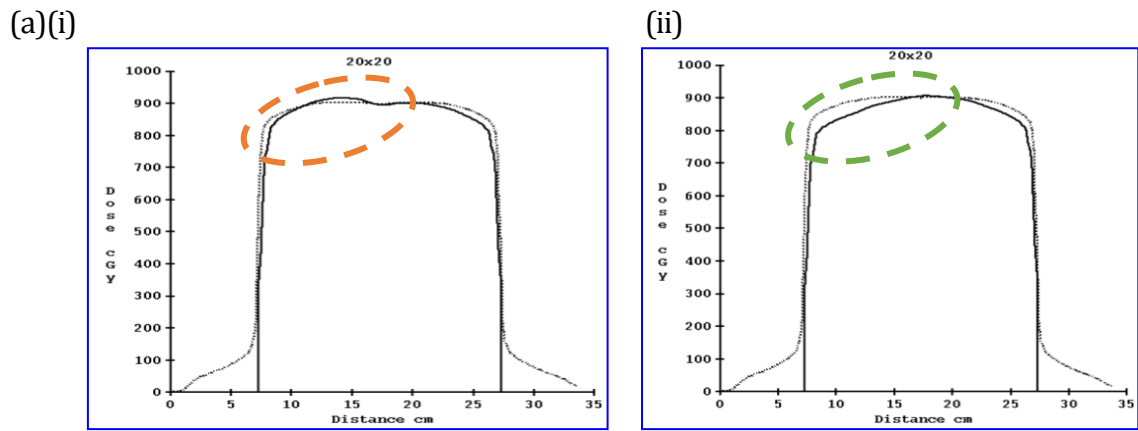
5.3.3 Results

After a preliminary analysis of the efficacy of the correction method on the series of square fields, in summary it was found that using the M4 correction matrix gave good agreement, i.e. less than 2% difference between Dosimetry Check and TPS dose at POI. Y axis profiles of the respective square fields showed improvement in the symmetry of line profiles using the M4 correction. An average of 98% points passed gamma criterion of 3%/3mm for both coronal and sagittal planes of the POI after corrections compared to an average of 91% and 94% points for the coronal and sagittal planes respectively before correction.

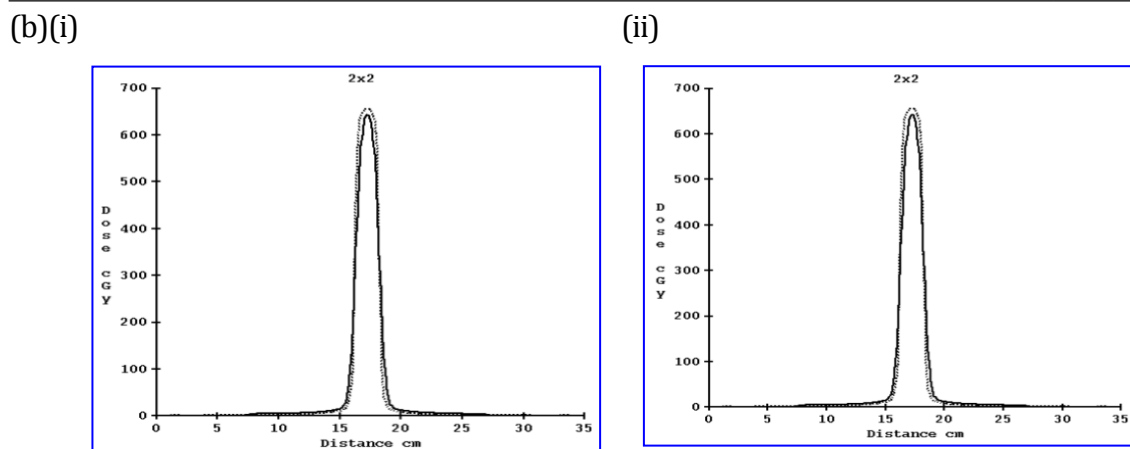
Table 5.1 illustrates the initial results obtained for the square fields. It was found that the correction matrix is only beneficially applicable to fields of equivalent square less than approximately 12cm (e.g. 9x20cm²). If the equivalent square field is greater than 12cm, there is no benefit in applying the correction (Figure 5.8 (a)). Moreover, due to the limitation of the Dosimetry Check software, the scattered radiation is assumed to be constant across the EPID. For a very small 2x2cm² field size (Figure 5.8 (b)), accurate calculation of POI dose is rather difficult and so there is no benefit in applying the correction.

Table 5.1- Results for several square field sizes tested with the M4 correction matrix. Dose at the POI after correction shows better than 2% agreement with TPS, the profiles are more symmetrical and gamma is improved for coronal and sagittal planes.

Square fields (cm ²)	Dose Difference		Y axis profiles (gantry-couch direction)		Gamma criterion of 3%3mm above threshold			
	before	after	Before	after	Coronal (%)		Sagittal (%)	
					before	after	before	after
10x10	3.32%	1.19%			85.50	96.8	90.00	96.87
5x5	2.58%	1.44%			94.80	100.00	100.00	100.00
3x3	1.55%	1.31%			91.21	95.81	91.13	95.84
	2.48%	1.31%	Mean		90.50	97.54	93.71	97.57
	0.89	0.13	Standard Deviation, SD		4.69	2.19	5.48	2.17



20x20cm ²	Difference compared with TPS dose (%)	Gamma (above 20%), 3%3mm	
	Point of Interest	Coronal	Sagittal
without correction	0.18	64.87	88.55
with 'M4' correction	-2.94	50.57	72.95



2x2cm ²	Difference compared with TPS dose (%)	Gamma (above 20%), 3%3mm	
	Isocentric point	Coronal	Sagittal
without correction	-2.00	86.96	86.11
with 'M4' correction	-2.22	85.51	82.82

Figure 5.8 - (a) Profile for a 20x20cm² field in the Y direction generated by Dosimetry Check illustrates that (i) The 'humps' before correction are overcorrected by the application of M4 (b) Profile for a 2x2cm² field (i) before correction, (ii) after the application of the correction

The preliminary investigations also involved analysis of several equidistant sample points along the Y axis (superior-inferior) to assess the level of improvement of profile for all rectangular field sizes ($2 \times 20 \text{cm}^2$, $3 \times 20 \text{cm}^2$, $5 \times 20 \text{cm}^2$ and $9 \times 20 \text{cm}^2$) after application of the M4 correction matrix (Figure 5.9 (a) and (b)). It was found that the percentage difference in asymmetry before and after correction was reduced by an average of 3% as tabulated in Table 5.2 (a) and (b).

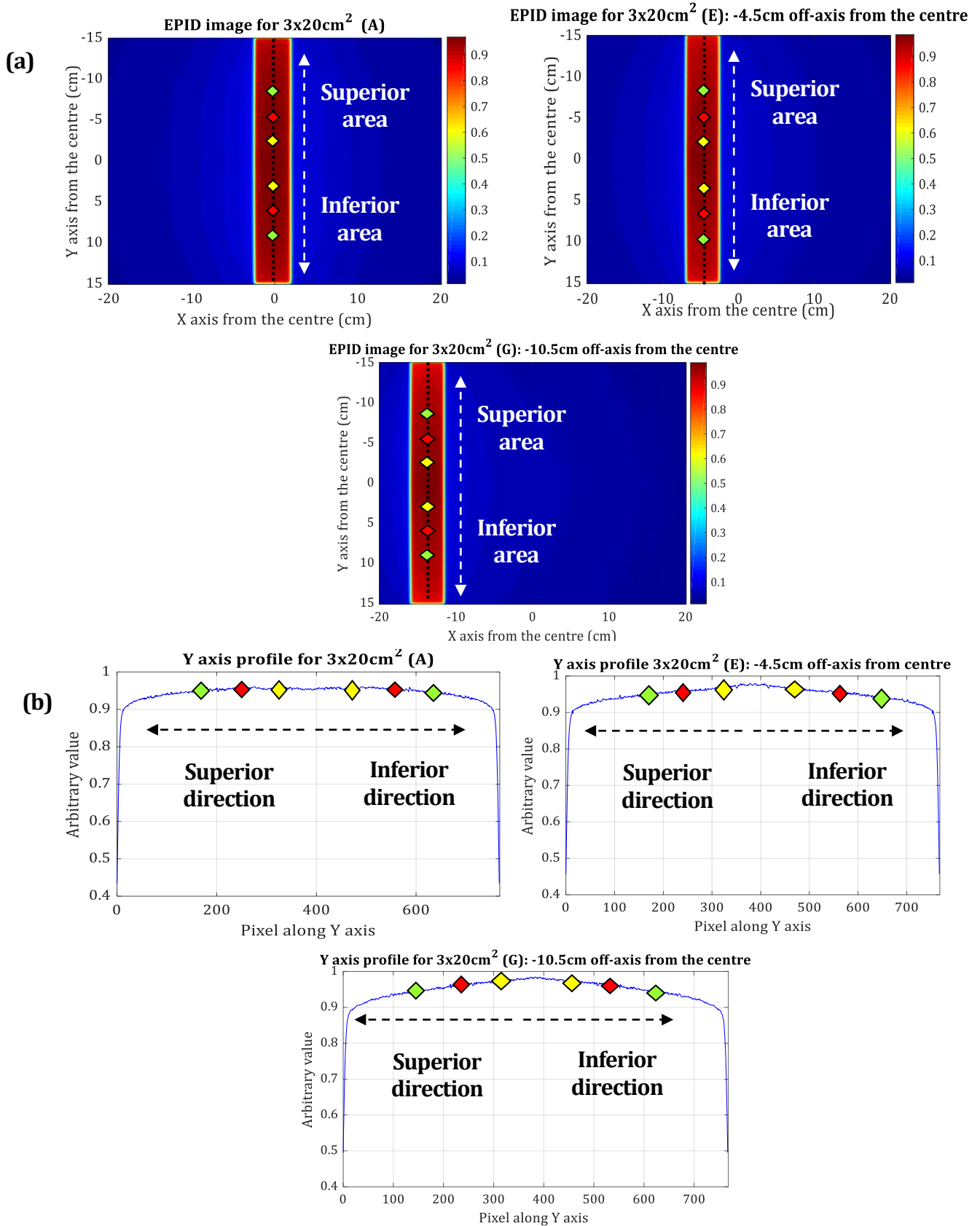


Figure 5.9 – (a) Examples of 2D colourmaps of 3x20cm² strips with equidistant points taken along the superior-inferior direction from the central row of the EPID respectively to certain off-axis distance from the central pixel after correction. Yellow-3cm, red-6cm, green-9cm. (b) Corresponding points illustrated on symmetric profiles with the same colour coded marks.

Table 5.2 - Examples of improvement in asymmetry before (β) and after (α) correction for equidistant points on several strips including some off-axis strips (a) 3x20cm² field size (b) 5x20cm²

Strips / Points (a)	Percentage difference in asymmetry at 3cm (Sup-Inf.)		Percentage change (%)	Percentage difference in asymmetry at 6cm (Sup-Inf.)		Percentage change (%)	Percentage difference in asymmetry at 9cm (Sup-Inf.)		Percentage change (%)
	Before (%)	After (%)		Before (%)	After (%)		Before (%)	After (%)	
	β	α	β	α	β	α			
3x20cm ² (central)	3.25	0.57	2.68	4.02	0.64	3.38	2.73	0.49	2.24
3x20cm ² (3cm Off-axis)	3.39	0.82	2.57	4.01	0.82	3.19	2.63	0.65	1.98
3x20cm ² (9cm Off-axis)	2.70	0.97	1.73	3.32	1.30	2.02	1.64	0.71	0.93

Strips / Points (b)	Percentage difference in asymmetry at 5cm (Sup-Inf.)		Percentage change (%)	Percentage difference in asymmetry at 10cm (Sup-Inf.)		Percentage change (%)
	Before (%)	After (%)		Before (%)	After (%)	
	β	α	β	α		
5x20cm ² (central)	3.54	0.16	3.38	2.83	0.52	2.31
5x20cm ² (5cm Off-axis)	3.23	0.20	3.03	2.43	0.70	1.73
5x20cm ² (10cm Off-axis)	2.19	0.20	1.99	1.58	0.42	1.16

In addition, to show the effect on some off-axis fields after the application of backscatter correction, the correction matrix has also been verified with a series of square field 'patches' off-axis ($2 \times 2 \text{ cm}^2$ - A, C, E and G, $3 \times 3 \text{ cm}^2$ - A, C and E, and $5 \times 5 \text{ cm}^2$ - A and C) inferior to the EPID (gantry side) (Figure 5.10). This was done to confirm whether this correction could also be applied to off-axis square fields. The corresponding results shown in Table 5.3.

For point dose measurements made off-axis, after application of the correction there was good agreement with TPS calculations, the difference in general being less than 3% compared to the situation before correction, which showed differences of over 5%.

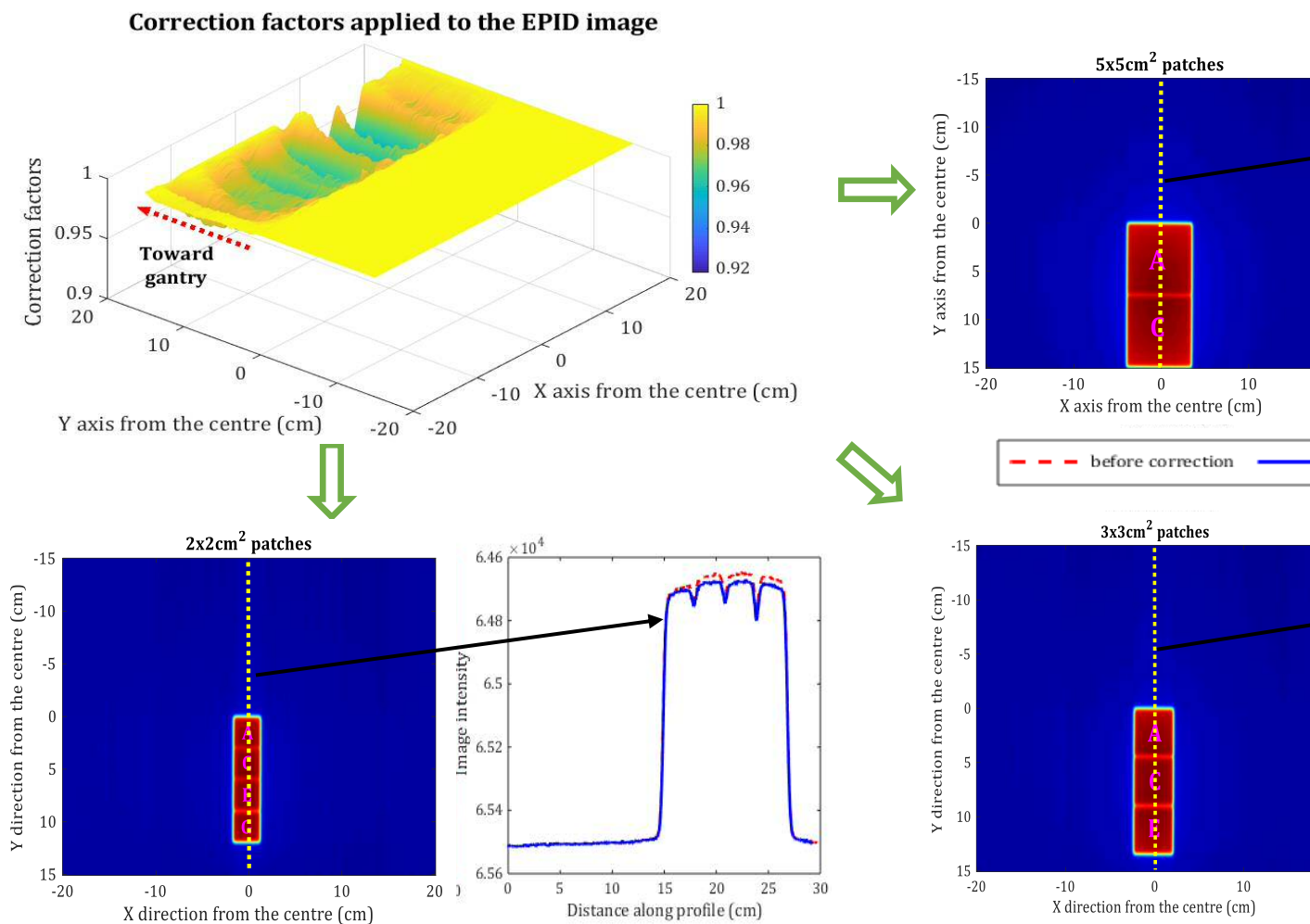


Figure 5.10 – Testing of correction matrix with series of off-axis square field patches (labelled with A, C, E and G in the EPID image) with 2x2cm², 3x3cm² and 5x5cm² field sizes). Cut through profiles show improvement after correction (before correction (red dotted lines)).

Table 5.3 - Percentage point dose measurement difference between Oncentra MasterPlan TPS and Dosimetry Check showing agreement within 3% after application of correction and indicating that this method can be applied to off-axis fields.

Off-axis square field patches (distance from the centre)	Point dose measurement difference (%)	
	before	after
2x2cm ² A (-1cm)	1.39	0.14
2x2cm ² C (-3cm)	1.90	1.17
2x2cm ² E (-5cm)	3.42	1.90
2x2cm ² G (-7cm)	2.97	1.97

Off-axis square field patches (distance from the centre)	Point dose measurement difference (%)	
	before	after
3x3cm ² A (-1.5cm)	3.36	1.63
3x3cm ² C (-4.5cm)	6.56	2.89
3x3cm ² E (-7.5cm)	5.14	2.16

Off-axis square field patches (distance from the centre)	Point dose measurement difference (%)	
	before	after
5x5cm ² A (-2.5cm)	4.68	2.28
5x5cm ² C (-7.5cm)	5.66	2.67

After correction was applied to the example IMRT Head-and-Neck case (Figure 5.11), the improvement in point dose measurement in the inferior region (gantry side) of the EPID image (where the non-uniform backscatter effect is predominant) was assessed in terms of percentage difference for all beams relative to the point doses given by the TPS. It was found that the average dose difference was reduced by approximately 3% at the point of interest (POI) in the inferior region of the EPID image and at the d_{\max} POI respectively (Table 5.4 (a)). In summary, for transit dosimetry (dose delivered through a patient or phantom), the Dosimetry Check dose discrepancy relative to the TPS dose after correction was reduced by about 3% compared to the situation before correction.

The sample points were positioned in the inferior region of the IMRT image at a distance from the central axis towards the gantry. Points less than 1cm from the panel edge were excluded, since the correction factor was set to 1 (at ~ 1 cm from the panel edge) to reduce uncertainties due to lateral scatter within the EPID. Thus, the outcomes after correction are promising, with significant removal of the effect of non-uniform backscatter in complex treatment plans, such as the example IMRT Head-and-Neck plan with individual segmented beam profiles.

For the coronal view, an average of 95% of points passed a gamma criterion of 5%/3mm (at both POI and d_{\max} POI) with the backscatter correction applied, compared to an average of 90% and 85% (at POI and d_{\max} of POI respectively) before correction. The gamma 5%/3mm criterion was chosen for the case of transit dosimetry (in-vivo) following the recommendation in ICRU report 83, which set a pass rate of 85% (ICRU, 2010). Similarly, in the sagittal view, 93% of points passed the gamma criterion at POI whereas 97% passed at d_{\max}

POI, compared to an average of 85% and 95% (at POI and d_{\max} POI respectively) before the application of the correction (Table 5.5 (a) and (b)).

Note that the all POIs placed in the inferior part of the IMRT beams are in the following order and coordinates;

i.e. Beam N = (x, y, z), where N is the beam number,

x = x-axis coordinate in cm,

y = y-axis coordinate in cm,

z = z-axis coordinate in cm.

- 1) Beam01 = (-4.6, -6.3, 0.0)
- 2) Beam02 = (2.2, -5.1, 0.0)
- 3) Beam03 = (-2.8, -5.7, 0.0)
- 4) Beam04 = (-2.9, -3.1, 0.0)
- 5) Beam05 = (-4.3, -3.1, 0.0)
- 6) Beam06 = (1.4, -4.1, 0.0)
- 7) Beam07 = (-1.6, -3.4, 0.0)
- 8) Beam08 = (-2.2, -3.4, 0.0)
- 9) Beam09 = (3.6, -3.9, 0.0)
- 10) Beam10 = (3.0, -5.5, 0.0)
- 11) Beam11 = (-3.3, -7.1, 0.0)
- 12) Beam12 = (5.4, -6.0, 0.0)

Table 5.4 - Percentage reduction in point dose for Dosimetry Check relative to the TPS after the application of the correction for (a) transit in-vivo dosimetry (b) pre-treatment dosimetry

	Beams (transit)	Dose difference for Dosimetry Check relative to TPS (%)					
		POI			d _{max} POI		
		before	after	Percentage changed	before	after	Percentage change
(a)	B01	3.38	1.19	-2.19	3.73	1.32	-2.41
	B02	5.22	1.80	-3.42	6.20	2.76	-3.85
	B03	0.68	-0.39	-1.07	4.35	1.07	-3.28
	B04	7.70	4.51	-3.09	7.34	2.65	-3.39
	B05	8.07	4.93	-3.14	7.54	4.25	-3.29
	B06	2.20	-0.81	-3.01	2.30	-0.91	-3.21
	B07	7.39	4.38	-3.01	8.39	5.05	-3.34
	B08	8.82	5.83	-2.69	9.07	6.09	-2.98
	B09	2.14	1.09	-1.05	3.89	0.45	-3.44
	B10	5.44	1.86	-3.58	5.92	2.34	-3.58
	B11	3.77	0.87	-2.90	6.69	3.75	-2.94
	B12	3.08	-0.11	-3.19	3.96	0.94	-3.02
		Average	4.79	2.10	-2.70	5.78	2.48
	σ	2.64	2.26	0.84	2.12	2.04	0.54
	Beams (pre- treatment)	Dose difference for Dosimetry Check relative to TPS (%)					
		POI			d _{max} POI		
		before	after	Percentage changed	before	after	Percentage change
(b)	B01	4.29	1.22	-3.07	4.3	1.20	-3.10
	B02	4.32	1.09	3.23	6.92	2.53	-4.39
	B03	3.88	0.76	-3.12	6.22	2.09	-4.13
	B04	5.07	1.20	3.87	6.27	2.21	-4.06
	B05	4.42	1.29	-3.13	5.09	2.03	-3.06
	B06	3.48	0.97	-2.51	1.84	-0.57	-2.41
	B07	3.57	1.06	-2.51	4.84	1.91	-2.93
	B08	4.21	1.69	-2.52	5.36	2.92	-2.44
	B09	3.40	0.45	-2.95	4.88	2.11	-2.77
	B10	4.34	0.56	-3.78	5.42	1.63	-3.79
	B11	5.06	2.37	-2.69	7.07	3.97	-3.10
	B12	4.37	1.44	-2.93	5.88	2.86	-3.02
		Average	4.20	1.18	-3.03	5.34	2.07
	σ	0.55	0.52	0.45	1.39	1.09	0.66

Similar results were obtained for the case of pre-treatment delivery, which involves verification of dose delivered without a patient or phantom. Point dose difference relative to the TPS was reduced by about 3% compared to the situation before correction (Table 5.4 (b)). A 95% pass rate for routine Gamma Index criteria of 3%/3mm for doses above a 20% threshold was used for the pre-treatment situation and the results are shown Table 5.6 (a) and (b).

After correction, 98% and 95% points passed the gamma criterion for POI and d_{\max} respectively in the coronal view, compared to 87% and 82% before correction. The Gamma Index pass rate also improved in the sagittal view from 83% and 92% before correction to 96% and 97% for POI and d_{\max} POI respectively after correction. Simple point dose comparison is currently implemented clinically in Velindre Cancer Centre for conformal treatment, and the correction method described above improves in-line beam profiles in the inferior region (away from the gantry) for a sample IMRT plan. For example, in Figure 5.12 (a), a beam profile (B03-RPO) which cuts through the Y-axis at EPID imager level, demonstrated a significant improvement after the application of the correction. Agreement between Dosimetry Check and TPS profiles to within 1% at the inferior end after correction also can be seen in Figure 5.12 (b). In addition, improvement was also achieved when correction was applied to a small segmented beam profile in the inferior region as shown in Figure 5.13.

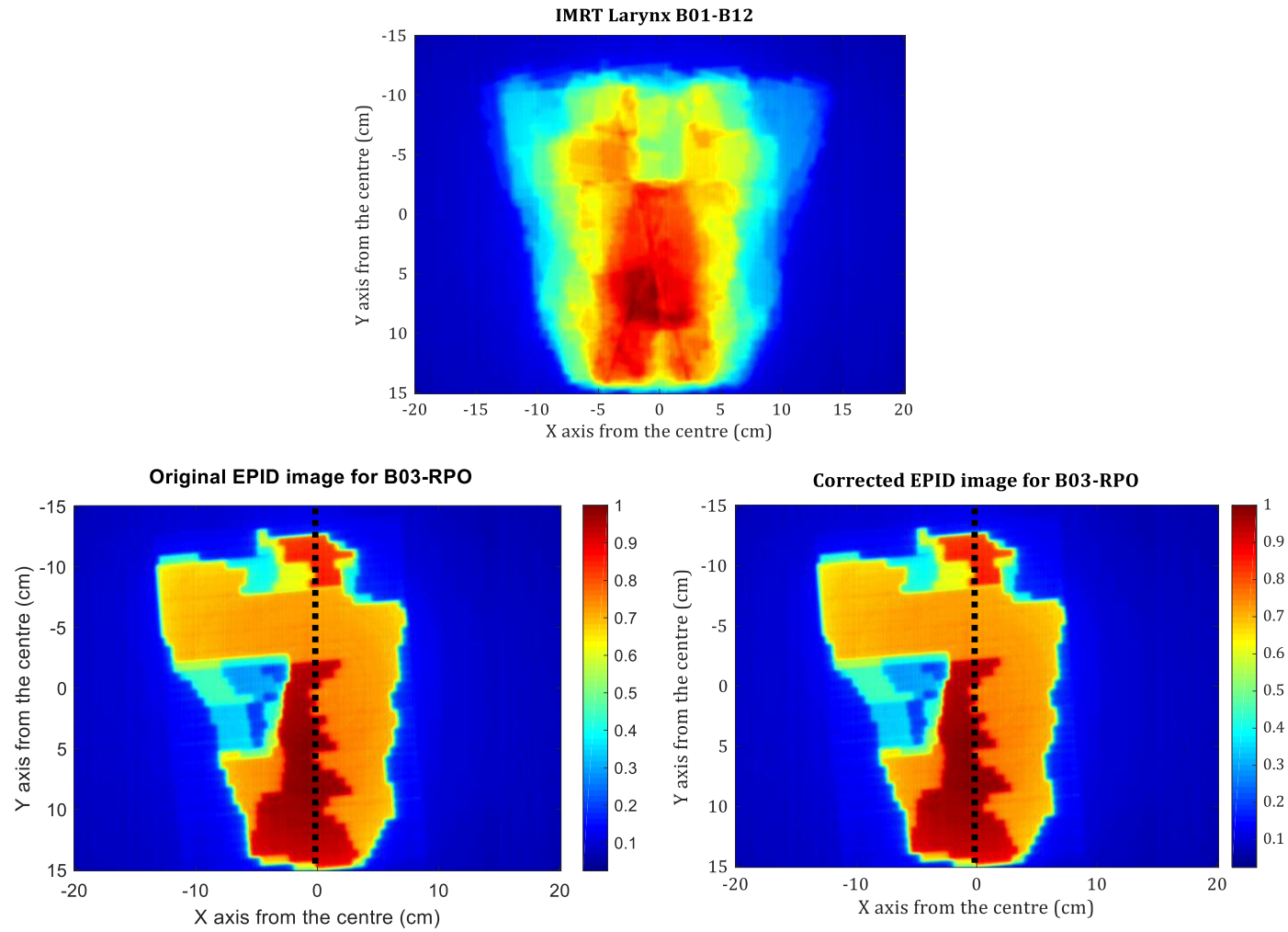


Figure 5.11 - Representation of a beam profile B03 cut along Y axis of the EPID image before and after the application of the correction for an IMRT Head-and-Neck case.

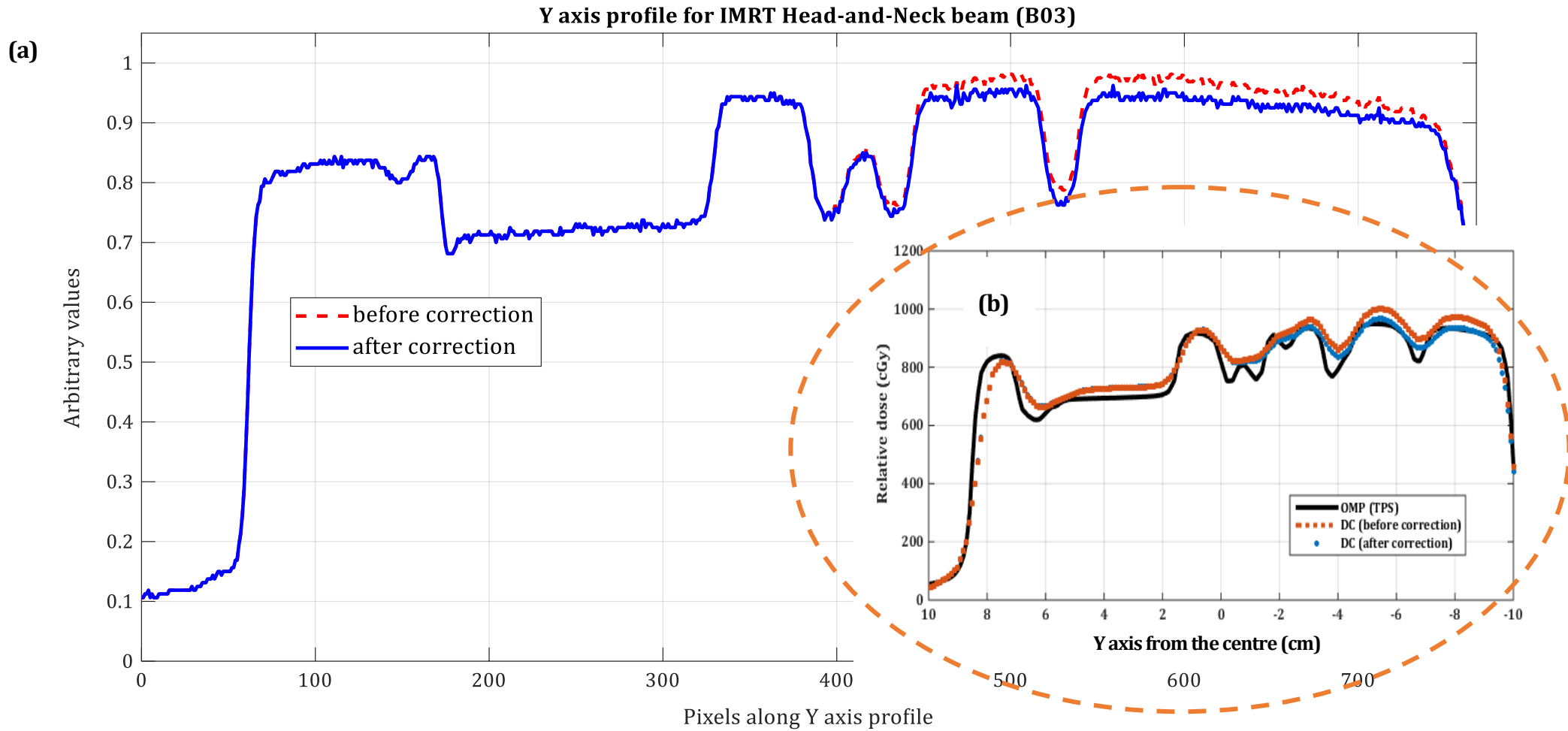


Figure 5.12 - (a) Change in image intensity at the EPID level before and after correction. (b) Profile comparison between TPS dose and EPID reconstructed dose (in vivo) given by the Dosimetry Check software. Black solid line is TPS dose, red dotted line is DC dose before correction and blue dotted line is Dosimetry Check dose after correction. Agreement between black solid line and blue dotted line is within 1% after correction from more than 3% before correction.

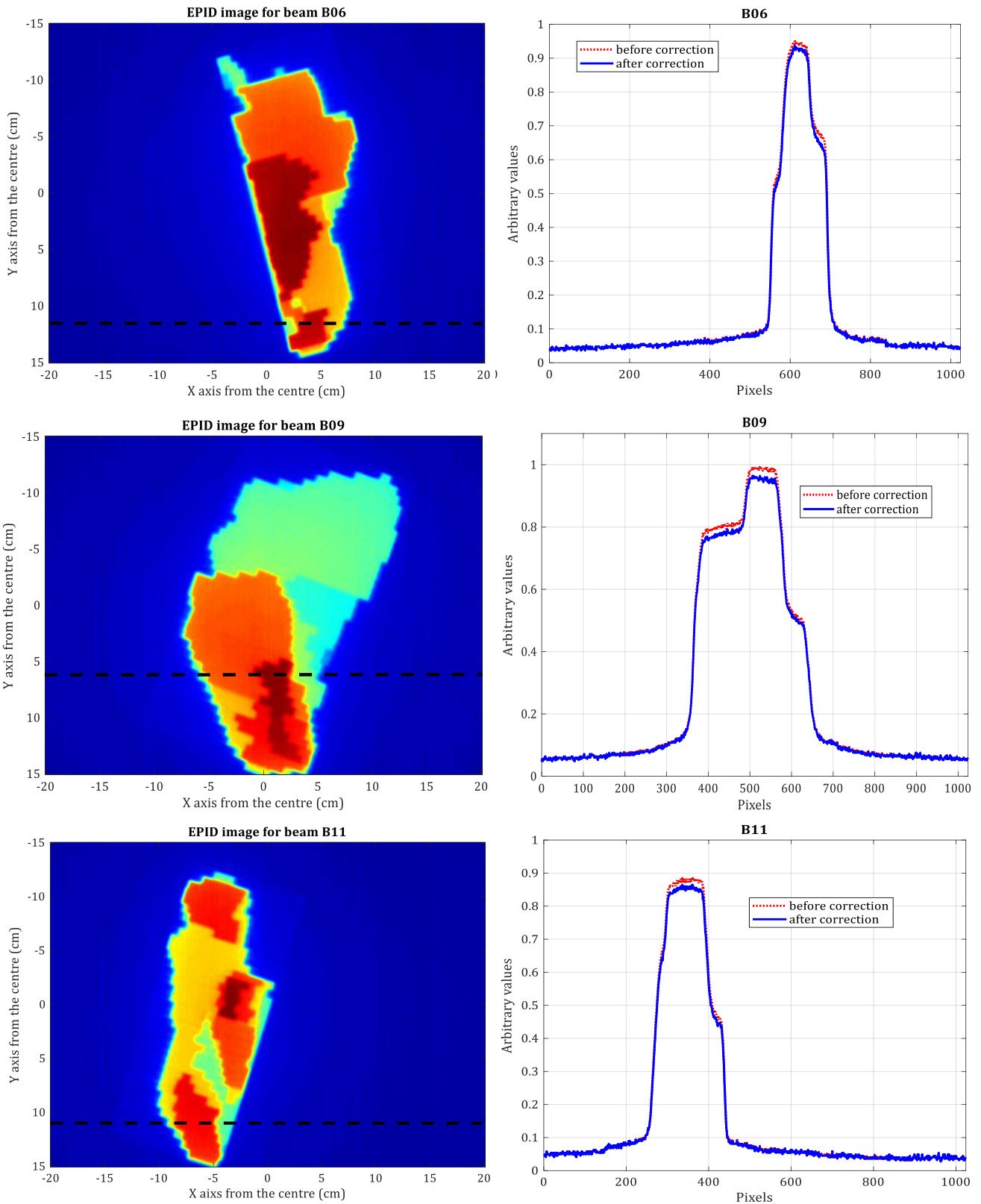


Figure 5.13 - Examples of beams involving small segmented fields in the inferior region (the cut through black dashed line varies for each beam). The cut-through profiles show improvement after application of the correction.

Table 5.5 - Percentage of points passing gamma criterion of 5%/3mm above a threshold of 20% for transit dosimetry at (a) POI and (b) d_{\max} POI.

	Beams	Gamma 5%/3mm (coronal)		Gamma 5%/3mm (sagittal)	
		Before correction (%)	After correction (%)	Before correction (%)	After correction (%)
(a) Gamma pass rate (%) for all beams- (cut through POI of the beam)	B01	98.36	100.00	96.05	99.76
	B02	89.47	95.52	81.87	90.02
	B03	91.83	97.42	85.60	91.80
	B04	94.74	99.95	94.24	99.00
	B05	87.10	94.46	69.16	86.35
	B06	97.62	98.23	91.98	96.91
	B07	85.69	92.78	76.90	92.44
	B08	72.68	85.22	61.07	75.34
	B09	89.09	98.47	96.97	97.85
	B10	86.74	94.22	86.98	92.94
	B11	89.11	91.68	99.92	100.00
	B12	93.29	96.88	83.35	95.23
	Average	89.64	95.40	85.34	93.14
σ	6.76	4.18	11.78	7.01	
(b) Gamma pass rate (%) for all beams- (cut through d_{\max} POI of the beam)	B01	95.52	98.87	98.76	100.00
	B02	77.22	92.02	85.73	91.10
	B03	90.10	97.70	95.75	97.55
	B04	88.62	99.68	96.70	99.06
	B05	82.18	91.14	86.24	95.05
	B06	97.01	98.93	96.42	98.94
	B07	82.61	92.17	89.37	98.74
	B08	66.38	78.70	81.32	91.18
	B09	86.52	98.15	98.65	96.02
	B10	79.28	90.83	95.32	96.61
	B11	82.75	99.50	99.94	100.00
	B12	91.62	96.17	97.73	98.76
	Average	84.98	94.49	93.49	97.00
σ	8.52	6.05	6.17	3.11	

Table 5.6 - Percentage of points passing gamma criterion of 3%/3mm above a threshold of 20% for pre-treatment dosimetry at (a) POI and (b) d_{max} POI

	Beams	Gamma 3%/3mm (coronal)		Gamma 3%/3mm (sagittal)	
		Before correction (%)	After correction (%)	Before correction (%)	After correction (%)
(a) Gamma pass rate (%) for all beams- (cut through POI of the beam)	B01	85.51	96.47	88.34	97.85
	B02	74.25	95.22	60.89	92.94
	B03	73.83	99.00	70.88	100.00
	B04	84.55	96.93	84.10	95.23
	B05	83.93	96.18	77.87	93.99
	B06	98.88	99.91	93.35	96.13
	B07	94.70	99.92	85.50	98.66
	B08	82.93	99.64	80.49	96.57
	B09	89.18	100.00	94.21	95.63
	B10	89.29	98.94	81.40	93.46
	B11	95.80	99.51	97.76	99.91
	B12	95.44	100.00	85.00	96.27
	Average	87.36	98.48	83.32	96.39
	σ	8.13	1.76	10.27	2.35
(b) Gamma pass rate (%) for all beams- (cut through d_{max} POI of the beam)	B01	85.66	97.98	77.31	92.67
	B02	77.15	94.00	88.90	93.32
	B03	81.67	96.67	90.72	93.89
	B04	84.34	95.98	91.15	98.34
	B05	68.49	88.85	86.48	97.77
	B06	88.85	97.55	97.91	98.97
	B07	87.03	99.04	92.85	99.07
	B08	75.69	92.99	92.97	98.82
	B09	85.28	97.57	98.89	99.03
	B10	70.81	90.10	90.86	97.53
	B11	83.70	88.58	99.85	99.91
	B12	91.62	99.85	95.38	98.73
	Average	81.69	94.93	91.94	97.34
	σ	7.18	3.97	6.15	2.53

A further component of the analysis involved the Gamma index pass rates calculated by the Dosimetry Check software for two simple example arbitrary volumes²⁷, V1 and V2 (Figure 5.14). For V1, 92% and 97% of points passed the 5%/3mm gamma criterion after correction, compared to 84% and 93% before correction for POI and d_{\max} respectively in transit dosimetry verification. For pre-treatment dosimetry, the Gamma Volume pass rate results for V1 improved to 94% and 98% after correction, compared to 85% and 93% before correction for POI and d_{\max} respectively (Table 5.7). The pass rates for V2 also improved to a maximum of 98% for pre-treatment dosimetry and 97% for transit dosimetry from minima of 82% before correction for both cases (Table 5.8).

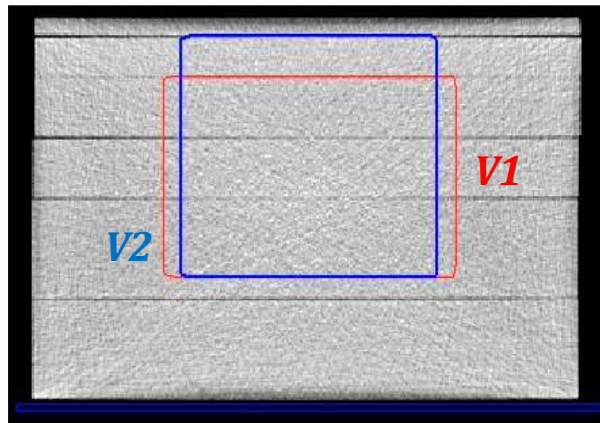


Figure 5.14 - Outlines of arbitrary volumes V1 (red) and V2 (blue) within a water phantom to demonstrate the difference in Gamma Volume results calculated by Dosimetry Check.

²⁷ Arbitrary volume– refers to a random choice rather than any particular reason for defining a volume

Table 5.7 - Gamma index pass rates results for volume V1 delineated within a water phantom.

	Beams	Transit dosimetry, cumulative Gamma index				Pre-treatment dosimetry, cumulative Gamma index			
		Before correction (%)		After correction (%)		Before correction (%)		After correction (%)	
		POI	d _{max}	POI	d _{max}	POI	d _{max}	POI	d _{max}
Gamma results for V1	B01	92.57	98.30	98.76	99.98	71.70	81.19	85.87	90.76
	B02	82.94	88.25	92.98	94.34	71.32	87.12	86.26	92.54
	B03	86.27	96.39	94.20	98.41	93.53	93.39	95.99	96.74
	B04	90.38	97.19	98.98	99.78	95.42	98.36	98.97	99.27
	B05	81.17	91.24	90.12	96.45	75.80	88.97	90.43	97.41
	B06	94.84	97.47	96.81	97.99	93.97	99.24	96.57	99.88
	B07	81.88	90.16	90.32	94.09	91.68	96.54	99.27	99.63
	B08	67.21	82.18	79.76	92.44	78.79	89.76	96.34	99.10
	B09	85.59	94.38	94.02	98.78	83.80	93.21	95.86	99.86
	B10	78.53	92.81	88.14	95.47	80.84	92.72	90.96	98.62
	B11	84.26	91.02	87.12	93.50	89.60	95.04	94.96	98.65
	B12	87.73	95.34	93.73	97.04	90.44	96.72	98.21	99.82
	Average	84.45	92.89	92.08	96.52	84.74	92.69	94.14	97.69
	σ	7.24	4.66	5.44	2.54	8.85	5.21	4.66	3.01

Table 5.8 - Gamma index results for volume V2 delineated within a water phantom.

	Beams	Transit dosimetry, cumulative Gamma index				Pre-treatment dosimetry, cumulative Gamma index			
		Before correction (%)		After correction (%)		Before correction (%)		After correction (%)	
		POI	d _{max}	POI	d _{max}	POI	d _{max}	POI	d _{max}
Gamma results for V2	B01	91.35	98.79	98.45	99.99	71.08	78.97	83.36	89.90
	B02	82.05	87.75	94.09	95.85	70.44	84.18	86.48	95.98
	B03	82.89	96.02	92.75	99.33	90.98	90.80	98.67	99.67
	B04	88.13	95.70	98.97	99.90	93.86	97.59	97.68	99.99
	B05	76.12	88.07	86.58	95.13	72.12	85.16	89.13	96.11
	B06	95.56	98.26	98.20	99.03	91.48	97.90	94.80	98.96
	B07	80.36	89.36	89.79	94.37	89.71	95.04	98.99	99.49
	B08	62.89	78.74	76.31	90.59	73.92	86.51	93.49	98.16
	B09	83.43	93.11	92.66	98.76	78.15	91.31	91.57	99.47
	B10	74.63	91.16	85.97	95.50	75.55	88.57	87.25	95.98
	B11	82.99	89.72	86.26	92.57	87.27	93.01	93.30	97.20
	B12	84.87	94.63	92.12	96.96	85.19	95.44	95.26	99.53
	Average	82.11	91.78	91.01	96.50	81.65	90.37	92.50	97.54
σ	8.41	5.60	6.55	3.04	8.56	5.61	4.84	2.74	

5.3.4 Discussion

Ensuring accurate patient dose calculation is a crucial aspect of the radiotherapy process. In the context of this work, the removal (or at least the reduction) of the effect of non-uniform backscatter due to the EPID arm and its auxiliary components underneath the panel, is clearly an important observation. The introduction of a novel correction method to overcome the issue when using Dosimetry Check software leads to more accurate treatment verification with advanced radiotherapy techniques. A visible “hump” on the left of the Y-axis profile measured by Dosimetry Check which resulted from the backscatter was reported during commissioning due to the effect of calibration of the acquired image with flood field image. Both of these images experienced backscatter from the arm which cancelled each other out at one side and left the other side with a pronounced “hump”. On the other hand, the “rounding” of the profile with increasing field size (Figure 5.2), has been confirmed by Math Resolutions™ to be due to a limitation of the software, in which scattered radiation is assumed to be constant across the EPID.

One of the major aims of this study was to correct for asymmetries in the EPID raw image. The backscatter correction matrix developed by this work has the potential to improve significantly both pre-treatment and in-vivo transit dose verification using Dosimetry Check. It is evident that improvement in gamma pass rates demonstrates that this method would be suitable for application in advancing the accuracy of the existing Dosimetry Check verification tool, especially in a clinical setting where only point dose measurement is being routinely applied at the moment.

Prior to implementing this correction clinically, further steps would be required in the form of setting up and commissioning procedures for all the relevant linacs, to ensure the general effectiveness of the correction. In addition, the correction is also intended to apply to VMAT treatment techniques; the segmented IMRT technique described in this chapter is just one of a number of advanced radiotherapy delivery methods employed at Velindre Cancer Centre. The potential application of this correction matrix approach to VMAT is discussed in the next chapter on a 'proof of principle' basis.

Chapter 6

APPLICATION OF DOSIMETRY CHECK TO THE VERIFICATION OF VOLUMETRIC MODULATED ARC THERAPY

6.1 NEW VERIFICATION TOOL FOR VMAT TREATMENT VERIFICATION

The theme of this chapter is an extension of the investigations of Dosimetry Check undertaken for IMRT described in Chapter 5. In this chapter, Dosimetry Check is investigated as a tool for VMAT treatment verification (discussed in Chapter 1 and 2). VMAT is one of the most advanced treatment techniques currently available, with shorter treatment delivery times than segmented IMRT for example. VMAT delivery verification using cine images²⁸ for both pre-treatment and transit dosimetry is discussed and relevant results presented. When fully commissioned for VMAT verification, it is anticipated that Dosimetry Check will provide a key facility in the Velindre Cancer Centre.

6.1.1 EPID challenges with VMAT delivery technique

In recent years, newer treatment techniques, such as VMAT, have necessitated more sophisticated planning and delivery facilities and achieved higher dose conformity with shorter

²⁸ Cine images – Continuous sequence of images taken in a full VMAT delivery cycle.

treatment times compared to IMRT. With VMAT, the linear accelerator rotates around the patient during treatment and simultaneously, the machine's MLC continuously reshapes and changes the intensity of the radiation beam as it does so. The arc of rotation is associated with variable gantry speed and dose-rate. VMAT has received extensive attention recently, and it has moved from research into clinical implementation to treat most of the cancers for which radiotherapy is used (Mijnheer et al., 2013b, Greer, 2013, Aristophanous et al., 2016). However, VMAT is an even more complex delivery technique than IMRT (Chapter 2). In order to create a satisfactory dose plan with a single arc, it is necessary to optimise the field shapes and beam intensities for a large number of gantry angles (so-called control points). Where necessary Velindre Cancer Centre plans with 2 arcs – one with clockwise and the other with anticlockwise rotation. Hence, a robust system of patient dosimetric QA using EPIDs, needs to be available for the verification.

Most dosimetric investigations to date have been undertaken using the aSi-EPID imager in an 'integrating' acquisition mode (as for IMRT), where the image signal is integrated over an entire irradiation to produce a single dosimetric image (Van Esch et al., 2004, Iori et al., 2010, Blake et al., 2014, Bawazeer et al., 2017). More recent studies have examined the potential dosimetric characteristics of the aSi-EPID imager operated in 'cine' acquisition mode (continuous mode) where the image signal is read out electronically throughout an irradiation to produce a series of images (Ansbacher et al., 2010, Rowshanfarzad et al., 2011, 2012, Bawazeer et al., 2016).

Similar to the 'traditional' EPID-based IMRT QA, VMAT QA techniques verify MLC positions as a function of delivered MU directly or by a pixel intensity-based comparison. It has been noted that EPID-based pre-treatment QA for VMAT could be more effective if the gantry angle were also routinely recorded, along with the MLC position and delivered MU. However, by design, the gantry angle rotation cannot be detected by the EPID due to its fixed position on the gantry. A straightforward solution is to apply a recorded gantry angle provided by the linac vendor in the DICOM header of the cine images. However, this has been shown to give poor precision for some vendors' systems (Ansbacher et al., 2010). The application of an inclinometer has also been utilised to verify gantry angle rotation. It has the advantage of providing an independent measurement of gantry angle, although it requires synchronisation with the linac and/or the acquired EPID images, and the inclinometer also may be subjected to time delay and inertia²⁹ effects from the moving gantry (Barnes et al., 2016). A previous review has discussed some difficulties associated with using an EPID for VMAT pre-treatment verification (Greer, 2013).

First, there is the effect of EPID 'sagging' or 'flexing' during an arc. The detector panel experiences gravitational sagging as a function of gantry angle and this causes displacement of the acquired frames from each other, with subsequent blurring of the integrated dose. Rowshanfarzad et al. (2012) used a marker placed at the isocentre and corrected for marker

²⁹ Inertia - is the resistance of any physical object to any change in its state of motion (including a change in direction). In other words, it is the tendency of objects to keep moving in a straight line at constant linear velocity.

displacement during the arc rotation. They found that the reproducibility of the sag pattern in a Varian EPID system is linac dependent. The sag was more pronounced in the in-line direction (approximately 1mm) compared to the crossline direction (approximately 0.5mm). The use of an additional holding device to clamp the mounting accessory, which held the EPID in position during rotation, was a physical approach developed by Iori et al. (2010). They have been able to limit the EPID sag to less than 1mm with this device. However, no investigation of EPID sagging was done during the course of this work due to time limitations, hence this must be taken into account when verifying VMAT for clinical use.

A second issue cited by Greer (2013) is the use of cine mode image acquisition, which is required in order to verify dose as a function of gantry angle for VMAT delivery. In cine mode, individual images are acquired continuously during treatment delivery. In contrast, the standard 'integrated' image aggregates the dose information from all gantry angles into one image and therefore cannot fully validate the delivery. Several studies have examined cine-mode image acquisition using different EPID systems. For example, Piermattei et al. (2009) investigated cine-mode for the IAS2 system³⁰ with a 0.6Hz acquisition rate and found that imaging with a low dose-rate (of 100MUmin⁻¹) gave good signal stability of $\pm 1\%$ over a period of 3 months. McCurdy and Greer (2009) compared the use of cine-mode of the IAS3 system³¹ (7.5Hz) against integrated mode in terms of dosimetric performance. This approach allowed discarded frames due to loss of beam signal or beam-off to be identified and, at the same time,

³⁰ IAS2 – an Image Acquisition Software for Varian aSi500 Electronic Portal Imaging Device (EPID)

³¹ IAS3 – an Image Acquisition Software for Varian aSi1000 Electronic Portal Imaging Device (EPID)

reduced memory overflow problems during delivery. However, it has been demonstrated (Ansbacher et al., 2010, McCowan et al., 2017) that gantry angle uncertainty during rotation related to images acquired with a Varian aSi-EPID typically exceeds the tolerance of 1° specified by the AAPM TG142 report (Klein et al., 2009).

Thirdly, banding artefacts may be evident due to different rows of the imager being read out at slightly different times (Woodruff and Greer, 2013). Each row can therefore integrate different numbers of beam pulses depending on when the pulses are dropped. As the rows also are read out in batches, with each batch read out simultaneously, the solution to minimising the artefacts is to average the multiple frames for the angles subtended by each of the cine-mode EPID images. However, known drawbacks are the effect of dose averaging on those frames with degradation of the portal image quality (Hansjoerg et al., 2010) and a decrease in the EPID's angular resolution (McCowan and McCurdy, 2016).

6.1.2 Rationale of Dosimetry Check use in VMAT verification

A number of studies have reported the use of Dosimetry Check software for the pre-treatment verification of VMAT techniques (Pinkerton et al., 2010, Greer, 2013, Villaggi, 2016, McCowan et al., 2017), but there are very few reports on 'in vivo' dosimetry (Reilly, 2016b, Villaggi, 2016). Therefore, in this work, the investigation of the use of Dosimetry Check in VMAT is intended to complement and improve on the current pre-treatment verification methods available.

6.1.3 Methods

The fact that the acquisition modes (continuous or integrated) work in a different way for portal dosimetry verification, necessarily means that the Dosimetry Check software also works differently for each case. Hence, certain preliminary investigations must be carried out beforehand on (a) the Dosimetry Check dose response with different dose rates and different Monitor Units (MUs) in continuous mode, (b) the difference (if any) between continuous and integrated images and (c) the appropriate calibration method to be used in Dosimetry Check for the cine images. The EPID was set at 150cm SDD for all measurements unless stated otherwise.

6.1.3.1 Dosimetry Check dose response against Monitor Units and dose rate in continuous mode

The linearity of Dosimetry Check dose response against MU delivered at different dose rates in continuous mode was investigated by acquiring images with a static field size of 10x10cm². A series of images were obtained with totals of 25, 50, 100, 300 and 600 MU delivered. All calibrations and irradiations were carried out at dose rates of 300MUmin⁻¹ and 600MUmin⁻¹.

Images were exported to Dosimetry Check to obtain the measured dose calculated by the software. This test did not look at dose difference or agreement between OMP and Dosimetry Check as generated in the Dosimetry Check report. The focus was on the linearity of dose response by Dosimetry Check when conditions were varied in terms of dose rate and the total MU delivered.

Further analysis was made to evaluate the number of acquired cine images in each MU delivery with different dose rates and a constant frame acquisition rate (~ 9.57 frames per second). In order to calculate 'missing' images, the number of acquired images in each MU delivery was subtracted from the expected number of acquired images. The expected number of acquired images was directly taken from the linac service mode with the same delivery set up, on the assumption that service mode operation gave the true number of images in proportion to total MU increment.

6.1.3.2 Reproducibility of dose in continuous mode

Dose reproducibility in continuous mode was also investigated. Several evaluation points were set on a $10 \times 10 \text{cm}^2$ field size, the dose calculated using OMP TPS (Figure 6.1) and exported to Dosimetry Check. Multiple images were acquired in continuous mode for 300 and 600MU exposures at dose rates of 300MUmin^{-1} and 600MUmin^{-1} . The difference between dose measured by Dosimetry Check at 600MUmin^{-1} relative to dose measured by Dosimetry Check at 300MUmin^{-1} was calculated for each delivery.

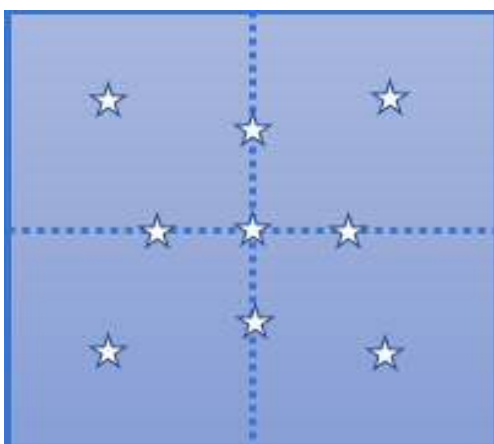


Figure 6.1 - Points of interest (POI) set up in TPS on a $10 \times 10 \text{cm}^2$ square field size to calculate the difference in dose measured by Dosimetry Check for software reproducibility

6.1.3.2.1 Results and discussion

Figure 6.2 shows Dosimetry Check dose response per MU delivered for the two dose rates (300MUmin^{-1} and 600MUmin^{-1}). Linearity is clearly seen for integrated mode across the total MU delivered with dose difference between the dose rates consistently close to zero. However, for continuous mode (Figure 6.3), about 4% dose difference was observed at higher monitor units (600MU) between the two dose rates with a slight under-response of 0.04cGy/MU at 600MU for a delivery rate of 600MUmin^{-1} compared to 300MUmin^{-1} . This is probably due to loss of Relative Monitor Unit (RMU) fluence signal resulting from some missing images or frames during irradiation in continuous mode at higher MU ($\sim 600\text{MU}$ in this case). However, at lower MUs ($<50\text{MU}$ in this case), the dose difference was around 1.7%. This was due to the fact that fewer frames were acquired in total by the IAS3 image acquisition system. Hence, a slight dose discrepancy was observed as the result of the frame averaging effect.

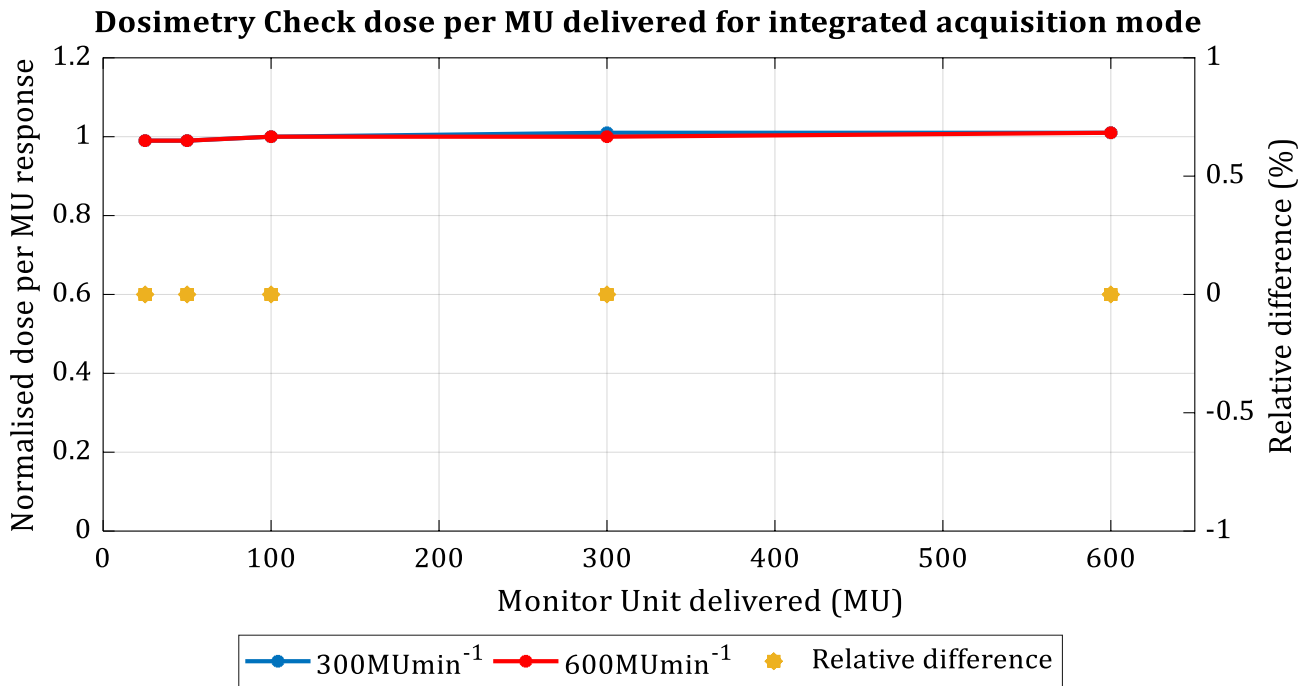


Figure 6.2 – Dosimetry Check dose response per MU delivered as a function of total MU and dose rate for the integrated acquisition mode showing nearly 0% difference between the two dose rates. Dose responses were normalised at 100MU.

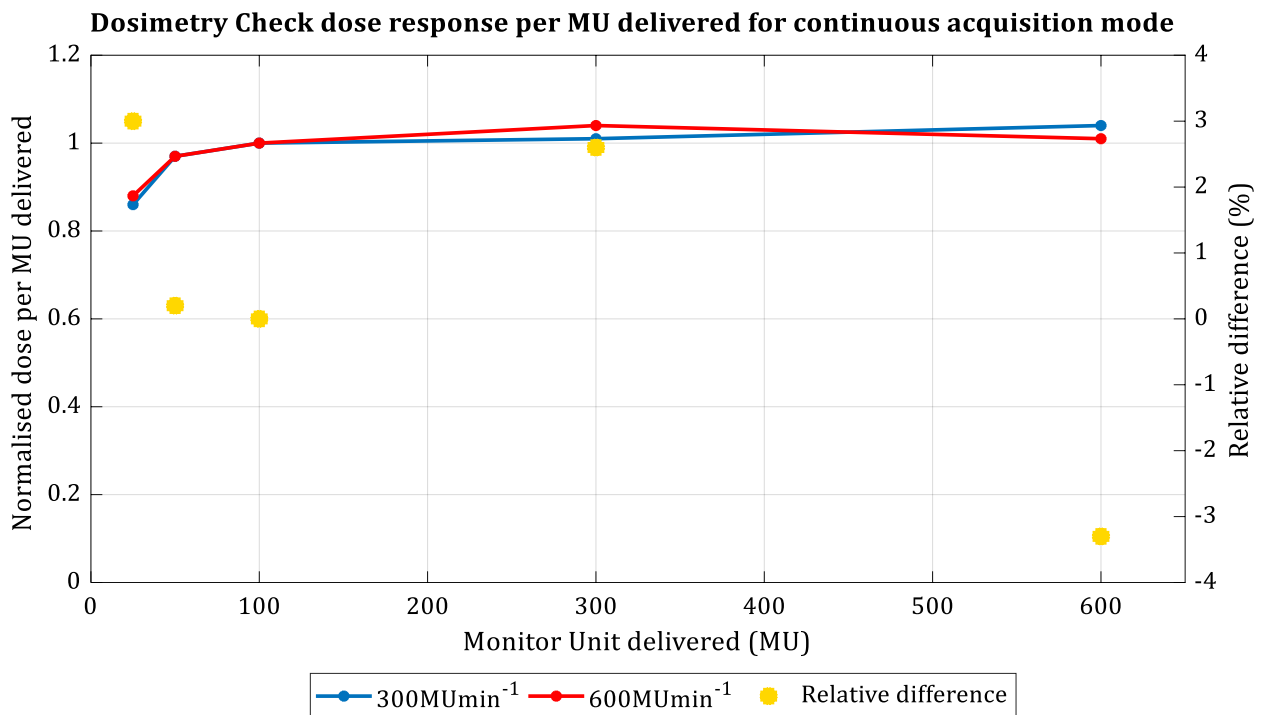


Figure 6.3 - Dosimetry Check dose response per MU delivered as a function of total MU and dose rate for the continuous acquisition mode. Dose responses were normalised at 100MU.

The corresponding number of images generated in continuous acquisition as a function of MU delivery is shown in Table 6.1 for 300MUmin⁻¹ and 600MUmin⁻¹ dose rates. For values of total MU up to 300, it was found that the number of EPID images recorded in each delivery was the same as the number of expected cine images in that delivery. However, the number of acquired images decreased at 600MU delivery, with 1 image and 7 images being lost during acquisition for 300 and 600MUmin⁻¹ dose rates respectively. This effect was believed (and subsequently confirmed by the vendor) to be the result of a loss of communication in continuous mode. This is because, in continuous mode, the image can be captured between beam pulses. Therefore, if pulses are dropped with dynamic treatments, the IAS3 loses its synchronisation with the linac pulses. In this case, the acquisition can drop images before capturing images again. Physically, the array of TFTs which are embedded inside the aS1000 EPID panel were rapidly integrating the resulting charges and caused the desynchronization.

Table 6.1 - Number of acquired images in continuous mode irradiation for a clinical setting compared to number of images acquired in service mode (true value).

Total MU delivered	300MU/min (images)		600MU/min (images)	
	Service Mode	Clinical Mode	Service Mode	Clinical Mode
25	4	4	4	4
50	16	16	9	9
100	33	33	18	18
300	100	100	56	56
600	200	199	112	105
Difference	200-199 = 1 image		112-105 = 7 images	

Results of the comparison of point doses assessed by Dosimetry Check in continuous mode acquisition for 600MU delivered are tabulated in Table 6.2 (a). On average, there was a dose difference of 4.7% obtained between the two delivery dose rates. The results confirmed the non-linearity of dose response at higher MU (600MU) (Figure 6.3). However, for delivery at lower MU (300MU), good agreement was obtained with an average dose difference between the dose rates less than 2% (Table 6.2 (b)).

Table 6.2 - (a) Comparison between dose generated by Dosimetry Check for 600MU 10x10cm² square field in continuous mode. (b) Comparison between dose generated by Dosimetry Check for 300MU 10x10cm² square field in continuous mode.

(a) No. of points	Coordinates in field	Dosimetry Check dose (cGy)		Percentage difference (%)
		300MU/min	600MU/min	
1	(0, 0, 0)	501.1	478.7	-4.68
2	(0, 2, 0)	499.8	476.9	-4.80
3	(2, 0, 0)	502.4	480.0	-4.67
4	(0, -2, 0)	505.9	483.1	-4.72
5	(-2, 0, 0)	502.2	479.9	-4.65
6	(-3.8, 3.8, 0)	475.1	453.5	-4.76
7	(3.8, 3.8, 0)	475.9	454.2	-4.78
8	(3.8, -3.8, 0)	487.1	464.9	-4.78
9	(-3.8, -3.8, 0)	485.1	463.1	-4.75
(a) Average σ				-4.73 0.06
(b) No. of points	Coordinates in field	Dosimetry Check dose (cGy)		Percentage difference (%)
		300MU/min	600MU/min	
1	(0, 0, 0)	243.4	246.6	1.30
2	(0, 2, 0)	250.6	246.0	1.87
3	(2, 0, 0)	244.2	247.3	1.25
4	(0, -2, 0)	245.6	248.6	1.21
5	(-2, 0, 0)	244.2	247.3	1.25
6	(-3.8, 3.8, 0)	232.0	235.0	1.28
7	(3.8, 3.8, 0)	232.5	235.4	1.23
8	(3.8, -3.8, 0)	237.5	240.2	1.12
9	(-3.8, -3.8, 0)	236.6	239.4	1.17
(b) Average σ				1.33 0.22

6.1.3.3 Calibration method used in Dosimetry Check for continuous mode verification

From the results obtained so far, it is apparent that there is the possibility of some loss of accuracy when images are acquired for extended periods (~1min) or when dose is delivered at a high rate. With Dosimetry Check, a single image produced by an integrated mode is calibrated or normalised by using a standard 10x10cm² field size image acquired in the same mode. Similarly, calibration of continuous images (e.g. for VMAT fields) with Dosimetry Check should be performed with set of standard 10x10cm² images acquired in continuous mode. As explained previously, there is the possibility of inaccuracy in continuous mode due to loss of image frames. When this happens, there will be some discrepancy between the dose measured by Dosimetry Check and that calculated by the OMP TPS.

Hence, a calibration method was developed and used for the rest of the VMAT verification investigations with Dosimetry Check. To begin with, images were acquired for a 10x10cm² field delivered through a 360° arc from -180° to 180° with a total 600MU at each dose rate (300MUmin⁻¹ and 600MUmin⁻¹), and the images exported to Dosimetry Check. Then, the cine images from the arc were calibrated with a set of images for a 10x10cm² field at 100MU also acquired in continuous mode. For comparison, the same arc was also calibrated against images for a 10x10cm² field at 100MU acquired in integrated mode. Doses recorded by Dosimetry Check were investigated for any significant discrepancies. When a discrepancy or image loss was identified, a correction step in the calibration method (3rd calibration option available in Dosimetry Check) was needed for continuous acquisition. Determination of the

correction factor involved calibrating the continuous arc images with the result of integration of these arc images into a single image.

6.1.3.3.1 Results and discussion

As illustrated in Figure 6.4, VMAT dose using continuous images acquired with 600MU gave good agreement between Dosimetry Check and OMP when calibrated with cine images at 300MUmin⁻¹. Differences at the isocentre were less than 1%. On the other hand, Figure 6.5 shows that the percentage difference between OMP and Dosimetry Check dose was somewhat greater, especially at the isocentre (~1.5%) for 600MU at 600MUmin⁻¹. This was due to some loss of radiation dose through missing frames or images. However, when a single integrated image of an arc was used as the calibration file, the agreement was excellent (less than 1% at isocentre) as illustrated in Figure 6.6. Dosimetry Check incorporates the correction using this method by computing a single correction factor, let us say k , as a ratio for all pixels (which have ≥ 0.25 of the maximum pixel value in each image), of the measured dose and the value from the sum of continuous images at the same pixel location. The average k ratio is then computed and taken as the correction factor.

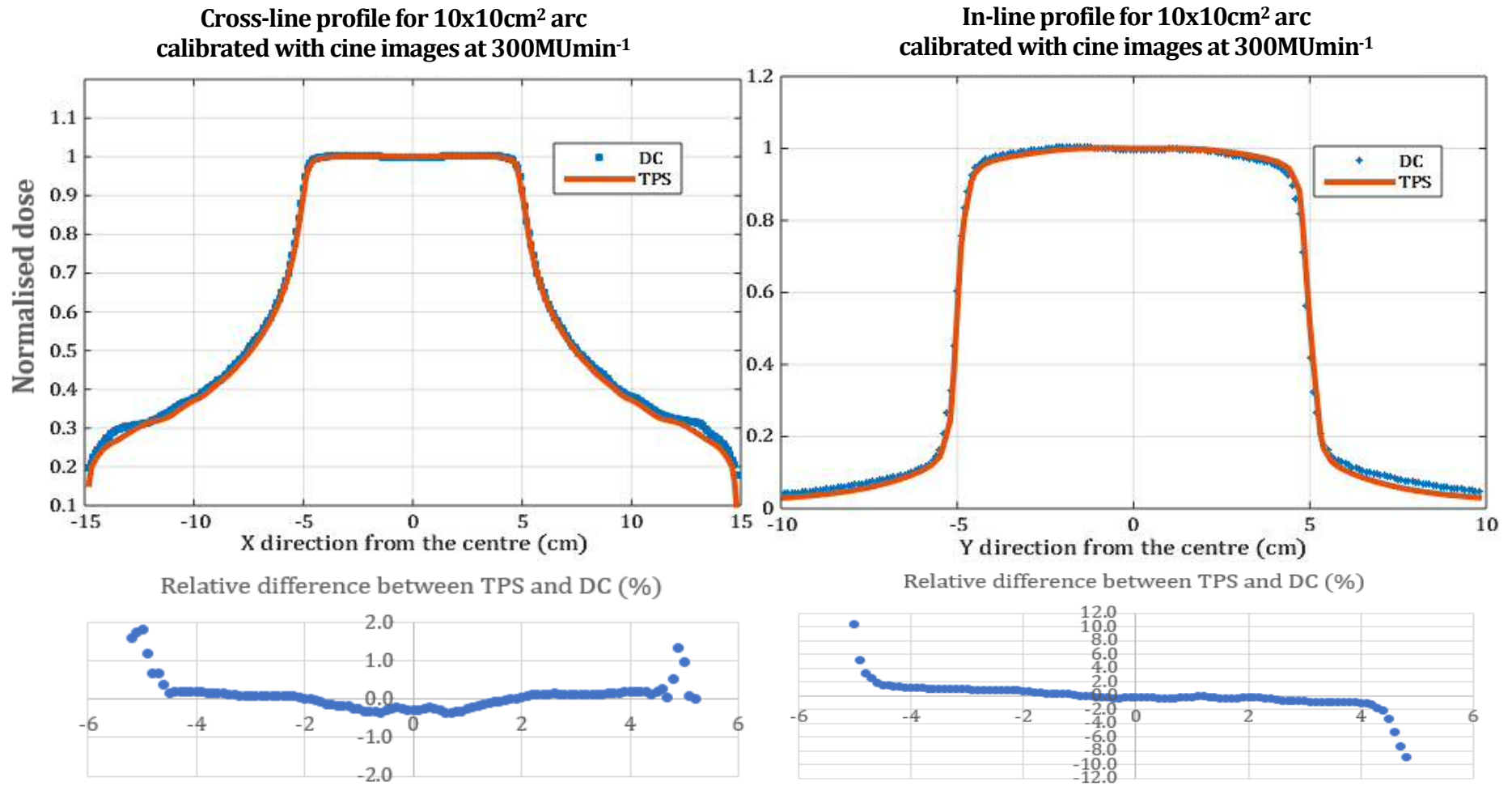


Figure 6.4 - Dose profiles in the cross-line and in-line directions for a 10x10cm² arc irradiated at 600MU and calibrated at 300MUmin⁻¹ with their respective percentage difference (within $\pm 1\%$ in high dose region).

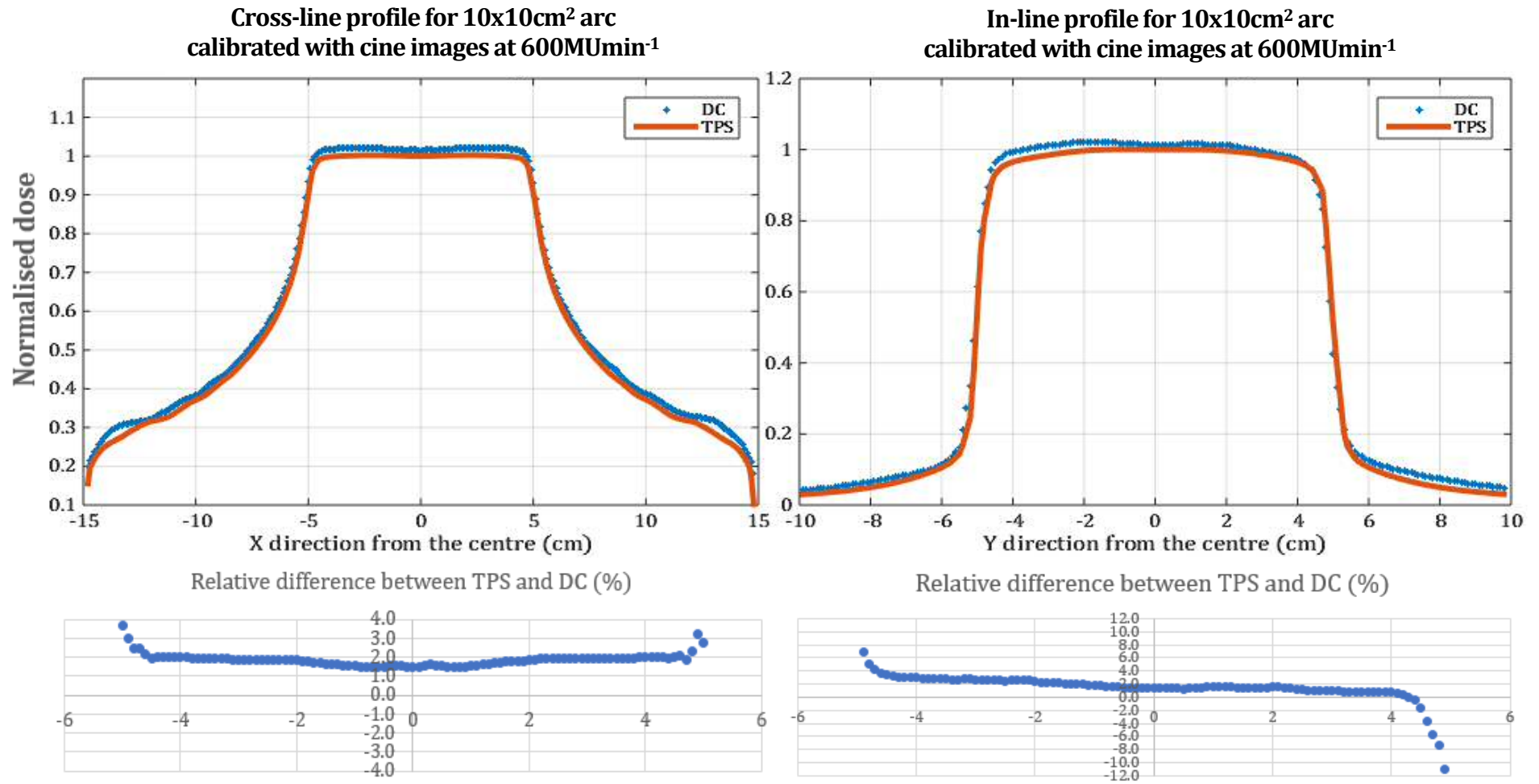


Figure 6.5 - Dose profiles in the cross-line and in-line directions for a 10x10cm² arc irradiated at 600MU and calibrated at 600MUmin⁻¹ with their respective percentage difference (mostly greater than 1.5% in high dose region).

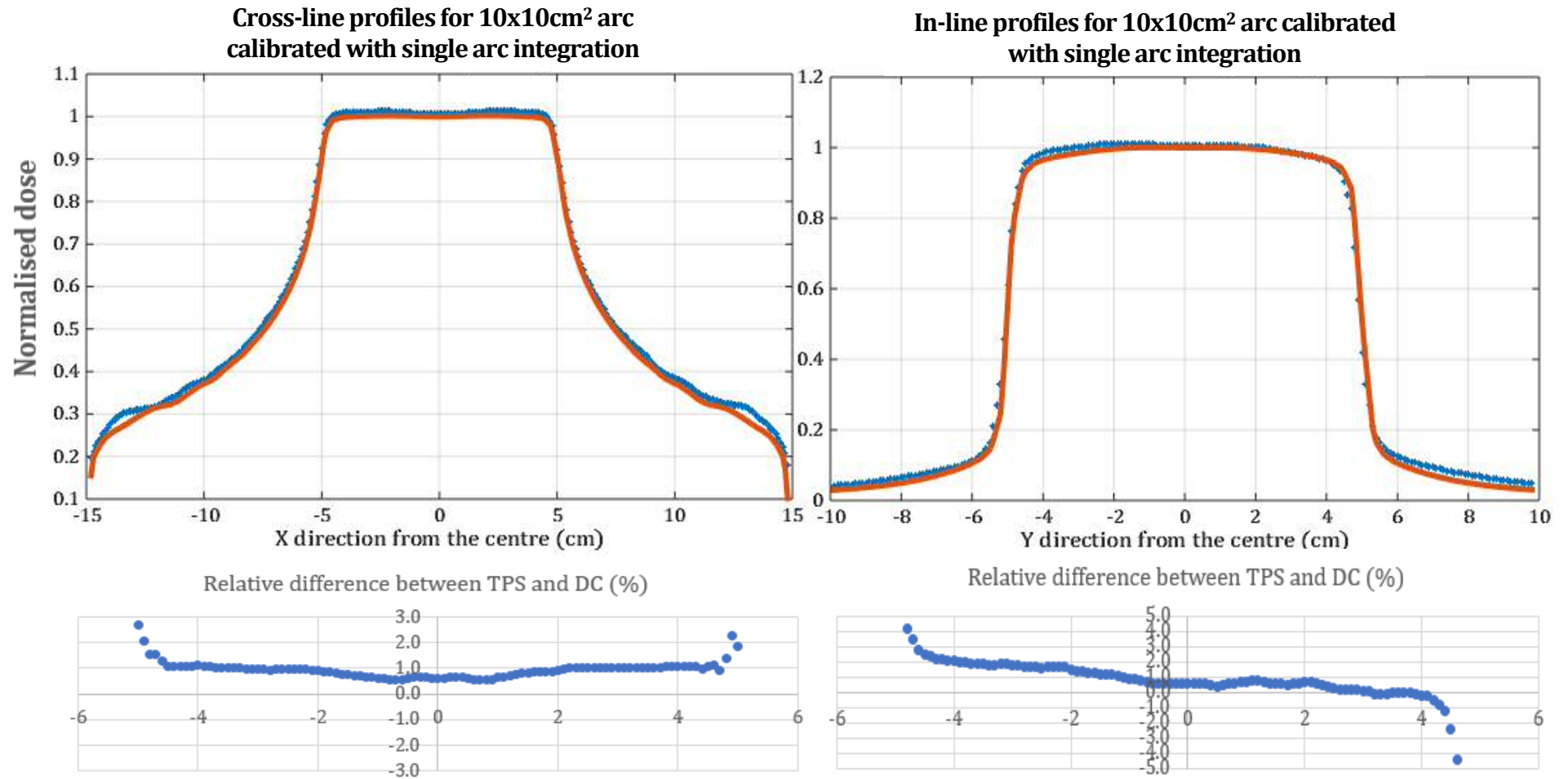


Figure 6.6 - Dose profiles in the cross-line and in-line directions for a 10x10cm² arc irradiated at 600MU and calibrated with a single image produced by the integration of an arc with their respective percentage difference (within 2% in most high dose region).

6.1.4 Introduction of backscatter correction into the VMAT technique

This section describes the incorporation of correction for backscatter from the linac robotic arm in VMAT using the key correction matrix that was investigated in Chapter 5.

6.1.4.1 Methods

The implementation of the correction matrix (M4) with VMAT treatment delivery was investigated with some basic arcs (with field sizes $10 \times 10 \text{cm}^2$ and $5 \times 18 \text{cm}^2$) and a water phantom. Images for both arcs were acquired for 300MU at a dose rate of 300MUmin^{-1} . The same approach as before (Matlab script) was used to obtain a set of corrected cine images by multiplying the M4 matrix with the set of raw EPID cine images (see example in Figure 6.7). Data were analysed for beam profiles across the Y-axis before and after the application of the correction.

```
dirName=cd('Y:DICOM images\VMAT images\Arc10x10_600MU');
dcmfiles=dir (fullfile(dirName, '*dcm'));
resultsVMAT='Y:\DICOM images\VMAT images\Arc10x10_600MU\RI_VMAT10x10_correction';

for j=1: length(dcmfiles);
    files=dcmfiles(j).name;
    fulldcm=fullfile(dirName,files);

    %Read and rescale the original image to obtain the meaningful data
    Arc1=(double(dicomread(fulldcm)));
    Inf1=dicominfo (fulldcm, 'dictionary','dicom-dict-mod2.txt');
    Arc1dat=inf1.RescaleIntercept+inf1.RescaleSlope. *Arc1;

    %%Apply M4 correction matrix to the rescaled values to obtain the
    %%corresponding pixel values
    Arc1newdat=Arc1dat.*(M4);
    Arc1newat=uint16((Arc1newdat-inf1.RescaleIntercept). /(inf1.RescaleSlope));

    %%write new corrected image as DICOM file and display new corrected image
    dicomwrite (Arc1newdat,[resultsVMAT,num2str(j), '.dcm'],inf1, 'CreateMode',
'copy');
end;
```

Figure 6.7 - Example of coding in Matlab script used to obtain a set of corrected cine images.

6.1.4.1 Results and discussion

Figure 6.8 and Figure 6.9 show that the backscatter effect was reduced by an average of approximately 2% from the centre of Y-axis to the left edge of the beam for both the 10x10cm² arc and the 5x18cm² arc. With the correction applied, agreement between TPS and Dosimetry Check dose improved from an average of $\approx 2.4\%$ to $\approx 0.4\%$ for the 10x10cm² arc and from an average of $\approx 2.5\%$ to $\approx 0.1\%$ for the 5x18cm² arc. This demonstrates that the method of correction is appropriate to be used for VMAT verification using Dosimetry Check.

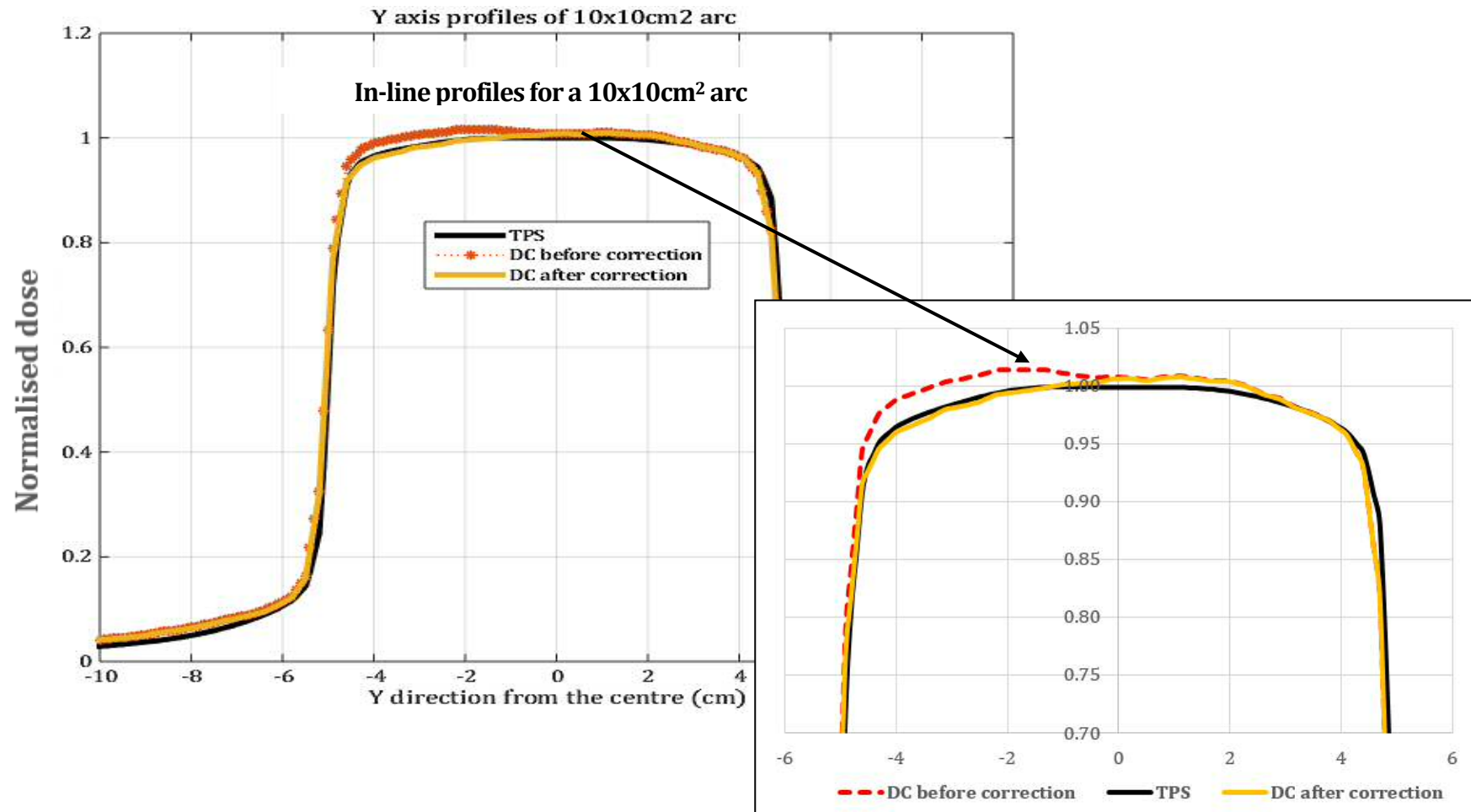


Figure 6.8 - Y-axis profiles of TPS (*black bold line*) and Dosimetry Check dose before and after correction for a 10x10cm² arc. The Dosimetry Check dose profile before correction (*red dotted line*) shows the effect of backscatter from the linac arm on the left. The backscatter is improved after correction (*yellow bold line*). The profiles are normalised to the TPS central axis dose. A zoomed plot is also shown for clarity.

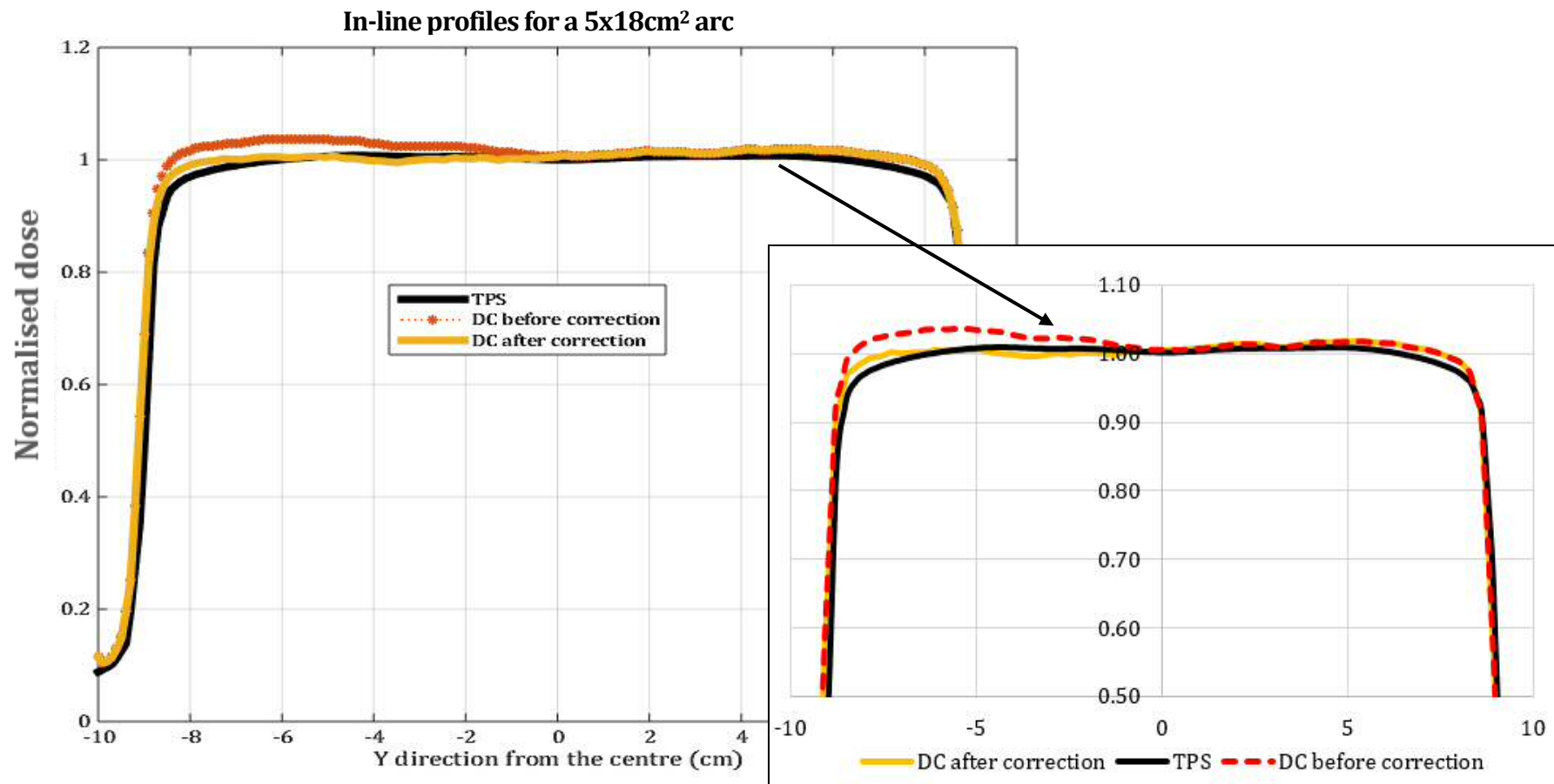


Figure 6.9 - Y-axis profiles of TPS (*black bold line*) and Dosimetry Check dose before and after correction for a 5x18cm² arc. The Dosimetry Check dose profile before correction (*red dotted line*) shows the effect of backscatter from the linac arm on the left. The backscatter is improved after correction (*yellow bold line*). The profiles are normalised to the TPS central axis dose. A zoomed plot is also shown for clarity.

6.2 CASE STUDY: VMAT HEAD-AND-NECK PRE-TREATMENT VERIFICATION

The feasibility of applying the backscatter correction matrix method to a clinical VMAT plan was investigated with the expectation of improving the accuracy of verification using Dosimetry Check. Gamma evaluation was also included in the analysis of this plan.

6.2.1 Methods

The same Head-and-Neck plan as discussed previously (in Chapter 5) was used after re-planning for VMAT delivery with the same linac (LA5). The plan was re-optimised and calculated in OMP with a cylindrical Head-and-Neck phantom (Figure 6.10 (a)). The calculation dose grid was set to be 0.3cm (similar to the situation previously discussed in Chapter 5). Due to the fact that the cylindrical Head-and-Neck phantom was too short to cover the whole VMAT beam from the superior to inferior edge (Figure 6.10 (b)), the phantom was shifted 4cm inferiorly. This resulted in the plan extending further than the phantom superiorly, but the inferior region of the beam was the area of interest in order to highlight the effect of the backscatter from the arm. A ROI (Figure 6.10 (c)) was introduced within the external volume of the phantom with a 3cm margin inwards, for the evaluation of a Gamma Volume Histogram during dose reconstruction using Dosimetry Check. The plan was acquired pre-treatment on LA5 and delivered at a 600MUmin^{-1} dose rate.

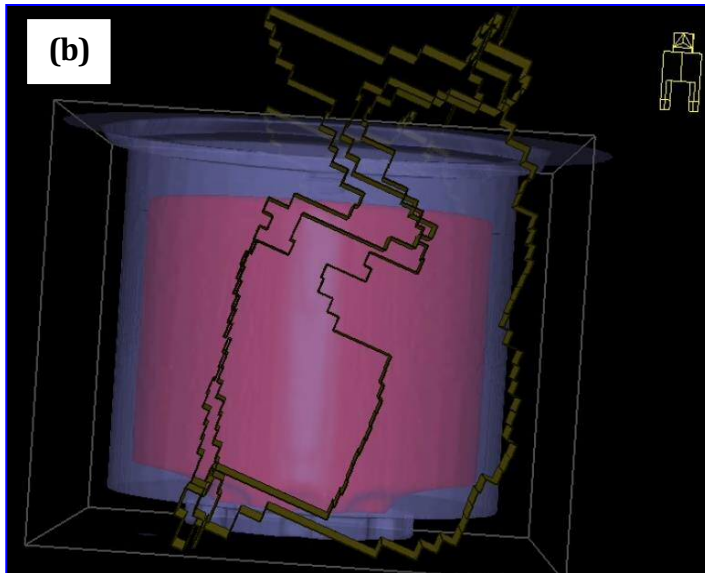
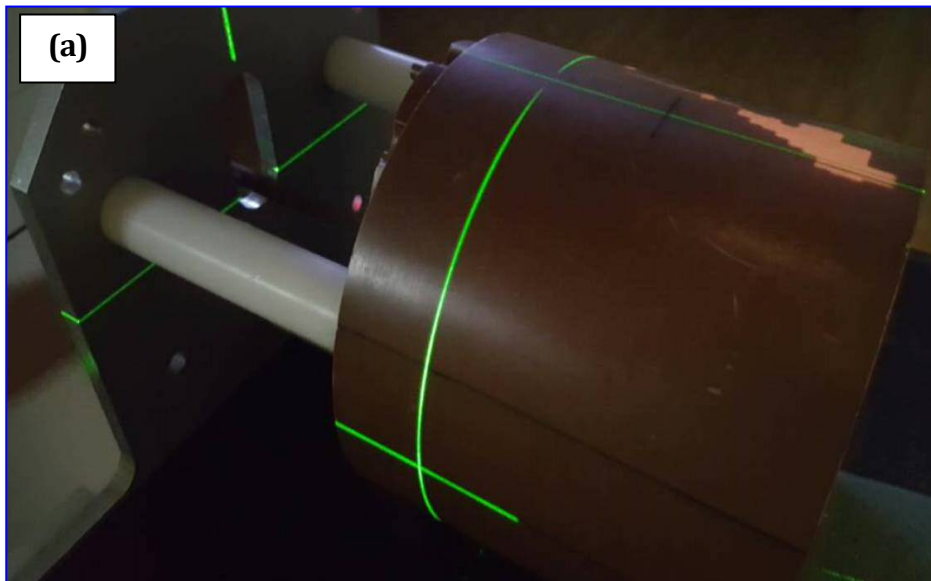
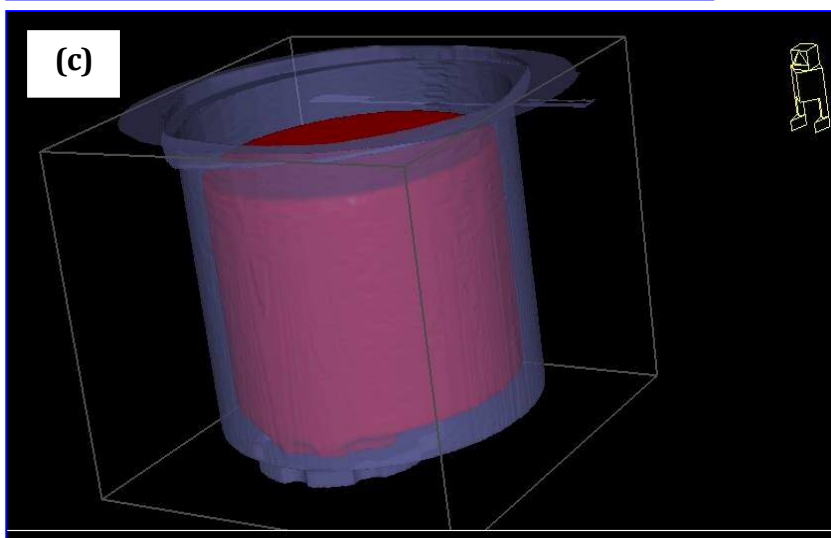


Figure 6.10 – (a) Head and Neck phantom used as the RT structure image in the optimisation process through OMP TPS.

(b) Head and Neck phantom with the VMAT irradiation beams optimised and calculated in OMP TPS.

(c) ROI (*red volume*) created internally within the phantom for the evaluation of GVH during dose reconstruction using Dosimetry Check.



Finally, several aspects of the data obtained before correction and after correction were evaluated:

- i) improvement of the beam profiles along in-line direction (Gantry-Couch),
- ii) pass rate of the gamma criteria 3%/5mm and 3%3mm
- iii) pass rate of Gamma Volume (Chapter 5) for the VMAT pre-treatment plan

6.2.2 Results and discussion

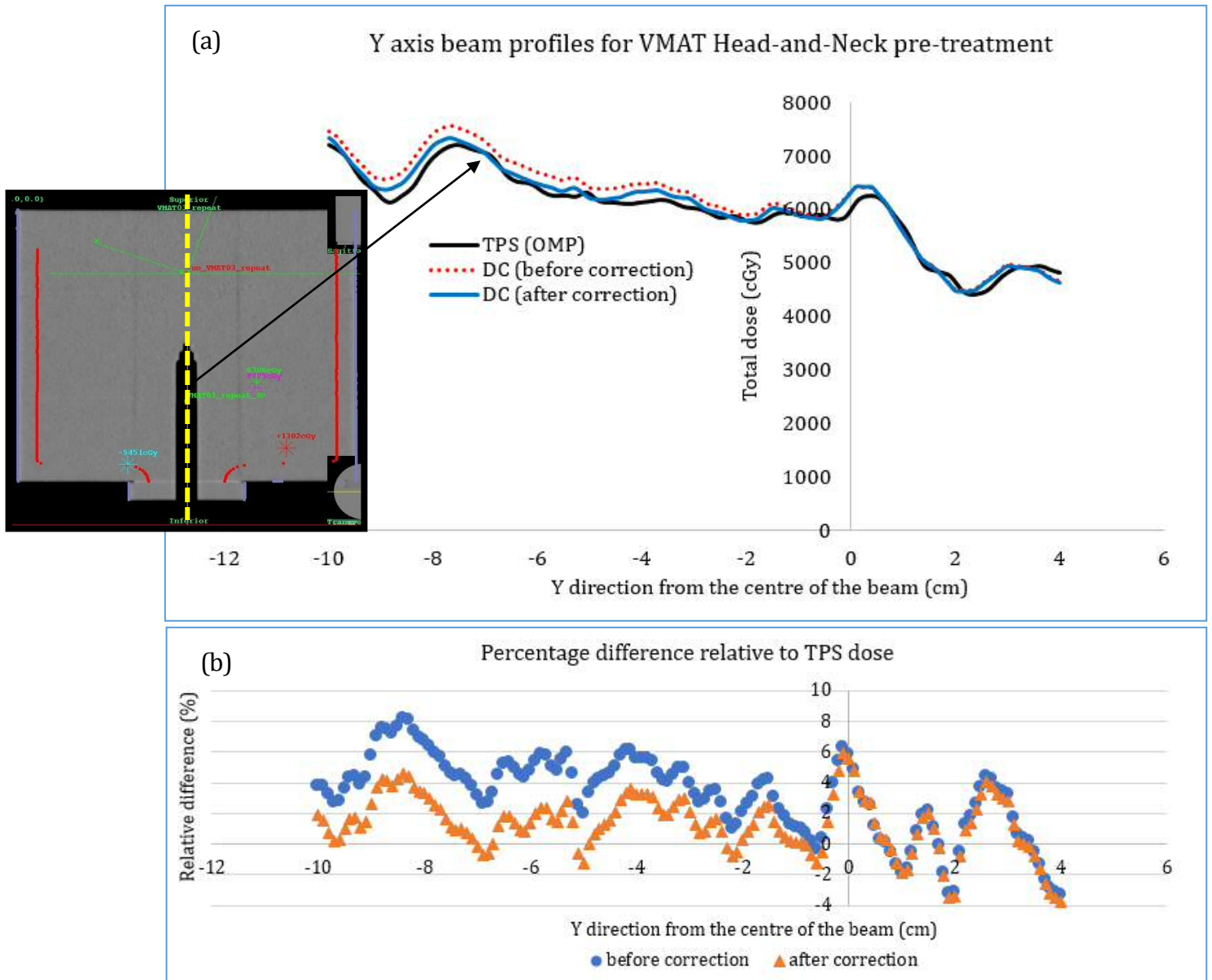


Figure 6.11 - (a) Profiles cut through the Y axis of a coronal plane of the VMAT plan (*yellow dotted line*) before (*red dotted line*) and after correction (*blue bold line*) for backscatter compared with TPS calculated dose (*black bold line*). (b) Correction produced an average reduction of 3% in dose difference (taken from the central axis 0cm to-10cm) relative to TPS dose.

Figure 6.11 shows that the average percentage difference relative to TPS dose improved from 4.2% before correction to around 1.7% after correction. The relative differences were taken from the centre point to the end of inferior part of the coronal view plane (negative values on the X-axis of the graph).

It was found that 95% and 97% of points passed gamma criterion of 3%/5mm for coronal and sagittal planes respectively. Points passing a 3%/3mm criterion were also evaluated and showed a good result with a pass rate of more than 85% for both planes. Gamma Volume for the ROI outlined within the Head-and-Neck phantom also improved from 73% before correction to 87% after correction for a 3%/3mm gamma criterion, and from 89% to 95% for a 3%/5mm criterion. Detailed results are tabulated in Table 6.3 and a pictorial description is presented in Figure 6.12.

Table 6.3 - Tabulated result of points passing the gamma criterion and GVH for a pre-treatment VMAT Head-and-Neck pre-treatment plan.

VMAT Head-and-Neck pre-treatment plane	Gamma criteria pass rate (%)			
	3%/3mm		3%/5mm	
	Before	After	Before	After
Coronal	69.63	86.47	84.33	95.25
Sagittal	75.16	90.02	87.84	97.12
Average	72.40	88.36	86.09	96.19

Gamma criteria	Cumulative Gamma Volume index on ROI	
	Before correction	After correction
3%3mm	72.62%	87.03%
3% 5mm	88.52%	95.42%

CHAPTER 6: APPLICATION OF DOSIMETRY CHECK TO THE VERIFICATION OF VOLUMETRIC MODULATED ARC THERAPY

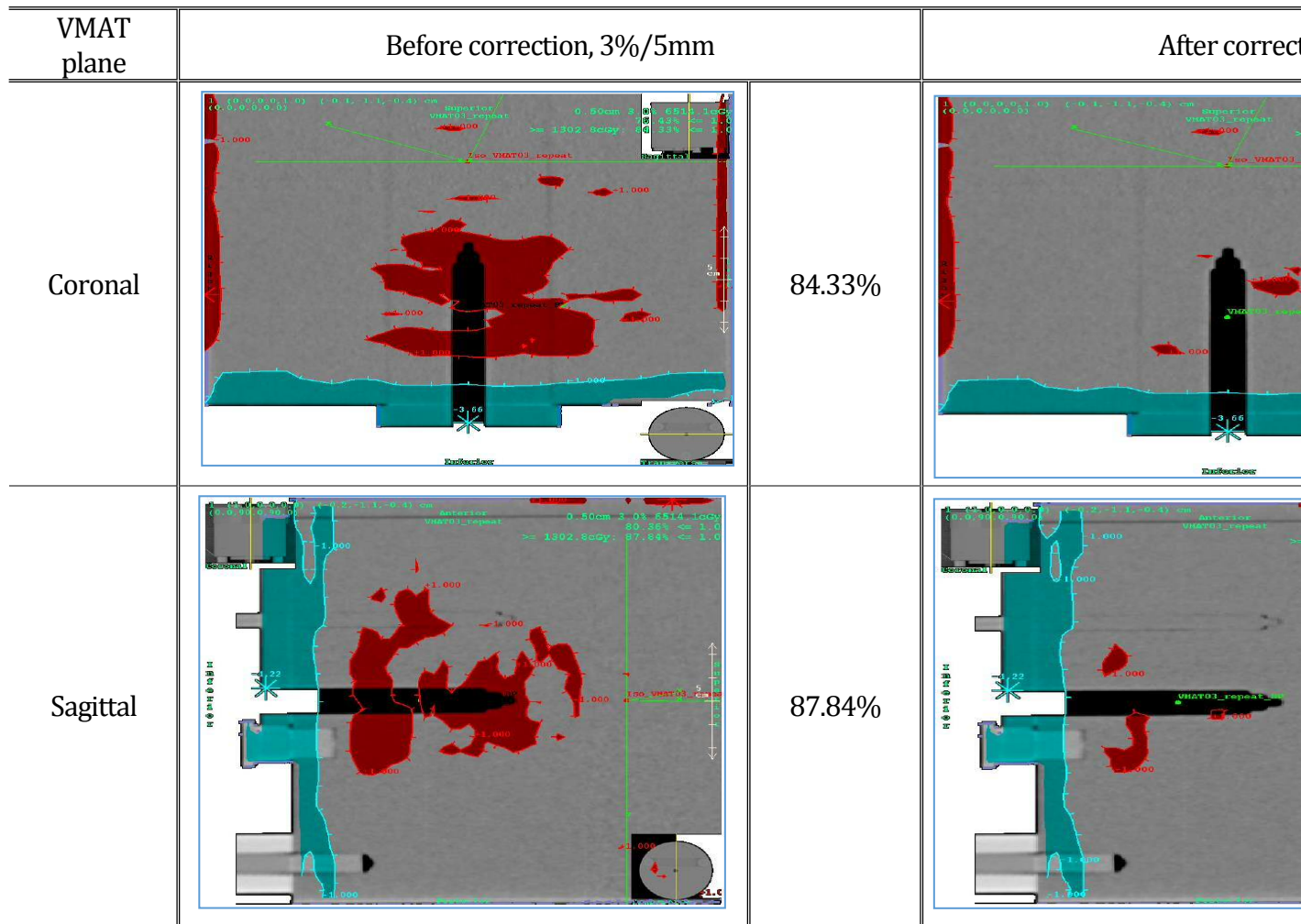


Figure 6.12 - Graphic presentation of 2D gamma evaluation of the pre-treatment Head-and-Neck VMAT plan for regions with failing gamma reconstructed and reported in Dosimetry Check.

The investigation of this correction method demonstrated that it can be applied effectively to improve the accuracy of treatment verification. Although the experiment only verified the case using a water equivalent phantom, it should be a good basis for further investigations leading to patient specific QA verification.

Since VMAT is a very complex type of treatment technique, it is crucial that plans are verified before treatment delivery. Evidently, the improvement in gamma and Gamma Volume pass rate shows that this method would be suitable for enhancement of the existing Dosimetry Check verification system.

6.3 ADAPTIVE ARM BACKSCATTER SOLUTION (ADABS) FOR TREATMENT VERIFICATION USING DOSIMETRY CHECK

From the series of experiments that were carried out to investigate the arm backscatter effect, with extended application to IMRT and VMAT treatment techniques, it was apparent that the correction matrix method was suitable for use to reduce systematic uncertainties due to the effect and promised improved accuracy for the verification system.

To accommodate the future application of this approach and to facilitate its systematic use in the clinic, a more convenient way of routinely applying the correction matrix was explored. This was required because a large number of plans must be verified, and these must be accurate as possible. Hence, to avoid having to utilise a long Matlab-based scripted system external to Dosimetry Check to generate a corrected image for each plan, an alternative solution

step was developed for future use. For simplicity, this is called Adaptive Arm Backscatter Solution (AdABS) from this point onwards.

In Dosimetry Check, there is an option (“**Correct with Flood View**”), which may be used if there is a need to shift the EPID from the central axis for a field measurement. Under these circumstances, a correction for a flood view must be applied to obtain the correct shape of the beam profile relative to the flattening filter. However, there is no EPID shifting involved in this work, and so this facility offers an easy-to-apply method to correct for backscatter from the linac arm that may be applied to all images at the same time.

However, if a measurement requires the EPID to be shifted to an off-set panel position, the same correction should not be applied when “**Correct with Flood View**” is required at the same time. Therefore, a new correction needs to be formulated for the off-set panel position first, then both corrections (flood field and backscatter from the arm) could be combined. The steps involved in the process of converting EPID images to Relative Monitor Units are shown in Figures 6.13 - 6.15 as screen-shots of the Dosimetry Check software.

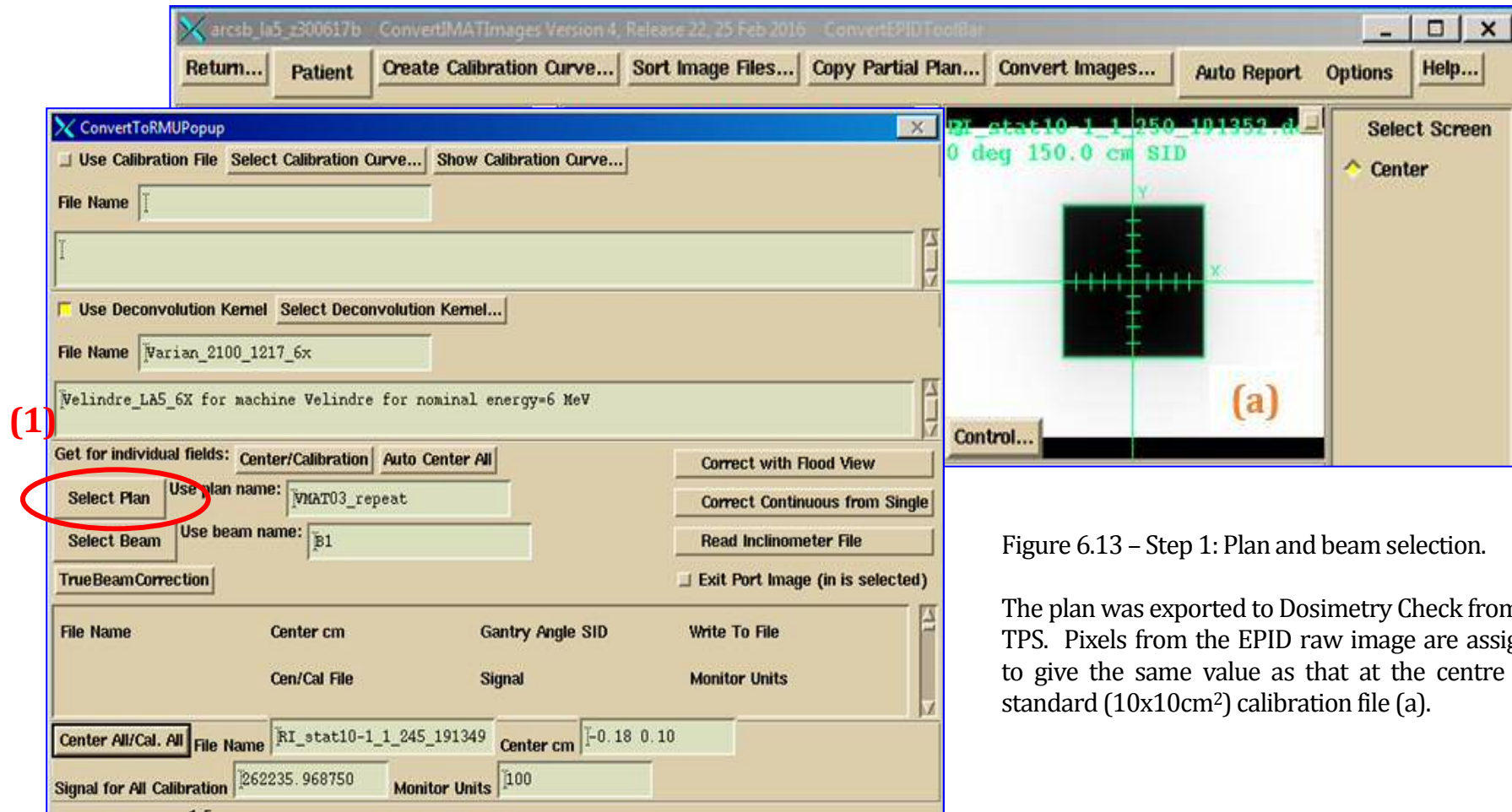


Figure 6.13 – Step 1: Plan and beam selection.

The plan was exported to Dosimetry Check from the TPS. Pixels from the EPID raw image are assigned to give the same value as that at the centre of a standard (10x10cm²) calibration file (a).

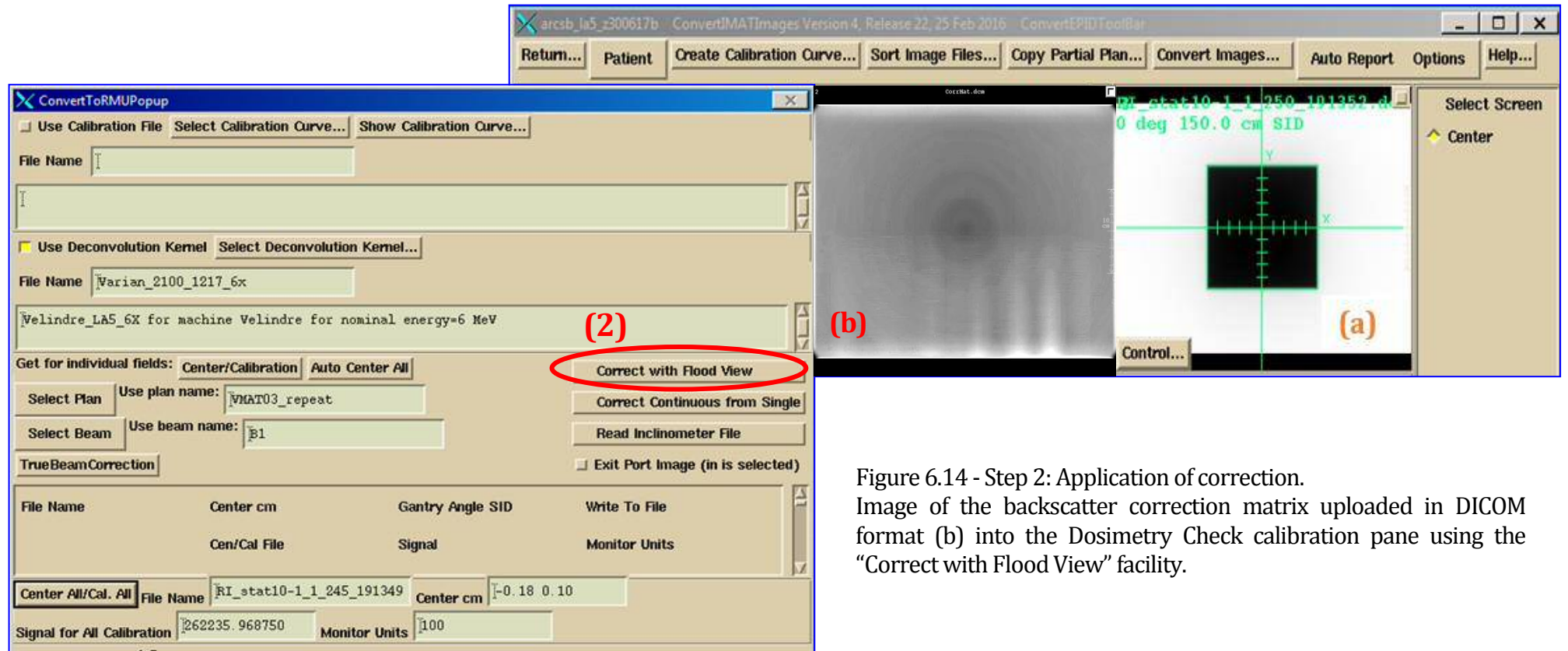


Figure 6.14 - Step 2: Application of correction. Image of the backscatter correction matrix uploaded in DICOM format (b) into the Dosimetry Check calibration pane using the "Correct with Flood View" facility.

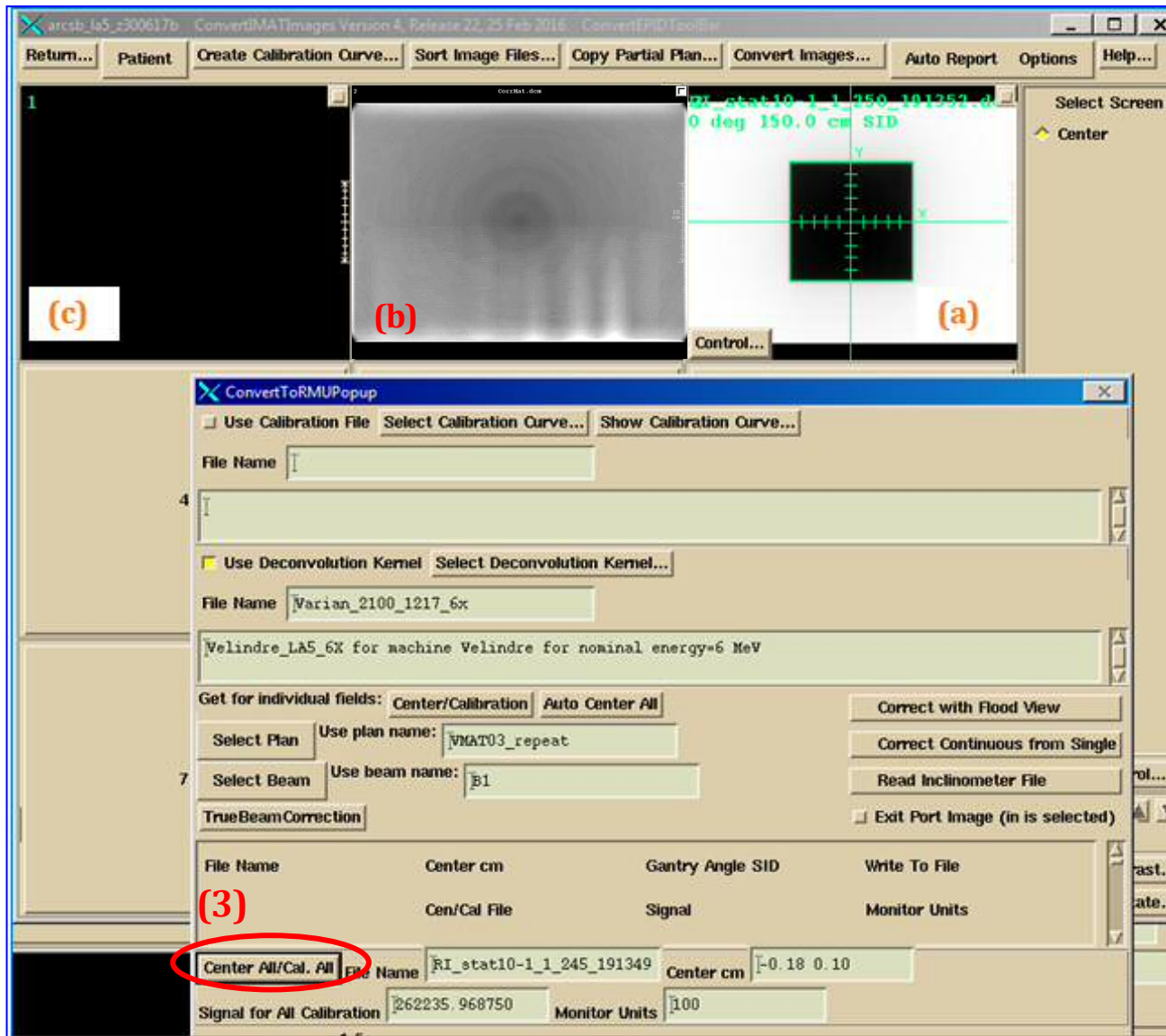


Figure 6.15 - Step 3: Calibration of the image.

Set of calibration images (c) selected to centre all field images (VMAT cine images in this example) with known signal and Monitor Units. Ratio of MU/signal generated as a calibration constant which is automatically applied to all field images.

To assess the effectiveness of the application of AdABS, dose profiles for static fields of $10 \times 10 \text{cm}^2$ and $5 \times 20 \text{cm}^2$ dimension were investigated. TPS profiles were compared with (i) DC profiles without backscatter correction, (ii) Dosimetry Check profiles corrected with the Matlab script and (iii) Dosimetry Check profiles corrected with AdABS. A large field ($20 \times 20 \text{cm}^2$) was also examined in the same way.

6.3.1 Results and discussion

Figure 6.16 shows cross-line beam plots for the two simple fields ($10 \times 10 \text{cm}^2$ and $5 \times 20 \text{cm}^2$). For both fields, profiles corrected for backscatter with the scripted method and with AdABS showed excellent agreement, with percentage differences of less than 1.5% compared to TPS suggesting that AdABS is a feasible correction method that may be applied in the clinic for more accurate treatment verification.

However, the test with a larger $20 \times 20 \text{cm}^2$ field (Figure 6.17), showed an adjustment to the profiles which seems non-beneficial with both the methods applied, although their difference remained at nearly 1%. This demonstrates that the generic correction matrix retains some field dependence as stated previously in Chapter 5. In addition, this effect was not known but yet believed to be part of backscatter related to the cross-line direction, therefore indicating the limitation in the method employed in this work to produce a universal correction for all field sizes. However, in practice, for most of the clinical applications involving advanced radiotherapy, fields much smaller than $20 \times 20 \text{cm}^2$ are involved.

One of the reasons for the difference between script-based correction images and the AdABS application is the effect of acquiring the image matrix from the flat image in DICOM format using Matlab. The flat image is derived from the normalisation of a flood image with itself. The easiest way to mitigate this effect is to apply the matrix correction directly to the flood field image rather than the flat image, so that the profile shape can be retained.

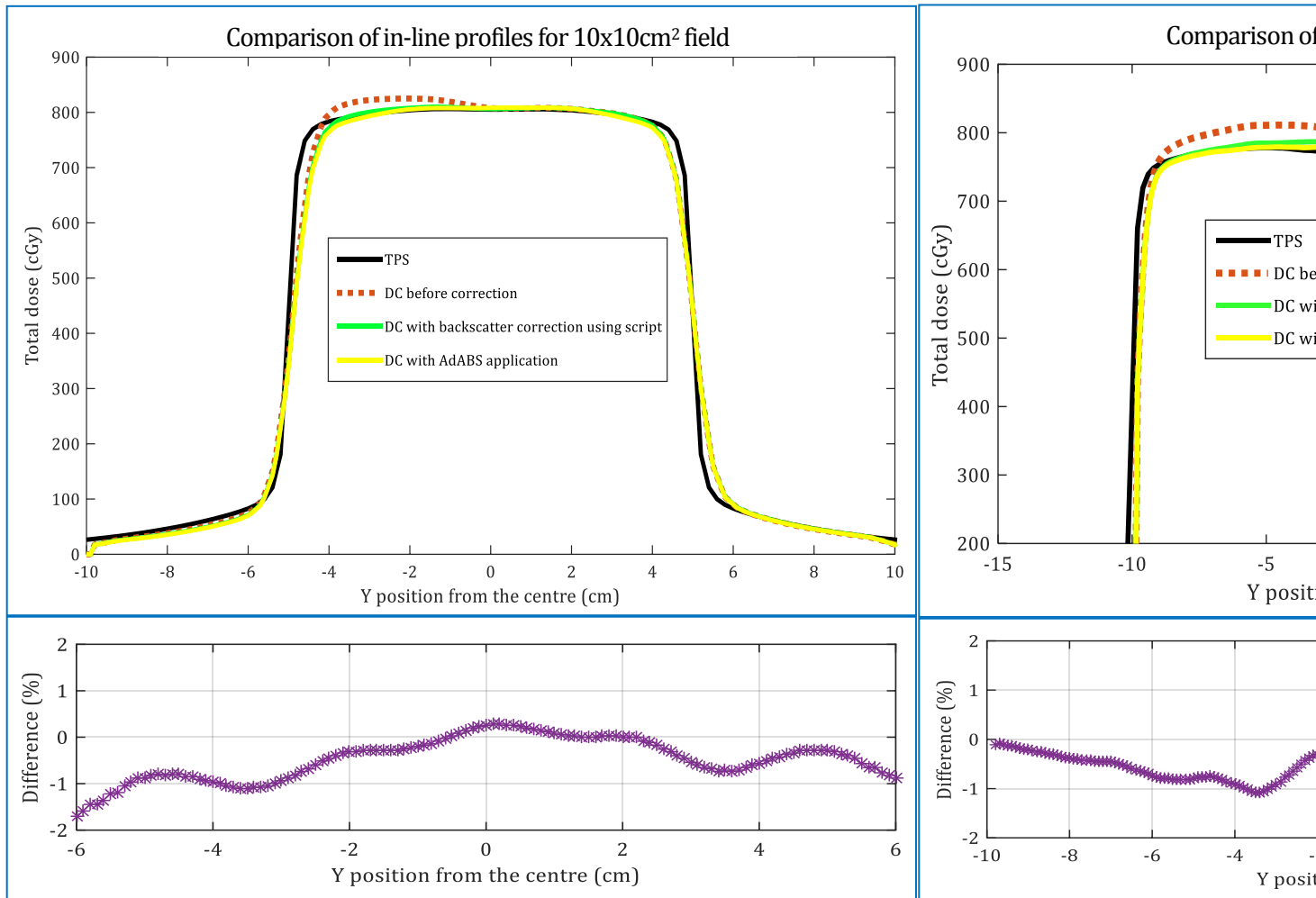


Figure 6.16 - Comparison of in-line profiles for simple fields (10x10cm² and 5x20cm²) before correction (red dashed line), backscatter correction using script (green bold line) and AdABS (yellow bold line). Black dashed line is the TPS dose. Good agreement is achieved with the correction methods (purple dotted line).

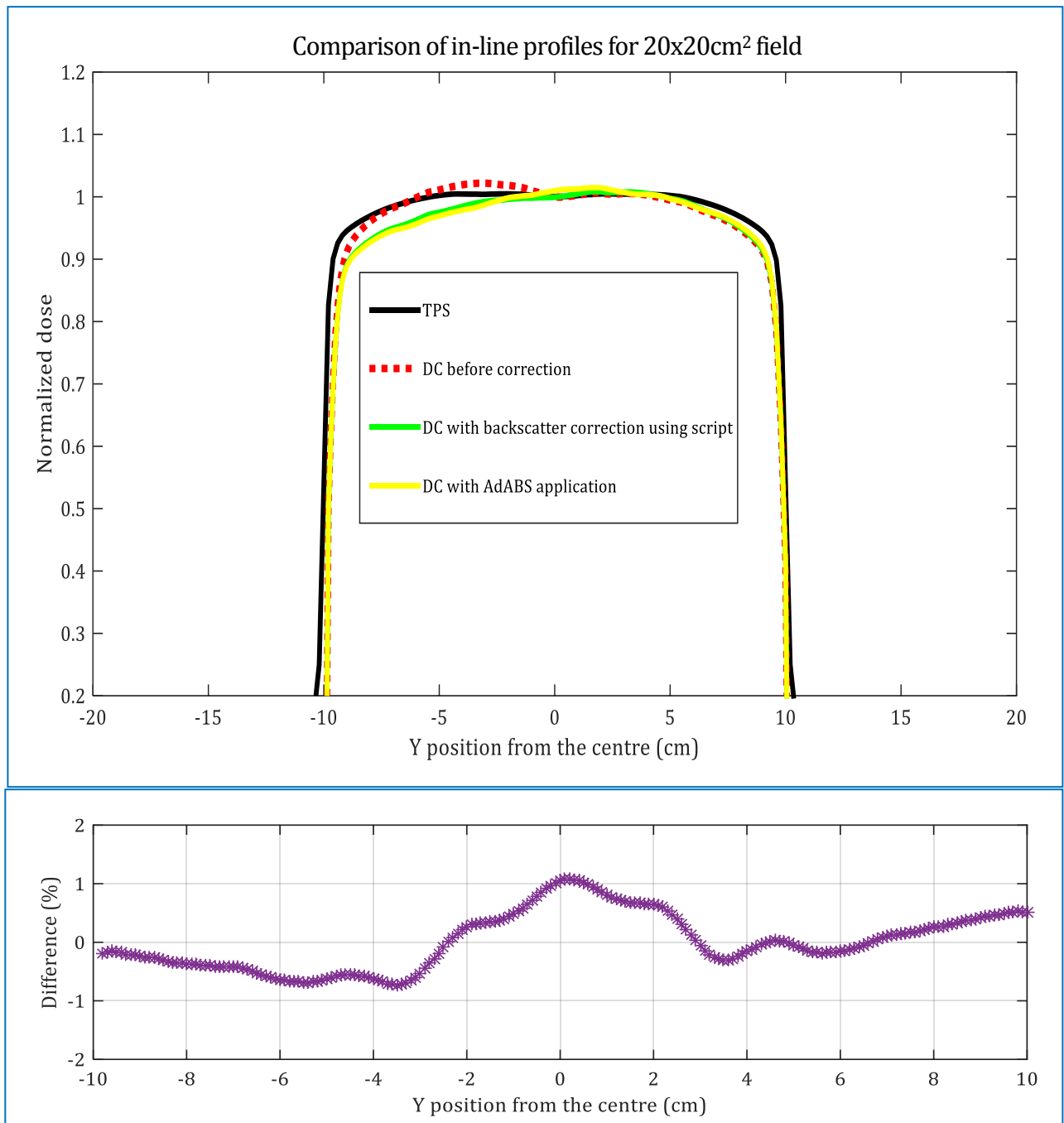


Figure 6.17 – In-line profiles for a 20x20cm² field size before correction (*red dashed line*) and after backscatter correction. The plots show the adjustment to the part of the field (left side of the plots) using the correction matrix for the Matlab script and AdABS methods. However, both methods were in agreement with nearly 1% in percentage dose difference (*purple dotted line*).

While Dosimetry Check is already proven to be a versatile tool, this work suggests that it could benefit from the implementation of backscatter correction to improve its performance as regards to verification accuracy. The correction matrix provides a ready solution that may be incorporated into Dosimetry Check for any linac with the same EPID panel. Thus, this may prove to be an essential tool for RT verification with Dosimetry Check, which may be introduced into clinical practice in the near future.

Chapter 7

CONCLUSION

7.1 CONCLUSION

This work focused on the development of techniques for the verification of advanced radiotherapy (specifically IMRT & VMAT) by portal dosimetry. The following main goals were achieved.

1. A correction method for backscatter from the EPID arm (Varian aS1000) was developed (Chapter 5). The solution was derived from quantification of the non-uniform backscatter reaching the EPID from the arm and resulted in fully symmetrical profiles being generated across the EPID. The technique proved effective and efficient in correcting for the effect of non-uniform backscatter on equivalent square field sizes $\leq 12\text{cm}$. This solution has also been shown to be suitable for application to clinical IMRT, an example of which involved a Head-and-Neck case. Incorporating the solution improved the Gamma Index pass rate analysed for the example case from 82% to 98% for pre-treatment dosimetry (evaluated at 3%/3mm) and from 85% to 97% for the transit dosimetry (evaluated at 5%/3mm).

2. The work in Chapter 5 also demonstrated that the Dosimetry Check portal dosimetry software system performed well as a verification tool, in terms of accuracy in the verification of IMRT treatments, with an average 3% reduction in linac arm backscatter effect as a result of the correction method.
3. This work showed that by applying the backscatter correction method in Dosimetry Check, wider treatment plan verification could be employed clinically (at Velindre Cancer Centre and elsewhere) using beam profile measurement and 2D dose image comparison, in addition to the point dose measurements employed at the moment.
4. A 'proof-of-concept' of this novel correction method was shown to give benefit to pre-treatment VMAT verification techniques (Chapter 6). This solution also improved the agreement between TPS calculated dose and Dosimetry Check measured dose by applying the correction matrix to a continuous set of images obtained during the arc treatment. Average pre-treatment Gamma Index pass rates (for 3%/5mm criterion) improved from 86% to 96% after correction, with an average of 3% reduction in percentage dose difference inferior to the in-line direction between Dosimetry Check and TPS on coronal beam profiles of the arc.
5. The application of AdABS as an efficient method (Chapter 6) of utilising the correction to verify treatment plans within the Dosimetry Check system was investigated. This technique provided a feasible way of applying the correction within Dosimetry Check without the need to generate corrected images using external software (Matlab) scripts for every plan. Ultimately, this will benefit clinical advanced radiotherapy

treatment plan verification by providing a ready solution that will help with (a) minimising storage requirements for saving images and (b) implementing a quick and efficient workflow in Dosimetry Check.

7.2 FUTURE WORK

One of the areas for further development of the work described in this thesis relates to the fact that the matrix-based correction method retains some degree of field-size dependence. However, as the main aim of this work was to enhance clinical treatment verification for IMRT/VMAT, the segmented field sizes involved are generally sufficiently small to benefit from the method. In the future, a suitable correction matrix should be investigated for larger field sizes (>12 cm equivalent square field). Indeed, it is possible that a library of suitable correction matrices could be generated to apply for a fuller range of field sizes.

Furthermore, this work concentrated on Head-and-Neck planning and it could be extended to the verification of IMRT of other tumour sites. Increasing the number of clinical cases would provide more evidence for confidence in the usefulness of the correction strategy. With further work, it is possible that the correction matrix approach could be applied effectively to a wide range of clinical treatments.

Although the correction matrix method was shown to be effective in the verification of VMAT treatment delivery with the Dosimetry Check software, in this work only pre-treatment verification was investigated and discussed. Although the results are very encouraging, further

work is necessary to fully verify the application of the correction to the transit dosimetry of clinical VMAT.

Further work on the AdABS approach to arc delivery is also necessary so ensure that the technique piloted here fully utilises Dosimetry Check to calculate dose within the patient and provides an accurate dose comparison with the TPS.

Finally, the use of the Varian aS1000 EPID employed in this work should not imply that the procedure applies only to this device. Any panel that is similarly affected by non-uniform backscatter should be able to benefit from this correction method to improve the performance and accuracy of in-vivo dosimetry.

REFERENCES

- Ahnesjo, A. 1989. Collapsed cone convolution of radiant energy for photon dose calculation in heterogeneous media. *Med Phys*, 16, 577-592.
- Ahnesjo, A. & Aspradakis, M. M. 1999. Dose calculations for external photon beams in radiotherapy. *Phys Med Biol*, 44, R99-R155.
- Ahnesjo, A., Saxner, M., & Trepp, A. 1992. A pencil beam model for photon dose calculation. *Med Phys*, 19, 263-273.
- Aird, E. G. 1989a. Radiotherapy today and tomorrow--an introduction to optimisation of conformal radiotherapy. *Phys Med Biol*, 34, 1345-1348.
- Aird, E. G. A. 1989b. Radiotherapy today and tomorrow-an introduction to optimisation of conformal radiotherapy. *Physics in Medicine and Biology*, 34, 1345.
- Ali, E. S. M. & Rogers, D. W. O. 2008. Benchmarking EGSnrc in the kilovoltage energy range against experimental measurements of charged particle backscatter coefficients. *Physics in Medicine & Biology*, 53, 1527-1543.
- Althof, V. G., et al. 1996. Physical characteristics of a commercial electronic portal imaging device. *Med Phys*, 23, 1845-1855.
- Alvarez-Moret, J., Pohl, F., Koelbl, O., & Dobler, B. 2010. Evaluation of volumetric modulated arc therapy (VMAT) with Oncentra MasterPlan(R) for the treatment of head and neck cancer. *Radiat Oncol*, 5, 110-120.
- Ansbacher, W., Swift, C. L., & Greer, P. B. 2010. An evaluation of cine-mode 3D portal image dosimetry for Volumetric Modulated Arc Therapy. *Journal of Physics: Conference Series*, 250, 1-4.
- Antonuk, L. E. 2002. Electronic portal imaging devices: a review and historical perspective of contemporary technologies and research. *Phys Med Biol*, 47, R31-R65.
- Antonuk, L. E., et al. 1998. Initial performance evaluation of an indirect-detection, active matrix flat-panel imager (AMFPI) prototype for megavoltage imaging. *International Journal of Radiation Oncology*Biology*Physics*, 42, 437-454.
- Antonuk, L. E., et al. 1996. Megavoltage imaging with a large-area, flat-panel, amorphous silicon imager. *Int J Radiat Oncol Biol Phys*, 36, 661-672.

- Anvari, A., Aghamiri, S. M., Mahdavi, S. R., & Alaei, P. 2015. Dose response characteristics of a novel CCD camera-based electronic portal imaging device comparison with OCTAVIUS detector. *J Cancer Res Ther*, 11, 765-769.
- Aristophanous, M., et al. 2016. Initial clinical experience with ArcCHECK for IMRT/VMAT QA. *J Appl Clin Med Phys*, 17, 1-14.
- Arjomandy, B., et al. 2010. Energy dependence and dose response of Gafchromic EBT2 film over a wide range of photon, electron, and proton beam energies. *Med Phys*, 37, 1942-1947.
- Aspradakis, M. M., Morrison, R. H., Richmond, N. D., & Steele, A. 2003. Experimental verification of convolution/superposition photon dose calculations for radiotherapy treatment planning. *Phys Med Biol*, 48, 2873-2893.
- Baiotto, B., et al. 2009. Quality assurance of a record-and-verify system. *Tumori*, 95, 467-472.
- Bakhtiari, M., et al. 2011. Using an EPID for patient-specific VMAT quality assurance. *Med Phys*, 38, 1366-1373.
- Barnes, M. P., Rowshanfarzad, P., & Greer, P. B. 2016. VMAT linear accelerator commissioning and quality assurance: dose control and gantry speed tests. *J Appl Clin Med Phys*, 17, 246-261.
- Bawazeer, O., Herath, S., Sarasanandarajah, S., & Deb, P. Electronic Portal Imaging Device Dosimetry for IMRT: a Review on Commercially Available Solutions. World Congress on Medical Physics and Biomedical Engineering, June 7-12, 2015, Toronto, Canada, 2015. Springer Publishing, pg.553-556.
- Bawazeer, O., Herath, S., Sarasanandarajah, S., Kron, T., & Deb, P. 2017. The influence of acquisition mode on the dosimetric performance of an amorphous silicon electronic portal imaging device. *Journal of Medical Physics*, 42, 90-95.
- Bawazeer, O., Sarasanandarajah, S., Herath, S., Kron, T., & Deb, P. 2016. SU-F-T-263: Dosimetric Characteristics of the Cine Acquisition Mode of An A-Si EPID. *Medical Physics*, 43, 3523-3523.
- Bedford, J. L. 2009. Treatment planning for volumetric modulated arc therapy. *Med Phys*, 36, 5128-5138.
- Berger, L., Francois, P., Gaboriaud, G., & Rosenwald, J. C. 2006. Performance optimization of the Varian aS500 EPID system. *J Appl Clin Med Phys*, 7, 105-114.
- Berry, S. L., Polvorosa, C. S., & Wu, C.-S. 2010. A field size specific backscatter correction algorithm for accurate EPID dosimetry. *Medical Physics*, 37, 2425-2434.
- Bertelsen, A., Hansen, C. R., Johansen, J., & Brink, C. 2010. Single Arc Volumetric Modulated Arc Therapy of head and neck cancer. *Radiotherapy and oncology : journal of the European Society for Therapeutic Radiology and Oncology*, 95, 142-148.

- Blake, S. J., et al. 2014. Monte Carlo simulation of the transit dosimetric response of an a-Si electronic portal imaging device. *Journal of Physics: Conference Series*, 489, 1-10.
- Blake, S. J., et al. 2013. Characterization of optical transport effects on EPID dosimetry using Geant4. *Medical Physics*, 40, 1-14.
- Boissard, P., François, P., & Mazal, A. 2009. The use of aSi EPID for in vivo dosimetry in photon beams: clinical experience. In: DÖSSEL, O. & SCHLEGEL, W. C. (eds.) *World Congress on Medical Physics and Biomedical Engineering*, Munich, Germany Berlin, Heidelberg: Radiation Oncology.
- Boyer, A. L., et al. 1992. A review of electronic portal imaging devices (EPIDs). *Medical Physics*, 19, 1-16.
- Buzdar, S. A., Afzal, M., & Todd-Pokropek, A. 2010. Comparison of pencil beam and collapsed cone algorithms, in radiotherapy treatment planning for 6 and 10 MV photon. *J Ayub Med Coll Abbottabad*, 22, 152-154.
- Bzdusek, K., et al. 2009. Development and evaluation of an efficient approach to volumetric arc therapy planning. *Med Phys*, 36, 2328-2339.
- Chavaudra, J. & Bridier, A. 2001. [Definition of volumes in external radiotherapy: ICRU reports 50 and 62]. *Cancer radiotherapie : journal de la Societe francaise de radiotherapie oncologique*, 5, 472-478.
- Chetty, I. 2008. *Monte Carlo Treatment Planning—An Introduction: Report 16 of the Netherlands Commission on Radiation Dosimetry*.
- Chetty, I. J., et al. 2007. Report of the AAPM Task Group No. 105: Issues associated with clinical implementation of Monte Carlo-based photon and electron external beam treatment planning. *Medical Physics*, 34, 4818-4853.
- Chin, P. W., Spezi, E., & Lewis, D. G. 2003. Monte Carlo simulation of portal dosimetry on a rectilinear voxel geometry: a variable gantry angle solution. *Phys Med Biol*, 48, N231-N238.
- Cremers, F., et al. 2004. Performance of electronic portal imaging devices (EPIDs) used in radiotherapy: Image quality and dose measurements. *Medical Physics*, 31, 985-996.
- Cufflin, R., Spezi, E., Millin, A., & Lewis, D. G. 2011. 522 ORAL TREATMENT PLANNING SYSTEM BASED EXIT DOSIMETRY. *Radiotherapy and Oncology*, 99, Supplement 1, S212-S212.
- Cufflin, R., Spezi, E., Millin, T., & Lewis, G. 2009. DEVELOPMENT OF A MONTE CARLO BASED TECHNIQUE TO IMPROVE ACCURACY OF PORTAL DOSIMETRY. *Radiotherapy and Oncology*, 92, Supplement 1, S212-S212.
- Cufflin, R. S. 2012. *Verification of Intensity Modulated Radiotherapy*. PhD, Cardiff University.

- Cufflin, R. S., Spezi, E., Millin, A. E., & Lewis, D. G. 2010. An investigation of the accuracy of Monte Carlo portal dosimetry for verification of IMRT with extended fields. *Phys Med Biol*, 55, 4589-4600.
- Devic, S. 2011. Radiochromic film dosimetry: past, present, and future. *Phys Med*, 27(3), 122-134.
- Devic, S., et al. 2005. Precise radiochromic film dosimetry using a flat-bed document scanner. *Med Phys*, 32, 2245-2253.
- Donaldson, S. L. 2007. On the state of public health: Annual report of the Chief Medical Officer 2006 London Department of Health.
- Downes, P., et al. 2009. High-performance computing for Monte Carlo radiotherapy calculations. *Philos Trans A Math Phys Eng Sci*, 367, 2607-2617.
- El-Maraghy, K. A., Metwaly, M., Mahmoud El-Sayed, E.-S., & Mohamed Sallam, A. 2014. A quality assurance technique for the static multileaf collimator mode based on intrinsic base lines. *Journal of Radiation Research and Applied Sciences*, 7, 230-240.
- Essers, M., Boellaard, R., Van Herk, M., Lanson, H., & Mijnheer, B. 1996. Transmission dosimetry with a liquid-filled electronic portal imaging device. *Int J Radiat Oncol Biol Phys*, 34, 931-941.
- Essers, M. & Mijnheer, B. J. 1999. In vivo dosimetry during external photon beam radiotherapy. *Int J Radiat Oncol Biol Phys*, 43, 245-259.
- Ezzell, G. A., et al. 2003. Guidance document on delivery, treatment planning, and clinical implementation of IMRT: report of the IMRT Subcommittee of the AAPM Radiation Therapy Committee. *Med Phys*, 30, 2089-2115.
- Fafi, S., et al. 2013. Clinical experience of in vivo dosimetry 3D (dosimetry check) by portal imaging for treatment of breast cancer. *Physica Medica*, 29, Supplement 1, E32-E33.
- Fraass, B. A. 2008. QA issues for computer-controlled treatment delivery: This is not your old R/V system any more! *Int J Radiat Oncol Biol Phys*, 71, S98-S102.
- Francescon, P., Cora, S., & Chiovati, P. 2003. Dose verification of an IMRT treatment planning system with the BEAM EGS4-based Monte Carlo code. *Medical Physics*, 30, 144-157.
- Franken, E. M., De Boer, J. C., Barnhoorn, J. C., & Heijmen, B. J. 2004. Characteristics relevant to portal dosimetry of a cooled CCD camera-based EPID. *Med Phys*, 31, 2549-2551.
- Franken, E. M., De Boer, J. C., & Heijmen, B. J. 2006. A novel approach to accurate portal dosimetry using CCD-camera based EPIDs. *Med Phys*, 33, 888-903.

- Galvin, J. M., et al. 2004. Implementing IMRT in clinical practice: a joint document of the American Society for Therapeutic Radiology and Oncology and the American Association of Physicists in Medicine. *Int J Radiat Oncol Biol Phys*, 58, 1616-1634.
- Gillies, R. J., Kinahan, P. E., & Hricak, H. 2015. Radiomics: Images Are More than Pictures, They Are Data. *Radiology*, 278, 563-577.
- Gimeno, J., et al. 2014. Commissioning and initial experience with a commercial software for in vivo volumetric dosimetry. *Physica Medica*, 30, 954-959.
- Greer, P. B. 2013. 3D EPID based dosimetry for pre-treatment verification of VMAT – methods and challenges. *Journal of Physics: Conference Series*, 444, 1-7.
- Greer, P. B., Cadman, P., Lee, C., & Bzdusek, K. 2009. An energy fluence-convolution model for amorphous silicon EPID dose prediction. *Medical Physics*, 36, 547-555.
- Greer, P. B. & Popescu, C. C. 2003. Dosimetric properties of an amorphous silicon electronic portal imaging device for verification of dynamic intensity modulated radiation therapy. *Med Phys*, 30, 1618-1627.
- Hansjoerg, W., et al. 2010. Fast kilovoltage/megavoltage (kVMV) breathhold cone-beam CT for image-guided radiotherapy of lung cancer. *Physics in Medicine and Biology*, 55, 4203-4217.
- Hasenbalg, F., Fix, M. K., Born, E. J., Mini, R., & Kawrakow, I. 2008. VMC++ versus BEAMnrc: a comparison of simulated linear accelerator heads for photon beams. *Med Phys*, 35, 1521-1531.
- Heath, E. & Seuntjens, J. 2003. Development and validation of a BEAMnrc component module for accurate Monte Carlo modelling of the Varian dynamic Millennium multileaf collimator. *Phys Med Biol*, 48, 4045-4063.
- Heijmen, B. J. M., et al. 1995. Portal dose measurement in radiotherapy using an electronic portal imaging device (EPID). *Physics in Medicine & Biology*, 40, 1943-1955.
- Hong, L., et al. 1996. A pencil beam algorithm for proton dose calculations. *Phys Med Biol*, 41, 1305-1330.
- Hurter, F. a. D., V.C. 1890. Photochemical Investigations and a New Method of Determination of the Sensitiveness of Photographic Plates. *J Soc Chem Industry*, 9, 455-469.
- ICRU Report 37 (1984), 'Stopping Powers for Electrons and Positrons'.
- ICRU Report 50 (1994), 'Prescribing, Recording and Reporting Photon Beam Therapy'.
- ICRU Report 62 (1999), 'Prescribing, Recording and Reporting Photon Beam Therapy (Supplement to ICRU Report 50)'.

ICRU Report 83 (2010), 'Prescribing, Recording, and Reporting Intensity-Modulated Radiation Therapy (IMRT)'.

International Atomic Energy Agency (2017). *Record and Verify Systems for Radiation Treatment of Cancer: Acceptance Testing, Commissioning and Quality Control*. [Online] Available at: <http://www-pub.iaea.org/books/IAEABooks/8941/Record-and-Verify-Systems-for-Radation-Treatment-of-Cancer-Acceptance-Testing-Commissioning-and-Quality-Control> [Accessed on 9 Nov 2017].

Iori, M., Cagni, E., Paiusco, M., Munro, P., & Nahum, A. E. 2010. Dosimetric verification of IMAT delivery with a conventional EPID system and a commercial portal dose image prediction tool. *Medical Physics*, 37, 377-390.

Jabbari, K. 2011. Review of Fast Monte Carlo Codes for Dose Calculation in Radiation Therapy Treatment Planning. *Journal of Medical Signals and Sensors*, 1, 73-86.

Jaffray, D. A., Battista, J. J., Fenster, A., & Munro, P. 1994. X-ray scatter in megavoltage transmission radiography: physical characteristics and influence on image quality. *Med Phys*, 21, 45-60.

Jonathan, R. S. & Peter, C. W. 1998. An experimental investigation of the tongue and groove effect for the Philips multileaf collimator. *Physics in Medicine & Biology*, 43, 3157-3165.

Joseph, A. M. & Jeffrey, V. S. 2005. Verification of the optimal backscatter for an aSi electronic portal imaging device. *Physics in Medicine and Biology*, 50, 2341-2350.

Kawrakow, I. 2000. Accurate condensed history Monte Carlo simulation of electron transport. I. EGSnrc, the new EGS4 version. *Medical Physics*, 27, 485-498.

Kawrakow, I. & Bielajew, A. F. 1998. On the condensed history technique for electron transport. *Nuclear Instruments and Methods in Physics Research Section B: Beam Interactions with Materials and Atoms*, 142, 253-280.

Kawrakow, I. & Rogers, D. W. O. 2013. The EGSnrc code system: Monte Carlo simulation of electron and photon transport. National Research Council Canada (NRCC), Ottawa, Canada.

Kawrakow, I., Rogers, D. W. O., & Walters, B. R. B. 2004. Large efficiency improvements in BEAMnrc using directional bremsstrahlung splitting. *Medical Physics*, 31, 2883-2898.

Kawrakow, I. & Walters, B. R. 2006. Efficient photon beam dose calculations using DOSXYZnrc with BEAMnrc. *Med Phys*, 33, 3046-3056.

Keall, P. J., Siebers, J. V., Arnfield, M., Kim, J. O., & Mohan, R. 2001. Monte Carlo dose calculations for dynamic IMRT treatments. *Phys Med Biol*, 46, 929-941.

Khan, F. M. & Gibbons, J. P. 2014. *Khan's The Physics of Radiation Therapy*, Wolters Kluwer Health.

- Klein, E. E., et al. 2009. Task Group 142 report: quality assurance of medical accelerators. *Med Phys*, 36, 4197-4212.
- Knoos, T., Ahnesjo, A., Nilsson, P., & Weber, L. 1995. Limitations of a pencil beam approach to photon dose calculations in lung tissue. *Physics in Medicine and Biology*, 40, 1411-1420.
- Knoos, T., et al. 2006. Comparison of dose calculation algorithms for treatment planning in external photon beam therapy for clinical situations. *Phys Med Biol*, 51, 5785-5807.
- Langmack, K. A. 2001. Portal imaging. *Br J Radiol*, 74, 789-804.
- Langmack, K. A. & Goss, V. 1999. Characterization of new portal film systems for radiotherapy verification. *Br J Radiol*, 72, 479-484.
- Law, M. Y., Liu, B., & Chan, L. W. 2009. DICOM-RT-based Electronic Patient Record Information System for Radiation Therapy. *Radiographics*, 29, 961-972.
- Leal, A., et al. 2003. Routine IMRT verification by means of an automated Monte Carlo simulation system. *Int J Radiat Oncol Biol Phys*, 56, 58-68.
- Li, X. A., Ma, L., Naqvi, S., Shih, R., & Yu, C. 2001. Monte Carlo dose verification for intensity-modulated arc therapy. *Phys Med Biol*, 46, 2269-2282.
- Liu, H. H., Mackie, T. R., & Mccullough, E. C. 1997a. Calculating output factors for photon beam radiotherapy using a convolution/superposition method based on a dual source photon beam model. *Med Phys*, 24, 1975-1985.
- Liu, H. H., Mackie, T. R., & Mccullough, E. C. 1997b. A dual source photon beam model used in convolution/superposition dose calculations for clinical megavoltage x-ray beams. *Med Phys*, 24, 1960-1974.
- Liu, H. H., Mackie, T. R., & Mccullough, E. C. 2000. Modeling photon output caused by backscattered radiation into the monitor chamber from collimator jaws using a Monte Carlo technique. *Medical Physics*, 27, 737-744.
- Low, D. A., Harms, W. B., Mutic, S., & Purdy, J. A. 1998. A technique for the quantitative evaluation of dose distributions. *Med Phys*, 25, 656-661.
- Lung, K., Jong Oh, K., & Jeffrey, V. S. 2004. Investigation of the optimal backscatter for an aSi electronic portal imaging device. *Physics in Medicine and Biology*, 49, 1723-1738.
- Ma, C. M. & Li, J. S. Monte Carlo Dose Calculation for Radiotherapy Treatment Planning: Dose to Water or Dose to Medium? *In: DÖSSEL, O. & SCHLEGEL, W. C., eds. World Congress on Medical Physics and Biomedical Engineering, September 7 - 12, 2009, Munich, Germany, 2009// 2009 Berlin, Heidelberg. Springer Berlin Heidelberg, 326-329.*

- Ma, C. M., et al. 2005. Effect of statistical uncertainties on Monte Carlo treatment planning. *Physics in Medicine and Biology*, 50, 891-907.
- Ma, C. M., et al. 2000. Monte Carlo verification of IMRT dose distributions from a commercial treatment planning optimization system. *Phys Med Biol*, 45, 2483-2495.
- Mancosu, P., et al. 2015. In-vivo dosimetry with Gafchromic films for multi-isocentric VMAT irradiation of total marrow lymph-nodes: a feasibility study. *Radiation Oncology (London, England)*, 10, 1-9.
- Mans, A., et al. 2010. Catching errors with in vivo EPID dosimetry. *Med Phys*, 37, 2638-2644.
- Math Resolutions, LLC. 2017. Dosimetry Check Manual Version 5, Release 4 Columbia, Maryland
- Mayles, P., Nahum, A., & Rosenwald, J. C. 2007. *Handbook of Radiotherapy Physics: Theory and Practice*, CRC Press, Michigan, USA.
- Mccowan, P. M., et al. 2017. A model-based 3D patient-specific pre-treatment QA method for VMAT using the EPID. *Physics in Medicine and Biology*, 62, 1600-1612.
- Mccowan, P. M. & Mccurdy, B. M. 2016. Frame average optimization of cine-mode EPID images used for routine clinical in vivo patient dose verification of VMAT deliveries. *Med Phys*, 43, 254-261.
- Mccurdy, B. M. & Greer, P. B. 2009. Dosimetric properties of an amorphous-silicon EPID used in continuous acquisition mode for application to dynamic and arc IMRT. *Med Phys*, 36, 3028-3039.
- Mccurdy, B. M. C., Luchka, K., & Pistorius, S. 2001. Dosimetric investigation and portal dose image prediction using an amorphous silicon electronic portal imaging device. *Medical Physics*, 28, 911-924.
- Mccurdy, B. M. C. & Pistorius, S. 2000. A two step algorithm for predicting portal dose images in arbitrary detectors. Proceedings of the 22nd Annual International Conference of the IEEE Engineering in Medicine and Biology Society (Cat. No.00CH37143). 1062-1065
- Mcdermott, L. N., Louwe, R. J., Sonke, J. J., Van Herk, M. B., & Mijnheer, B. J. 2004. Dose-response and ghosting effects of an amorphous silicon electronic portal imaging device. *Med Phys*, 31, 285-295.
- Mijnheer, B., Beddar, S., Izewska, J., & Reft, C. 2013a. In vivo dosimetry in external beam radiotherapy. *Medical Physics*, 40, 1-19.
- Mijnheer, B., et al. 2013b. 3D EPID-based in vivo dosimetry for IMRT and VMAT. *Journal of Physics: Conference Series*, 444, 1-7.

- Mijnheer, B., et al. 2015. Current status of 3D EPID-based in vivo dosimetry in The Netherlands Cancer Institute. *Journal of Physics: Conference Series*, 573, 1-4.
- Mijnheer, B., et al. 2017. New developments in EPID-based 3D dosimetry in The Netherlands Cancer Institute. *Journal of Physics: Conference Series*, 847, 1-4.
- Mohammed, M., Chakir, E., Boukhal, H., Saeed, M., & El Bardouni, T. 2016. Evaluation of variance reduction techniques in BEAMnrc Monte Carlo simulation to improve the computing efficiency. *Journal of Radiation Research and Applied Sciences*, 9, 424-430.
- Monville, M. E., Kuncic, Z., & Greer, P. B. 2014. An improved Monte-Carlo model of the Varian EPID separating support arm and rear-housing backscatter. *Journal of Physics: Conference Series*, 489, 1-5.
- Moylan, R., Aland, T., & Kairn, T. 2013. Dosimetric accuracy of Gafchromic EBT2 and EBT3 film for in vivo dosimetry. *Australasian Physical & Engineering Sciences in Medicine*, 36, 331-337.
- Munjal, R. K., et al. 2006. Impact of 6MV photon beam attenuation by carbon fiber couch and immobilization devices in IMRT planning and dose delivery. *Journal of Medical Physics / Association of Medical Physicists of India*, 31, 67-71.
- Munro, P. 1995. Portal Imaging Technology: Past, Present, and Future. *Semin Radiat Oncol*, 5, 115-133.
- Narayanasamy, G., Zalman, T., Ha, C. S., Papanikolaou, N., & Stathakis, S. 2015. Evaluation of Dosimetry Check software for IMRT patient-specific quality assurance. *J Appl Clin Med Phys*, 16, 329-338.
- Nelson, W. R., Hirayama, H., & Rogers, D. W. O. 1985. EGS4 code system. Stanford Linear Accelerator Center, Menlo Park, CA (USA).
- Nishimura, Y. & Komaki, R. 2015. *Intensity-Modulated Radiation Therapy: Clinical Evidence and Techniques*, Japan, Springer Japan.
- Nucletron 2008a. Physics and Algorithms. *Oncentra - External Beam v4.3*
- Nucletron 2008b. Radiation Commissioning and Quality Assurance *Oncentra - External Beam v4.3*
- Olch, A. J., Gerig, L., Li, H., Mihaylov, I., & Morgan, A. 2014. Dosimetric effects caused by couch tops and immobilization devices: Report of AAPM Task Group 176. *Medical Physics*, 41, 1-30.
- Otto, K. 2008. Volumetric modulated arc therapy: IMRT in a single gantry arc. *Med Phys*, 35, 310-317.

- Paelinck, L., De Neve, W., & De Wagter, C. 2007. Precautions and strategies in using a commercial flatbed scanner for radiochromic film dosimetry. *Phys Med Biol*, 52, 231-242.
- Parent, L., Fielding, A. L., Dance, D. R., Seco, J., & Evans, P. M. 2007. Amorphous silicon EPID calibration for dosimetric applications: comparison of a method based on Monte Carlo prediction of response with existing techniques. *Physics in Medicine and Biology*, 52, 3351-3368.
- Parsaei, H., El-Khatib, E., & Rajapakshe, R. 1998. The use of an electronic portal imaging system to measure portal dose and portal dose profiles. *Med Phys*, 25, 1903-1909.
- Pasma, K. L., Kroonwijk, M., De Boer, J. C., Visser, A. G., & Heijmen, B. J. 1998. Accurate portal dose measurement with a fluoroscopic electronic portal imaging device (EPID) for open and wedged beams and dynamic multileaf collimation. *Phys Med Biol*, 43, 2047-2060.
- Pejman, R., Mahsheed, S., Daryl, J. O. C., & Peter, B. G. 2010. Reduction of the effect of non-uniform backscatter from an E-type support arm of a Varian a-Si EPID used for dosimetry. *Physics in Medicine and Biology*, 55, 6617-6632.
- Pianykh, O. S. 2008. *Digital Imaging and Communications in Medicine: A Practical Introduction and Survival Guide*, Berlin, Heidelberg, Springer Publishing Company, Incorporated.
- Piermattei, A., et al. 2009. In patient dose reconstruction using a cine acquisition for dynamic arc radiation therapy. *Med Biol Eng Comput*, 47, 425-433.
- Pinkerton, A., Hannon, M., Kwag, J., & Renner, W. D. 2010. Experience Using DosimetryCheck software for IMRT and RapidArc Patient Pre-treatment QA and a New Feature for QA during Treatment. *Journal of Physics: Conference Series*, 250, 1-5.
- Public Health England (PHE), UK (2017a). Safer Radiotherapy - Radiotherapy Newsletter of Public Health England, January 2017 Issue 21. [Online] Available at: http://www.gov.uk/government/uploads/system/uploads/attachment_data/file/587813/safer_radiotherapy_newsletter_issue_21.pdf [Accessed on 8 Jan. 2018].
- Public Health England (PHE), UK (2017b). Safer Radiotherapy - Radiotherapy Newsletter of Public Health England, January 2017 Issue 23. [Online] Available at: http://www.gov.uk/government/uploads/system/uploads/attachment_data/file/648243/safer_radiotherapy_newsletter_issue_23.pdf [Accessed on 8 Jan. 2018].
- Radiology Imaging. (2017). Principles and Practice of Radiation Treatment Planning. [Online] Available at: <https://radiologykey.com/principles-and-practice-of-radiation-treatment-planning/> [Accessed on 10 Nov 2017].
- Reilly, A. 2016a. Evaluation of a new electronic portal imaging device (EPID) for in vivo dosimetry applications. *Physica Medica: European Journal of Medical Physics*, 32, E20-E20.

- Reilly, A. 2016b. *Next Generation MV Image Detector - Raising Portal Dosimetry to a New Level* [Online]. Varian Medical System. Available: <https://varian.force.com/apex/CpWebSummary?id=a0OE000000jonkmMAA> [Accessed on 20 April 2018].
- Reilly, A., Rutkowska, E., Gilmore, M., Gately, A., & Furlong, C. 2013. Clinical implementation of 'Dosimetry Check' for patient in vivo dosimetry using transit electronic portal images acquired during treatment. *Physica Medica*, 29, 568-575.
- Renner, W. D., Norton, K., & Holmes, T. 2005. A method for deconvolution of integrated electronic portal images to obtain incident fluence for dose reconstruction. *J Appl Clin Med Phys*, 6, 22-39.
- Renner, W. D., Sarfaraz, M., Earl, M. A., & Yu, C. X. 2003. A dose delivery verification method for conventional and intensity-modulated radiation therapy using measured field fluence distributions. *Medical Physics*, 30, 2996-3005.
- Rogers, D. W. O. 2006. Fifty years of Monte Carlo simulations for medical physics. *Physics in Medicine and Biology*, 51, R287-R301.
- Rogers, D. W. O., et al. 1995. BEAM: A Monte Carlo code to simulate radiotherapy treatment units. *Medical Physics*, 22, 503-524.
- Rogers, D. W. O., Walters, B. R. B., & Kawrakow, I. 2011. BEAMnrc users manual. National Research Council Canada (NRCC), Ottawa, Canada.
- Rowshanfarzad, P., et al. 2010a. Measurement and modeling of the effect of support arm backscatter on dosimetry with a Varian EPID. *Medical Physics*, 37, 2269-2278.
- Rowshanfarzad, P., Sabet, M., O'connor, D. J., & Greer, P. B. 2010b. Reduction of the effect of non-uniform backscatter from an E-type support arm of a Varian a-Si EPID used for dosimetry. *Phys Med Biol*, 55, 6617-6632.
- Rowshanfarzad, P., et al. 2012. Detection and correction for EPID and gantry sag during arc delivery using cine EPID imaging. *Med Phys*, 39, 623-635.
- Rowshanfarzad, P., Sabet, M., O'connor, J., & Greer, P. 2011. Verification of the linac isocentre for stereotactic radiosurgery using cine-EPID imaging and arc delivery. *Med Phys*, 38, 3963-3970.
- Sabet, M., Rowshanfarzad, P., Vial, P., Menk, F. W., & Greer, P. B. 2012. Transit dosimetry in IMRT with an a-Si EPID in direct detection configuration. *Phys Med Biol*, 57, N295-N306.
- Salari, E., Men, C., & Romeijn, H. E. 2011. Accounting for the tongue-and-groove effect using a robust direct aperture optimization approach. *Med Phys*, 38, 1266-1279.

- Sankar, A., et al. 2006. Comparison of Kodak EDR2 and Gafchromic EBT film for intensity-modulated radiation therapy dose distribution verification. *Medical Dosimetry*, 31, 273-282.
- Scott, A. J., Nahum, A. E., & Fenwick, J. D. 2008. Using a Monte Carlo model to predict dosimetric properties of small radiotherapy photon fields. *Med Phys*, 35, 4671-4684.
- Scott, A. J. D., Nahum, A. E., & Fenwick, J. D. 2009. Monte Carlo modeling of small photon fields: Quantifying the impact of focal spot size on source occlusion and output factors, and exploring miniphantom design for small-field measurements. *Medical Physics*, 36, 3132-3144.
- Seco, J. & Verhaegen, F. 2013. *Monte Carlo Techniques in Radiation Therapy*, CRC Press.
- Sempau, J., et al. 2001. Monte Carlo simulation of electron beams from an accelerator head using PENELOPE. *Phys Med Biol*, 46, 1163-1186.
- Sheikh-Bagheri, D., Rogers, D. W., Ross, C. K., & Seuntjens, J. P. 2000. Comparison of measured and Monte Carlo calculated dose distributions from the NRC linac. *Med Phys*, 27, 2256-2566.
- Siochi, R. A., Molineu, A., & Orton, C. G. 2013. Point/Counterpoint. Patient-specific QA for IMRT should be performed using software rather than hardware methods. *Med Phys*, 40, 1-3.
- Soukal, P. & Spahn, M. 2012. *Flat image detector and method for the generation of medical digital images*. United States patent application 13/211,800.
- Spezi, E. & Lewis, D. G. 2002. Full forward Monte Carlo calculation of portal dose from MLC collimated treatment beams. *Physics in Medicine and Biology*, 47, 377-390.
- Spezi, E., Lewis, D. G., & Smith, C. W. 2002. A DICOM-RT-based toolbox for the evaluation and verification of radiotherapy plans. *Physics in Medicine and Biology*, 47, 4223-4232.
- Stroom, J. C. & Heijmen, B. J. M. 2002. Geometrical uncertainties, radiotherapy planning margins, and the ICRU-62 report. *Radiotherapy and Oncology*, 64, 75-83.
- Tangboonduangjit, P., Wu, I., Butson, M., Rosenfeld, A., & Metcalfe, P. 2003. Intensity modulated radiation therapy: film verification of planar dose maps. *Australas Phys Eng Sci Med*, 26, 194-199.
- Tateoka, K., et al. 2006. Dosimetric properties of the liquid ionization chamber electronic portal imaging device (EPID). *Igaku Butsuri*, 26, 28-38.
- Thames, H. D. 1992. On the origin of dose fractionation regimens in radiotherapy. *Seminars in Radiation Oncology*, 2, 3-9.
- Thames, H. D., Jr., Withers, H. R., Peters, L. J., & Fletcher, G. H. 1982. Changes in early and late radiation responses with altered dose fractionation: implications for dose-survival relationships. *Int J Radiat Oncol Biol Phys*, 8, 219-226.

- The Royal College of Radiologists, Society and College of Radiographers, Institute of Physics and Engineering in Medicine, National Patient Safety Agency, British Institute of Radiology. 2008a. Towards Safer Radiotherapy. London: *The Royal College of Radiologists*.
- The Royal College of Radiologists, Society and College of Radiographers, Institute of Physics and Engineering in Medicine. 2008b. On target: Ensuring Geometric Accuracy in Radiotherapy.. London: *The Royal College of Radiologists*.
- Van Elmpt, W., Ezzell, G. A., & Orton, C. G. 2009. Point/Counterpoint. EPID dosimetry must soon become an essential component of IMRT quality assurance. *Med Phys*, 36, 4325-4327.
- Van Elmpt, W., et al. 2008. A literature review of electronic portal imaging for radiotherapy dosimetry. *Radiotherapy and Oncology*, 88, 289-309.
- Van Esch, A., Depuydt, T., & Huyskens, D. P. 2004. The use of an aSi-based EPID for routine absolute dosimetric pre-treatment verification of dynamic IMRT fields. *Radiother Oncol*, 71, 223-234.
- Van Herk, M. & Meertens, H. 1988. A matrix ionisation chamber imaging device for on-line patient setup verification during radiotherapy. *Radiother Oncol*, 11, 369-378.
- Van Prooijen, M., Kanesalingam, T., Islam, M. K., & Heaton, R. K. 2010. Assessment and management of radiotherapy beam intersections with the treatment couch. *Journal of Applied Clinical Medical Physics*, 11, 128-139.
- Verhaegen, F. & Seuntjens, J. 2003. Monte Carlo modelling of external radiotherapy photon beams. *Phys Med Biol*, 48, R107-R164.
- Villaggi, E. 2016. EPID-based dosimetry using a commercial software: Gamma analysis and DVH metrics for VMAT pre-treatment and in vivo QA. *Physica Medica*, 32, 262-270.
- Vinall, A. J., Williams, A. J., Currie, V. E., Esch, A. V., & Huyskens, D. 2010. Practical guidelines for routine intensity-modulated radiotherapy verification: pre-treatment verification with portal dosimetry and treatment verification with in vivo dosimetry. *The British Journal of Radiology*, 83, 949-957.
- Wang, X., et al. 1996. Dosimetric verification of intensity-modulated fields. *Med Phys*, 23, 317-327.
- Winkler, P., Hefner, A., & Georg, D. 2005. Dose-response characteristics of an amorphous silicon EPID. *Med Phys*, 32, 3095-3105.
- Woodruff, H. C. & Greer, P. B. 2013. 3D Dose reconstruction: Banding artefacts in cine mode EPID images during VMAT delivery. *Journal of Physics: Conference Series*, 444, 1-4.
- Yaikhom, G., et al. A distributed simulation framework for conformal radiotherapy. 2008 IEEE International Symposium on Parallel and Distributed Processing, 14-18 April 2008 2008. 1-8.

Zhang, P., et al. 2014. A new pencil beam model for photon dose calculations in heterogeneous media. *Physica Medica*, 30, 765-773.

PUBLICATIONS/PRESENTATIONS

Published conference abstract:

- i. Md Radzi, Y., Windle, R. S., Lewis, D. G., & Spezi, E. 2017. EP-1473: Improving the accuracy of dosimetry verification by non-uniform backscatter correction in the EPID. *Radiotherapy and Oncology*, 123, S787-S787.

Proffered conference poster presentation:

- i. 'Evaluation of non-uniform backscatter correction to aS1000 EPID for in vivo dosimetric verification', UK Radiological and Radiation Oncology Congress (UKRC/UKRO) Manchester 2017.
- ii. 'Improving the accuracy of Dosimetry Verification by non-uniform backscatter correction in the EPID', European Society for Therapeutic Radiation and Oncology (ESTRO) 36, Vienna, Austria, 2017.

Proffered conference oral presentation:

- i. 'Enhancing in vivo dosimetry verification of patient specific QA using EPID-based DC software', All-Wales Medical Physics and Medical Engineering Summer Meeting, Swansea, UK, 2017. – Awarded prize for the best presentation in the rapid update session.